Inclusive Scattering of Polarized Electrons from Polarized Protons in the Δ - Excitation Region with BLAST

BY

Octavian Florin Filoti

M.S. in Physics, University of Bucharest, 1996
Diploma of Eng. in Engineering Physics, University of Bucharest, Romania, 1995
B.S. in Physics, University of Bucharest, Romania, 1995

DISSERTATION

Submitted to the University of New Hampshire
in partial fulfillment of
the requirements for the degree of

Doctor of Philosophy

in

Physics

April 2007

This dissertation has been examined and approved.

Director, J. R. Calarco
Professor of Physics

W. F. Hersman
Professor of Physics

J. F. Dawson
Professor of Physics

J. M. Ryan
Professor of Physics

T. W. Donnelly
Senior Research Scientist (MIT)

M. Kohl
Research Scientist (MIT)

Date

Dedication

To my parents.

Acknowledgments

I want to thank my advisor Prof. John Calarco for his support, patience and guidance during my Ph.D. program.

I like to thank Prof. Apostol Stefan who opened the "physics door" for me.

I would like to thank my Professors from the University of Bucharest for teaching me modern physics.

After College, I worked for three years at the Institute for Nuclear Research, Pitesti, Romania: thank you all for everything.

I also like to thank my Professors from the University of New Hampshire for expanding my 'horizon' in physics.

I would also like to thank to MIT-Bates Laboratory staff for the nice environment and for making BLAST possible.

I thank my doctoral committee members for their encouragements.

To all graduate students working at BLAST: I could not make it without you guys, thanks a lot.

To Alexander Ilyichev (Sasha): thank you for teaching me radiative corrections.

To George Caia: thanks for explaining me the pion production theory.

Many thanks to the BLAST collaboration for a job well done.

To all my friends and my family for your love and support: I love you.

Table of Contents

List of Figures

List of Tables

ABSTRACT

Inclusive Scattering of Polarized Electrons from Polarized Protons in the Δ - Excitation Region with BLAST

by

Octavian Florin Filoti
University of New Hampshire, April, 2007

Inclusive scattering of polarized electrons from polarized protons has been studied using the BLAST detector at MIT-Bates Linear Accelerator Center. The Bates Large Acceptance Spectrometer Toroid (BLAST) is a detector designed to study in a comprehensive and precise way the spin-dependent electromagnetic response in one and few-body systems over a large kinematic range. It has been used to measure spin-dependent scattering from the elastic to the nucleon resonance region for hydrogen and deuterium using a longitudinally polarized electron beam at a beam energy of 850 MeV stored in the MIT-Bates South Hall Ring, and polarized internal gas targets of hydrogen and deuterium. There are several reasons for studying the inclusive $\vec{p}(\vec{e}, e')$ reaction: first, since all pion production models predict its observables, this is a stringent test for these models; second, due to detector acceptance confinements, inclusive scattering provides a higher statistical accuracy than exclusive scattering, where a hadron is measured in coincidence with the scattered electron, and additional systematic uncertainties from the exclusive reaction, due to the energy and angular resolution of the hadron detector, are avoided as well; third, the double-polarized scattering with BLAST over a range of momentum transfer $Q^2 = [0.08, 0.38]\ GeV^2$ provides unique, accurate data to check these models.

CHAPTER 1

Introduction

1.1 History

One of the major quests of the contemporary nuclear physics is the search for a complete understanding of the fundamental interactions between elementary particles. In order of decreasing strength, the four fundamental forces of nature are strong, electromagnetic, weak and gravity [24, 25, 26]. The gravitational force is important for the existence of stars, galaxies, and planetary systems, but, up to date, it seems to avoid a unified description within a quantum field theoretical framework. The electromagnetic force appears inside atoms and is caused by the electric charge of its constituents. The weak force manifests itself in nuclear β-decay. The strong force binds quarks to form protons and neutrons. The last three lead to the corresponding fundamental interactions between the elementary particles.

A big achievement was the unification of the electromagnetic and weak forces in the 1960s and 1970s in a single, electroweak theory due to Weinberg [27] and Salam [28]. One of the biggest success of the theoretical description of elementary particles is based on the predictive power of the electroweak theory, and in particular of Quantum Electrodynamics (QED), due to the smallness of electromagnetic fine structure constant $\alpha \equiv e^2/\hbar c \approx 1/137$, which allows for a perturbative expansion of the theory in powers of α. This proved very accurate in predicting the experimental data. Unfortunately, this technique does not entirely work in the case of Quantum Chromodynamics (QCD), the theory that drives the

strong force. At sufficiently high energies, QCD exhibits a perturbative behaviour similar to QED, where the color coupling constant, α_s of QCD becomes very small. Therefore, at high energy, quarks, which are confined by the strong color force, can be treated using the perturbation theory, denoted by pQCD. In contrast to the electromagnetic force, the color coupling becomes large at low energies, hence "confining" the quarks into the observed particles. This fact prevents QCD from being investigated using perturbation theory. A good description of QCD in this regime can be achieved through Wilson's lattice gauge theory [29]. He presented a method of quantizing a gauge field theory such as QCD on a discrete four dimensional lattice in Euclidian space-time, while preserving exact gauge invariance. In this way, the extraction of qualitative non-perturbative QCD becomes possible. However, due to enormous computational power needed by lattice QCD, effective quark models of hadrons have been developed [30, 31], which are aimed at predicting the properties of hadrons by reducing the strong self-interacting multi-quark and gluon systems to an effective two- or three-quark system. Since these two approaches are far from being able to offer practical solutions at low and intermediate energies, "effective methods" that describe the dynamical structure of these processes have been created. These effective methods account for the inner structure of the baryons by introducing explicit baryon resonance states, whose properties are then extracted by comparison with experimental observables. The idea of the effective models is to account for the symmetries of the fundamental theory (QCD) by including only effective degrees of freedom instead of quarks. These effective degrees of freedom are modeled using the properties of known baryons and mesons (which exist as bound quark states). This gives more perceptive insight on the dynamics of the reaction and makes the interpretation of the results somewhat easier.

In the framework of these effective models of hadrons, the nucleon and the pion are among the most important particles. The pion is responsible for the long range nucleon-nucleon interactions and plays an important role in mediating the nuclear force. The general properties of pions are listed in Table 1.1.

	I^G	J^{PC}	mass [MeV]	lifetime [s]	Decay modes	branching ratio [%]
$\pi^{\pm}$	1^-	0^-	139.57	$2.60 \cdot 10^{-8}$	$\mu\nu_\mu$	100
π^0	1^-	0^{-+}	134.98	$8.40 \cdot 10^{-17}$	$\gamma\gamma$	98.8

Table 1.1: Basic properties of pions

The pion production reactions are a very useful tool in investigating the structure of nucleons and nuclei. The theory of pion production on the nucleon was published in the 1950s. Kroll and Ruderman [32] derived the model independent predictions of the observables in the threshold region, called the low energy theorems (LET), by applying gauge and Lorentz invariance to the reaction $\gamma + N \rightarrow \pi + N$. The general formalism, though, was developed by Chew *et al.* [33] (CGLN amplitudes). Fubini *et al.* [34], in 1965, extended the predictions of the LET by including the hypothesis of a partially conserved axial current (PCAC). They succeeded in describing the threshold amplitudes as a power series in the ratio m_π/m_N up to terms of order $(m_\pi/m_N)^2$. In 1967, Berends *et al.*[35] analyzed the existing data at energies up to 500 MeV in the laboratory frame, in terms of multipole decomposition, coupled with theoretical dispersion calculations and presented tables of the various multipole amplitudes contributing in this energy region as a function of photon energy. In 1969, Peccei [36] introduced for the first time an effective chiral Lagrangian for single pion photo-production[1] and explicitly included a phenomenological $\pi N\Delta$ interaction.

The main difference in the various effective Lagrangian approaches is the treatment of the Δ resonance. In 1977, Blomqvist and Laget [37] introduced a very simple effective pion production model from the nucleon, which provided a very good description of the data up to the first resonance region. Their model could be easily incorporated in nuclear physics applications [38, 39]. A different approach was proposed by Nozawa *et al.* in

[1]pion photo-production occurs at $Q^2 = 0$, while electro-production takes place at $Q^2 \neq 0$.

1990, namely, a dynamical model that takes into account off-shell effects in the final πN interaction, but, in order to obtain a good fit of the data, they introduced a cut-off parameter to multiply the Born cross section with, hence a strong dependence on this cutoff was obtained. Sato and Lee [40, 19] introduced a dynamical model (known as the SL model) that describes the pion production[2] in terms of photon and hadron degrees of freedom, but the disadvantage of it comes from the way they satisfy current conservation, by assuming the same electromagnetic form factors at each vertex in the Born cross section. A unitary isobar model was developed by Drechsel *et al.* [1, 41] (known as MAID model), which uses the prescriptions of the isobar model of Walker [42] and Morehouse *et al.* [43], by assuming that the resonance contributions in the multipoles have Breit-Wigner form. Due to its parametrization of each of the resonant contributions, this simple and practical model describes the individual multipoles and agrees with the experimental data quite well. A most recent model has been developed at Ohio University and is known as the Ohio model [44]. This model uses a Lorentz-covariant approach based on solving relativistic coupled channel scattering equations in the pion-photon space. The effect of the final-state interaction is also included and the Watson theorem is obeyed. This model is currently under implementation at Jefferson Lab.

1.2 Motivation

Pion production reactions serve as a critical test of models of hadrons. The need for experimental data to test these models is obvious. The single pion production above the pion threshold region is dominated by the excitation of the nucleon resonances. The total photo-absorbtion cross section of the proton and its decomposition into selected channels as a function of the photon energy in the center of mass frame is given in Figure 1-1. Three main peaks are evident in this figure, corresponding to the magnetic dipole ($M1$), electric

[2]by pion production I refer to both pion photo- and electro-production

dipole ($E1$), and electric quadrupole ($E2$). The notation of the multipoles is associated with the electromagnetic nature of the excitation modes induced by the photon: $S_{l\pm}$ ($L_{l\pm}$), $M_{l\pm}$, $E_{l\pm}$ are the scalar (longitudinal), magnetic and electric multipoles, respectively, where the $\pm$ sign is the abreviation for $J = l \pm \frac{1}{2}$, l is the relative orbital momentum of the πN system with parity $(-1)^{l+1}$, and $\frac{1}{2}$ is the nucleon spin. The transverse polarizations $\lambda = \pm 1$ of the photon, lead to magnetic and electric multipole transitions, ML and EL, while the longitudinal polarization $\lambda = 0$ (only for the virtual photon), leads to the Coulomb transitions, CL. The lowest electromagnetic excitation modes are given in Table 2.1. The analysis of pion production reactions allows for the determination of the multipoles that correspond to the nucleon resonances. Extraction of these multipoles provides a set of quantities representing the experimental data to be compared to the existing theoretical models. Figure 1-2 shows the predictions of different models for the E2 and C2 quadrupole strengths over the transverse dipole M1 as function of Q^2.

Several unpolarized pion production experiments took place at LEGS and MAMI [45, 46, 47], ELSA [48] and Jefferson Lab [16], single-polarized experiment at MIT-Bates Lab [49] and MAMI [14], double-polarized experiment at MAMI [13], NIKHEF [6] and Jefferson Lab [50]. The results are shown in Figure 1-3, together with the model predictions presented in Figure 1-2. The uncertainty in C2 is large and hence, restricts the extraction of a real good value. The extracted values of E2/M1 and C2/M1 are dominated by statistics, which are limited by the measuring time (proportional to the beam charge) and polarizations.

Up to now, the sensitivity of the correlation parameters, $A_{TT'}$ and $A_{TL'}$ to the quadrupole strengths, E2 and C2, in the Δ-region is still uncertain. Figure 1-4 shows the sensitivities of the correlation parameters as a function of E2, C2 quadrupole strengths using the MAID model at a momentum transfer of $Q^2 = 0.11\ GeV^2$. Dashed lines (bottom) correspond to both the E2/M1 (for C2=0) and C2/M1 (for E2=0) ratios of -2.4%, solid line (middle) to the value of 0 and the dotted line (top) to the value of +2.4%.

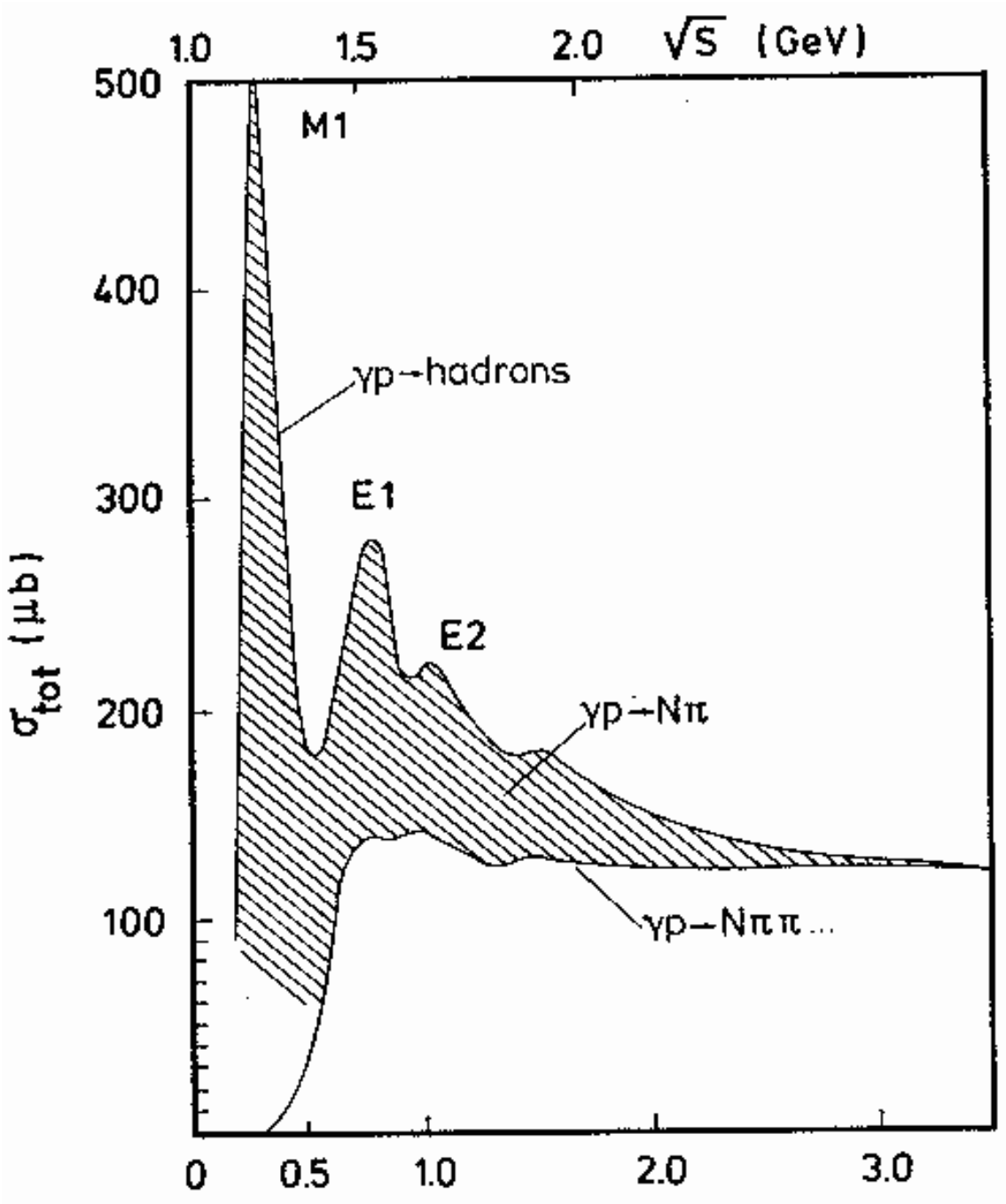

Figure 1-1: The total photo-absorption cross section of the proton and its decomposition into exclusive channels as a function of the photon energy $[GeV]$ in the center of mass frame. Figure taken from [1].

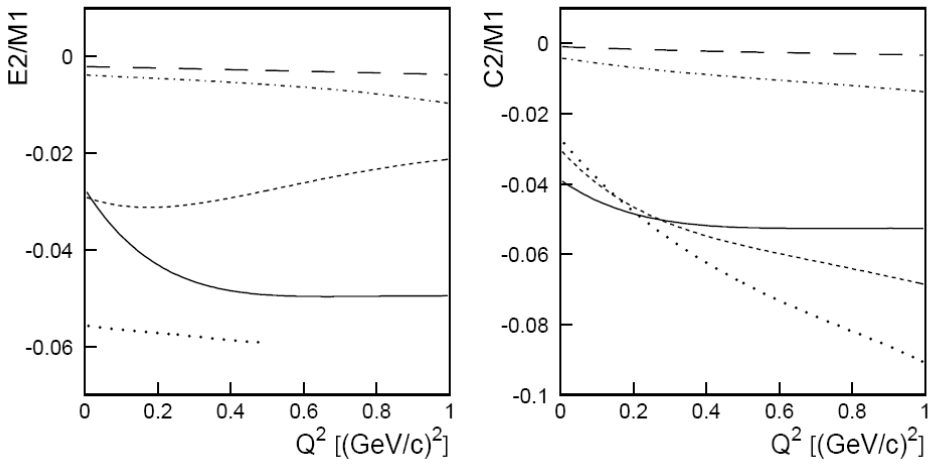

Figure 1-2: Predictions of E2/M1 (left) and C2/M1 (right). MAID model is the solid line, SL is the short dashed curve; long dashed [2], dot-dashed [3] and dotted only left [4] represent different constituent quark models; dotted line only in the right [5] is a Skyrme model. Figure from [6].

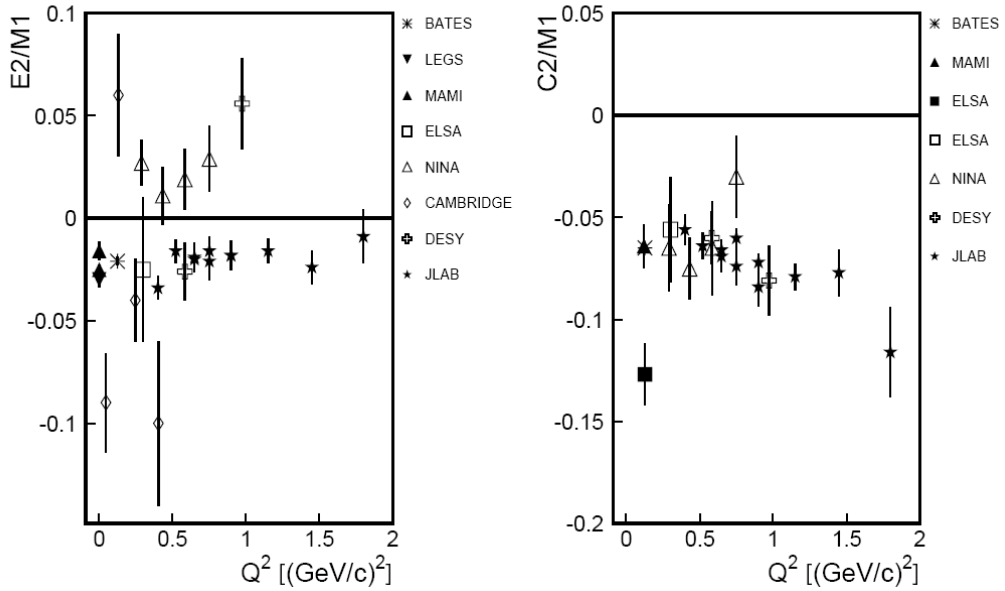

Figure 1-3: E2/M1 and C2/M1 world data. The predictions from Figure 1-2 are added for comparison. Figure from [6].

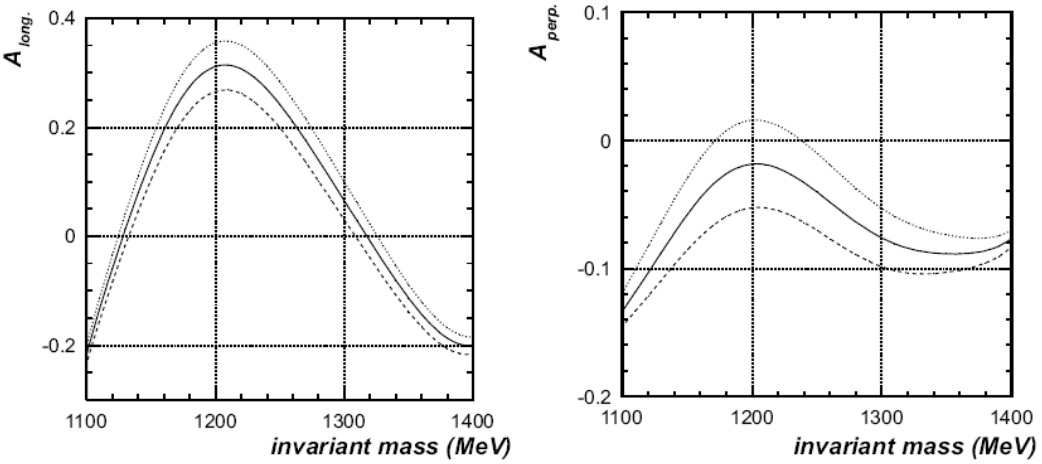

Figure 1-4: Sensitivity of the longitudinal and perpendicular spin asymmetries to the E2 (left) and C2 (right) amplitudes in the MAID model. The bands correspond to $E2/M1$ and $C2/M1$ rates of $0 \pm 2.4\%$. Figure from [6].

	MAID	SL (dressed)	SL (bare)
E2/M1	-2.2%	-2.0%	-1.3%
C2/M1	-6.5%	-4.2%	-3.2%

Table 1.2: Standard quadrupole strengths.

Figure 1-5 shows the spin-correlation parameters $A_{TT'}$ and $A_{TL'}$ as a function of the invariant mass for E2/M1 and C2/M1 at standard strengths (see Table 1.2) and at zero strength for both the MAID and SL (Sato and Lee) models, for a momentum transfer $Q^2 = 0.11\ GeV^2$ and beam energy $E_e = 720$ MeV.

In comparison with the SL model, where the *bare* and *dressed* contributions to the $N \rightarrow \Delta$ excitation are separated and the quadrupole transition strengths affect only the *bare* contribution, in the MAID model, the quadrupole strengths affect both of these

contributions. Hence, a higher sensitivity of the correlation parameters to the quadrupole transition strengths is obtained in this model.

Spin-dependent electron scattering from polarized protons or deuterons provides new information on the electro-magnetic response of the nucleon and two-body system, with an enhanced sensitivity to small amplitudes which enter the cross-section via an interference with large amplitudes. Information on the quadrupole form factors, E2 and C2, of the $N \rightarrow \Delta(1232)$ transition, which are related to the orbital angular momentum content in this system (D-state admixture in the wave function), can be obtained by measuring the spin correlation parameters of the $\vec{p}(\vec{e}, e')$ reaction. Without the tensor interaction included in $N - N$ interaction, the $N \rightarrow \Delta$ transition occurs only through the magnetic multipole, M1, transition, whereas, due to the tensor interactions, the transition can occur through electric and coulomb quadrupole, E2 and C2, transitions as well.

Data for the double-polarized electron-proton scattering in the Δ-region have been recently available from NIKHEF [6, 51, 9] for a square momentum transfer $Q^2 = 0.11$ GeV^2, beam energy of $E_e = 720$ MeV and a total beam charge of 54 kC for longitudinal spin orientation and 40 kC for sideways respectively. BLAST offers a deeper insight, because of a bigger range of square momentum transfer, Q^2 from 0.08 GeV^2 to 0.38 GeV^2 [3] all covered simultaneously, beam energy $E_e = 0.85$ GeV and a total beam charge of almost 300 kC.

In this experiment longitudinally polarized electrons were scattered from a polarized hydrogen target. The beam polarization was around 65% and the target polarization was around 80%. The beam had a 25 minute lifetime at 175 mA ring current. The target gas was injected from an atomic beam source into the target cell. Large acceptance, left-right symmetric spectrometer detector, BLAST (Bates Large Acceptance Spectrometer Toroid) permits simultaneous parallel/perpendicular, in-plane/out-of-plane asymmetry measure-

[3] actually Q^2 unit is $(GeV/c)^2$, but we use Bjorken [52] convention, i.e. c = 1

ments. From these asymmetries, we extract the correlation parameters $A_{TT'}$ and $A_{TL'}$ at different Q^2 values. These polarized structure functions provide a sensitive test of the different physical models of the $\gamma^* p \rightarrow \Delta$ transition, including the role of the pion field in the Δ-excitation region. These models can be used further in the extraction of the quadrupole strengths, $E2$ and $C2$.

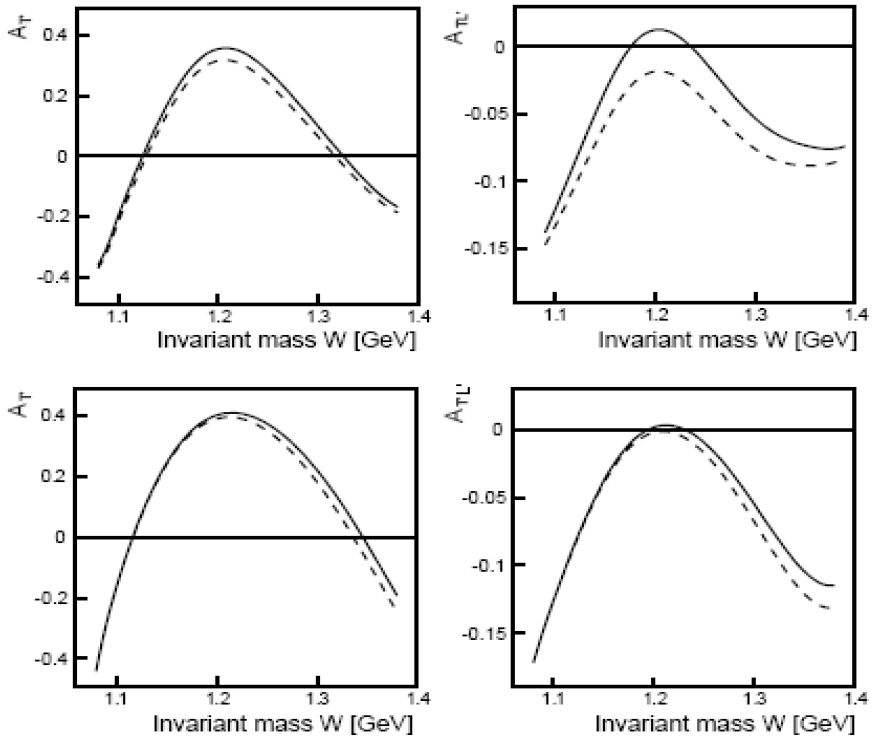

Figure 1-5: Spin-correlation parameters $A_{TT'}$ and $A_{TL'}$. Top (bottom) figures are MAID (SL) model predictions for standard strengths (solid line) and for zero strength (dashed line), for a momentum transfer $Q^2 = 0.11\ GeV^2$ and beam energy $E_e = 720$ MeV. Figure from [6].

CHAPTER 2

Theoretical Framework

2.1 Formalism

The fundamental theory that underlies the inclusive electron scattering from nuclei is Quantum Electrodynamics (QED) which describes the electromagnetic interaction of spin-$\frac{1}{2}$ leptons. The electromagnetic interaction is governed by the fine structure constant $\alpha = \hbar c \approx 1/137$ which is relatively small, hence the one-photon-exchange approximation (OPE) is accurate enough to describe the lepton-hadron interaction (has an accuracy of about 1% for electron-proton scattering [1]). In this limit, i.e. of OPE, the electron tests the proton (hadron) currents at a well defined energy and momentum transfer.

The formalism of scattering polarized electrons from polarized nuclei has been developed by Donnelly and Raskin [53, 54, 55]. The Feynman diagram corresponding to the one-photon-exchange process (or first-order Born approximation) is given in Figure 2-1.

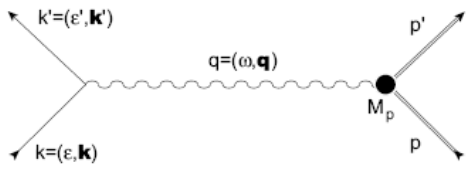

Figure 2-1: Feynman diagram for electron-proton scattering in the one photon exchange approximation

The four-momenta of the initial and final electrons are denoted by K and K', where $K = (\epsilon, \mathbf{k})$ and $K' = (\epsilon', \mathbf{k}')$ [1], whereas the initial and final hadron are labeled $P = (E_i, \mathbf{p})$ and $P' = (E_f, \mathbf{p}')$. The four-momentum transfer $q = (\omega, \mathbf{q})$ is given by:

$$q \;=\; K - K' \;=\; P' - P, \quad q^2 = -Q^2 = (\epsilon - \epsilon')^2 \;-\; (\mathbf{k} - \mathbf{k}')^2 \;\leq\; 0 \tag{2.1}$$

where:

$$\mathbf{q} \;=\; \mathbf{k} - \mathbf{k}' \;=\; \mathbf{p}' - \mathbf{p} \tag{2.2}$$

$$\omega \;=\; \epsilon - \epsilon' \;=\; E_f - E_i \tag{2.3}$$

Following Bjorken and Drell [52], the differential cross section in the laboratory frame [2] is given by

$$d\sigma \;=\; \frac{1}{\beta}\frac{m_e}{\epsilon}\overline{\sum_{if}} \mid \mathcal{M}_{fi} \mid^2 \frac{m_e}{\epsilon'}\frac{d^3\mathbf{k}'}{(2\pi)^3}\frac{M_{target}}{E_f}\frac{d^3\mathbf{p}'}{(2\pi)^3}(2\pi)^4\delta^{(4)}(K + P - K' - P') \tag{2.4}$$

where $\beta = \mid \mathbf{k} \mid / \epsilon = \mid \mathbf{v_e} \mid$ and $\overline{\sum_{if}}$ is the average sum over the initial and final states.

The invariant matrix is defined as:

$$\mathcal{M}_{fi} = \frac{ie}{q^2}\left(\frac{\epsilon\epsilon'}{m_e^2}\right)^{1/2} j_e(K', S'; K, S)_\mu J^\mu(P', P)_{fi} \tag{2.5}$$

where S, S' are the spin four-vectors of the initial and final electron. The electromagnetic current of the electron is:

$$j_e(K', S'; K, S)_\mu = -e\left(\frac{m_e^2}{\epsilon\epsilon'}\right)^{1/2} \overline{u}_e(K', S')\gamma_\mu u_e(K, S) \tag{2.6}$$

where $\overline{u}_e$ and u_e are the Dirac spinors for the final and initial electron, and the nuclear

[1] we use the space-time metric $g_{\mu\nu}$ from Bjorken and Drell [52] and take $\hbar = c = 1$

[2] in the laboratory frame: $\mathbf{p} = 0$ and $E_i = M_{target} \equiv M_P$, see Figure 2-2

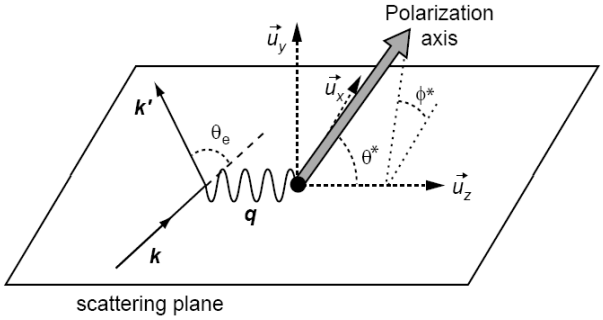

Figure 2-2: Scattering plane conventions

electromagnetic transition current in momentum space is defined as:

$$J^{\mu}(P', P)_{fi} = J^{\mu}(q)_{fi} \tag{2.7}$$

In the case of inclusive scattering, where only the outgoing electron is detected, hence its momentum is measured, we have to integrate over $\mathbf{p}'$ and we get

$$\left(\frac{d\sigma}{d\Omega_e}\right)_{fi} = \frac{m_e^2 k'}{(2\pi)^2 k} f_{rec}^{-1} \overline{\sum_{fi}} \mid \mathcal{M}_{fi} \mid^2 \tag{2.8}$$

where f_{rec} is the nuclear recoil factor and is given by

$$f_{rec} = 1 + \frac{\epsilon k' - \epsilon' \cos\theta_e}{k' M_{target}} \tag{2.9}$$

Then, the invariant matrix element becomes

$$\mathcal{M}_{fi} = -i\frac{e^2}{q^2}\overline{u}_e(K', S')\gamma_\mu u_e(K, S) J^{\mu}(q)_{fi} \tag{2.10}$$

and the sum is

$$\overline{\sum_{if}} \mid \mathcal{M}_{fi} \mid^2 = \frac{(4\pi\alpha)^2}{(q^2)^2} \eta_e(K', S'; K, S)_{\mu\nu} W^{\mu\nu}(q)_{fi} \tag{2.11}$$

where the electron tensor $\eta_e(K', S'; K, S)_{\mu\nu}$ is defined as

$$\eta_e(K', S'; K, S)_{\mu\nu} = \overline{\sum_{if}} [\overline{u}_e(K', S')\gamma_\mu u_e(K, S)]^* [\overline{u}_e(K', S')\gamma_\mu u_e(K, S)] \tag{2.12}$$

and the nuclear tensor being defined as

$$W^{\mu\nu}(q)_{fi} = \overline{\sum_{if}} J^{\mu *}(q)_{fi} J^{\nu}(q)_{fi} \tag{2.13}$$

From these we get the inclusive cross section

$$\left(\frac{d\sigma}{d\Omega_e}\right)_{fi} = \frac{\alpha^2}{(q^2)^2} \frac{4m_e^2 k'}{k} f_{rec}^{-1} \eta_e(K', S'; K, S)_{\mu\nu} W^{\mu\nu}(q)_{fi} \tag{2.14}$$

The general cross section for the scattering of polarized electrons from protons (and nuclei in general) can be seen to contain terms of the following types:

1. terms which occur when no electron polarization is involved
2. terms that occur when only the incident electron is polarized
3. terms which occur if only the outgoing electron polarization is involved
4. terms that occur when the incident electron is polarized and the polarization of the scattered electron is measured

If we denote the incident electron polarization by h (i.e. the beam polarization), and for the case of BLAST, when only the initial electron is polarized, then the cross section

can be written in the form (see **Appendix A** for details):

$$\left(\frac{d\sigma}{d\Omega_e}\right)^h_{fi} = \Sigma_{fi} + h\Delta_{fi} \tag{2.15}$$

where

$$\Sigma_{fi} = \left(\frac{d\sigma}{d\Omega_e}\right)^{unpol}_{fi} = \frac{1}{2}\left\{\left(\frac{d\sigma}{d\Omega_e}\right)^{+1}_{fi} + \left(\frac{d\sigma}{d\Omega_e}\right)^{-1}_{fi}\right\} \tag{2.16}$$

is the unpolarized cross section, and

$$\Delta_{fi} = \left(\frac{d\sigma}{d\Omega_e}\right)^{pol}_{fi} = \frac{1}{2}\left\{\left(\frac{d\sigma}{d\Omega_e}\right)^{+1}_{fi} - \left(\frac{d\sigma}{d\Omega_e}\right)^{-1}_{fi}\right\} \tag{2.17}$$

is the polarized cross section. The electron tensor becomes

$$\begin{aligned} 4m_e^2\eta_e(K', S'; K, S)_{\mu\nu} = &\quad K_\mu K'_\nu + K'_\mu K_\nu - g_{\mu\nu}(K\cdot K' - m_e^2) - im_e\epsilon_{\mu\nu\alpha\beta}q^\alpha S^\beta \\ \equiv &\ \chi_e(K'; K, S)_{\mu\nu} \end{aligned} \tag{2.18}$$

and, since $K\cdot K' - m_e^2 = -\frac{1}{2}q^2$, we get

$$\left(\frac{d\sigma}{d\Omega_e}\right)^h_{fi} = \frac{\alpha^2}{(q^2)^2}\frac{k'}{k}f_{rec}^{-1}\mathcal{R}_{fi} \tag{2.19}$$

where

$$\mathcal{R}_{fi} = \chi_e(K'; K, S)_{\mu\nu}W^{\mu\nu}(q)_{fi} \tag{2.20}$$

The contraction between the electron and hadronic tensors can be expressed as

$$4m_e^2\eta_e(K', S'; K, S)_{\mu\nu}W^{\mu\nu}(q)_{fi} = v_0\sum_K v_K\mathcal{R}^K_{fi} \tag{2.21}$$

where $K = \{L, T, TT, TL, TT', TL'\}$. The labels L and T refer to the longitudinal and transverse components of the virtual photon polarization, hence they correspond to the

electromagnetic nuclear current components with respect to the direction of $\mathbf{q}$. The unprimed terms arise from the product of the symmetric parts of the electron and hadronic tensors, thus they enter Σ_{fi}, while the primed terms occur from the antisymmetric parts of the tensors. Hence they enter Δ_{fi}. The symmetric-antisymmetric cross terms ($\underline{TT}$, $\underline{TL}$, and $\underline{TL'}$) vanish. Hence we do not mention them. $\mathcal{R}^K_{fi}$ are the hadronic response functions and contain all of the hadronic structure information. v_0 and V_K are electron kinematic and polarization factors, and for the case of the inclusive scattering they are given by [3]

$$\begin{aligned}
v_0 &= (\epsilon + \epsilon')^2 - \mathbf{q}^2 \\
v_L &= \left(\frac{q^2}{\mathbf{q}^2}\right)^2 \\
v_T &= -\frac{1}{2}\left(\frac{q^2}{\mathbf{q}^2}\right) + \tan^2\left(\frac{\theta_e}{2}\right) \\
v_{TT} &= \frac{1}{2}\left(\frac{q^2}{\mathbf{q}^2}\right) \\
v_{TL} &= \frac{1}{\sqrt{2}}\left(\frac{q^2}{\mathbf{q}^2}\right)\sqrt{-\left(\frac{q^2}{\mathbf{q}^2}\right) + \tan^2\left(\frac{\theta_e}{2}\right)} \\
v_{T'} &= \sqrt{-\left(\frac{q^2}{\mathbf{q}^2}\right) + \tan^2\left(\frac{\theta_e}{2}\right)}\tan\left(\frac{\theta_e}{2}\right) \\
v_{TL'} &= \frac{1}{\sqrt{2}}\left(\frac{q^2}{\mathbf{q}^2}\right)\tan\left(\frac{\theta_e}{2}\right)
\end{aligned} \tag{2.22}$$

The total differential cross section can be written as [54]

$$\begin{aligned}
\left(\frac{d\sigma}{d\Omega_e}\right)^h_{fi} = \left(\frac{d\sigma}{d\Omega_e}\right)_{Mott} f_{rec}^{-1}\Big[&\left(v_L\mathcal{R}^L_{fi} + v_T\mathcal{R}^T_{fi} + v_{TT}\mathcal{R}^{TT}_{fi} + v_{TL}\mathcal{R}^{TL}_{fi}\right) + \\
&+ h\left(v_{T'}\mathcal{R}^{T'}_{fi} + v_{TL'}\mathcal{R}^{TL'}_{fi}\right)\Big]
\end{aligned} \tag{2.23}$$

Then the unpolarized cross section is

$$\Sigma_{fi} = \left(\frac{d\sigma}{d\Omega_e}\right)_{Mott} f_{rec}^{-1}\Big[\left(v_L\mathcal{R}^L_{fi} + v_T\mathcal{R}^T_{fi} + v_{TT}\mathcal{R}^{TT}_{fi} + v_{TL}\mathcal{R}^{TL}_{fi}\right)\Big] \tag{2.24}$$

[3] in this work we assume ultra relativistic limit: $\epsilon, \epsilon' \gg m_e$

and the polarized cross section

$$\Delta_{fi} = \left(\frac{d\sigma}{d\Omega_e}\right)_{Mott} f_{rec}^{-1}\left(v_{T'}\mathcal{R}_{fi}^{T'} + v_{TL'}\mathcal{R}_{fi}^{TL'}\right) \tag{2.25}$$

The Mott cross section represents the scattering of electrons from a structureless target with charge $+e$ and infinite mass

$$\left(\frac{d\sigma}{d\Omega_e}\right)_{Mott} = \frac{\alpha^2}{4E_e^2}\frac{\cos^2(\theta_e/2)}{sin^4(\theta_e/2)} \tag{2.26}$$

Note that the kinematic factors v_L and v_T occur in the Rosenbluth formula for scattering of unpolarized electrons from unpolarized nuclei. The sensitivity to the interference terms TT and TL can be obtained only in exclusive scattering experiments. Also, the kinematic factors $v_{T'}$ and $v_{TL'}$, which belong to the polarized electron scattering, are proportional to $\tan(\theta_e/2)$ and thus Δ_{fi} will be suppressed relative to Σ_{fi} at small scattering angles.

2.2 Multipole Decomposition

The nuclear response functions $\mathcal{R}_{fi}^{K}$ can be expressed in terms of the nuclear electromagnetic multipole form factors. The contributing form factors are limited by the conservation of the total angular momentum J and parity, P.

Since the virtual photon carries an intrinsic spin of 1, the total spin J and parity are not sufficient to describe a γN helicity state. An additional characteristic is introduced which is the total helicity $\lambda = \lambda_{\gamma^*} - \lambda_N = 0, \pm\frac{1}{2}, \pm\frac{3}{2}$. The parity conserving amplitudes for pion electro-production represent the transition amplitude from the $\gamma^* N$ partial-wave state [56, 57]

$$|J, \lambda; \pm\rangle = \frac{|J, +\lambda\rangle \mp |J, -\lambda\rangle}{\sqrt{2}} \tag{2.27}$$

to the πN partial-wave state

$$|J,\lambda';\pm\rangle = \frac{|J,+\lambda'\rangle \mp |J,-\lambda'\rangle}{\sqrt{2}}, \tag{2.28}$$

where the total helicity of final state $\lambda' = \pm\frac{1}{2}$ (since the pion is a spin-0 particle). The parity of these states is $P = (-1)^{J\pm\frac{1}{2}}$. Hence, the 6 independent two-particle helicity state amplitudes of total spin J are ($T^{J\pm}_{\lambda'\lambda} = \langle J,\lambda';\pm|T^J|J,\lambda;\pm\rangle$):

$$\begin{aligned}
T^{J\pm}_{\frac{1}{2}\frac{3}{2}}(\gamma^*N \to \pi N) &= T^J_{+\frac{1}{2}+\frac{3}{2}} \mp T^J_{+\frac{1}{2}-\frac{3}{2}} \\
T^{J\pm}_{\frac{1}{2}\frac{1}{2}}(\gamma^*N \to \pi N) &= T^J_{+\frac{1}{2}+\frac{1}{2}} \mp T^J_{+\frac{1}{2}-\frac{1}{2}} \\
T^{J\pm}_{\frac{1}{2}0}(\gamma^*N \to \pi N) &= T^J_{+\frac{1}{2}+0} \mp T^J_{+\frac{1}{2}-0}
\end{aligned} \tag{2.29}$$

It is common to describe the photon field in terms of the electrodynamics quantities of magnetic (M), electric (E), and scalar (S) photon states. The first two are transversely polarized with respect to $\mathbf{q}$ and involve combinations of the polarization vectors $\epsilon^\mu_{\pm1}(q) = \frac{\mp1}{\sqrt{2}}(0,1,\pm i,0)$, while the latter one is longitudinally polarized (only exists for a virtual photon) and hence is proportional to $\epsilon^\mu_0(q) = \frac{1}{\sqrt{Q^2}}(|\vec{q}|,0,0,\omega)$. This *multipole decomposition* is the one that is commonly used for the experimental partial-wave decomposition of $\gamma^*N \to \pi N$. Denoting the total spin of the photon state by j_{γ^*} and the photon angular momentum by l_{γ^*} (with $j_{\gamma^*} = l_{\gamma^*} \bigoplus 1$), then one can construct a direct relation between the two-particle helicity states $|J,\lambda;\pm\rangle$ and the magnetic, electric and scalar photon nucleon states [58, 59]:

$$\begin{aligned}
|J = j_{\gamma^*} + \frac{1}{2}, M(E)\rangle &= \mp\frac{1}{\sqrt{2(j_{\gamma^*}+1)}}\left(\sqrt{j_{\gamma^*}}|J,\frac{1}{2};\pm\rangle + \sqrt{j_{\gamma^*}+2}|J,\frac{3}{2};\pm\rangle\right) \\
|J = j_{\gamma^*} - \frac{1}{2}, M(E)\rangle &= \mp\frac{1}{\sqrt{2(j_{\gamma^*}+1)}}\left(\sqrt{j_{\gamma^*}+1}|J,\frac{1}{2};\mp\rangle - \sqrt{j_{\gamma^*}-1}|J,\frac{3}{2};\mp\rangle\right) \\
|J = j_{\gamma^*} \pm \frac{1}{2}, S\rangle &= \pm|J,0;\mp\rangle.
\end{aligned} \tag{2.30}$$

Placing the interaction matrix T between the multipole states (2.30) and the πN of definite parity helicity states (2.28), and considering relations (2.29) and using the relation between $l_\pi = l$ (the orbital momentum of the πN system) and j_{γ^*}, the multipole amplitudes for the transition to a pion nucleon helicity state are [60]:

$$
\begin{aligned}
M_{l+} &= \frac{\sqrt{2}}{4(l+1)}\left(T^{J+}_{\frac{1}{2}\frac{1}{2}} + \sqrt{\frac{l+2}{l}}T^{J+}_{\frac{1}{2}\frac{3}{2}}\right) \\
M_{l-} &= \frac{\sqrt{2}}{4l}\left(-T^{J-}_{\frac{1}{2}\frac{1}{2}} + \sqrt{\frac{l-1}{l+1}}T^{J-}_{\frac{1}{2}\frac{3}{2}}\right) \\
E_{l+} &= \frac{\sqrt{2}}{4(l+1)}\left(T^{J+}_{\frac{1}{2}\frac{1}{2}} - \sqrt{\frac{l}{l+2}}T^{J+}_{\frac{1}{2}\frac{3}{2}}\right) \\
E_{l-} &= \frac{\sqrt{2}}{4l}\left(T^{J-}_{\frac{1}{2}\frac{1}{2}} + \sqrt{\frac{l-1}{l+1}}T^{J-}_{\frac{1}{2}\frac{3}{2}}\right) \\
S_{l+} &= -\frac{1}{2(l+1)}T^{J+}_{\frac{1}{2}0} \\
S_{l-} &= -\frac{1}{2l}T^{J-}_{\frac{1}{2}0}.
\end{aligned}
\tag{2.31}
$$

In the initial state the photon has spin 1 and its transverse polarizations, $\lambda_{\gamma^*} = \pm 1$ lead to electric and magnetic multipole transitions, EL and ML respectively, while its longitudinal polarization, $\lambda_{\gamma^*} = 0$ leads to longitudinal or Coulomb transitions, CL.

The final state is described by an orbital momentum l of the pion relative to the recoiled nucleon, with parity $(-1)^{l+1}$. Since the total spin of the final state, J has to equal the total spin of the initial state, namely

$$
J = |l \pm \frac{1}{2}| = |L \pm \frac{1}{2}|\,, \qquad L = L_{target} + L_{\gamma^*}
$$

we find that

$$
\begin{aligned}
&CL,\, EL: && (-1)^L = (-1)^{l+1} \rightarrow |L-l| = 1 \\
&ML: && (-1)^{L+1} = (-1)^{l+1} \rightarrow L = l
\end{aligned}
$$

L	Electromagnetic multipole	πN system J	l	Pion electoproduction multipole
0	$C0$	1/2	1	L_{1-}
1	$E1/C1$	1/2	0	E_{0+}/L_{0+}
		3/2	2	E_{2-}/L_{2-}
	$M1$	1/2	1	M_{1-}
		3/2	1	M_{1+}
2	$E2/C2$	3/2	1	E_{1+}/L_{1+}
		5/2	3	E_{3-}/L_{3-}
	$M2$	3/2	2	M_{2-}
		5/2	2	M_{2+}

Table 2.1: Amplitudes for pion electroproduction.

In Table 2.1 we give the lowest order electromagnetic excitation modes and the corresponding states of the πN system [1]. The first index of the pion multipoles describes the orbital momentum, l, and the second one characterizes the orientation of the spin and the orbital momentum of the nucleon, i.e. parallel is +1, which means $J = l + \frac{1}{2}$. From this table we see that the Δ resonance, where $J = \frac{3}{2}$ and $l = 1$, can be excited by both $M1$ and $E2/C2$ transitions.

This decomposition allows us to calculate the more customary CGLN amplitudes [33, 35] in terms of the multipoles using:

$$
\begin{aligned}
F_1 &= \sum_{l\geq 0}\{(lM_{l+} + E_{l+})P'_{l+1} + [(l+1)M_{l-} + E_{l-}]P'_{l-1}\} \\
F_2 &= \sum_{l\geq 1}[(l+1)M_{l+} + lM_{l-}]P'_l \\
F_3 &= \sum_{l\geq 1}[(E_{l+} - M_{l+})P''_{l+1} + (E_{l-} + M_{l-})P''_{l-1}] \\
F_4 &= \sum_{l\geq 2}(M_{l+} - E_{l+} - M_{l-} - E_{l-})P''_l \\
F_5 &= \sum_{l\geq 0}[(l+1)L_{l+}P'_{l+1} - lL_{l-}P'_{l-1}] \\
F_6 &= \sum_{l\geq 1}[lL_{l-} - (l+1)L_{l+}]P'_l
\end{aligned}
\tag{2.32}
$$

where $P_l^{'}$, $P_l^{''}$ are the first and the second order derivatives, respectively, of the Legendre polynomials, P_l; they are functions of the polar angle of the pion in the CM frame, $\theta = \theta_\pi^{CM}$. Note that in the literature, the scalar transitions are often described by $S_{l\pm}$ multipoles, which correspond to the decomposition of the amplitudes $F_7 = |\mathbf{k}|F_6/\omega$ and $F_8 = |\mathbf{k}|F_5/\omega$. They are connected to the longitudinal ones by $S_{l\pm} = |\mathbf{k}|L_{l\pm}/\omega$ through current conservation. This allows us to use only six CGLN amplitudes in expressing the observables for pion electro-production.

The inclusive cross section can be defined as [61, 21]

$$\sigma = \sigma_T + \epsilon\,\sigma_L + Px^*\sqrt{2\epsilon(1-\epsilon)}\,\sigma_{TL'} + Pz^*\sqrt{1-\epsilon^2}\,\sigma_{TT'} \tag{2.33}$$

where the expansion of the partial cross sections, σ_L, σ_T, $\sigma_{TL'}$ and $\sigma_{TT'}$ as a function of multipoles, is given in **Appendix A**. x^*, z^* are the projections of the target spin onto the $\mathbf{u}_{x,z}$ axes (see Figure 2-2), and $P = P_b\,P_t$ is the beam and target polarization product. The kinematic factor ϵ (virtual photon transverse polarization) is given in the laboratory frame by

$$\epsilon = \left[1 + 2\frac{\mathbf{q}^2}{Q^2}\tan^2\frac{\theta_e}{2}\right]^{-1} \tag{2.34}$$

The inclusive cross section can be rewritten as

$$\sigma = \sigma_T + \epsilon\,\sigma_L + P\left[\sqrt{2\epsilon(1-\epsilon)}\,\sigma_{TL'}\,\sin\theta^*\cos\phi^* + \sqrt{1-\epsilon^2}\,\sigma_{TT'}\,\cos\theta^*\right] \tag{2.35}$$

The relation between the spin-correlation parameters and $\sigma_{TT'}$, $\sigma_{TL'}$ is given by

$$A_{TT'} = \sqrt{1-\epsilon^2}\,\frac{\sigma_{TT'}}{\sigma_T + \epsilon\sigma_L} = \sqrt{1-\epsilon^2}\,\frac{\sigma_{TT'}}{\sigma_0} \tag{2.36}$$

$$A_{TL'} = \sqrt{2\epsilon(1-\epsilon)}\,\frac{\sigma_{TL'}}{\sigma_T + \epsilon\sigma_L} = \sqrt{2\epsilon(1-\epsilon)}\,\frac{\sigma_{TL'}}{\sigma_0} \tag{2.37}$$

2.3 Nucleon Models

2.3.1 Phenomenological Models

Two more recent models are worth mentioning: MAID, the unitary isobar model developed by Drechsel *et al.* [1, 41] and the SL (Sato and Lee) dynamical model [40, 19].

MAID uses the prescriptions of the isobar model of [42, 43] which assumes that the resonance contributions in the relevant multipoles have Breit-Wigner forms. They include nucleon resonances such as: $P_{33}(1232)$, $P_{11}(1440)$, $D_{13}(1520)$, $S_{11}(1535)$, $F_{15}(1680)$ and $D_{33}(1700)$. The Q^2 dependence of the γNN^* vertices is determined via the corresponding helicity amplitudes. The multipole amplitudes relevant to the resonant regions are (in Breit-Wigner form):

$$A_{l\pm}(W) = \overline{\mathcal{A}}_{l\pm} f_{\gamma N}(W) \frac{\Gamma_{tot} W_R e^{i\phi}}{W_R^2 - W^2 - iW_R\Gamma_{tot}} f_{\pi N}(W) C_{\pi N} \tag{2.38}$$

where $f_{\pi N}$ is the Breit-Wigner factor which describes the decay of the N^* resonance with total width Γ_{tot} and partial width $\Gamma_{\pi N}$. $C_{\pi N}$ is the isospin factor of the resonance. The factor $f_{\gamma N}(W)$ is a parametrization of the W dependence of the γNN^* vertex below the resonance peaks and W_R is the total energy in the center-of-momentum frame (CM) at the resonance position. The electromagnetic amplitudes $\overline{\mathcal{A}}_{l\pm}$ are linear combinations of the usual electromagnetic helicity amplitudes $A_{1/2}$ and $A_{3/2}$. The non-resonant contributions are described by traditional evaluation of the Feynman diagrams, derived from an effective Lagrangian density function. These non-resonant contributions are referred to as the Born terms and are described using a mixed pseudovector-pseudoscalar πNN coupling, hence taking into account the consistency of the pseudo-vector coupling with low energy theorems, while the renormalizability of pseudo-scalar coupling implies a better description of the data at higher energies (above 500 MeV). MAID implements both schemes by introducing a gradual transition between them. Their effective Lagrangian called a *hybrid*

model (HM) is written as

$$\mathcal{L}^{HM}_{\pi NN} = \frac{\Lambda^2}{\Lambda^2 + \vec{q}_0^{\,2}} \mathcal{L}^{PV}_{\pi NN} + \frac{\vec{q}_0^{\,2}}{\Lambda^2 + \vec{q}_0^{\,2}} \mathcal{L}^{PS}_{\pi NN} \tag{2.39}$$

where $\vec{q}_0$ is the asymptotic pion momentum in the πN CM frame and the cut-off parameter $\Lambda = 450\ MeV$. PV stands for pseudovector, while PS for pseudoscalar. The two PS and PV πNN coupling are given by

$$\mathcal{L}^{PV}_{\pi NN} = ig\overline{\psi}\gamma_5 \tau \cdot \psi\pi$$
$$\mathcal{L}^{PS}_{\pi NN} = -\frac{f}{m_\pi}\overline{\psi}\gamma_5\gamma_\mu \tau \cdot \partial^\mu \pi\psi$$

where $g^2/4\pi = 14.28$ and $f/m_\pi = g/2m_N$. PV coupling is preferred at low energies, since it is consistent with low energy theorems (LET) and fulfills PCAC (partially conserved axial current), while the renormalizable PS coupling gives a better description at higher energies. The unitarity of the model is implemented via the parameter ϕ in (2.38) and its role is to adjust the phase of the total multipoles to the corresponding pion-nucleon scattering phase shift $\delta_{\pi N}$. The latter values are taken from the analysis of the former VPI group (SAID program) [22]. For pion electro-production, MAID assumes the same electromagnetic form factors at each relevant vertex in the Born terms in order to satisfy current conservation. Such a simple and practical model, due to the parametrization of each of the resonant contributions, describes the individual multipoles very well and overall agrees extremely well with the experimental observables.

The SL model describes the pion production in terms of photon and hadron degrees of freedom. They start with the Hamiltonian

$$H = H_0 + H_I = H_0 + \sum_{M,B,B'} \Gamma_{MB \leftrightarrow B'} \tag{2.40}$$

where H_0 is the free Hamiltonian and $\Gamma_{MB\leftrightarrow B'}$ describes the absorption and emission of a meson (M) by a baryon (B). Such a Hamiltonian is obtained from a phenomenological Lagrangian for N, Δ, π, ρ, ω and photon fields. A unitary transformation is performed in (2.40) up to second order on $\sum \Gamma_{MB\leftrightarrow B'}$ to obtain an effective Hamiltonian:

$$H_{eff} = H_0 + v_{\pi N} + v_{\gamma\pi} + \Gamma_{\pi N\leftrightarrow\Delta} + \Gamma_{\gamma N\leftrightarrow\Delta} \tag{2.41}$$

where $v_{\pi N}$ and $v_{\gamma\pi}$ are the non-resonant $\pi N \leftrightarrow \pi N$ and non-resonant $\gamma N \leftrightarrow \pi N$ potentials, respectively. The Δ excitation is described by the vertex interactions $\Gamma_{\gamma N\leftrightarrow\Delta}$ and $\Gamma_{\pi N\leftrightarrow\Delta}$. The non-resonant $v_{\gamma\pi}$ consists of the usual pseudovector Born terms, ρ and ω exchanges, and the crossed Δ term. The idea behind this unitary transformation is to eliminate from the Hamiltonian the unphysical vertex interactions, $MB \leftrightarrow B'$ with $m_M + m_B < m_{B'}$. The resulting effective Hamiltonian H_{eff} is energy independent and hermitian. Hence the unitarity of the resulting amplitude is trivially satisfied. The drawback of the model is again the way they satisfy current conservation, by assuming the same electromagnetic form factors at each relevant vertex in the Born terms. MAID and

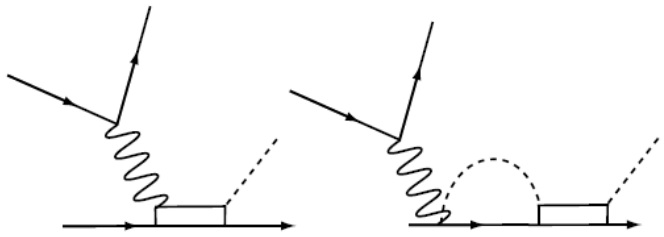

Figure 2-3: Sato and Lee: resonant pion production term (left) and non-resonant followed by resonant pion rescattering term (right)

SL differ mostly in the treatment of the non-resonant terms. MAID calculates *dressed* quantities of the $N-\Delta$ transition, whereas SL presents *bare* quantities. In the SL models the Δ production terms are separated into a resonant and non-resonant terms, followed by a resonant pion rescattering process (see Figure 2-3).

In the MAID model these terms are not separated (see Figure 2-4). In the SL model the non-resonant followed by resonant pion rescattering terms *dress* the *bare* $\gamma^* N \rightarrow \Delta$ vertex and strongly enhance its strength at low Q^2. Both SL and MAID models require the square transfer momentum, Q^2, and the invariant mass, W as input, and calculate the partial cross sections, σ_K, $K = L, T, TL, TT, TL', TT'$, that appear in the scattering cross section.

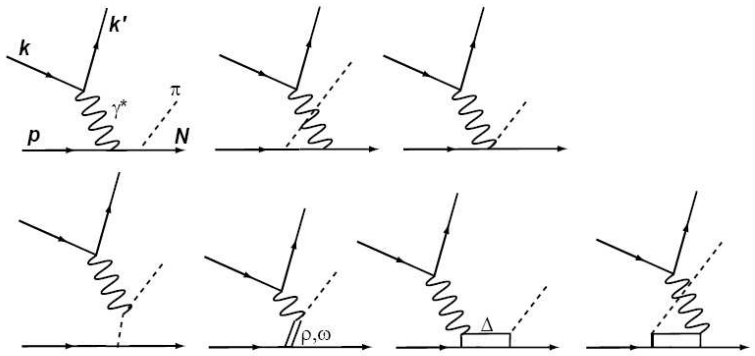

Figure 2-4: MAID first-order diagrams for pion production

A new model has been proposed by the Ohio University, known as Ohio model [44]. This model uses a manifestly Lorentz-covariant approach based on solving relativistic coupled-channel scattering equations in the pion-photon channel space. They approach the electromagnetic induced reactions in a way that satisfies the unitary dynamics by

setting up the following coupled-channel equations:

$$\begin{pmatrix} T_{\pi\pi} & T_{\pi\gamma^*} \\ T_{\gamma^*\pi} & T_{\gamma^*\gamma^*} \end{pmatrix} = \begin{pmatrix} V_{\pi\pi} & V_{\pi\gamma^*} \\ V_{\gamma^*\pi} & V_{\gamma^*\gamma^*} \end{pmatrix} + \begin{pmatrix} V_{\pi\pi} & V_{\pi\gamma^*} \\ V_{\gamma^*\pi} & V_{\gamma^*\gamma^*} \end{pmatrix} \begin{pmatrix} G_\pi & 0 \\ 0 & G_{\gamma^*} \end{pmatrix} \begin{pmatrix} T_{\pi\pi} & T_{\pi\gamma^*} \\ T_{\gamma^*\pi} & T_{\gamma^*\gamma^*} \end{pmatrix} \tag{2.42}$$

where T and V are the amplitudes and driving potentials of the πN scattering ($\pi\pi$), pion electro-production ($\gamma^*\pi$), absorption ($\pi\gamma^*$), and the nucleon Compton effect ($\gamma^*\gamma^*$), respectively, while G is the two-particle propagator. Figure 2-5 shows the Bethe-Salpeter (BS) equation in a schematic form for the two-body scattering equation. The effect of the pion-nucleon final state interaction is thus explicitly included in a way that is consistent with the two-body unitarity. Hence the Watson theorem is obeyed exactly. Special care is taken to satisfy current conservation for the Born terms by imposing the Ward-Takahashi identity at the nucleon and pion electromagnetic vertices, thereby allowing the use of realistic electromagnetic form factors.

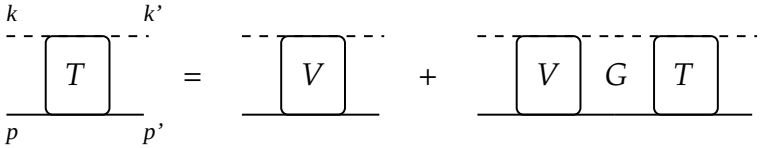

Figure 2-5: Two-body scattering equation: schematic form

This model is currently being implemented at Jefferson Lab. The main uncertainty of the model lies in the treatment of the u- and t-channel terms in the potential $V_{\pi\gamma^*}$.

2.3.2 Constituent Quark Models

In these models the nucleon consists of three quarks, which move in a confining potential. The proton (uud) and the neutron (ddu) are isospin symmetric: they transform into each other by interchanging the u- and d-quarks. The interaction binding quarks into hadrons is due to multi-gluon and pion exchange between the quarks. In the quark model of the nucleus, the Δ is the hyperfine partner of the nucleon, with its three quarks (uud) aligned such that $J_\Delta = 3/2$, i.e. the spins of the three constituent quarks have to be parallel. For example, for the Δ particles, the wave function is written in terms of constituent quarks

$$|\Delta^{++}\rangle = |u^\uparrow u^\uparrow u^\uparrow\rangle \qquad |\Delta^{+}\rangle = |u^\uparrow u^\uparrow d^\uparrow\rangle \qquad |\Delta^{0}\rangle = |u^\uparrow d^\uparrow d^\uparrow\rangle \qquad |\Delta^{-}\rangle = |d^\uparrow d^\uparrow d^\uparrow\rangle$$

where the arrow indicates the spin orientation.

Hadrons are classified in two groups: *baryons* which are fermions with half-integer spin, and *mesons*, which are bosons with integer spin. The three constituent quarks in the baryon must satisfy the Pauli principle: the total baryonic wave function

$$\psi_{total} = \xi_{spatial} \cdot \zeta_{flavour} \cdot \chi_{spin} \cdot \phi_{colour} \tag{2.43}$$

must be antisymmetric under the exchange of any of the two constituent quarks.

The constituent quark model predicts quite well the baryon magnetic moments. In the quark model, the proton magnetic moment in its ground state ($l = 0$) is given by the vectorial sum of the magnetic moments of the three constituent quarks:

$$\mu_P = \mu_u + \mu_u + \mu_d \tag{2.44}$$

and has the expectation value:

$$\mu_P = \langle \mu_P \rangle = \langle \psi_P | \mu_P | \psi_P \rangle \tag{2.45}$$

with ψ_P being the total antisymmetric quark wave function of the proton. Using the spin part of the wave function of the proton

$$\chi_P \left(J = \frac{1}{2}, m_J = \frac{1}{2} \right) = \sqrt{\frac{2}{3}}\, \chi_{uu}(1,1)\chi_d \left(\frac{1}{2}, -\frac{1}{2} \right) - \sqrt{\frac{1}{3}}\, \chi_{uu}(1,0)\chi_d \left(\frac{1}{2}, \frac{1}{2} \right) \tag{2.46}$$

we deduce that

$$\mu_P = \frac{2}{3}(\mu_u + \mu_u - \mu_d) + \frac{1}{3}\mu_d = \frac{4}{3}\mu_u - \frac{1}{3}\mu_d \tag{2.47}$$

where $\mu_{u,d}$ are the quark magnetons:

$$\mu_{u,d} = \frac{z_{u,d} e\hbar}{2m_{u,d}} \tag{2.48}$$

The measured magnetic moment of the proton is given by

$$\mu_P = 2.79\mu_N = 2.79\frac{e\hbar}{2M_P} \tag{2.49}$$

which is very close indeed to the quark model predictions.

Several approaches have been made to the constituent quark model. Isgur *et al.* [2] introduced hyperfine interactions, residual one-gluon and one-pion exchanges between the quarks, which resolved the degeneracy in the nucleon and Δ mass, but their electromagnetic properties were affected. Capstick [3] estimated the relativistic effects by using relativistic wave functions. As a results, the Q^2 dependence of $E2/M1$ and $C2/M1$ decreased. Buchmann *et al.* introduced a chiral symmetric quark model, but valid only at low energies. These approaches cannot offer practical solutions to intermediate energy scattering reactions.

2.3.3 Bag Models

The MIT bag model was formulated first by Chodos *et al.* [62, 63]. Their first Lagrangian consists of Dirac particles moving inside a *bag* described by a step function Θ_V, and there is a bag pressure that leads to a volume energy $\sim B$, and a bag surface term described by a surface delta function Δ_S

$$\mathcal{L}^{MIT} = \Big(\sum \overline{q}(i\partial\!\!\!/ - m_q)q - B \Big)\Theta_V - \frac{1}{2}\sum \overline{q}q\Delta_S \tag{2.50}$$

The solutions of this Lagrangian are the spherical Bessel functions with the wavenumbers quantized by the boundary condition where the component of the current in the direction n_μ perpendicular to the bag surface vanishes

$$n^\mu \overline{q}\gamma_\mu q\Delta_S = 0 \tag{2.51}$$

The isoscalar and isovector components of the electromagnetic current are conserved, but the axial current is not. To allow for this latter component to be conserved, isoscalar (σ) and isovector (π) mesons have been introduced in addition to quarks, hence the Lagrangian is replaced by a surface interaction of the quarks with these mesons:

$$\mathcal{L}^\sigma = \Big(\sum \overline{q}(i\partial\!\!\!/ - m_q)q - B \Big)\Theta_V + \frac{1}{2}(\partial_\mu\sigma)^2 + \frac{1}{2}(\partial_\mu\pi)^2 - \sum \overline{q}\frac{\sigma + i\tau\cdot\pi\gamma_5}{2(\sigma^2+\pi^2)^{1/2}}q\Delta_S \tag{2.52}$$

Viollier *et al.* [64] removed the degeneracy in the mass between the nucleon and the Δ by introducing the one-gluon-exchange interaction. Hence the Δ-bag gets deformed. In addition, Vento *et al.* [65] incorporated π-mesons, which cause a larger deformation of the bag surface. Cloudy bag models have been studied by [66, 67, 68] and the same behaviour has been observed. They give a value for the $\pi N\Delta$ coupling constant, $g_{\pi N\Delta}$, which is in

better agreement with the experimental value than other models.

2.3.4 Skyrme Models

The Lagrangian of the original Skyrme model [69] is given by [1]

$$\mathcal{L} = \frac{1}{4} f_\pi^2 Tr(\partial_\mu U \partial^\mu U^\dagger) + \frac{e^2}{32} Tr([U^\dagger \partial_\mu U, U^\dagger \partial_\nu U][U^\dagger \partial^\mu U, U^\dagger \partial^\nu U]) \tag{2.53}$$

where f_π is the pion decay constant, U an arbitrary $SU(2)$-matrix, and e a parameter which determines the size of the soliton. This Lagrangian is an effective description of the hadronic interactions at low energies in terms of mesonic degrees of freedom (i.e. weakly interacting pions). In this model a baryon consists of N_c quarks and is identified with a soliton. A soliton is "an isolated wave that propagates without dispersing its energy over larger and larger regions of space". The fact that solitons exhibit particle-like properties, because the energy is, at any instant, confined to a limited region of space, were proposed as models for elementary particles. The pion is coupled to the nucleon soliton solution in two different approaches: one sees the pion as a small amplitude fluctuation [70], and the other one sees it as a chiral perturbation [71].

The interest in this model is motivated by 't Hooft's observation [72] that for a large number of colors ($N_C \to \infty$), QCD reduces to a weakly interacting pions theory, hence baryons can be seen as solitons in this theory [73].

Walliser and Holzwarth [5] solved the equation of motion in the Skyrme model up to the order of $1/N_C^2$. From the soliton's rotation they extracted the quadrupole $C2/M1$ deformation.

The results of these models are shown in Figure 1-2.

CHAPTER 3

Experimental Setup

The experiment discussed in this thesis has been performed on the South Hall Ring (SHR) at the MIT-Bates Linear Accelerator Center using the Atomic Beam Source (ABS) and the **B**ates **L**arge **A**cceptance **S**pectrometer **T**oroid (BLAST) detector. The combination of a highly polarized electron beam, a highly polarized internal target, and a relatively large acceptance spectrometer detector, is rather unique for intermediate energy nuclear physics. The experimental setup is described in detail in this chapter, as well as the performance.

3.1 The MIT-Bates Linear Accelerator

The MIT-Bates Linear Accelerator delivers longitudinally polarized electrons to the BLAST detector. A schematic overview of the entire facility is given in Figure 3-1. Low energy polarized electrons are injected from the polarized source into the linear accelerator. The linear accelerator consists of 190m of accelerating RF cavities [74]. A recirculator transports the beam back to the beginning of the accelerator for a second pass through the RF cavities in order to accelerate the electrons. For this experiment the polarized beam leaves the linear accelerator at an energy of 0.850 ± 0.0008 GeV, and is injected into the SHR through a switchyard that guides the beam to various possible experimental areas. The beam is then circulated through the BLAST polarized internal target and spectrometer located in the Bates SHR. Over 3 Million Coulomb of integrated charge

have been delivered to BLAST for production data taking.

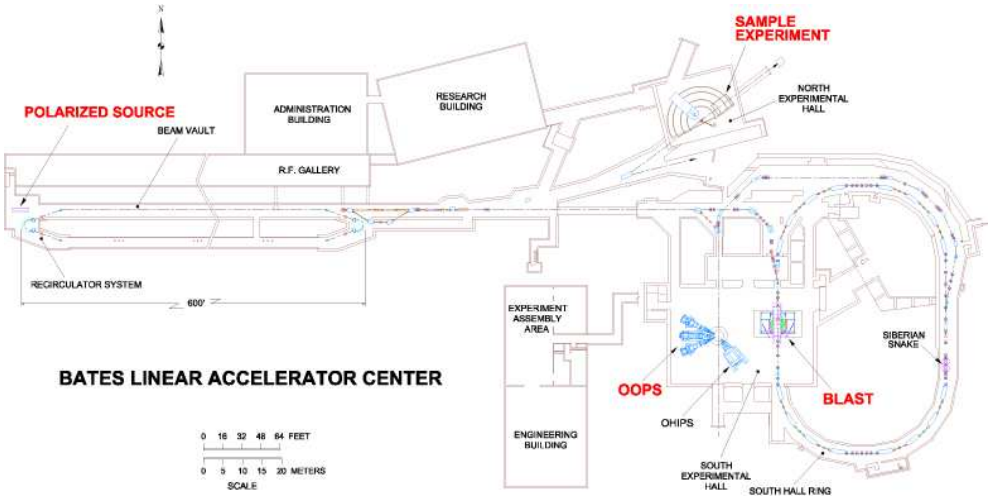

Figure 3-1: Overview of the MIT-Bates Linear Accelerator Center

3.1.1 The Polarized Source

Longitudinally polarized electrons are produced by photo-emission using a $\lambda = 810$ nm circularly-polarized multimode fiber-coupled diode array laser system incident on a $GaAs_{0.95}P_{0.05}$ crystal [75]. A Cesium coating is applied to reduce the work function of the crystal. The coating has to be restored about once a week.

The polarization state of the beam is determined by a half-wave plate in the path of the laser source. The plate is moved in or out with each "fill" (injection into the SHR), thus resulting in alternating fills having opposite polarization.

The energy of electrons entering linac is 0.36 MeV. The source is able to inject 6 mA into the accelerator.

The beam polarization at the source was measured periodically with a transmission polarimeter [76].

3.1.2 The Bates South Hall Ring

The SHR is designed to operate as either a storage ring for internal target experiments (such as BLAST) or as a pulse stretcher ring to produce nearly continuous-wave beam for external target experiments [77]. In the storage mode, currents in excess of 200 mA are achieved by stacking beam pulses of a few mA head-to-tail at an injection rate of $2 - 20$ Hz. This head-to-tail injection results in the storage ring having a duty factor of 99% [78].

The SHR has 16 dipole magnets each bending the beam by 22.5°. An RF cavity compensates for energy loss due to synchrotron radiation. The beam energy is calibrated by a precise field-map of the integrated magnetic field along the dipoles in the ring [79].

The longitudinal polarization of the electrons in the storage ring is preserved by two spin rotators (Siberian snake) on the opposite side of the ring to the internal target [76]. The snake was designed by the Budker Institute of Nuclear Physics in Novosibirsk, and consists of two superconducting solenoids and 5 quadrupoles. The solenoids rotate the electron spin by 180° about the momentum vector such that the precession of the electron spins in the north arc of the ring compensates for that in the south arc [80].

Four beam slits made of 1 cm thick Tungsten material, are installed upstream of the target in order to limit the amount of stray electrons hitting the detectors due to multiple scattering in the beam pipe. The position of the slits depends on the tune of the injection and is established empirically. The slits are operated by remotely controlled, motorized bellows and they are totally withdrawn for injection. After injection they are moved in slowly, until they begin to impact the beam lifetime, and at that point they are withdrawn only by 1 mm, essentially cutting away electrons outside of a 6σ beam distribution. The slits are located a few betatron $\lambda/2$ upstream of the target in order to image the cell.

The main specifications of the SHR during BLAST experiment are given in Table 3.1.

The beam current is measured non-destructively with a zero-flux Lattice DC Current Transformer (LDCCT) [81]. The LDCCT uses a primary core winding around the beam

Beam energy	E	$850.0 \pm 0.8\ MeV$
Beam spread	ΔE	$0.20\ MeV$
Max. Current	I	$230\ mA$
Lifetime	τ	$25\ min$
Beam Polarization	P_b	$0.6558 \pm 0.0007 \pm 0.04$
Ring length	L	$190.205\ m$
Harmonic number	h	1812
Rev. Frequency	$\beta c/L$	$1.577\ MHz$
RF frequency	$\approx h\beta c/L$	$2856\ MHz$
RF Wavelength	$\approx L/h$	$10.5\ cm$
Bending radius	ρ	$9.144\ m$
Magnetic rigidity	$B\rho$	$2.8353\ T\ m$

Table 3.1: South Hall Ring (SHR) specifications during BLAST experiment.

with a nonlinear magnetic response to the current. A secondary winding driven by a fixed signal is coupled to the primary. The second harmonic generated by the nonlinear response is proportional to the absolute beam current passing through the coil. The output voltage goes to a 16 bit analog-to-digital converter (ADC), and a voltage-to-frequency converter (VFC). The number of oscillations in the VFC is proportional to the instantaneous beam current passing through the LDCCT. The digitized voltage is sent to the Experimental Physics and Industrial Control System (EPICS) and the number of oscillations of the VFC are counted in two scaler channels, DCCT and BDCCT. The experiment trigger electronics inhibits counting in the BDCCT whenever data acquisition is inhibited because of electronic dead time, target transition between well-defined states or high voltage trips, hence by integrating the BDCCT over time, we measure the actual charge delivered through the target while the experiment is taking data.

The LDCCT is calibrated regularly with current injected into a calibration loop and measured by an ammeter with 1 pA resolution. Because of the nonlinearity of the VFC, the scaler read-outs are not exactly proportional to the beam current. The scalers are calibrated using fake runs when beam is turned off and currents from 0 to 200 mA, in

5 mA steps, are injected into the calibration loop. The beam current I, good up to 0.5% for currents between 20 and 250 mA, is given by

$$I[mA] = \left(2.90027 + 3.01409 \times 10^{-4}\, S + 6.18094 \times 10^{-10}\, S^2\right) \tag{3.1}$$

where S is the DCCT or BDCCT scaler value minus a pedestal of 2400 counts.

The integrated charge delivered to the BLAST experiment over the course of the 2004-2005 running period is given in Figure 3-2. The blue line indicates the distribution of the charge for beam in the South Hall Ring, the light yellow represents the distribution of the charge delivered to the experiment and the dark yellow is the charge used for data taking. Note that the plot includes charge delivered to both the hydrogen and deuterium experiments.

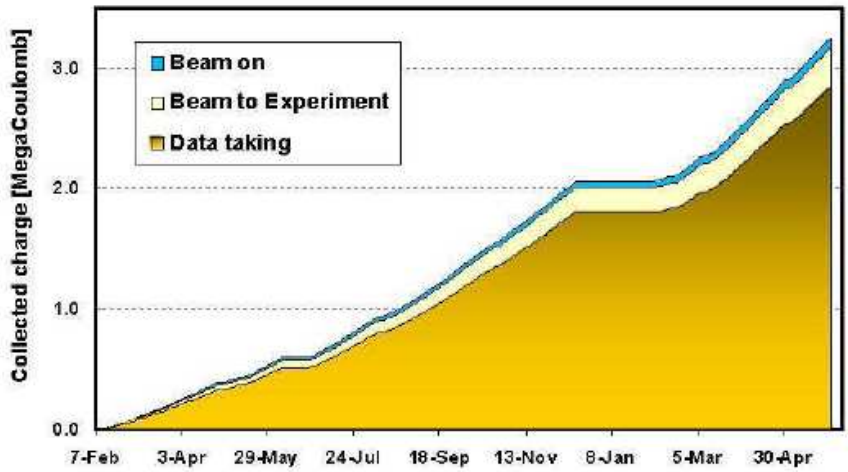

Figure 3-2: Integrated charge delivered to the BLAST experiment over the course of the 2004-2005 running period

Before the injection, the detector high voltages are ramped down to standby values

to protect the detectors. Once the ring is filled, the detectors are ramped up to their operating high voltage values, and data acquisition are started. The down time for each fill is between one to two minutes. The beam intensity in the ring dissipates because of the scattering of the beam electrons with target gas and the residual gas in the ring vacuum. The maximum current and lifetime depend on the quality of the stored beam. Figure 3-3 shows the typical current and lifetime monitored by LDCCT. The blue curve is the beam current stored in the ring. The yellow curve is the measured beam lifetime. For these series of fills, the ring was filled to 215 mA and dumped at 180 mA. The beam life time is about 28 minutes.

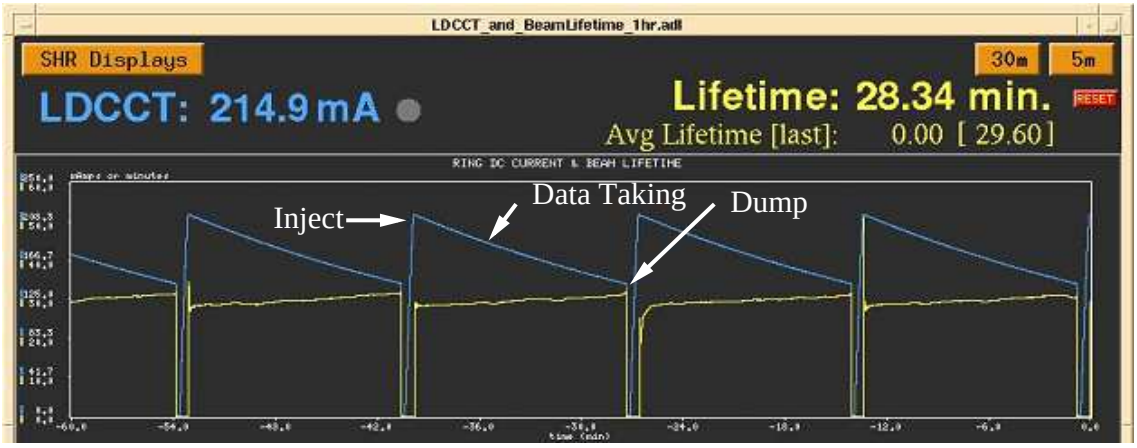

Figure 3-3: Beam current and lifetime

Assuming an exponential decay of the beam current

$$I(t) = I_{max} e^{-t/\tau}, \tag{3.2}$$

and defining the down time, t_{down}, as the time during which data acquisition is inhibited for the detector high voltages to be ramped down, beam in the ring to be dumped and

Target Mode	Beam Mode	LIGIT Pressure (Torr)
H ABS	stored	8.8E-08
H ABS	injection	1.2E-07
Empty	stored	8.8E-08
Empty	injection	1.2E-07

Table 3.2: LIGIT pressure for different operating modes

refilled, and detectors ramped back up to operating conditions, one can determine the optimal data acquisition time, t_{DAQ}, to maximize the average current,

$$t_{DAQ} \approx \sqrt{2 \cdot \tau \cdot t_{down}}. \tag{3.3}$$

During operation, Eq. 3.3 is used as a guide to choose the duration of the data taking runs before dumping and refilling.

Maintaining a good ring vacuum is very important in order to preserve the beam lifetime. Table 3.2 summarizes typical pressures in the target region for different operating modes. These pressures are measured by the Lattice Ion Gauge Internal Target (LIGIT)

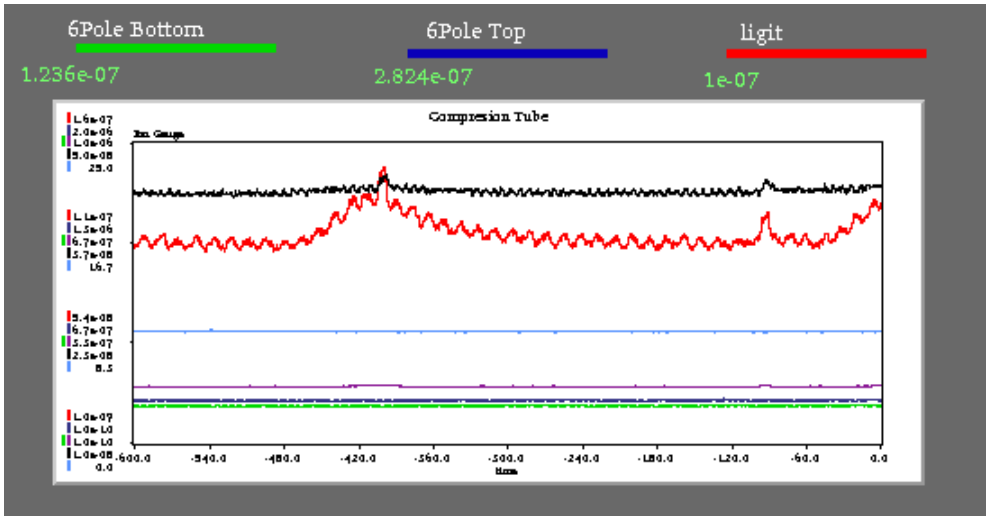

Figure 3-4: LIGIT Pressure vs Time

located in the region of the scattering chamber. Figure 3-4 shows a snapshot of the LIGIT pressure from the EPICS system, during data acquisition. Note the slight increase in LIGIT pressures during the injection.

3.1.3 Compton Polarimeter

The beam polarization in the ring is monitored in real time by a Compton polarimeter [82, 83]. The Compton polarimeter exploits the spin asymmetry of back-scattered polarized photons. Circularly polarized photons from a 5 W laser at 532 nm are incident on the stored electron beam in a section of the ring upstream of the target. Photons are scattered into a narrow cone centered around the incident photon path. By alternating the polarization of the incident photons via a Pockels cell [84], the spin-dependent asymmetry for this scattering can be measured. Backscattered photons are detected by a CsI crystal used as a calorimeter and the laser beam is chopped with a mechanical wheel to allow simultaneous background measurement. The helicity asymmetry as a function of photon energy is formed and fit to the theoretical asymmetry in order to extract the beam polarization. The analysis is performed in real time by a dedicated Compton control-analysis software package for immediate feedback. Then the complete data set is analyzed for secondary corrections. The typical helicity asymmetry and energy-dependent yield and from one fill are shown in Figures 3-5 and 3-6. A spin flipper [85] is used to reverse the helicity of the electron beam while in the ring. Its purpose is to study the false asymmetry in the Compton Polarimeter [86]. Sixteen sets of data are taken, each lasting around 5 hours. The helicity is flipped once during a fill such that the instrumental false asymmetries in the Compton Polarimeter are canceled. The flipper efficiency, defined as the polarization maintained after the flip, $\frac{(h^+ + h^-)_{after}}{(h^+ + h^-)_{before}}$, is around 96%. It has been concluded that the electron beam is equally polarized in the two helicity states.

The main causes of systematic errors in measuring the beam polarization are [86]: 1) Energy calibration of the CsI crystal calorimeter (± 0.03); 2) Laser polarization (± 0.02);

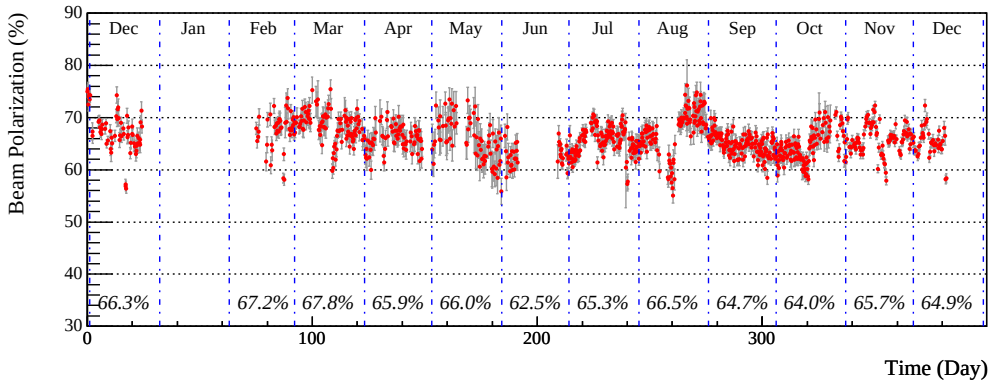

Figure 3-5: Compton polarimeter beam polarization data vs. time

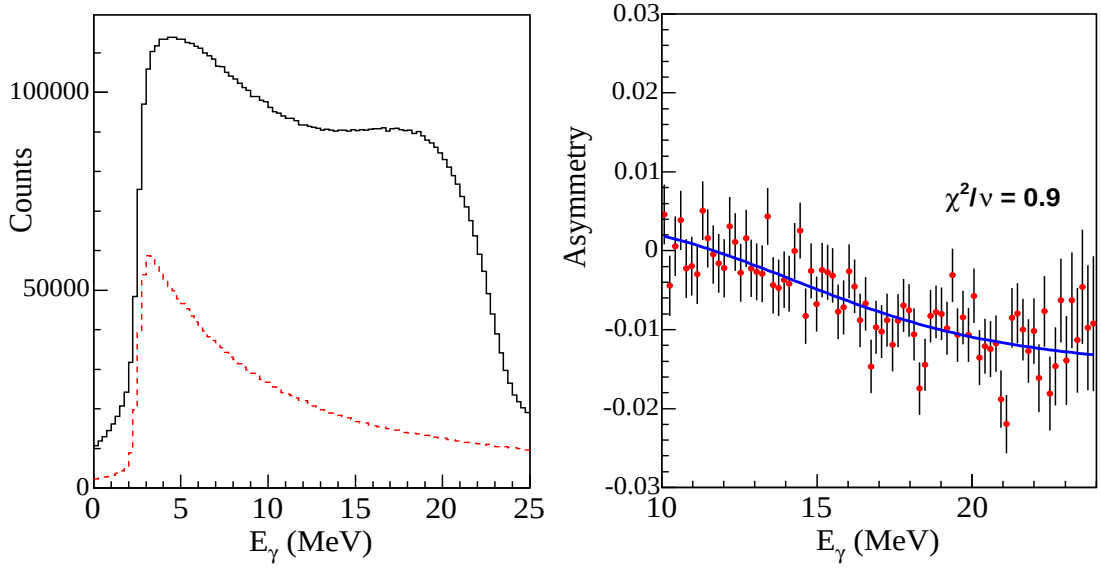

Figure 3-6: The yield (left) and asymmetry (right) of the Compton scattering during one fill of the storage ring. The total yield (solid black curve) is shown with the the background (dashed red curve). The laser helicity asymmetry is fit to the theoretical asymmetry to extract the beam polarization.

3) misalignment between the electron and laser beam (± 0.01). The average polarization for the hydrogen production run period from October to December of 2004 is $0.6558 \pm 0.0007_{stat} \pm 0.0004_{sys}$.

3.2 Polarized Internal Target

The BLAST polarized internal target uses an Atomic Beam Source (ABS) to inject polarized hydrogen or deuterium atoms into an internal storage cell. The ABS was originally used in the AmPS Ring at the NIKHEF laboratory [87] and modified to operate efficiently in the BLAST toroidal magnetic field [88].

3.2.1 Atomic Beam Source

The physical layout of the ABS is shown in Figure 3-7. Both deuterium and hydrogen are produced by the BLAST ABS. We focus here only on the hydrogen target. Molecular hydrogen is pumped into a dissociator. An RF frequency of 27.12 MHz is applied, and the molecular gas dissociates into its atomic constituents. The atomic beam is then ejected from the nozzle; the nozzle is cooled down to ~ 70 K to inhibit molecular recombination of the dissociated atoms as well as to reduce the individual atomic thermal velocities for more efficient focusing. The ejected beam is focused by the sextupole magnet system and passes into the ABS RF transition units. The atomic fraction α quantifies the degree of dissociation, which is defined as the population of selected atomic species versus total population in the target, and is given by

$$\alpha \;=\; \frac{P^a}{P^a + 2\kappa_\nu P^m} \tag{3.4}$$

where P^a and P^m are the partial pressures of the atomic and molecular gases in the target respectively [89]. The factor $\kappa_\nu \simeq 1/\sqrt{2}$ accounts for the different atomic and molecular velocities.

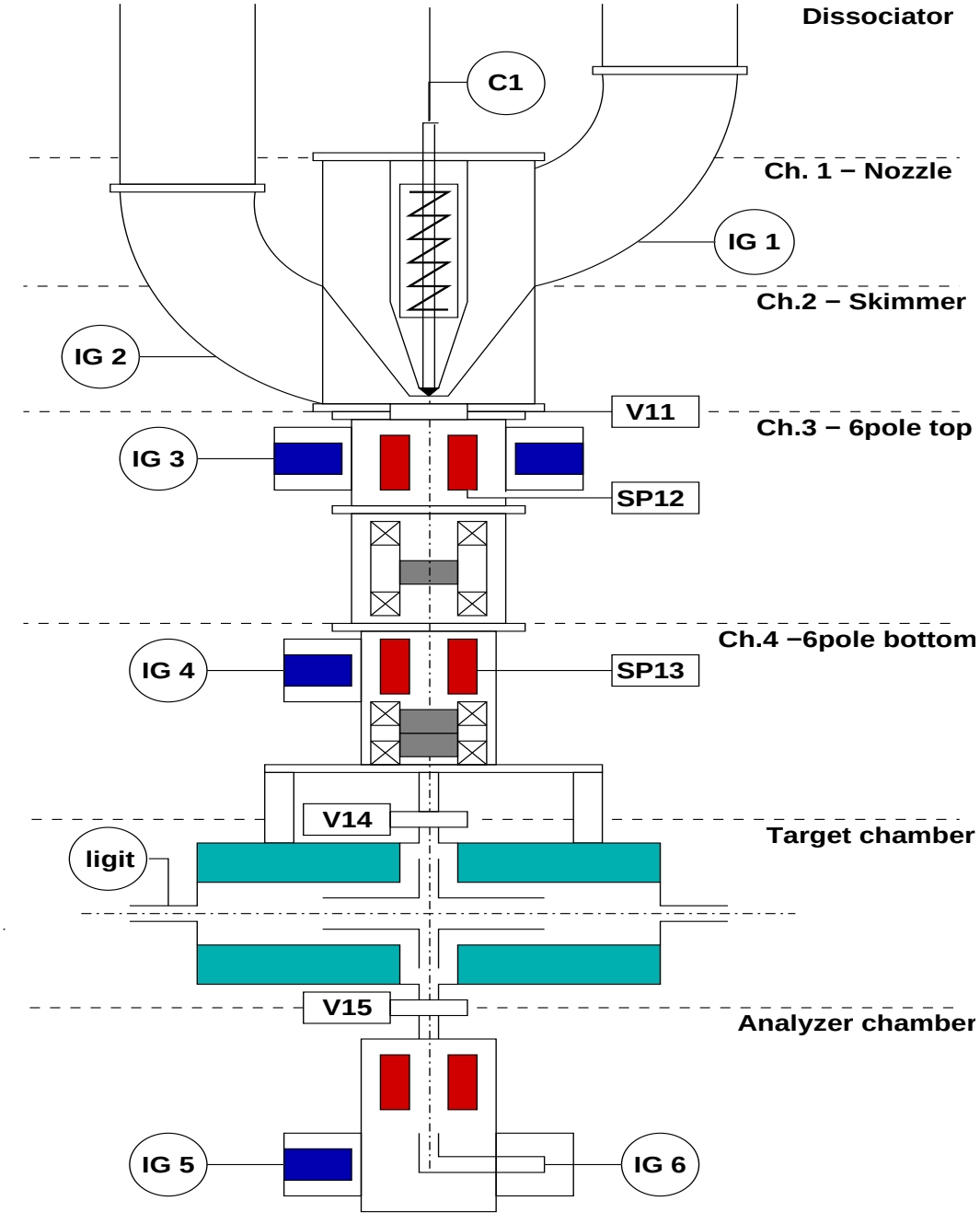

Figure 3-7: BLAST ABS and target storage cell.

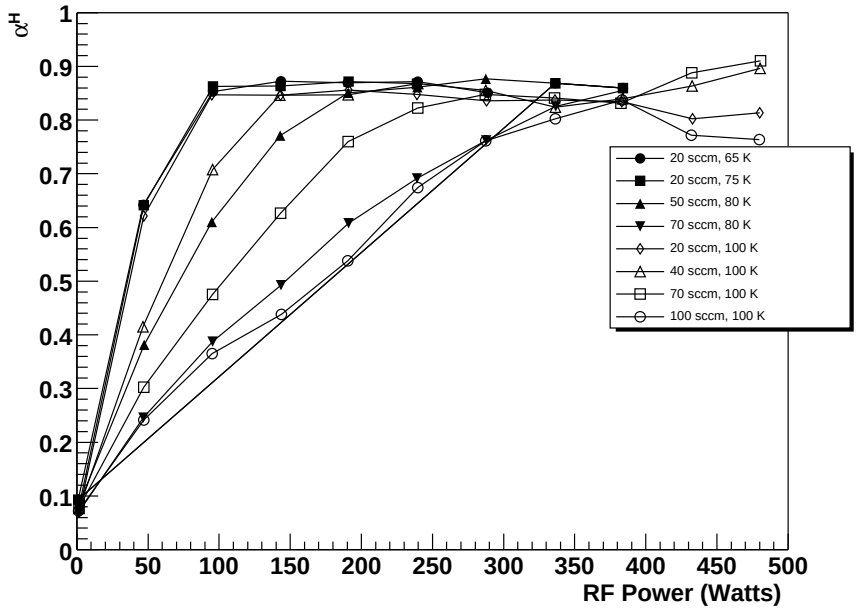

Figure 3-8: Hydrogen Atomic Fraction versus Flow Rate and Nozzle Temperature

Figure 3-8 shows the dependence of hydrogen atomic fraction on RF power for different flow rates in the dissociator and nozzle temperatures. As the flow rate increases, the atomic fraction decreases - so more RF power is required to obtain the same level of dissociation [89].

Polarization of the atomic beam is achieved by exploiting the hyperfine degeneracy of hydrogen spin states in the presence of a magnetic field (see Figure 3-9). By applying a superposition of a time-varying and static magnetic field, transitions between the hyperfine states can be induced. Atoms populating undesired hyperfine states are defocused by a sextupole (6-pole) magnet and removed from the atomic beam using the Stern-Gerlach effect [90]. Depending on the desired polarization state, the atomic beam passes through three kinds of transitions: a strong field transition (SFT), a weak field transition (WFT), and a medium field transition (MFT). The SFT uses a time-varying magnetic field directed perpendicular to a static one to cause atoms to switch populations between different

hyperfine multiplets; the WFT and MFT use a time-varying magnetic field directed along the static one to cause population changes within a hyperfine multiplet. By applying the correct sequence of transitions, it is possible to produce positively or negatively vector (P_Z) polarized hydrogen beams.

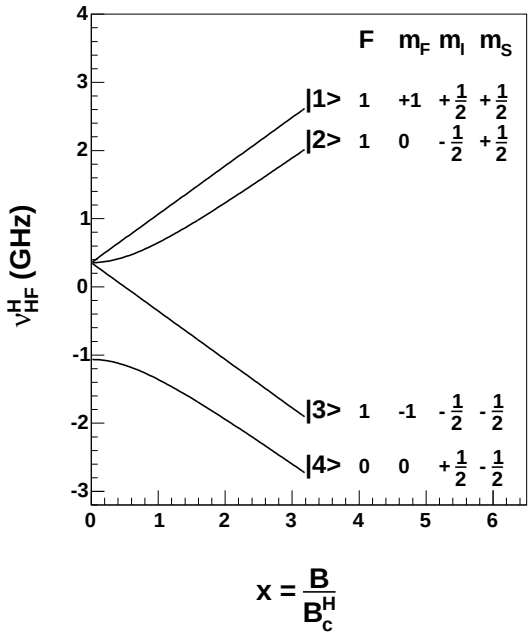

Figure 3-9: Hyperfine states of hydrogen.

The following multiplet occupation sequence shows the procedure followed to obtain *Vector minus* polarization for hydrogen:

$$\begin{pmatrix} n_1 \\ n_2 \\ n_3 \\ n_4 \end{pmatrix} \overset{\text{sixpole}}{\Longrightarrow} \begin{pmatrix} n_1 \\ n_2 \\ 0 \\ 0 \end{pmatrix} \overset{\text{MFT23}}{\Longrightarrow} \begin{pmatrix} n_1 \\ 0 \\ n_2 \\ 0 \end{pmatrix} \overset{\text{sixpole}}{\Longrightarrow} \begin{pmatrix} n_1 \\ 0 \\ 0 \\ 0 \end{pmatrix} \overset{\text{WFT13}}{\Longrightarrow} \begin{pmatrix} 0 \\ 0 \\ n_1 \\ 0 \end{pmatrix} \tag{3.5}$$

The ABS intensity is defined as

$$I(Q) \;=\; I_0 \cdot Q \cdot e^{-Q/Q_0} \tag{3.6}$$

where Q is the flow into the dissociator, I_0 is the intensity in the absence of rest gas scattering, and Q_0 is a factor parameterizing the beam attenuation due to rest gas scattering. An average hydrogen ABS intensity of $\simeq 2.6 \times 10^{16}$ atoms/s was achieved during the course of the experiment. This intensity corresponds to a target thickness of $\simeq 4.5 \times 10^{13}$ atoms/cm^2 [89].

3.2.2 Target Cell and Scattering Chamber

After the ABS chamber, the polarized atomic beam enters the target cell within the scattering chamber. The target cell is internal to the SHR and is cylindrical in shape with no end caps to interact with the beam. It has a diameter of 15 mm and a length of 60 cm along to the beam. The target cell is used to maximize the luminosity of the polarized atomic beam while preserving the stored electron beam in the SHR. The atomic beam enters via the inlet tube at the middle and disperses throughout the entire 60 cm length of the cell. The density profile along the cell is approximately triangular [91]. To decrease depolarization within the target cell, the inside of the cell is coated with Drifilm and kept at ~ 100 K. A holding field produced by two orthogonal sets of coils is used to define the target polarization axis. It is capable of generating longitudinal and transverse magnetic fields. The holding magnet is limited in length, however, to 40 cm. As such, only the innermost 40 cm of the target cell contain reliably polarized atoms. The polarization for the hydrogen target is derived from an electron-proton elastic scattering analysis. Coincidence and timing cuts are used to select good events and the beam-target asymmetry is compared to a Monte Carlo simulation.

The measured product of beam and target polarization for the data collected at the

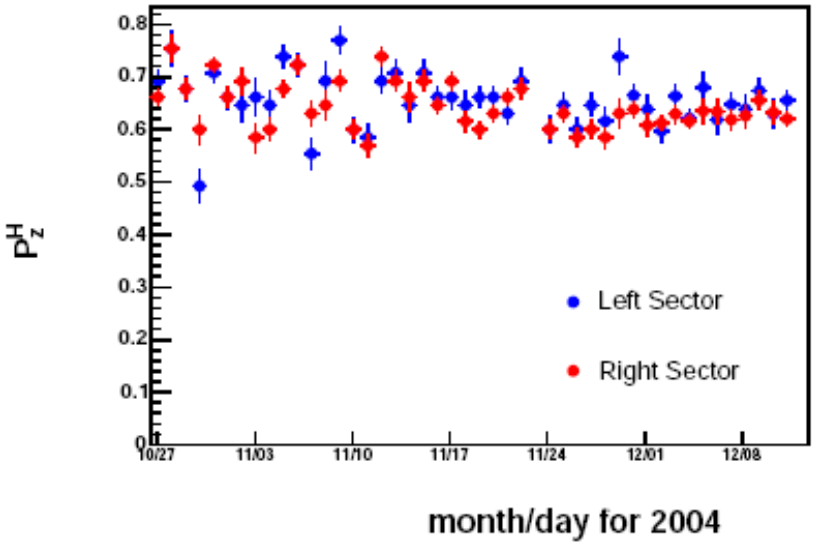

Figure 3-10: Hydrogen target polarization for fall 2004 data.

end of 2004 is shown in Figure 3-10 for the entire running period. Overall, using the beam polarization from the Compton polarimeter, we get $P_z = 0.8 \pm 0.0004\%$

3.3 BLAST Detector

The Bates Large Acceptance Spectrometer Toroid experiment, BLAST, at the MIT-Bates Linear Accelerator Laboratory was designed to study in a systematic manner the spin-dependent electromagnetic interaction in few-nucleon systems at momentum transfers below 1 GeV/c [92]. BLAST is able to make simultaneous measurements of several reaction channels for different combinations of beam helicity and target polarization (vector for hydrogen, both vector and tensor for deuterium). The large acceptance of the detector allows the measurement of observables over a broad kinematic range. The azimuthal symmetry and the two-opposite sectors (left and right) configuration allow for single-

arm, coincidence and super-ratio experiments. The detector package consists of individual detector arrays designed and instrumented for the intended measurements [93]. The design was driven by the experiment's requirements of timing resolution, momentum, tracking resolutions and particle identification. The BLAST detector is built around eight coils of a toroid magnet which divide the space around the beam line into eight sectors. The top and bottom sectors between the coils contain the ABS, while the two horizontal sectors are instrumented with the individual detectors, producing a left-right symmetrical design. Scattered particles originated from the target cell pass through, in an radially outward sequence, drift chambers (WC), Čerenkov detectors (CC), time-of-flight (TOF) scintillators and neutron counters (NC). The neutron detectors are the only asymmetric component of BLAST: the right sector has two extra sets of scintillators (LADS). Figure 3-11 shows the position of each individual component in the BLAST detector, and Figure 3-12 shows the size of the individual detectors. All these detectors have been used for the inclusive scattering studies.

3.3.1 BLAST Toroid Magnet

To determine the charge and momenta of the particles, a strong magnetic field is required in the region of the drift chambers. The BLAST toroidal magnetic field is generated by eight copper conductor coils symmetrically arranged around the beam line, as shown in Fig. 3-13.

The toroidal field provides a field-free target region so that the target holding field and incident electron beam are not negatively affected. The coils are shaped to provide maximum dispersion for the forward electrons and have a 1 m opening in the back to accommodate the ABS and internal target. The coils operate, during data taking, at their maximum current of 6731 A to provide maximal momentum resolution. The maximum magnetic field at this current is 3800 Gauss, which occurs $\sim$ 1 m from the beam line in the vicinity of the drift chambers. Strong aluminum frames support the coils in place,

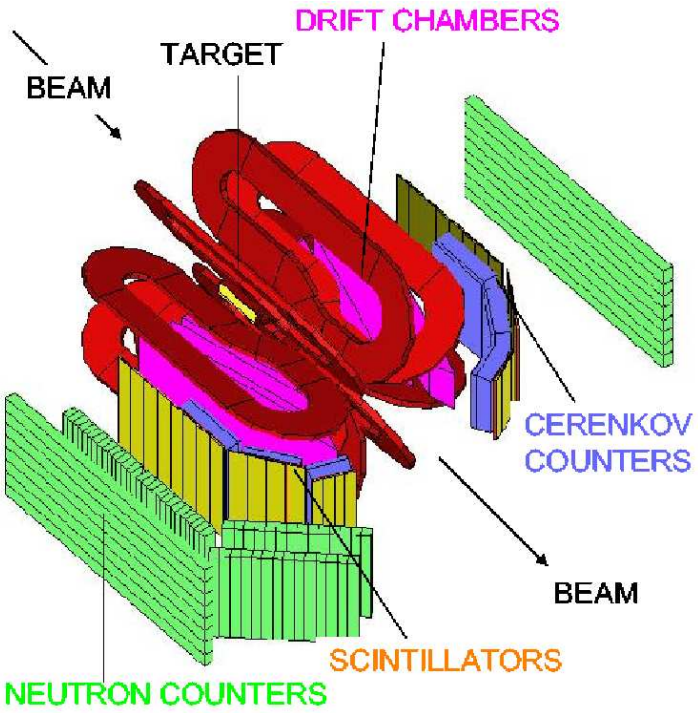

Figure 3-11: BLAST Detector

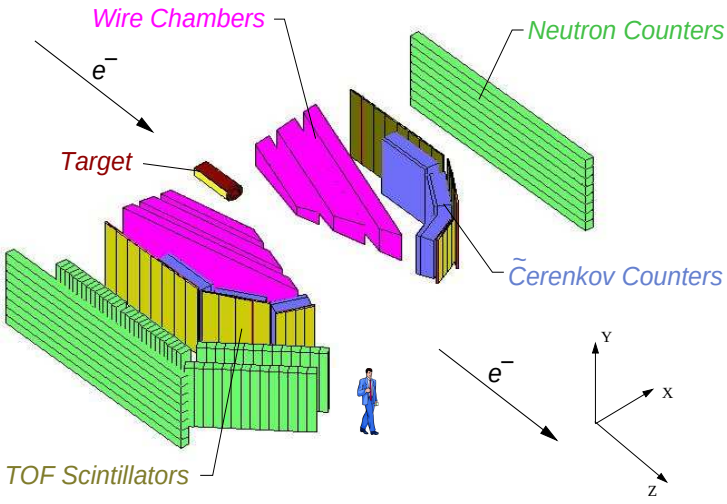

Figure 3-12: BLAST laboratory frame

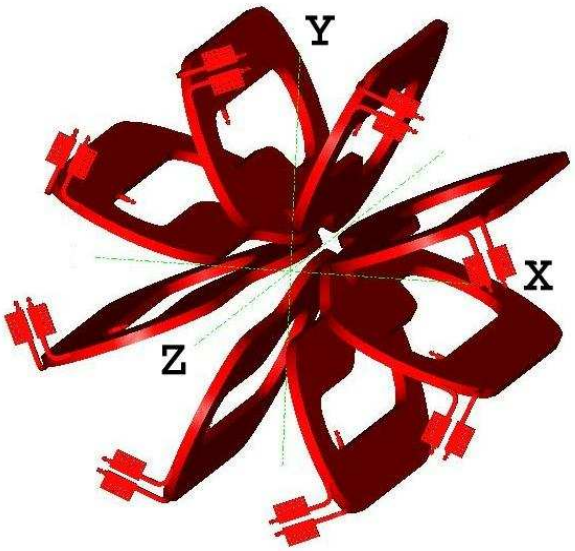

Figure 3-13: BLAST copper coils.

and the maximum deflection of the frame is 7-8 mm when the field is energized at full strength. The field mapping was done with an automated x-y-z table with a spatial resolution of 0.05 mm and two three-dimensional Hall probes with 0.1% precision. The probe positions are surveyed at 10 to 20 points and related to the x-y-z table coordinates. The uncertainties in the probe positions are $\sim$ 0.05 mm. The table coordinates and fields are recorded at each of the $\sim 43,000$ points, measured in a grid of 5 cm spacing in each direction. The mapped field is interpolated into a rectangular grid of 5 cm step in each direction in the BLAST coordinate system and is analytically extended beyond the measured region for a more robust trajectory fitting. The field is also modeled in TOSCA and an analytical Biot-Savart calculation, and the field map agrees with both models to within 1%. The 7-8 mm displacement observed in geometric survey of coil positions is also confirmed by the Bio-Savart calculation where coil positions are moved

to fit the observed field values. The interpolated and extended grid covers a rectangular volume of $-200\,\text{cm} \leq X \leq 200\,\text{cm}$, $-70\,\text{cm} \leq Y \leq 70\,\text{cm}$ and $-10\,\text{cm} \leq Z \leq 290\,\text{cm}$ (See Figure 3-12 for the definition of the coordinate system). There are about 150 points in the 143, 289-point grid where the mapped values differ from the Bio-Savart calculations by more than 200 G. This is attributed to occasional x-y-z table jamming during mapping, which caused missing field values for these points. The measured field value is replaced with the Bio-Savart calculations for these points [94]. The field-map of B_y in the central horizontal plane is shown in Fig. 3-14.

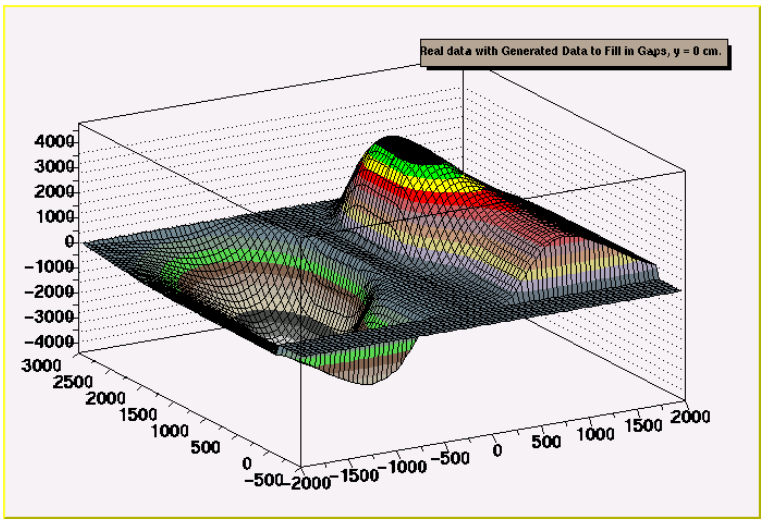

Figure 3-14: Magnetic field map of B_y in the central horizontal plane of BLAST.

3.3.2 Drift Chambers

In order to obtain the information for a detected particle (momentum, scattering vertex position, particle identification, etc.), drift chambers are used. Operation of the chambers depends on the principles of charged particles traveling through a gas volume [95, 96, 97].

Each sector contains three chambers made of one-piece aluminum frames that are

joined together with spacers into one single air-tight chamber (see Figure 3-15). The frames were pre-stressed to compensate for the deformation from the wire tension. A

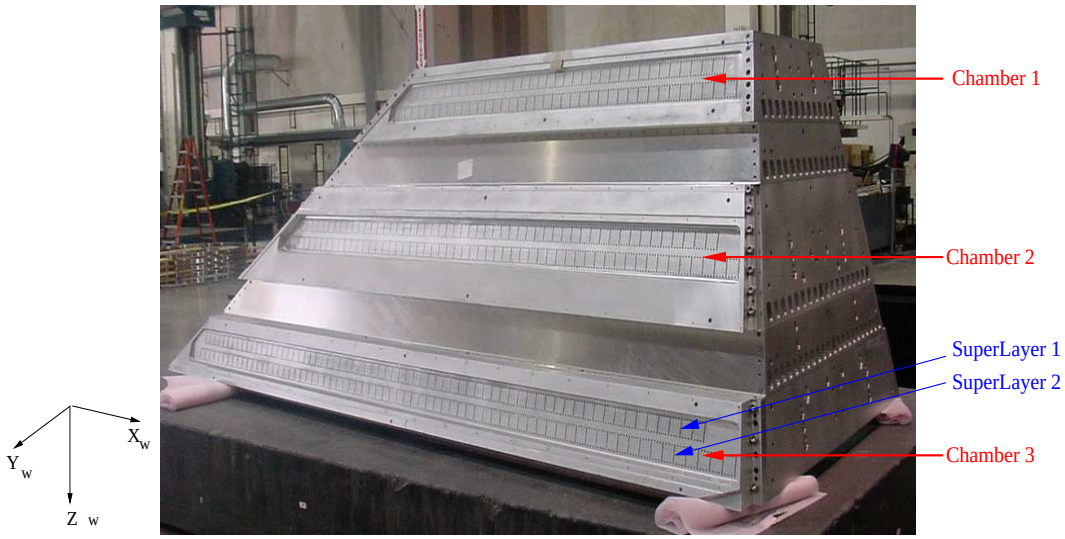

Figure 3-15: One sector drift chambers

coordinate system is defined for each of the six chambers where x_w is in the horizontal plane pointing toward the upstream direction at an angle of $\alpha = 163.5°$ with respect to the beam direction, y_w points vertically up in the left sector and down in the right sector and z_w forms a right-hand system with y_w and x_w. For all the chambers, z_w points away from the target (see Figure 3-15.

The drift chambers (WC) are placed in the horizontal openings between the coils and are designed to maximize the acceptance within the geometric constraints [98]. They cover a polar angle range of $20° < \theta_e < 80°$ and azimuthal angle range of $-17.5° \leq \phi_e \leq 17.5°$. Figure 3-16 shows a top-view of the chambers. Each chamber is divided into individual cells, namely, rectangular arrays of 39 wires with transverse dimensions $4\,\text{cm} \times 7.8\,\text{cm}$ [99]. There are three kinds of wires in the cells: *sense* wires, made of tungsten,

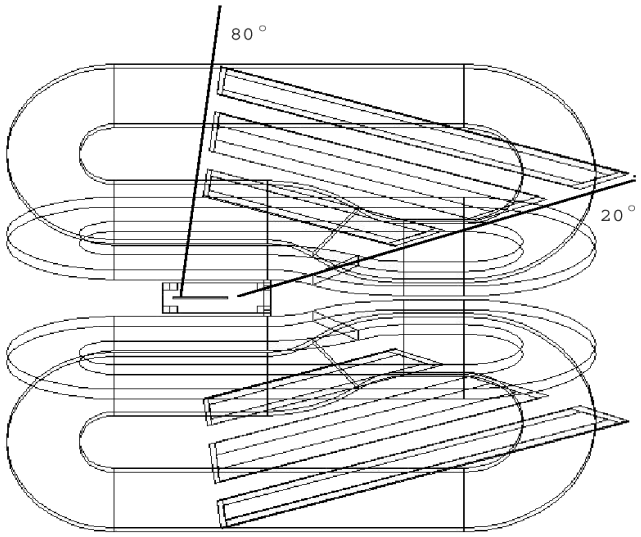

Figure 3-16: Top-view of the drift chambers

connected to amplifier-discriminator cards and used for readout, *guard* wires, made of copper, used for gain-matching of the sense wires, and *field* wires, also made of copper, used to shape the electric field in the sensitive region. Each chamber contains two *superlayers*, and each *superlayer* contains three *layers* of *sense* wires. Each *superlayer* is a plane, perpendicular to z_w and parallel to the x_w-y_w plane, where the wires string in an up-and-down orientation. The wires in the *inner superlayers* were rotated about the z_w direction by an angle of $+5°$ and those in the *outer superlayers* by $-5°$.

High voltages (HV) are applied to the field wires creating an electric gradient toward the sense wires. The HV on the guard wires are optimized to shape the field between the sense wires. The sense wires are set at 3850 V. The electric field produced with this arrangement is shown in Figure 3-17, that resembles two oppositely directed "jets" for each sense wire. In the absence of magnetic field, the ionized electrons drift along the electric field line. In the presence of the toroidal magnetic field, the drift lines are distorted. The

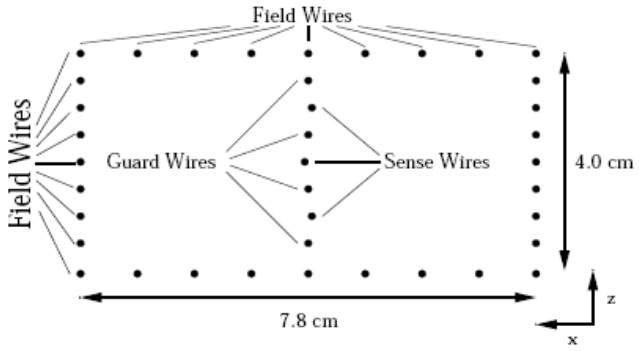

Figure 3-17: Cell wires.

effect of BLAST magnetic field is studied with a GARFIELD simulation and is included in Figure 3-18.

The chambers in a sector share a single gas volume. The gas mixture used to operate the chambers is composed of 82.3% Helium and 17.7% isobutane. helium is used as the *ionization gas*, while isobutane is used as a *quenching gas* in order to absorb photons created by electron recombination. Careful consideration has to be given to the mixture of ionization and quenching gas used in the chambers so that there is no reduction of the tracking efficiency. The entrances of the chambers were composed of two thin sheets of mylar in order to reduce multiple scattering. The gap between the mylar sheets is purged with nitrogen to protect phototubes on the adjacent detectors from helium poisoning [100]. The exit windows have a thicker acryllic window [100]. The reconstruction of the particle trajectory is performed in two stages: track linking and track fitting. Track linking contains four steps: hits, stubs, segments and tracks. The track linking is given in Figure 3-19. First the *hits* are reconstructed from TDCs with the time-to-distance conversion functions. The plane parallel to the wires with the minimal sum of square distances to the hits is called a *stub*. The two stub planes in the two superlayers within

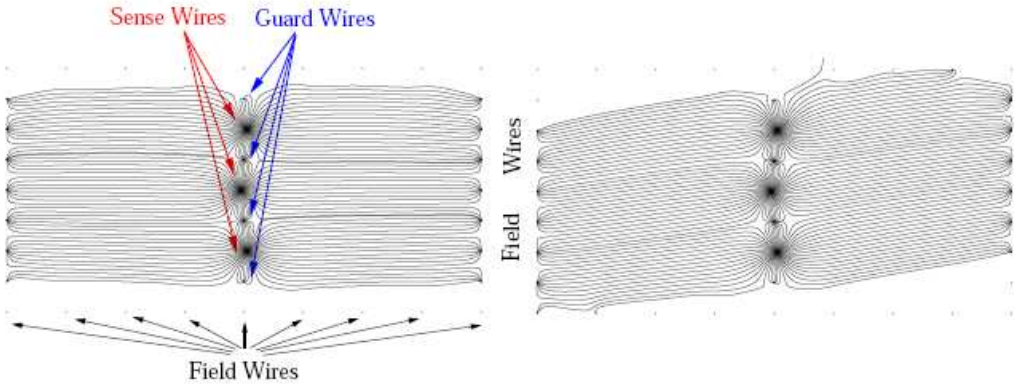

Figure 3-18: Drift lines in a cell without (left) and with (right) magnetic field.

a chamber intersect and determine a line *segment*. The toroidal nature of the BLAST magnetic field assures that the geometric track of the particle lies in the plane expanded by the beam line and its initial momentum, and if the magnetic field is approximately constant, the trajectory of a charged particle is a circle which can be determined by three degrees of freedom x_1, x_2 and x_3. The circle, known as a *track*, is parameterized by five variables $(p, \theta, \phi, z; q)$, where p is the momentum obtained from the curvature of the circle and the average magnetic field along the circle, z is the vertex, θ and ϕ are the polar and azimuthal direction of the momentum at the vertex and $q = \pm 1$ is the charge of the track deduced from the direction in which the center of the circle lies relative to the track. Track fitting is also done in two stages: first, all particles are treated as ultra-relativistic due to lack of timing information, then, once a solution is found, the trajectory is extended according to the equation of motion to outer detectors. The hits in the TOF, CC, NC are linked to the drift chamber tracks according to geometric intersections of the tracks and the detectors.

Kinematic resolution is measured by the over-determined kinematics in elastic $H(e, e'p)$ and $D(e, e'd)$ reactions. For example, the reconstructed electron momentum p_e is com-

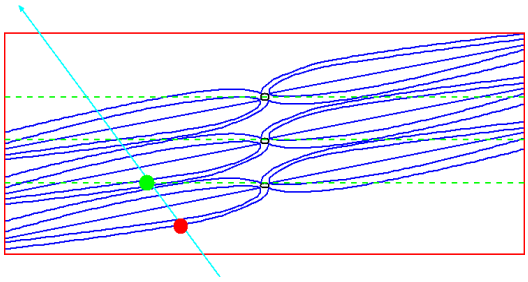

(a) Time-to-distance function calculates the perpendicular distance of the track from the wire

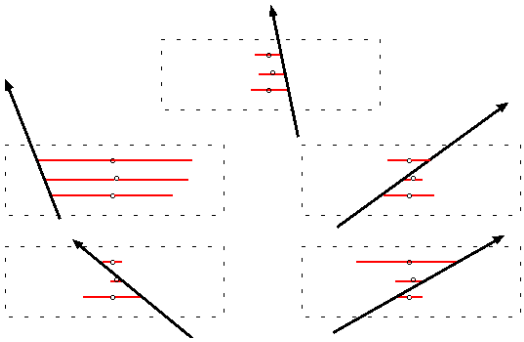

(b) Stub-finder determines to which side of each wire the track passed. 5 different cases of the 8 possibilities are shown

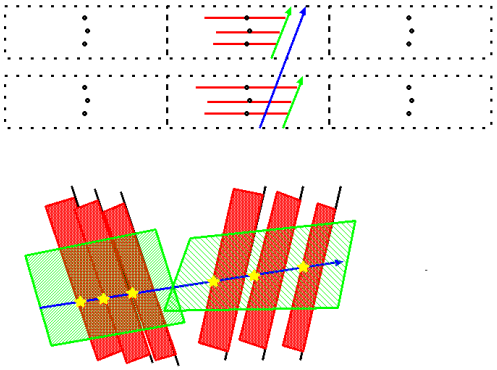

(c) In each chamber, the intersection of two stub planes forms a line segment

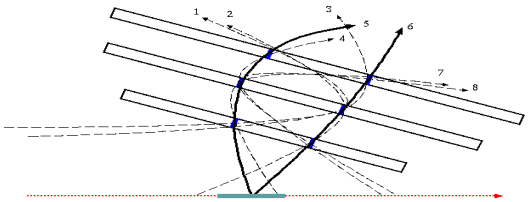

(d) The line segments are linked to form the most likely tracks

Figure 3-19: Steps of track reconstruction from hits in the drift chambers.

pared to the momentum value calculated from the reconstructed θ_e, and the standard deviation is used to measure the tracking resolution. Using the elastic electron-proton scattering events, the following resolution measures are extracted:

$$\begin{aligned} \Delta_{p_e} &= p_e - p_e(\theta_e), \\ \Delta_{\phi} &= \phi_{right} - \phi_{left} - 180^{\circ}, \\ \Delta_{z} &= z_e - z_p. \\ \Delta_{\theta_e} &= \theta_p - \theta_e(\theta_p), \\ \Delta_{p_p} &= p_p - p_p(\theta_e), \end{aligned} \tag{3.7}$$

Reconstruction Variable	Design Value	Measured Value
$\Delta k'$	2%	3%
$\Delta\theta_e$	0.30°	0.45°
$\Delta\phi_e$	0.50°	0.56°
Δz_e	1.0 cm	1.0 cm

Table 3.3: Drift Chamber Reconstruction Resolutions.

Using 130 μm as the intrinsic wire resolution and incorporating Monte Carlo studies of multiple scattering, the drift chamber reconstruction resolution values used in the inclusive reaction are given in Table 3.3.

3.3.3 Čerenkov Counters

The Čerenkov counters provide the primary electron/pion particle identification for BLAST [101].

A charged particle traveling in a medium with a speed greater than the speed of light in that medium emits Čerenkov radiation. A cone is formed (see Figure 3-20), and its half-angle θ is given by [102]:

$$\theta \;=\; \tan^{-1}(\sqrt{n^2\frac{v^2}{c^2}-1}) \tag{3.8}$$

Each counter has silica aerogel (manufactured by Matsushita Electric Works, Ltd.) as radiator. There are three counters per sector. The most forward counter contains an aerogel radiator 7 cm thick with an index of refraction $n = 1.02$, the other counters have 5 cm thick aerogel with $n = 1.03$. This arrangement is good enough to discriminate between pions and electrons up to at least 700 MeV/c. Each counter consists of a large box with diffusely reflective walls to collect the Čerenkov light into properly arranged photomultiplier tubes (PMTs).

An open counter is shown in Figure 3-21. All the interior surfaces are coated with

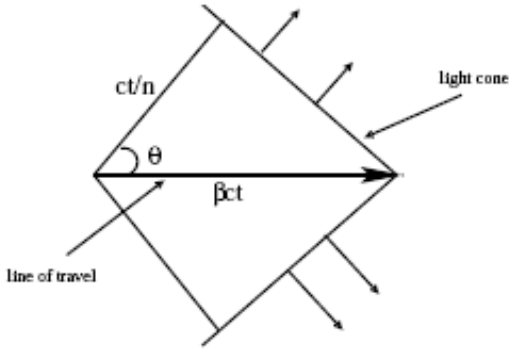

Figure 3-20: Čerenkov radiation.

a white reflective paint specially manufactured for diffusive reflection by Labsphere, Inc. The most forward counter (small) has six PMTs and covers the range of $20° < \theta_e < 35°$, the next counter (middle) has eight PMTs and covers the range $35° < \theta_e < 50°$, while the last one (big) has twelve PMTs and covers the range $50° < \theta_e < 65°$ (see Figure). All boxes cover the entire azimuthal acceptance of the respective BLAST sector and their dimensions vary slightly due to the magnetic coil shape. The dimensions of the largest boxes were 100 cm wide, 150 cm height, and 19 cm deep. Each counter is fed with a laser pulse for timing and gain monitoring. Some of the technical characteristics of the Čerenkov counters are summarized in Table 3.4. The photomultipliers are 5-inch diameter fast tubes

	Box 1	Box 2	Box 3
Number of PMTs	6	8	12
Angle subtending	$20° - 35°$	$35° - 50°$	$50° - 65°$
Aerogel thickness	7cm	5cm	5cm
Refraction index	1.02	1.03	1.03

Table 3.4: Čerenkov counter specifications.

Figure 3-21: A Čerenkov box (middle size box).

(Photonis type XP4500B). They are "heavily" shielded against the BLAST magnetic field, using both two concentric low-carbon steel cylinders, and extra thick iron plates in front of the coils. To minimize the loss of photons in the entrance region between the box and the PMT cylinder, a simple aluminum cone with a reflectivity of about 98% has been mounted.

The photo-electron signal and the average number of PMTs which trigger per event are used to perform a Monte Carlo simulation of the ADC spectrum for a particular Čerenkov counter. A Poisson event generator [101] is used to simulate the number of photo-electrons and their multiplication throughout the dynode stages in a linear focusing PMT. The Poisson distributed signal takes into account the diminuation of fluctuations around the mean from the first dynode to the next. This can be expressed by the equation,

$$\sigma_i = \left[PE \cdot \prod_{j=1}^{n} g_j \right]^{1/2}, \; n = i - 1 \tag{3.9}$$

where σ_i is the fluctuation in the distribution of the number of electrons at i^{th} stage, PE is the mean of the photo-electron distribution and g_js is the gain of the j^{th} stage. The

ADC spectrum for a particular counter is obtained by doing an event by event sum of the individual PMT ADCs that trigger an event. A pedestal-subtracted ADC spectrum produced by the Monte Carlo for a multiplicity of 4 is shown in Figure 3-22, including a fit with a Poisson distribution. These simulations fit the data for each individual counter.

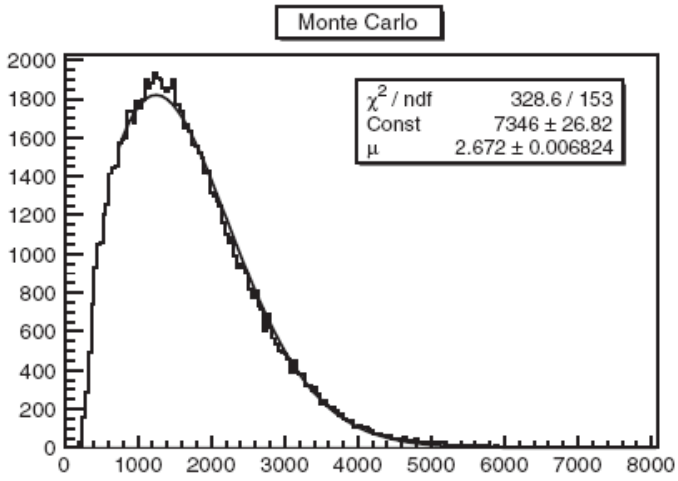

Figure 3-22: A simulated Čerenkov ADC.

Prior to installation into the BLAST detector, the counters were tested in the High Bay area of the MIT-Bates laboratory, and their efficiency was above 90% for all the boxes. Unfortunately, after installation, the huge magnetic field affected it drastically. Extra "heavy" shielding was required to decrease the intensity of the field inside the iron cylinder where the PMT lies. Gain-matching of the PMTs is done in situ using the electron-proton elastic scattering and monitor all phototubes. In order to compensate for the high magnetic field, the PMTs are gain-matched at higher voltage values than those used in the testing facility.

The efficiency is studied using again elastic ep scattering and the TOF detectors which are very efficient. In Figure 3-23 the efficiency results are shown as a function of TOF paddle, where 1 corresponds to the most forward TOF. The red-square represents the right sector counters, while the blue-diamond, the left sector respectively.

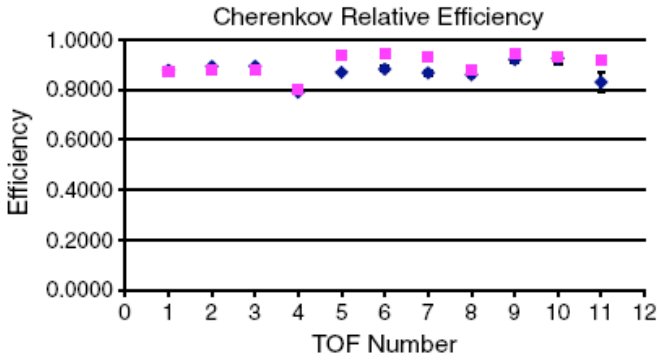

Figure 3-23: Čerenkov counters efficiency as a function of TOF number. Red square shows the right sector and blue diamond the left sector counters.

The lower efficiency corresponding to TOF number 4, 8 and 12 is caused by geometric effects: the counters are not 100% covered by the TOFs. Recall that each Čerenkov counter is "covered" by four TOFs. The efficiency results for the three counters on each sector along the box are shown in Figure 3-24. The $y-$axis ($-90°$ to $90°$) represents the detector length centered in the middle, and the $x-$axis shows the corresponding TOF paddle starting from the first most forward (0 in this case). This shows a uniform efficiency along each individual counter.

3.3.4 Time-of-Flight Scintillators

The time-of-flight scintillators (TOF) are used to obtain timing for the trigger, position information, and particle identification in coincidence events. There are sixteen TOFs in each sector, which cover the entire wire chamber geometry, $20° < \theta_e < 80°$, and additional

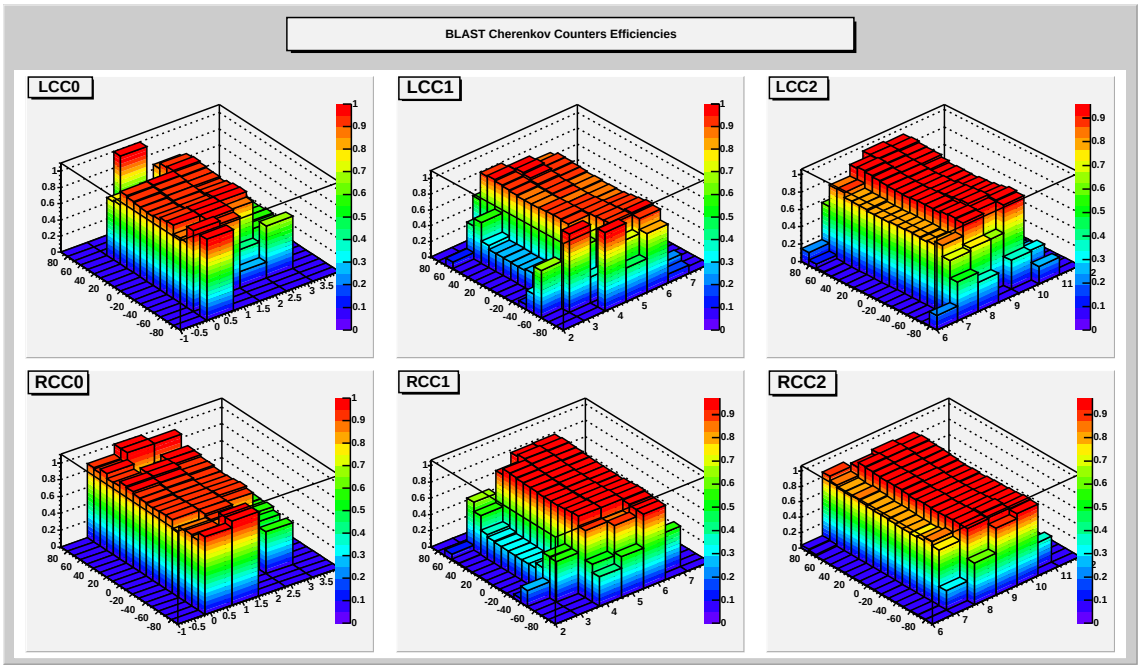

Figure 3-24: Čerenkov counters efficiencies along the box vs. TOF paddle. The left sector counters are on top, and the right sector on the bottom. The most forward TOF starts from 0.

four backward-angle cover the outside region $80° < \theta_e < 120°$. The TOFs are made of 2.5 cm thick Bicron BC-408 scintillator [103]. Properties of BC-408 scintillator are given in Table 3.5 [104].

The most forward four paddles are each 120 cm tall while the remaining twelve are 180 cm tall. The forward four TOFs are shorter because they are mounted closer to the beam line, needed to cover the same azimuthal acceptance of wire chamber at forward angle and have a higher background rate. All but the last four had 10 mil (0.254 mm) of lead shielding in front of the scintillator material (from X-rays). A photomultiplier tube (PMT) is mounted on each end of each TOF paddle through Lucite light guides. The light guides bend the path of light such that the PMTs are mounted with their cylindrical axis perpendicular to the residual BLAST magnetic field. The TOFs are mounted on aluminum subframes which could be pulled open to provide space for drift chamber and target work. A view of the BLAST right sector TOF placement is shown in Figure 3-

Base	Polyvinyltoluene
Refractive Index	1.58
Rise Time (ns)	0.9
Decay Time (ns)	2.1
Pulse Width, FWHM (ns)	∼2.5
Attenuation Length (cm)	210
Peak Wavelength (nm)	425

Table 3.5: Properties of Bicron BC-408 Organic Plastic Scintillator

25. The forward-angle scintillators are labeled with blue stripes, while the rest with red. Magnetic shielding (Mu-Metal) is placed around each PMT in order to provide shielding from the residual toroidal magnetic field. Each plastic TOF bar is wrapped in black kapton for light leaks prevention.

The electronic base for each PMT consists of an actively stabilized voltage divider supplying the high voltage to the PMT as well as returning the output signal of the PMT to the data acquisition system. By setting the voltage between the photocathode and the first dynode with a zener diode, the timing is made independent of the tube gain [103].

The TOF efficiency has been studied with ep-elastic events from hydrogen target runs. The efficiency of all the TOFs is above 99% [103].

3.3.5 Neutron Detectors

The TOF scintillators are too thin for efficient neutron detection, so a wall of 8 thick horizontal scintillators is placed behind each detector sub-frame. Because the target spin is oriented in the left sector of the detector, neutron detection is more important in the right sector (i.e. perpendicular kinematics) for the extraction of the neutron electric form-factor G_E^n from a coincidence measurement. Thus extra neutron detectors have been added to the right sector. The neutron counters consist of two eight-bar walls, known as Ohio walls, on each sector, plus an additional four Large Acceptance Detectors, LADS,

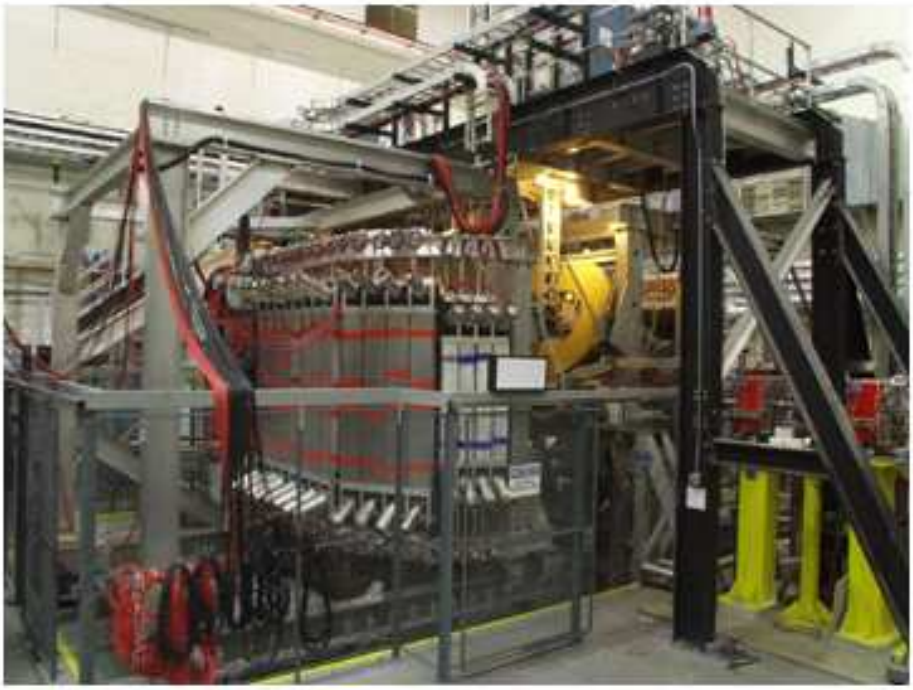

Figure 3-25: View of BLAST Right Sector TOFs

walls placed in the right sector from Paul Scherrer Institute (see Figure 3-11 and 3-12).

The farther the position of the NC and LADS walls from the target, the greater thickness, as well as veto capability from the drift chambers and TOFs, the better the neutron detection.

3.4 Data Acquisition

The BLAST trigger can be divided into three parts: first, it takes the analog signals from the detectors as inputs and returns digital logic signals that indicate which elements of the detectors received hits; second, it correlates the logic signals from the detectors in each sector; third, it correlates the logic signals from the two sectors.

3.4.1 First Level Trigger

The signal from each PMT of the Čerenkov counter is sent to a CAEN N407 analog adder, which adds together all the PMTs' signals for a box. One copy of the output signal is sent to the ADC through a delay unit, and the other copy to a single LeCroy Model 3412 leading edge discriminator. The output of the latter one is sent to a LeCroy 4418/32 delay/fanout, and its output to a LeCroy 4532 Pairwise OR unit and to TDCs and VME scalers.

The PMT signals from the TOFs (32) are fed into a splitter (custom built). One copy is sent to the ADCs, and the other to two LeCroy Model 3420 constant fraction discriminators (CFD), one for the top 16 and the other for the bottom 16 PMTs. The signals from the CFDs are then sent to an adjacent LeCroy Model 4418/4518 delay/fanout: one set of output signals from the fanout is sent to the TDCs and to the VME scalers for visualization, while the second set of output signals is sent to a LeCroy Model 4516 logic module where each pair of top and bottom PMT signals are ANDed together (coincidence of top-bottom PMTs); this eliminates many counterfeit signals from the trigger. The output of the coincidence logic is sent to another Model 4418/4518 delay/fanout to allow for equalization of signal timing between different scintillators. The output from this fanout is sent to the scalers and to the next sector logic. The signals are numbered 1-16 from small to large angles.

The electronics for the neutron counters are custom built and follow the same routine: a discriminator, then a logic AND, then a logic OR. A copy is sent to the ADCs before the discriminator, and one to the TDCs after it. Also copies are sent to the scaler from both the discriminator and logic AND.

Software-controllable LeCroy Model 2373 memory lookup units (MLUs) are used to correlate the signals from the various detectors. There is one for each sector. In order

bit no.	input signal
0-3	single TOFs no. 1-4
4-9	paired TOFs no. 5-16
10	ORed BATs
11	ORed Čerenkov
15	ORed Neutrons

Table 3.6: The sector MLU input bits assignment.

for the MLUs to function at a reasonable rate, it is necessary to reduce the number of inputs which must be processed. Channel reduction is carried out in two logic modules: a LeCroy 4532 Majority Logic Unit is used in its secondary mode as a fast pairwise OR for the Čerenkov counters and for the 12 large angle TOF scintillators (number 5 to 16) that are paired into 6 logical signals. The loss in resolution is acceptable since event rates are slower at large angles. A LeCroy 4564 OR module is used to perform the remaining channel reduction.

Table 3.6 shows the assigned bits for the corresponding input signals:

The final section of the trigger takes the output of the two sector MLUs as an input and sends gates and start signals to the digitization electronics. This is accomplished by another LeCroy Model 2373 memory lookup unit (MLU), called the cross-sector MLU (XMLU). The first six output bits from the right and left sector MLUs are mapped to input bits 0-5 and 6-11 of the cross-sector MLU, respectively. Bit number 14 is assigned to the flasher, the laser used to calibrate and monitor the TOFs, CCs and NCs.

The BLAST trigger diagram is shown in Figure 3-26.

3.4.2 Trigger Types

BLAST experiment has been designed to collect data for various reaction channels simultaneously. Table 3.7 summarizes the trigger types, their corresponding bits in the XMLU,

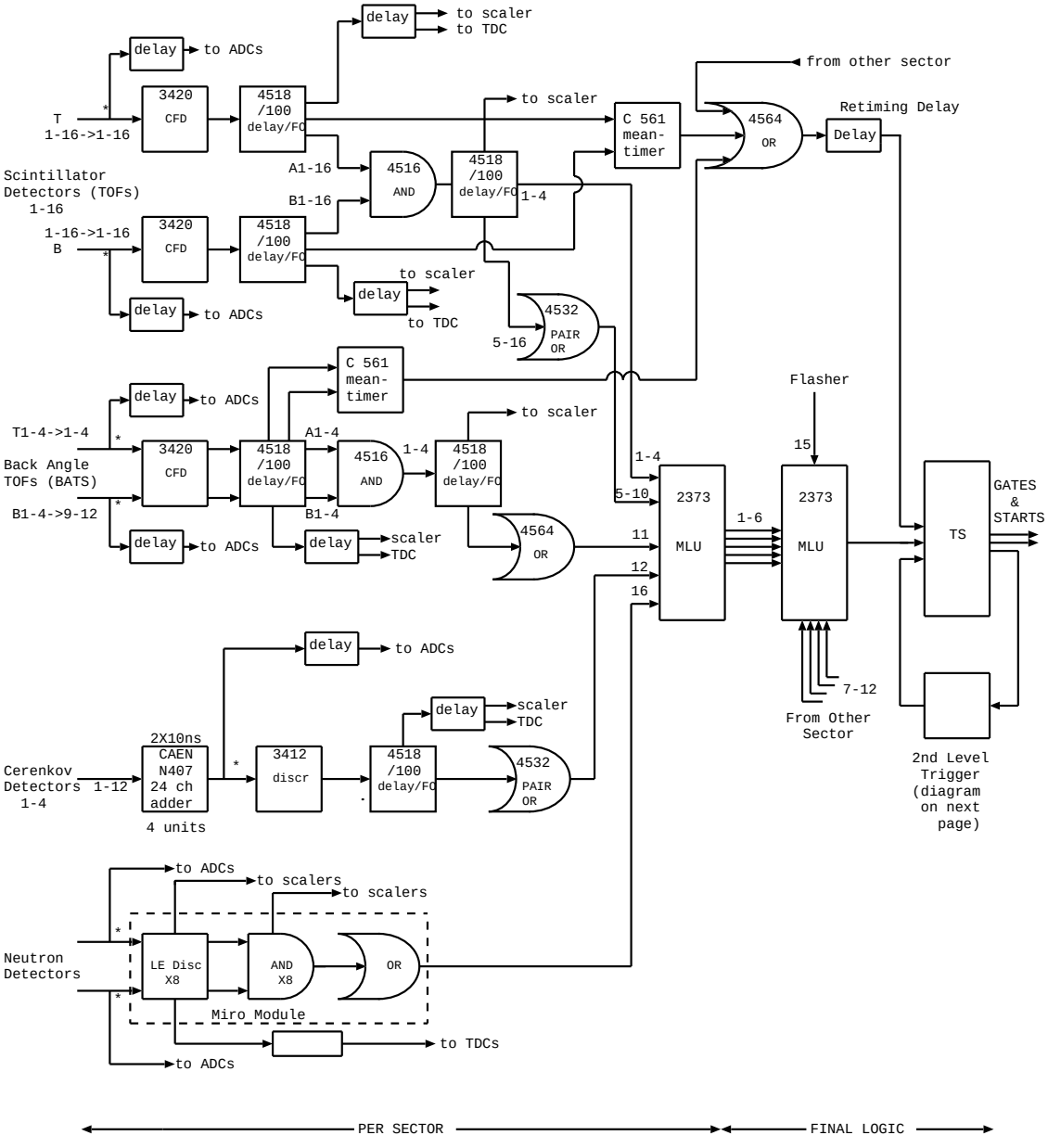

Figure 3-26: BLAST Trigger Electronics.

bit	trigger	label	purpose	scale	configuration
0	1	coinc	(e, e'p) (e, e'd)	1	1 TOF in each sector
1	2	neutron	(e, e'n)	1,2	1 TOF in one sector, NC in the other
2	3	pion	(e, e'$\pi^{\pm}$)	10	2 TOF in one sector with CC
3	4	double	(calib)	100	2 TOF in one sector
4	5	bats	(e, e'p)	1	1 TOF in one sector, BATS in the other
5	6	singles	(calib)	1000	1 TOF $\geq$ 12 in one sector
6	7	singles	(e, e')	9	1 TOF in one sector with CC
7	8	flasher	(calib)	1	flasher diode trigger

Table 3.7: BLAST trigger types assigned to XMLU bits.

and their description.

3.4.3 Second Level Trigger

In order to clean up the data, the second level trigger of the trigger supervisor has been used. This trigger requires a *good WC hit*, that is a hit in the inner, middle and outer chamber within a sector. A TTL output for a good WC hit is converted to a NIM signal and is passed to a NIM AND module with a first level trigger signal from the trigger supervisor (TS). The second level trigger reduces the recorded event rate by a factor of ten [78]. This allows the stored beam to be increased giving higher luminosity.

3.4.4 Data Acquisition Software

The CEBAF Online Data Acquisition (CODA) software [105] was used to record the data for the BLAST experiment. CODA allows various data acquisition systems to be built. For the BLAST program, the readout controllers (ROCs) collected the data in a buffer to reduce protocol overhead before sending it over the network. The various data streams are recorded, merged, and formatted by the Event Builder (EB). The EB sends the data to the Event Transport (ET) system which allows for other data streams (e.g.

scaler or EPICS data) to be added to the physics data. Then an event recorder (ER) function stores the data in the required format and location. The BLAST CODA uses information stored in an MySql database [103].

Scaler information for each trigger type is compared with the recorded data stream from CODA in order to check that the dead time is trigger independent. No significant variations were found.

In order to ensure that the time of flight of electrons is independent of the individual TOF paddle, and of the position along the detector, a CAEN C561 meantimer (MT) and a LeCroy 4564 OR module are added to the TOFs electronics: an extra output copy from the LeCroy Model 4418/4518 delay/fanout is fed to the meantimer and its output is sent to the logical OR unit. These delays are adjusted to compensate for TOF timing differences using a common start paddle temporarily placed adjacent to the wire chambers. LeCroy 4564 OR module provides the common strobe for the trigger supervisor (TS).

In the case of the inclusive scattering reaction, all of the BLAST detectors are used (see section 4.1.3).

For additional information regarding the BLAST experiment and its individual components see [89, 99, 106, 107, 108, 103, 109].

CHAPTER 4

Data Analysis

Data analysis for the inclusive scattering of polarized electrons from polarized protons is presented in this chapter. This includes the selection of the inclusive events (section 4.1) at BLAST, the experimental background contributions and corrections (section 4.2), the effect of radiative corrections (section 4.3) and the Monte Carlo simulations at BLAST (section 4.4).

The data for the inclusive scattering were taken during October-December 2004 and a summary is presented in Table 4.1. The list of run numbers for the above period includes

Running Period	October-December 2004
Run Numbers	12184-13266
Beam Charge	287kC
Beam Polarization	0.65
Target Length	60 cm
Target Thickness	$4.9 \times 10^{13}\ cm^{-2}$
Target Polarization	0.80
Target Spin Angle	48.84°
BLAST Polarity	nominal (electrons inbending)

Table 4.1: Beam, target, and spectrometer conditions for the data taking period of $\vec{p}(\vec{e}, e')$ with the ABS H_2 target.

the empty-target (i.e. no gas) runs as well, that were taken over the entire BLAST production data taking, with the purpose of background studies (see section 4.2).

4.1 Inclusive Scattering Events

The inclusive scattering of polarized electrons from polarized protons is defined in terms of outgoing reaction products as the measuring of scattered electrons only. With BLAST, the outgoing electrons is detected in each sector simultaneously, and from these measurements the sector-asymmetries are extracted, from which we extract the correlation parameters, $A_{TT'}$ and $A_{TL'}$.

The main goal of this analysis is to measure the scattered electrons accurately. This is explain in detail in this section.

4.1.1 Event Reconstruction

From the drift chamber information we extract the momentum, $p \equiv \vec{k'}$, polar scattering angle, θ_e, and azimuthal scattering angle, ϕ_e of the outgoing electron [1]. All other physics observables are calculated from these three quantities.

A particle of mass m and charge q moving in a magnetic field $\mathbf{B}$ with a velocity $\mathbf{v}$ experiences a force $q\mathbf{v} \times \mathbf{B}$. The bending radius of the particle's trajectory is given by:

$$r = \frac{p}{qB}, \qquad p = m|\mathbf{v}| \tag{4.1}$$

In the drift chambers, three stubs are linked to form a track, which is approximately circular and obeys the above formula. Then a fitter is used to calculate particle momentum from the radius of the track. Because of the noise, there are many stubs, hence many segments and thus candidate tracks are associated with the same physical track. In order to reduce these tracks, only the best candidates are kept at each stage of the reconstruction. In the track fitter, all these tracks are iterated together, then at every few iterations, the bad tracks are discarded. At this step, the reconstruction takes into account the missing

[1] we dropped the prime index for outgoing electron in the scattering angles, i.e. $\theta_e \equiv \theta_{e'}$, $\phi_e \equiv \phi_{e'}$

stubs, due to inefficient wires or bad readout cards.

The fitter uses a Newton-Raphson algorithm [110] that searches in the parameter space (p, θ, ϕ, z) for the root of the equation:

$$\mathbf{x}(t) - \mathbf{p}(p, \theta, \phi, z; q) = 0 \tag{4.2}$$

where q is the particle's charge, $\mathbf{x}(t)$ is up to an 18-dimension vector whose components are the wire chamber hit positions, that are measured from the WC TDC. The function $\mathbf{p}(p, \theta, \phi, z; q)$ represents the vector whose components are the positions where a track with charge q, momentum (p, θ, ϕ) originated from $(0, 0, z)$ intersects the wire planes [2]. Note that, the x and y vertex coordinates are set to 0, because beam position is well known compared to the track resolution.

Figure 4-1 outlines the steps involved in the track fitting. In order to find $\mathbf{p}(p, \theta, \phi, z; q)$ we numerically integrate the equation of motion of the charge particle in the magnetic field, and locate the intersection with each of the 18 wire planes. The reconstruction is slightly modified from the Newton-Rhapson method, which computes the least-square inverse of the Jacobian [110, 106] $J = df/dp$, defined by $J^{\dashv} \equiv \left(J^T\ J\right)^{-1} J^T$, where $\mathbf{x} = \mathbf{f}(\mathbf{p})$, while we compute the root directly. Compared to conventional χ^2 minimization methods, the root finding algorithm is more robust against local minima by preserving the directional information.

4.1.2 Standard Cuts

The basic cuts used in the inclusive electron scattering, $\vec{p}(\vec{e}, e')$, depend on the detector acceptance and are based on background contribution corrections (see section 4.2), trigger event selection (see section 4.1.3), target holding field efficiency (see subsection 3.2.2, and

[2] there are 2 superlayers for each chamber, each containing three sensing wires; since there are 3 chambers per sector, results in 18 sense wires

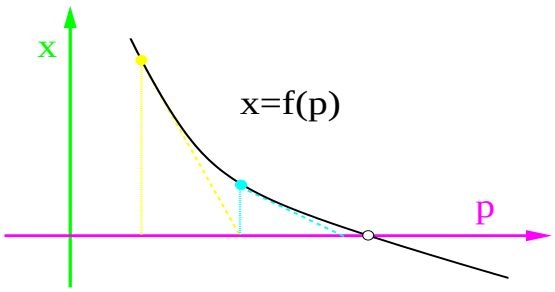

(a) In one dimension, the derivative of f maps the deviation dx from the initial guess to the adjustment dp, and so forth.

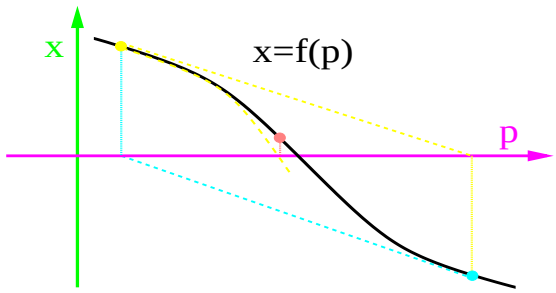

(b) In some cases the Newton method may fail to converge, and it is necessary to backtrack to a smaller correction dp.

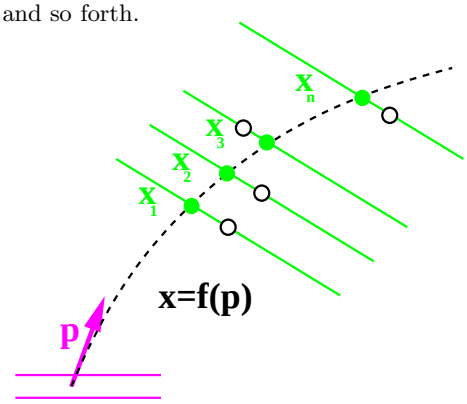

(c) For track fitting, the function f maps the 4-dimensional track trajectory $\mathbf{p}$ to the 18-dimensional vector of wire hits $\mathbf{x}$.

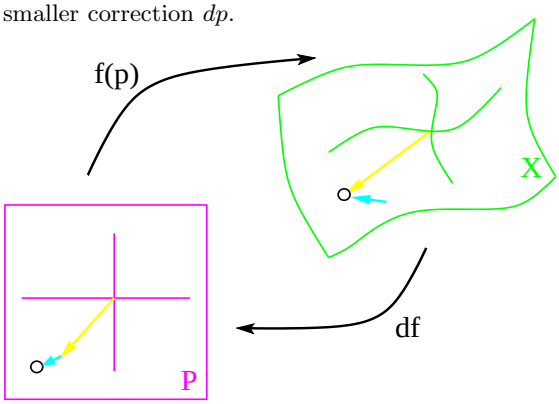

(d) In each iteration the trajectory $\mathbf{p}$ is corrected by $\mathbf{dp} = \mathbf{J}^{\dashv}\mathbf{dx}$, where J is the Jacobian derivative and $\mathbf{dx}$ is the deviation of the simulated track from the wire hits.

Figure 4-1: Newton-Rhapson method applied to track fitting.

on detector in-plane and out-of-plane limitations. They are summarized in Table 4.2, and throughout this work they are referred as the *standard cuts*.

The limitation in energy, $E_{e'} > 0.25\,GeV$, is due to the background effects in the Δ region from low energy scattered electrons; θ_e and ϕ_e ranges cover the acceptance of the Čerenkov counters, and the target position cut is based on the holding field magnet length, which covers only 40cm out of 60cm of the target cell. All physics triggers are used (see Table 3.7). Since only trigger no. 7 uses Čerenkov hits, a Čerenkov hit cut is added in the analysis, because CC is the only detector at BLAST that can differentiate between *electrons* and *pions* up to $0.7\,GeV$.

Name	Symbol	Cut (Accepted range)
Energy	$E_{e'}$	$0.25\,GeV < E_{e'} < 0.85\,GeV$
In-plane angle	θ_e	$22^\circ < \theta_e < 65^\circ$
Out-of-plane angle	ϕ_e	$-17.5^\circ < \phi_e < +17.5^\circ$
Vertex position	Z_{target}	$-20\,cm < Z_{target} < +20\,cm$
Trigger	trig	$trig = 1, 2, 3, 7$
Charge	q	$q = -1$
Detector hit	N/A	WC, CC, TOF

Table 4.2: Standard cuts for $\vec{p}(\vec{e}, e')$ reaction.

Trigger	Purpose	Other Reactions
1	(e, e'p)	(e, e'p)π^0, (e, e'π^+)n
2	(e, e'n)	(e, e'π^0)p
3	(e, e'$\pi^\pm$)	(e, e'p)π^0
7	(e, e')	all of the above

Table 4.3: BLAST trigger types and their detected reaction channels for the ABS H2 target.

4.1.3 Trigger Selection

The inclusive electron scattering cross section is an incoherent sum of the multipoles, while the exclusive (coincidence) cross section contains information on the relative phases of the multipoles [1], hence, in the case of $\vec{p}(\vec{e}, e')$ reaction, we detect the scattered electrons in one sector, while the other reaction products could or could not be in the acceptance of the detector. This is shown schematically in Figure 4-2.

The trigger types are shown in Table 3.7. Due to trigger and detector inefficiencies, besides the desired reactions, some other reaction channels are detected in each of these individual triggers. This is shown in Table 4.3.

For the inclusive reaction studies, all physics triggers (no. 1, 2, 3, and 7) [3] are used to

[3]BATs detectors are the most backward (last 4) TOFs. They are used in trigger no. 5 and are not of interest in the inclusive scattering, since they cover a square momentum transfer of $0.6GeV^2 < Q^2 < 0.9GeV^2$, and this region is outside of the interest region, and has very few events.

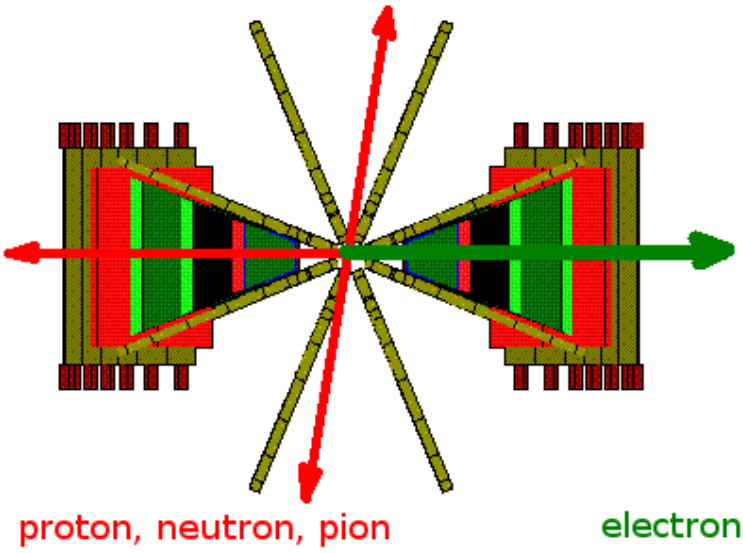

Figure 4-2: BLAST detector front/rear view (schematic). In the case of $\vec{p}(\vec{e},e')$ reaction, an electron is detected in one sector (green), while the other reaction products could be anywhere (red).

collect the data for $\vec{p}(\vec{e},e')$ reaction. The trigger prescaling factor is applied in the analysis only to the trigger type 7 (no. 7), for the reasons discussed bellow.

The trigger supervisor (TS) assigns the event type according to the lowest set bit (see Table 3.7 for the description of the bit assignment to the cross sector memory lookup unit, XMLU), that is, for example, if an event type qualifies for both trigger 1 and 2, it is assigned to trigger no. 1. In the case of a trigger type which is prescaled (trigger 2, 3 and 7) [4], things are a bit different: for example, if an event is of type 3, it is not assigned to trigger type 3, unless has happened 9 times before (10 is the prescale factor for trigger type 3), and if this event is not assigned to any other trigger type, it goes to trigger type 7 if it qualifies (i.e. if it has a Čerenkov hit), which, in turn, is prescaled by a factor of 9, hence if the event has not happened for 8 times before, it is discharged. The prescaling factors have been introduced to the corresponding triggers for the purpose of reducing the background rates and not exceeding the data acquisition maximum rate [78, 111].

[4] trigger no. 2 has been prescaled by 2 for December 2004 runs only 13001-13266.

4.1.4 Momentum Corrections

In order to account for the reconstruction errors, corrections to the electron momentum are required. Several methods are used to determine these corrections [112, 113].

One method uses the ${}^2\vec{H}(\vec{e}, e'p)$ reaction. For a series of bins over the desired Q^2 range, the reconstructed electron momentum is compared with its respective Monte Carlo momentum plots. In each Q^2 bin, the quasi-elastic electron momentum peak in the data is multiplied by a correction factor, $f_e(Q^2)$, in order to make it to coincide with the Monte Carlo electron momentum peak:

$$p_e(Q^2)|_{MC\ peak} = f_e(Q^2) \times p_e(Q^2)|_{Data\ peak} \tag{4.3}$$

From these correction factors, a polynomial of best-fit is constructed and used in the data.

Another method uses the elastic $\vec{H}(\vec{e}, e'p)$ reaction, and the same comparison, and Q^2 is calculated from the electron scattering angle, θ_e, since it has a better resolution compare to the reconstructed momentum, $E_{e'}$.

The results from the two methods agree pretty well, i.e. $< 1\%$. The corrections for the left sector are on the order of 3% to 5%, and for the right sector on the order of 2% to 8%.

4.1.5 Observables

In subsection 4.1.1 we describe the event reconstruction. From the drift chamber information we reconstruct the energy of the scattered electron, $E_{e'}$, its in-plane (polar) scattering angle, θ_e, and out-of-plane (azimuthal) scattering angle, ϕ_e. In the relativistic limit, $E_e, E_{e'} \gg m_e$, we have

$$E_e \approx |\vec{k}|, \qquad E_{e'} \approx |\vec{k}'| \tag{4.4}$$

From these three quantities, $E_{e'}$, θ_e, ϕ_e we reconstruct all the other physics quantities of interest for the inclusive scattering reaction.

If we denote the initial electron four-momentum by $K = (E_e, \vec{\mathbf{k}})$, the final electron four-momentum by $K' = (E_{e'}, \vec{\mathbf{k}'})$, and the four-momentum transfer by $q = (\omega, \vec{\mathbf{q}})$, using the conservation of the energy and momentum at the leptonic vertex ($e \rightarrow \gamma^* + e'$), we have

$$K = K' + q \equiv \begin{cases} E_e = E_{e'} + \omega \\ \vec{\mathbf{k}} = \vec{\mathbf{k}'} + \vec{\mathbf{q}} \end{cases} \tag{4.5}$$

The squared momentum transfer in the relativistic limit (4.4) can be written in terms of $E_{e'}$ and θ_e as [5]

$$\begin{aligned} q^2 &= (K - K')^2 = 2m_e^2 - 2K \cdot K' \approx -2K \cdot K' \\ &= -2E_{e'}E_e + 2\mathbf{k}' \cdot \mathbf{k} = -2E_{e'}E_e(1 - \cos\theta_e) \\ &= -4E_eE_{e'} \sin^2 \frac{\theta_e}{2} = -Q^2 \end{aligned} \tag{4.6}$$

where θ_e is the angle between the incoming and outgoing electron trajectories, $\mathbf{k}$, $\mathbf{k}'$, and

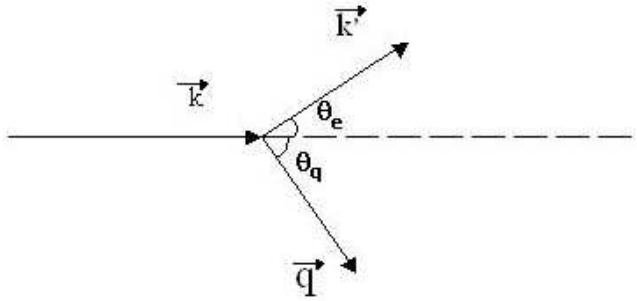

Figure 4-3: Electron (lepton) vertex: momentum conservation.

[5] if not specified otherwise, all variables are expressed in the laboratory frame, and $\vec{\mathbf{k}} \equiv \mathbf{k}$, $\vec{\mathbf{k}'} \equiv \mathbf{k}'$.

θ_q is the angle between the incoming electron trajectory, $\mathbf{k}$, and the photon momentum, $\mathbf{q}$, (see Figure 4-3).

Since the incoming electron path defines the $0z$ axis (see Figure 2-2 and **Appendix B** for the description of the BLAST laboratory frame), we can deduce the following relations:

$$\begin{aligned} |\mathbf{q}|\cos\theta_q + |\mathbf{k}'|\cos\theta_e &= |\mathbf{k}| \\ |\mathbf{q}|\sin\theta_q &= -|\mathbf{k}'|\sin\theta_e. \end{aligned} \tag{4.7}$$

From 4.7 we obtain θ_q as a function of $\mathbf{q}$, where $\mathbf{q}$ in the relativistic limit (4.4) is given by

$$|\mathbf{q}|^2 = E_e^2 + E_{e'}^2 - 2E_eE_{e'}\cos\theta_e \tag{4.8}$$

Using 4.6, 4.8 and $q^2 = \omega^2 - \mathbf{q}^2$, we get (energy conservation):

$$\omega = E_e - E_{e'}. \tag{4.9}$$

Ignoring the lepton "leg", the total 4-momentum of the reaction $\gamma^* + N \rightarrow N' + \pi$ expressed in the Mandelstam variable s, can be written, under the assumption that the target nucleon (proton) is at rest in the laboratory frame, and using the convention from Figure 4-4, as

$$s = W^2 = (q+P)^2 = M_N^2 + q^2 + 2M_N\omega = M_N^2 - Q^2 + 2M_N\omega \tag{4.10}$$

from which we get the following relation for ω,

$$\omega = \frac{W^2 - q^2 - M_N^2}{2M_N}. \tag{4.11}$$

where $M_N = M_p$ is the proton mass.

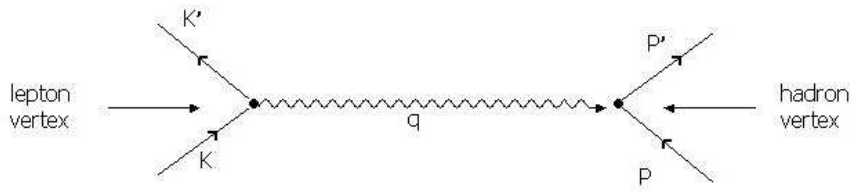

Figure 4-4: Lepton and hadron vertices notation.

In the relativistic limit (4.4), the invariant mass can be expressed in terms of $E_{e'}$ and θ_e as

$$\begin{aligned} W^2 &= (q+P)^2 = (K-K'+P)^2 \\ &= (E_e - E_{e'} + M_p)^2 - (\mathbf{k}-\mathbf{k}')^2 \\ &= (E_e - E_{e'} + M_p)^2 - E_e^2 - E_{e'}^2 + 2E_e E_{e'}\cos\theta_e \end{aligned} \tag{4.12}$$

The angles θ^* and ϕ^* of the target (proton) spin angle in the q-system, defined by $\mathbf{u}_x$, $\mathbf{u}_y$ and $\mathbf{u}_z = \mathbf{q}$ (see Figure 2-2) are given by

$$\cos\theta^* = -\sin\theta_T\,\cos\phi_e\,\sin\theta_q + \cos\theta_T\,\cos\theta_q \tag{4.13}$$

$$\cos\phi^* = \frac{\sin\theta_T\,\cos\phi_e\,\cos\theta_q + \cos\theta_T\,\sin\theta_q}{\sin\theta^*} \tag{4.14}$$

where θ_T is the target spin angle in the laboratory frame.

The description of the BLAST laboratory frame and target spin angles, θ^* and ϕ^* is given in **Appendix B**. Figures 4-5, 4-6, 4-7, 4-8, 4-9, 4-10, 4-11, 4-12, 4-13, 4-14, 4-15, 4-16, 4-19, 4-20, 4-18, 4-18, show these observables for each individual trigger type 1, 2, 3, and 7, using the *standard cuts* (subsection 4.1.2) for the ABS hydrogen data mentioned in Table 4.1. For the inclusive analysis these are "summed" up, and, as mentioned earlier, the data are prescaled by a factor of 9, only for trigger type 7.

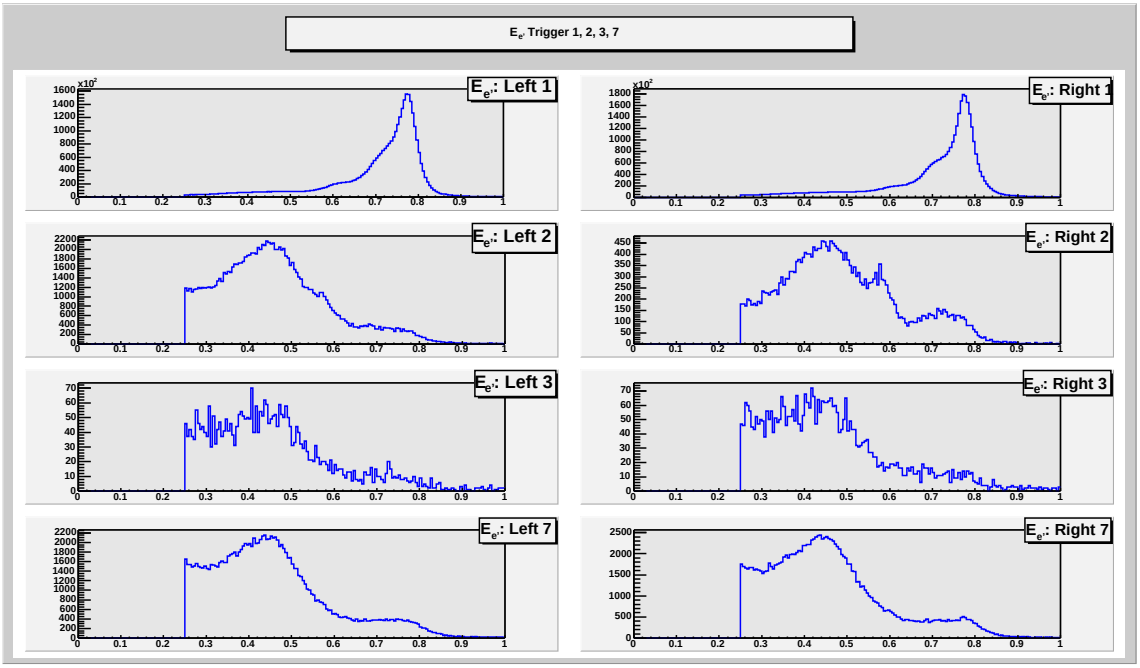

Figure 4-5: Distribution of $E_{e'}$ $[GeV]$ for each trigger type (1, 2, 3, 7) for ABS hydrogen data. Left sector is on the left, right sector on the right.

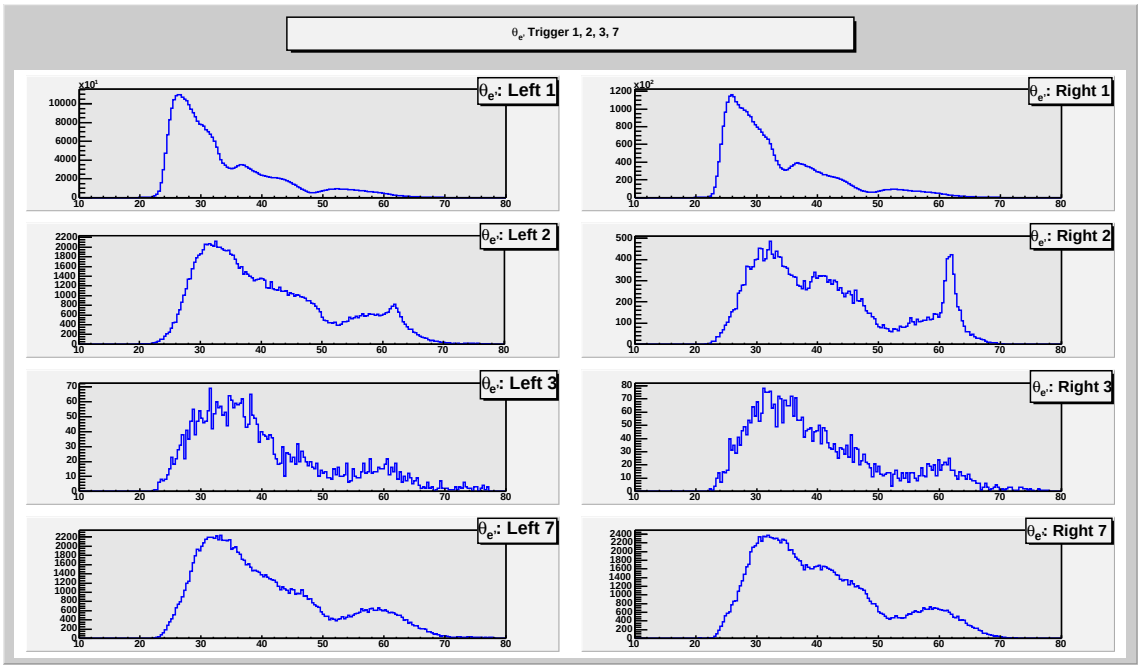

Figure 4-6: Distribution of θ_e $[^\circ]$ for each trigger type (1, 2, 3, 7) for ABS hydrogen data. Left sector is on the left, right sector on the right.

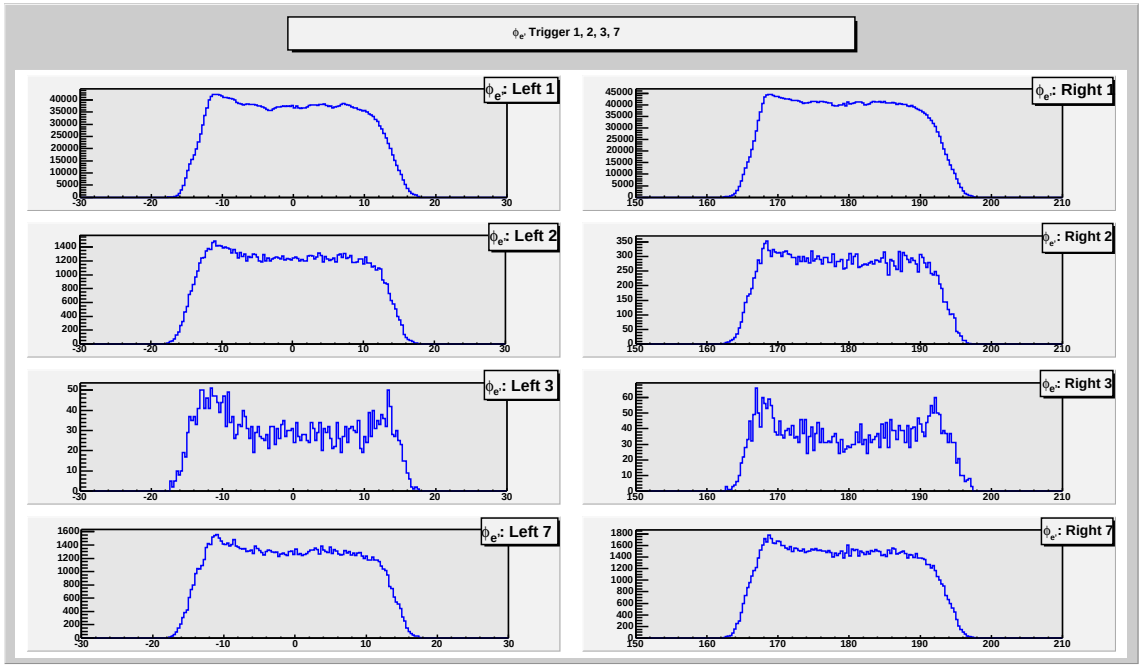

Figure 4-7: Distribution of ϕ_e [°] for each trigger type (1, 2, 3, 7) for ABS hydrogen data. Left sector is on the left, right sector on the right.

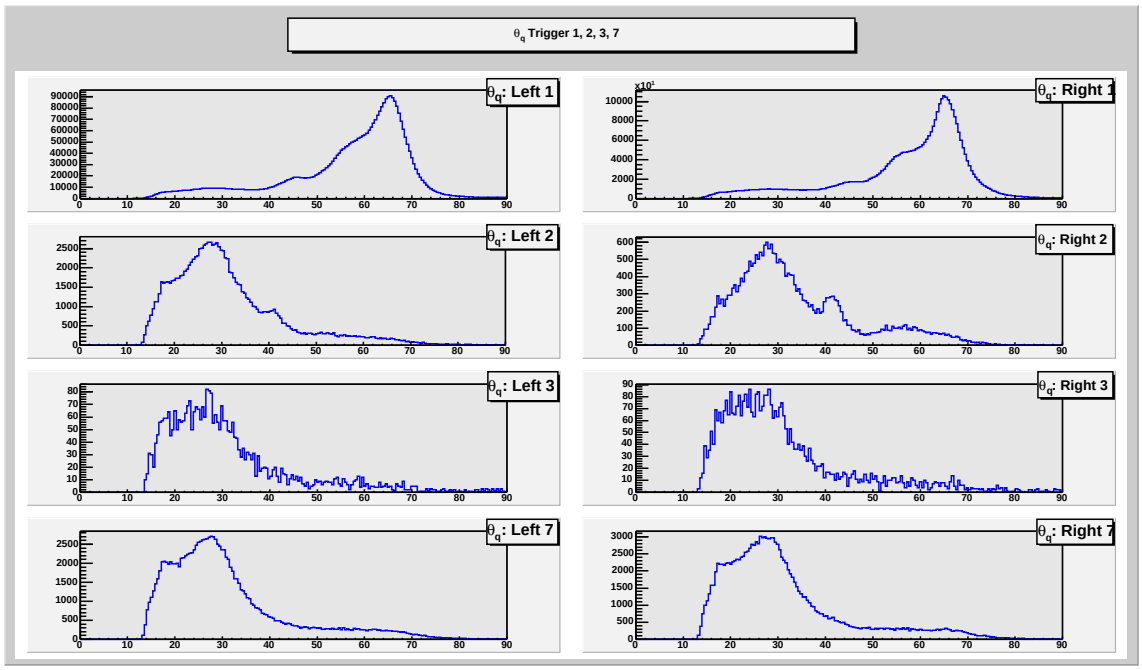

Figure 4-8: Distribution of θ_q [°] for each trigger type (1, 2, 3, 7) for ABS hydrogen data. Left sector is on the left, right sector on the right.

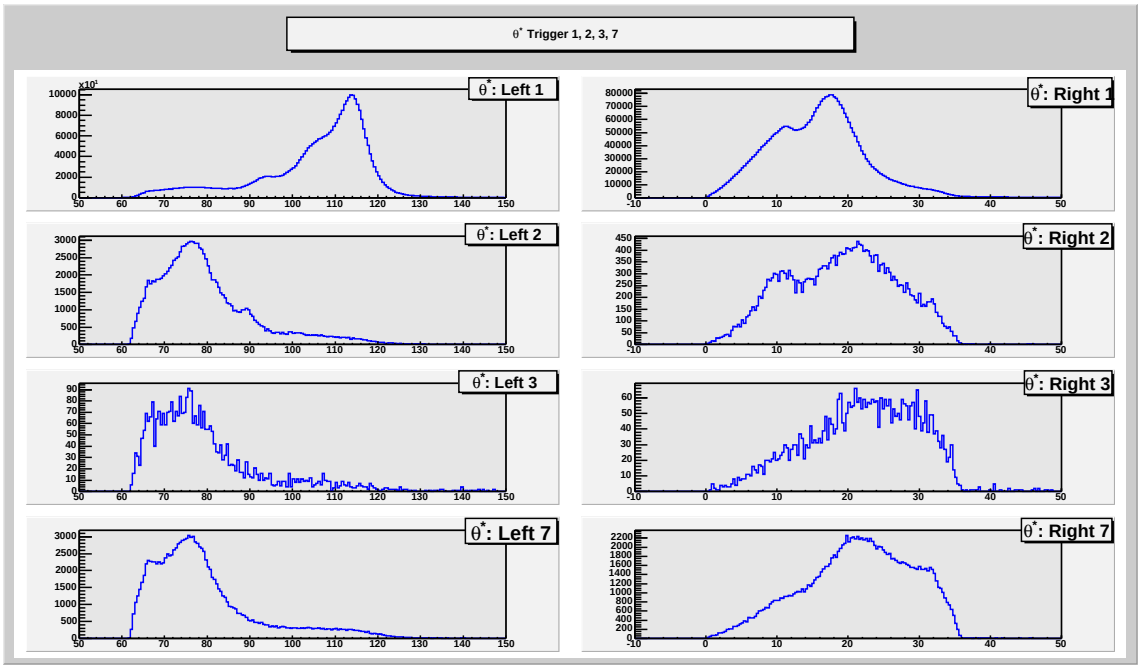

Figure 4-9: Distribution of θ^* [°] for each trigger type (1, 2, 3, 7) for ABS hydrogen data. Left sector is on the left, right sector on the right.

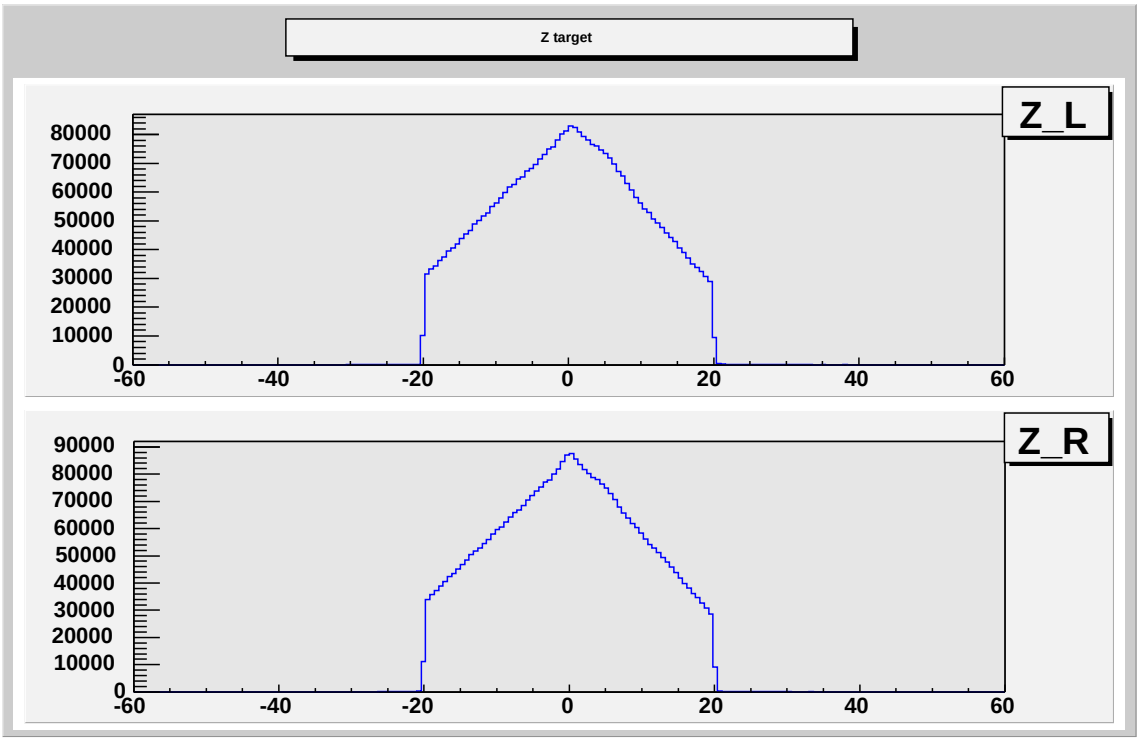

Figure 4-10: Distribution of Z_{target} $[cm]$ for ABS hydrogen data. Left sector is on top, right sector on the bottom.

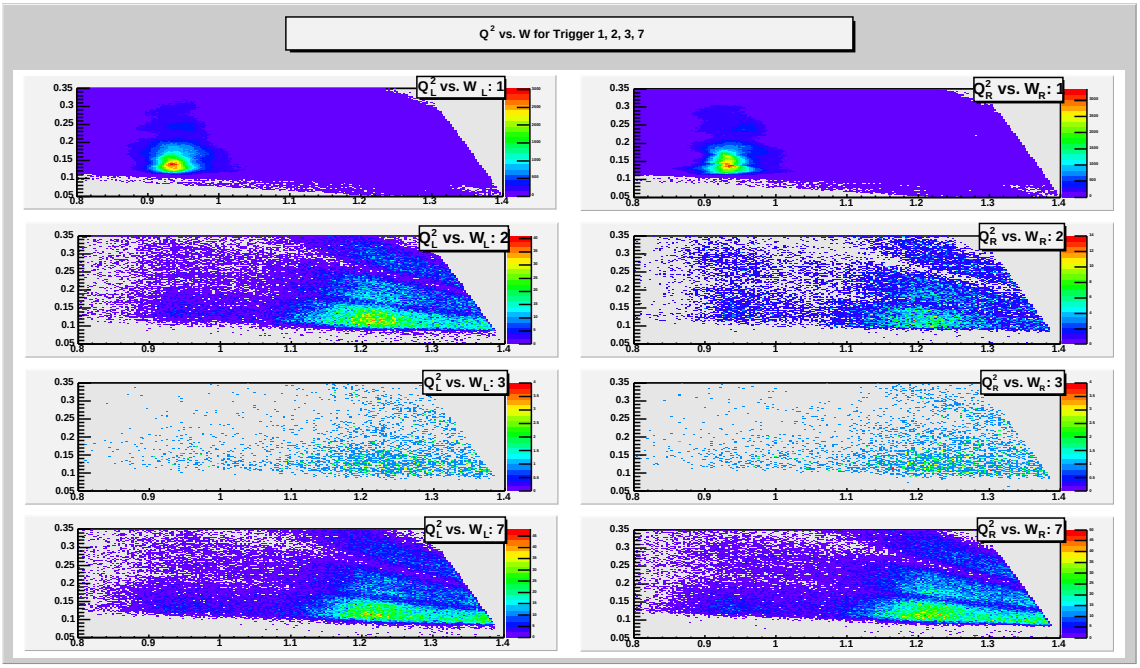

Figure 4-11: $Q^2\,[GeV^2]$ vs. $W\,[GeV]$ for each trigger type (1, 2, 3, 7) for ABS hydrogen data. Left sector is on the left, right sector on the right.

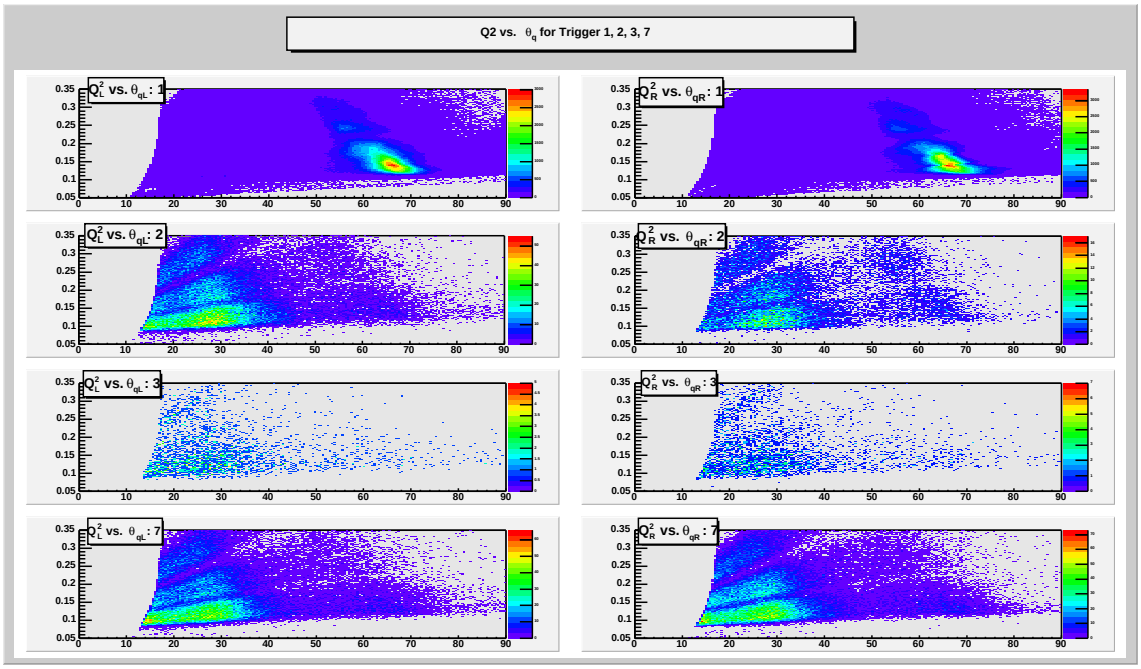

Figure 4-12: $Q^2\,[GeV^2]$ vs. $\theta_q\,[^\circ]$ for each trigger type (1, 2, 3, 7) for ABS hydrogen data. Left sector is on the left, right sector on the right.

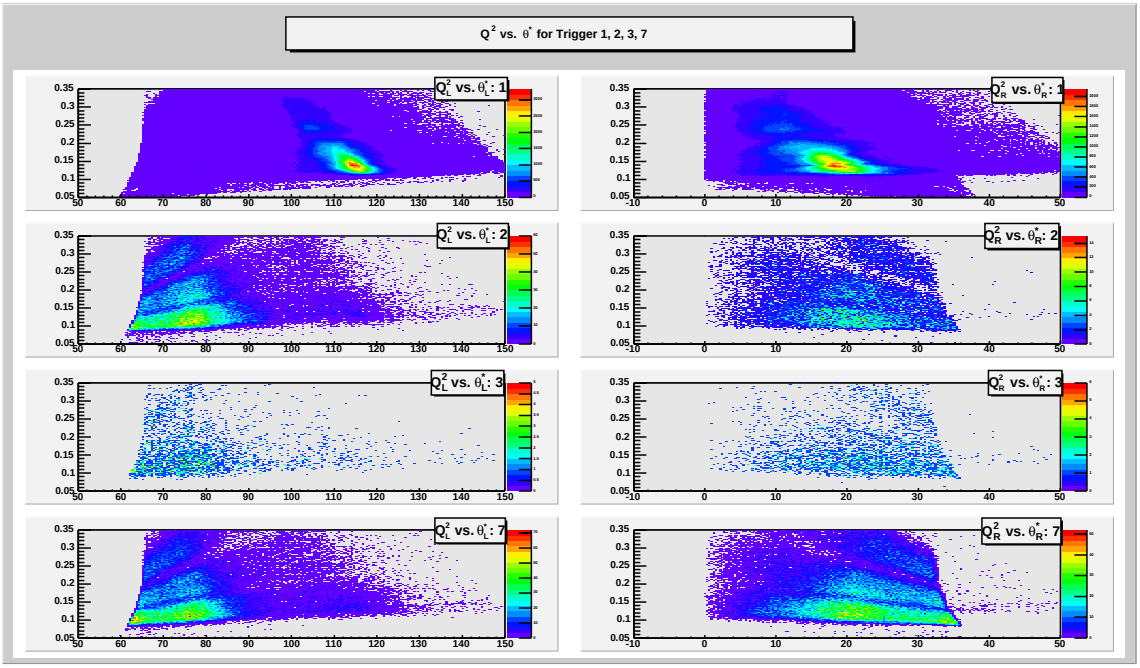

Figure 4-13: $Q^2\,[GeV^2]$ vs. $\theta^*\,[^\circ]$ for each trigger type (1, 2, 3, 7) for ABS hydrogen data. Left sector is on the left, right sector on the right.

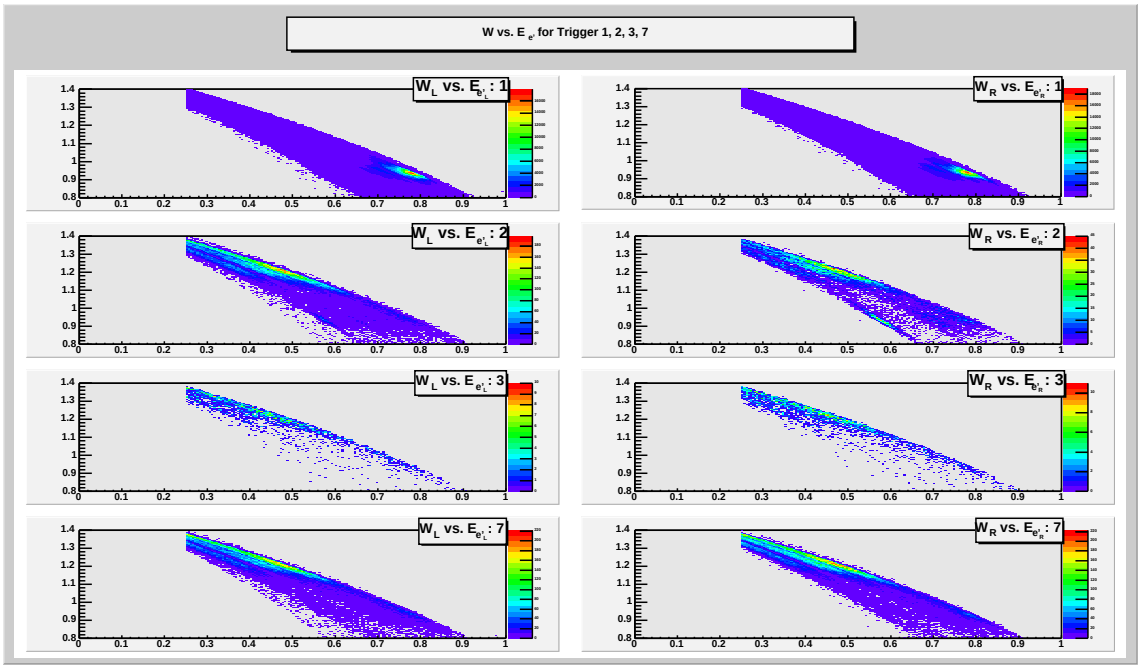

Figure 4-14: $W\,[GeV]$ vs. $E_{e'}\,[GeV]$ for each trigger type (1, 2, 3, 7) for ABS hydrogen data. Left sector is on the left, right sector on the right.

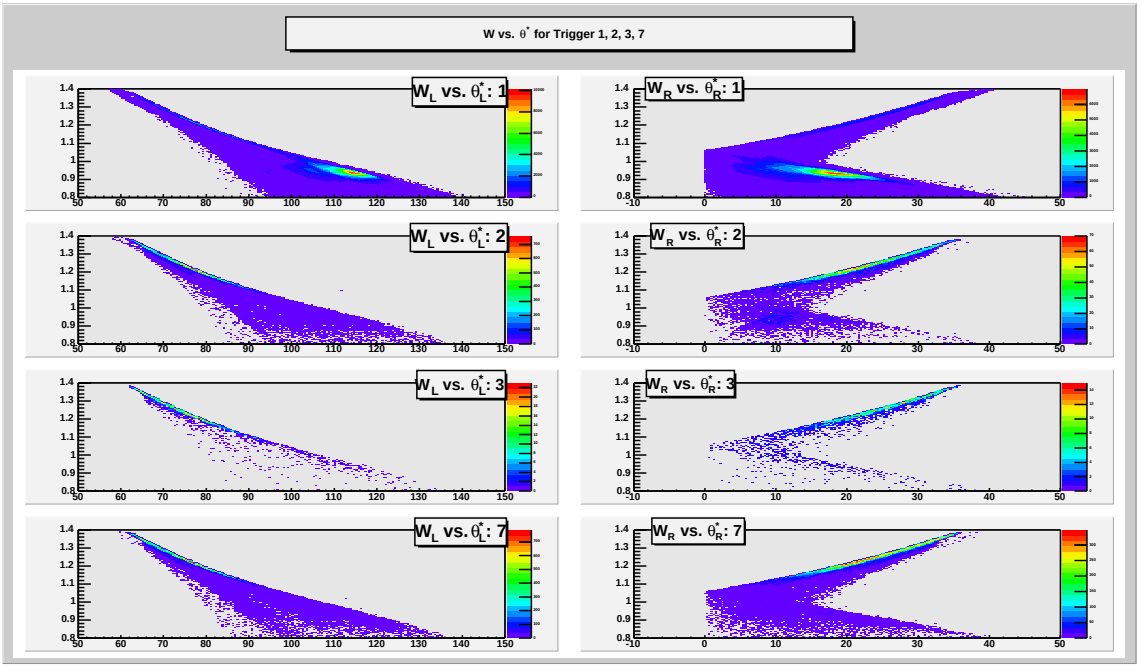

Figure 4-15: $W\,[GeV]$ vs. $\theta^*\,[^\circ]$ for each trigger type (1, 2, 3, 7) for ABS hydrogen data. Left sector is on the left, right sector on the right.

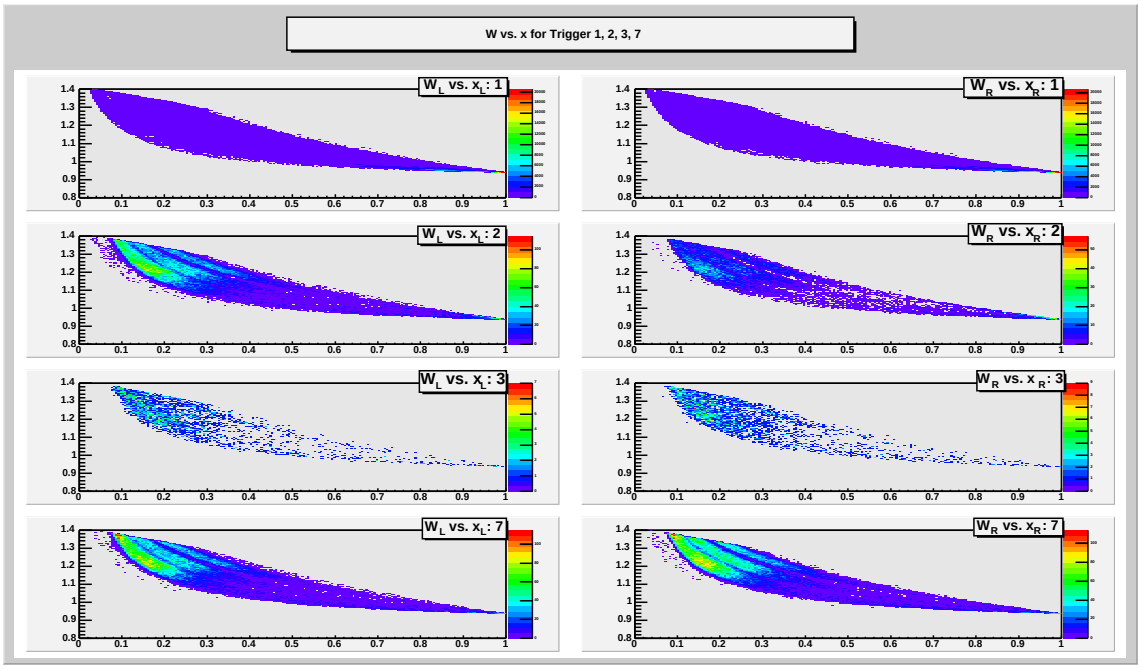

Figure 4-16: $W\,[GeV]$ vs. x for each trigger type (1, 2, 3, 7) for ABS hydrogen data. Left sector is on the left, right sector on the right.

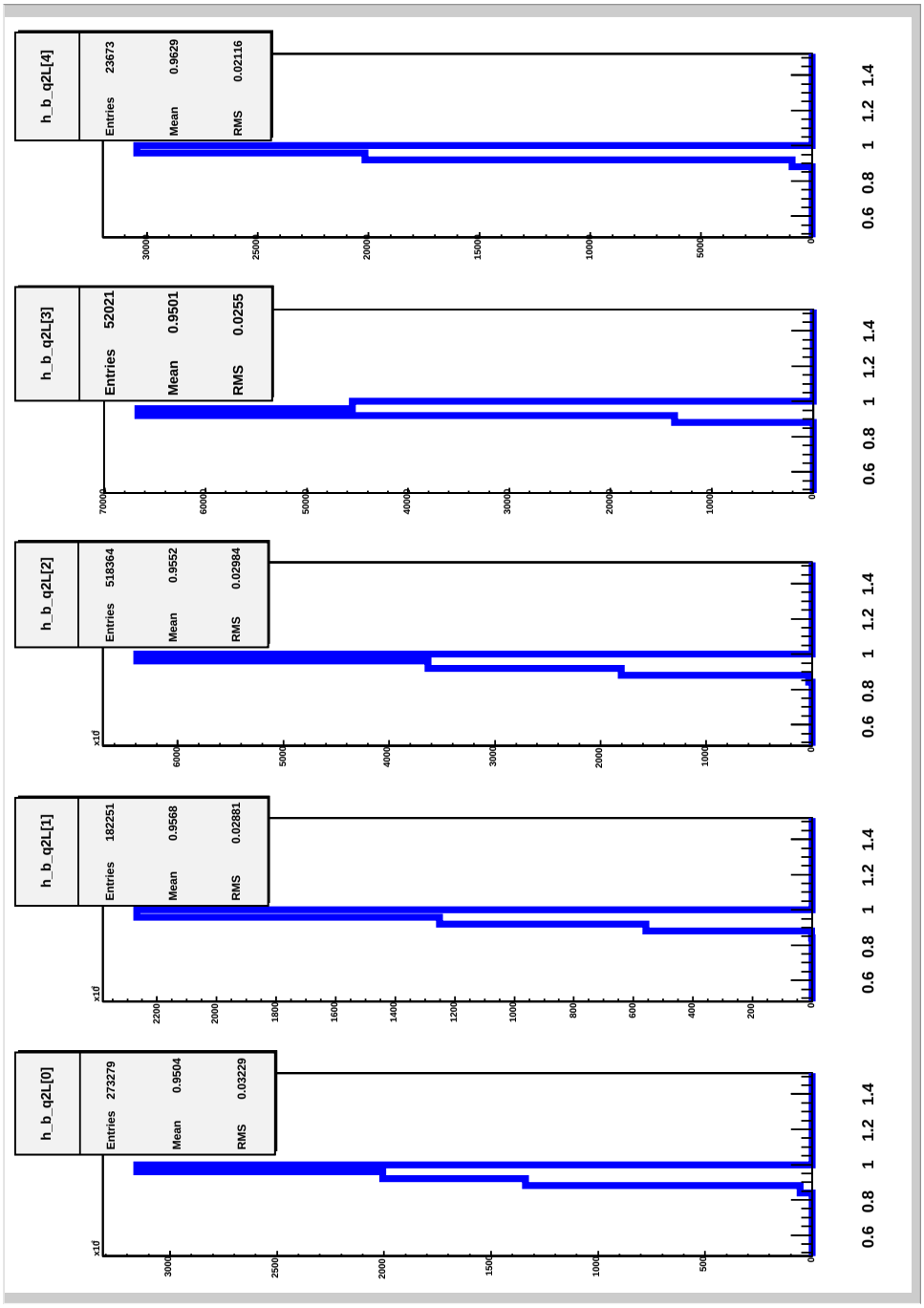

Figure 4-17: $x^* = \sin\theta^* \cos\phi^*$ for all trigger types (1, 2, 3, 7) for ABS hydrogen data, and for each Q^2 bin starting at $Q^2 = 0.08GeV^2$ (left) and ending at $Q^2 = 0.38GeV^2$ (right) in steps of $0.06GeV^2$ over the Δ region, when the electron is scattered in the left sector ($\theta^* \approx 90°$).

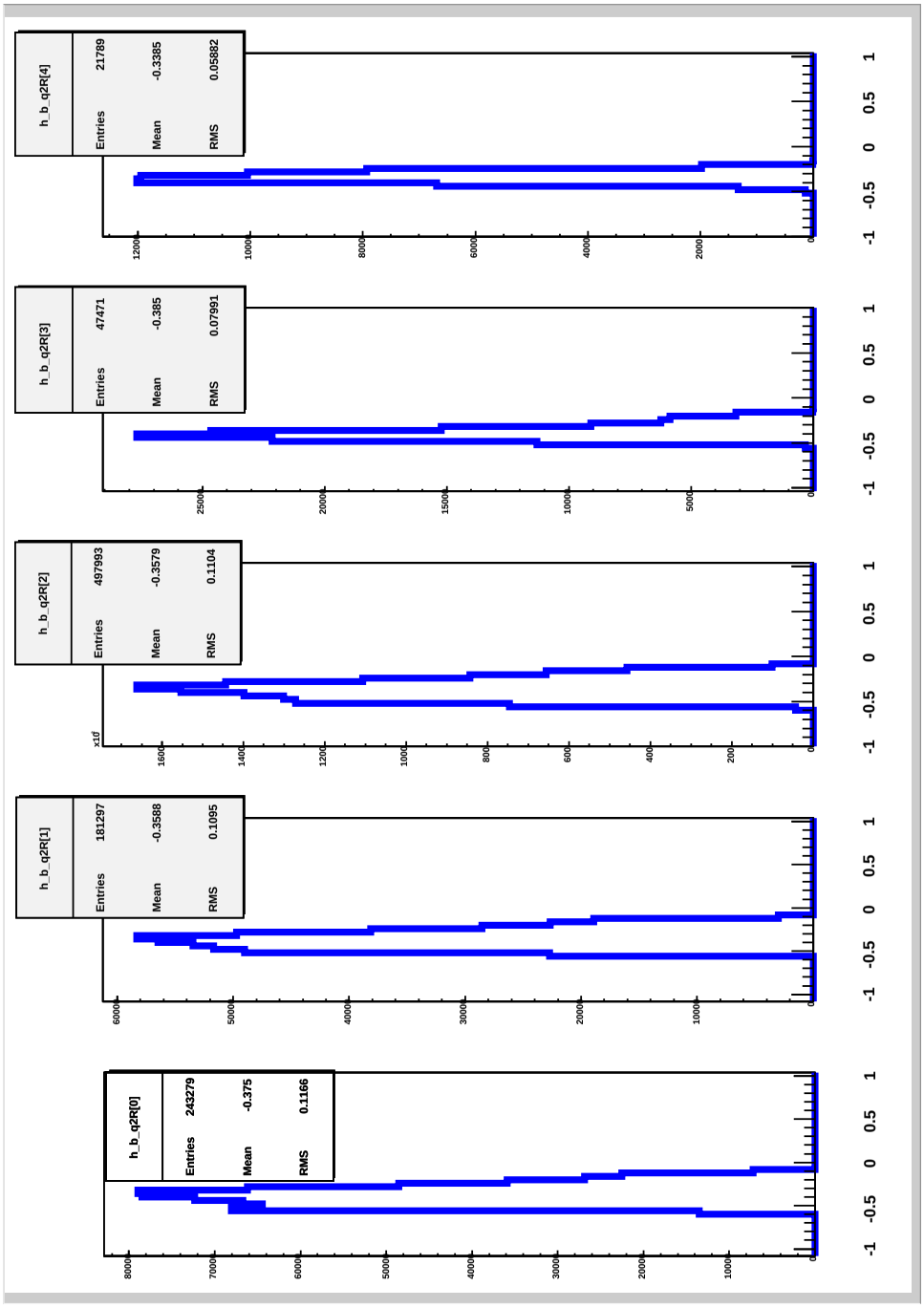

Figure 4-18: $x^* = \sin\theta^* \cos\phi^*$ for all trigger types (1, 2, 3, 7) for ABS hydrogen data, and for each Q^2 bin starting at $Q^2 = 0.08 GeV^2$ (left) and ending at $Q^2 = 0.38 GeV^2$ (right) in steps of $0.06 GeV^2$ over the Δ region, when the electron is scattered in the right sector ($\theta^* \approx 0°$).

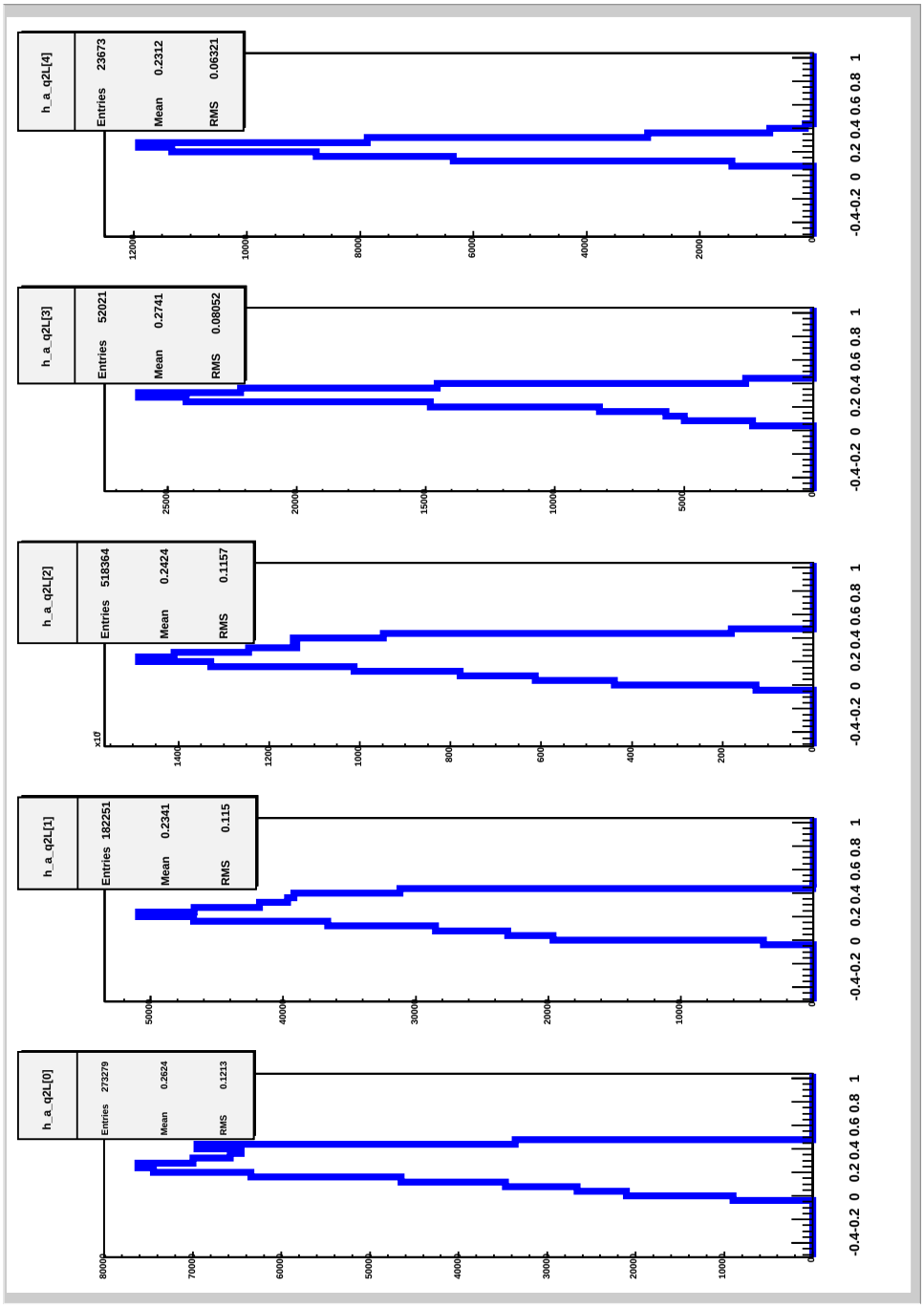

Figure 4-19: $z^* = \cos\theta^*$ for all trigger types (1, 2, 3, 7) for ABS hydrogen data, and for each Q^2 bin starting at $Q^2 = 0.08 GeV^2$ (left) and ending at $Q^2 = 0.38 GeV^2$ (right) in steps of $0.06 GeV^2$ over the Δ region, when the electron is scattered in the left sector ($\theta^* \approx 90°$).

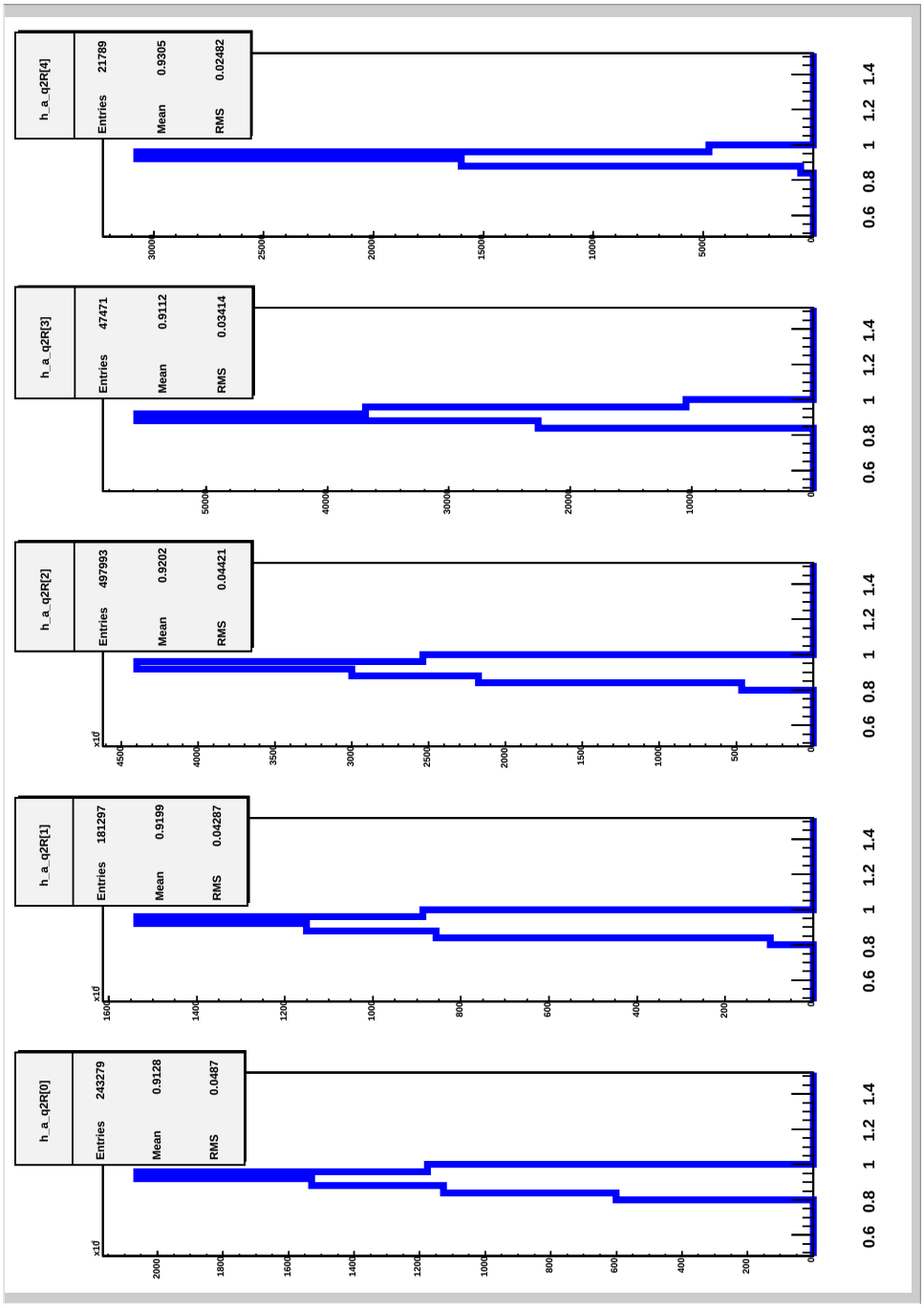

Figure 4-20: $z^* = \cos\theta^*$ for all trigger types (1, 2, 3, 7) for ABS hydrogen data, and for each Q^2 bin starting at $Q^2 = 0.08GeV^2$ (left) and ending at $Q^2 = 0.38GeV^2$ (right) in steps of $0.06GeV^2$ over the Δ region, when the electron is scattered in the right sector ($\theta^* \approx 0°$).

4.2 Background Contributions

The *standard cuts* (subsection 4.1.2) used for electron identification, do not suffice to eliminate all the background contributions. The majority of the background events arise through the electron scattering from metallic surfaces in the vicinity of the target and target walls, which are made of Aluminum.

Background contributions are relatively low in the elastic scattering region ($W \in [0.8,\, 1.0]\, GeV$), whereas they are considerably larger in the Δ-region, more precisely above one-pion production threshold ($W \in [1.07,\, 1.4]\, GeV$), hence for the asymmetries these contributions have to be taken into account.

In order to determine these contributions, measurements with the empty target cell are taken under the same conditions as the real data, from time to time, especially when the ABS target noozle needs to be cooled off. A total of $32\, kC$ of empty target cell runs have been gathered during 2004 for inclusive scattering background studies. In Figures 4-21, 4-22, 4-23, 4-24 we show the results of the empty target cell runs, in green, compare to the data runs in blue, and scaled to the corresponding charge (see Table 4.1).

If we assume that the background contribution is not spin dependent because only the hydrogen is polarized, that is

$$\frac{N^{++}_{empty}}{Q^{++}_{empty}} = \frac{N^{--}_{empty}}{Q^{--}_{empty}} = \frac{N^{+-}_{empty}}{Q^{+-}_{empty}} = \frac{N^{-+}_{empty}}{Q^{-+}_{empty}} \tag{4.15}$$

Under this assumption, the measured asymmetry can be written as

$$\begin{aligned} A_{meas} &= \frac{R^+ - R^-}{R^+ + R^-} \times \frac{R^+ + R^-}{R^+ + R^- - 4R_{empty}} \\ &= A_{uncor} \times f_{dil} \end{aligned} \tag{4.16}$$

The measured spin-dependent rates, R^+, R^-, and the spin-independent empty target cell

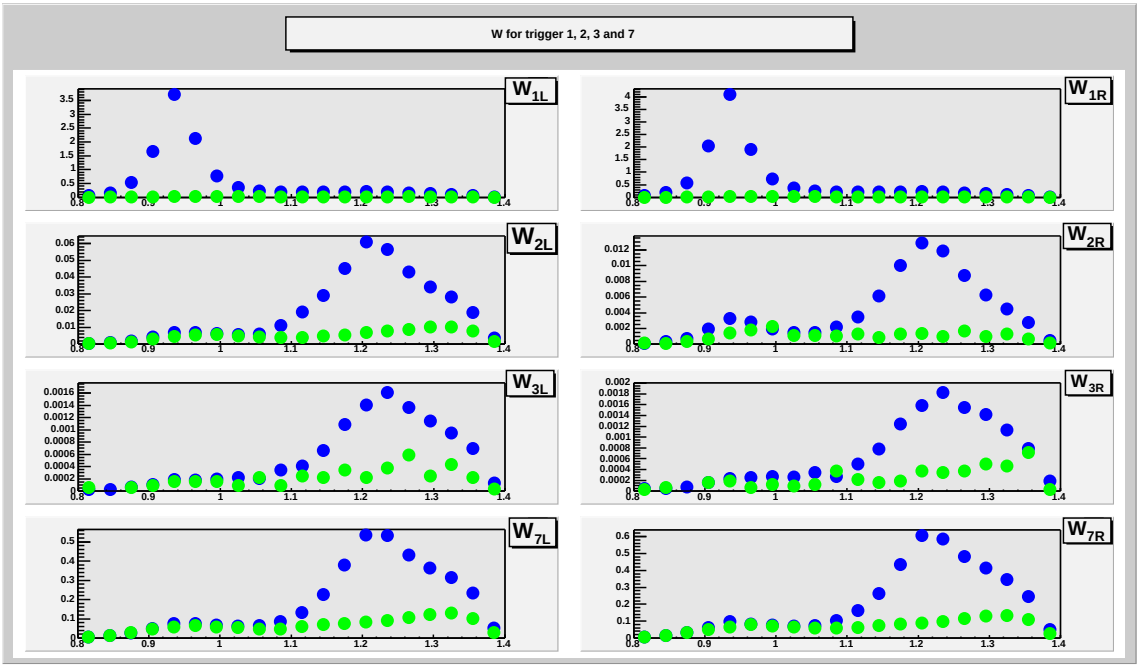

Figure 4-21: Rates of $W\,[GeV]$ for each trigger type (1, 2, 3, 7) and for $Q^2 \in [0.05, 0.35]\,GeV^2$. Data runs are in blue, empty runs in green. Left sector is on the left, right sector on the right.

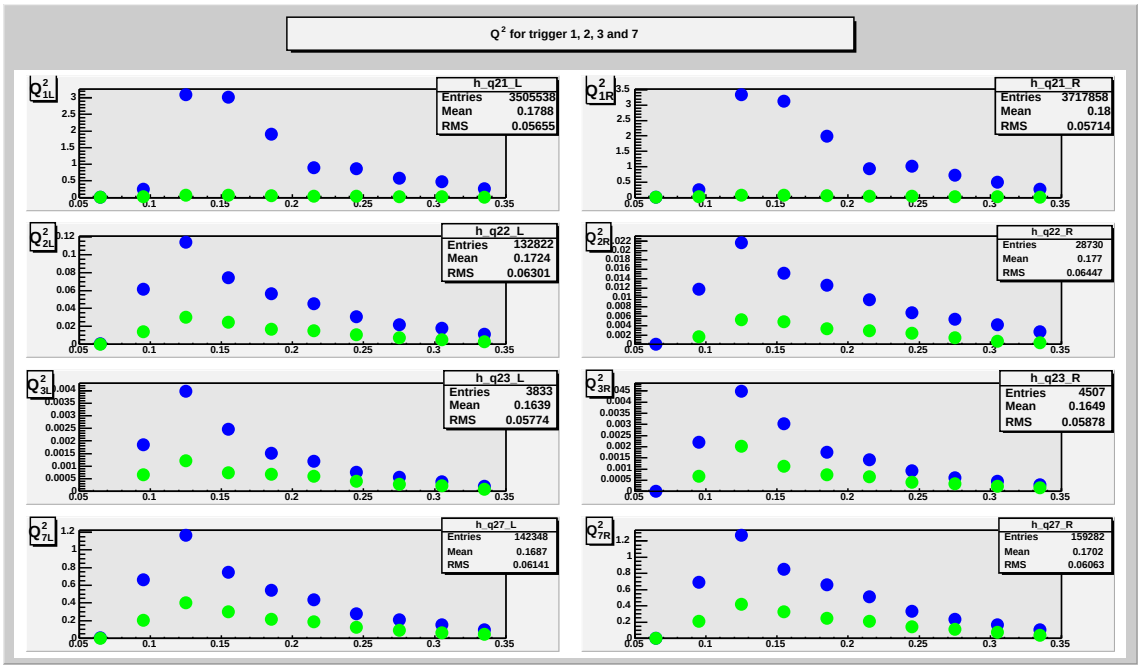

Figure 4-22: Rates of $Q^2\,[GeV^2]$ for each trigger type (1, 2, 3, 7). Data runs are in blue, empty runs in green. Left sector is on the left, right sector on the right.

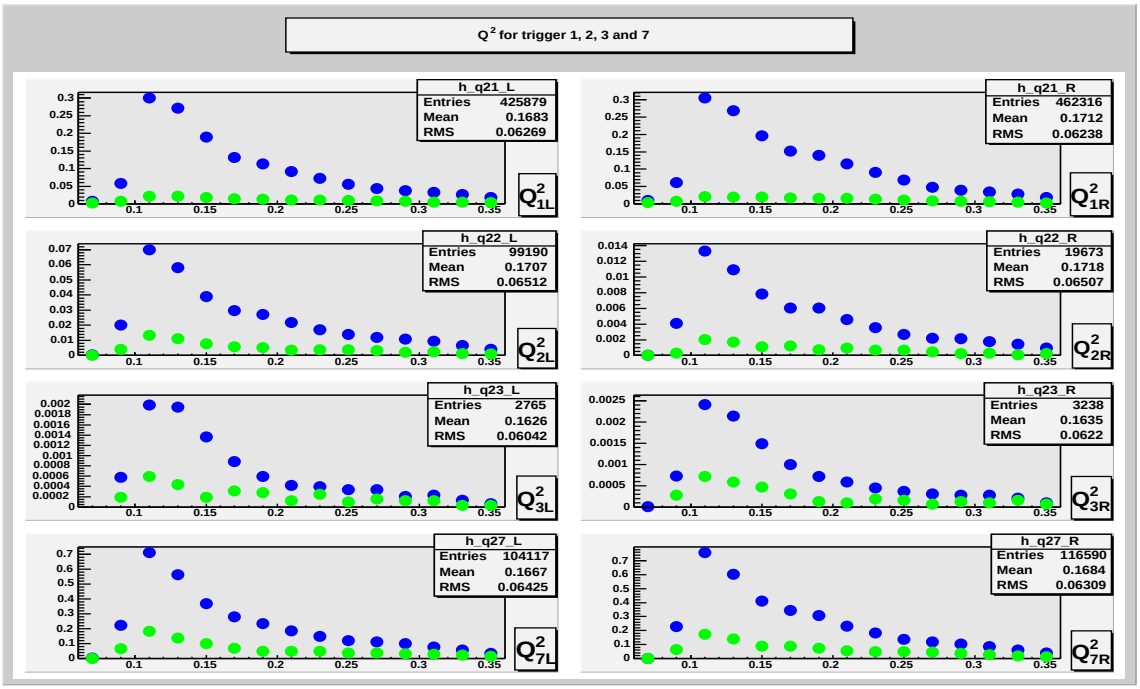

Figure 4-23: Rates of $Q^2\,[GeV^2]$ for each trigger type (1, 2, 3, 7) in the Δ region ($1.1 < W < 1.4\,(GeV)$). Data runs are in blue, empty runs in green. Left sector is on the left, right sector on the right.

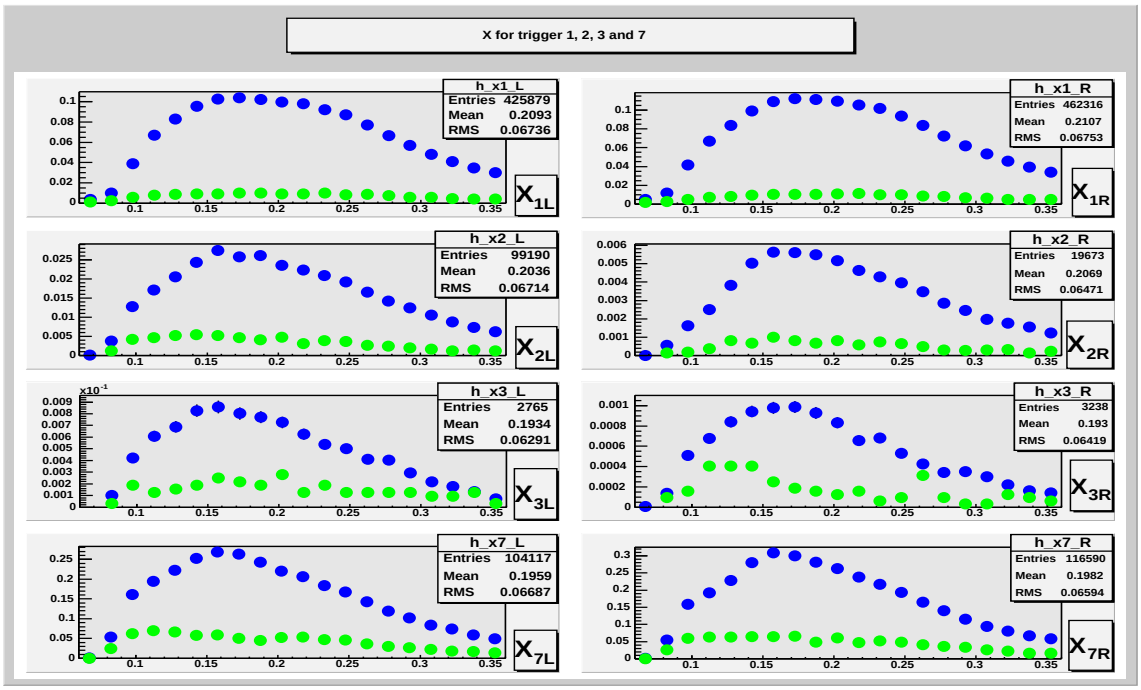

Figure 4-24: Rates of x for each trigger type (1, 2, 3, 7) in the Δ region ($1.1 < W < 1.4\,(GeV)$). Data runs are in blue, empty runs in green. Left sector is on the left, right sector on the right.

rate, R_{empty}, are given by

$$\begin{aligned} R^{+} &= \frac{N^{++}}{Q^{++}} + \frac{N^{--}}{Q^{--}} \\ R^{-} &= \frac{N^{+-}}{Q^{+-}} + \frac{N^{-+}}{Q^{-+}} \\ R_{empty} &= \frac{N_{empty}}{Q_{empty}} \end{aligned} \tag{4.17}$$

where $N^{\pm\pm}$ represents the number of events, and $Q^{\pm\pm}$ is the charge for each spin-state combination for the ABS hydrogen data, the first $\pm$ sign represents the electron helicity (spin projection parallel (+) or anti-parallel (−) to its momentum), and the second $\pm$ sign represents the spin orientation of the target nucleon, i.e. proton (parallel (+) or anti-parallel (−) to the magnetic holding field); N_{empty} is the number of events, and $Q_{empty} = 32\,kC$ is the total charge for the empty target data.

Figures 4-25, 4-26, 4-27, 4-28, 4-29, 4-30, 4-31, 4-32, 4-33, 4-34, 4-35 show almost the same observables as in 4.1.5 for each individual trigger type 1, 2, 3, and 7, but for the empty target cell runs. Recall that for the inclusive analysis these are "summed" up, and, as mention earlier, the data are prescaled by a factor of 9, only for trigger type 7.

Since most of the background events arise from the low-momentum scattered electrons as one can see from the empty target observables, the cut $E_{e'} > 0.25\,GeV$ has been applied (see Table 4.2). This cut drops the invariant mass, W, spectrum at high values (see Figure 4-21).

4.2.1 Beam blow-up Factor

The measurement of the empty target background is not sufficient to estimate the real background during data taken. When gas is inserted into the target, the background rates are likely to change (increase) due to the transverse emittance blow-up of the beam, caused by interactions of the beam with the target gas [114]. This beam blow-up effect

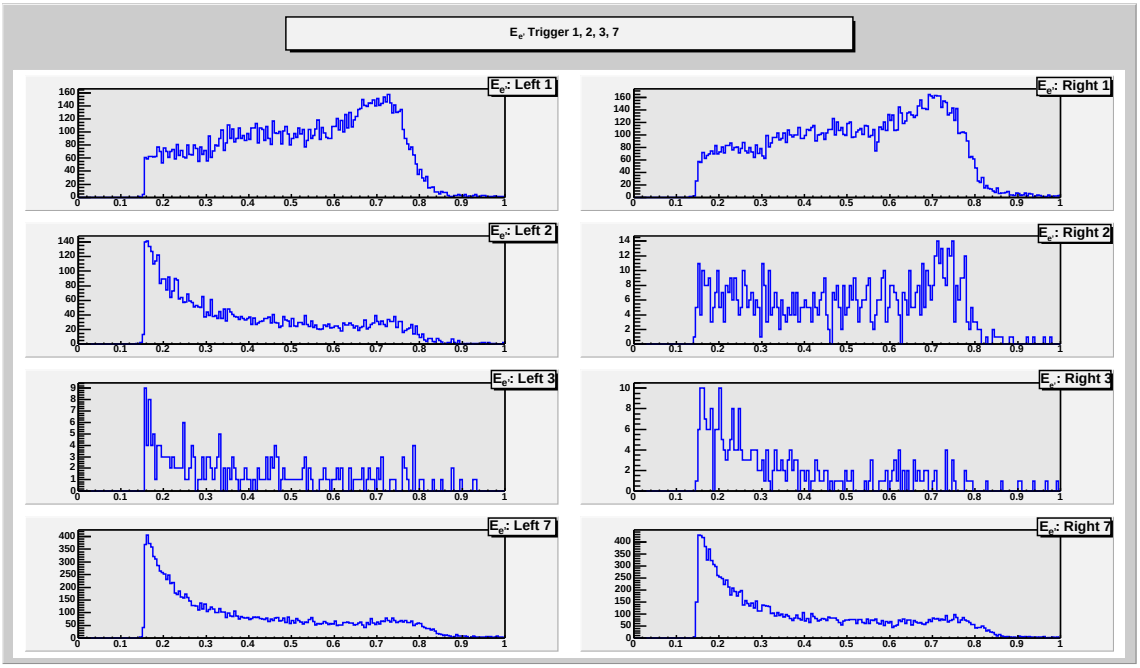

Figure 4-25: Distribution of $E_{e'}$ $[GeV]$ for each trigger type (1, 2, 3, 7) for empty target data. Left sector is on the left, right sector on the right.

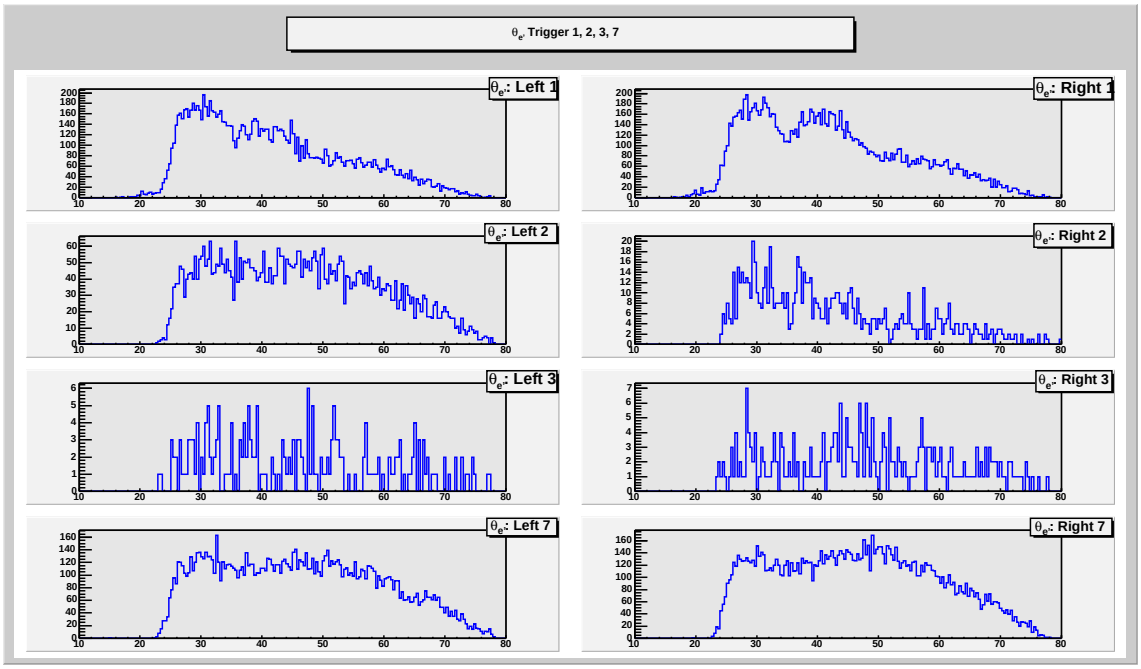

Figure 4-26: Distribution of θ_e $[^\circ]$ for each trigger type (1, 2, 3, 7) for empty target data. Left sector is on the left, right sector on the right.

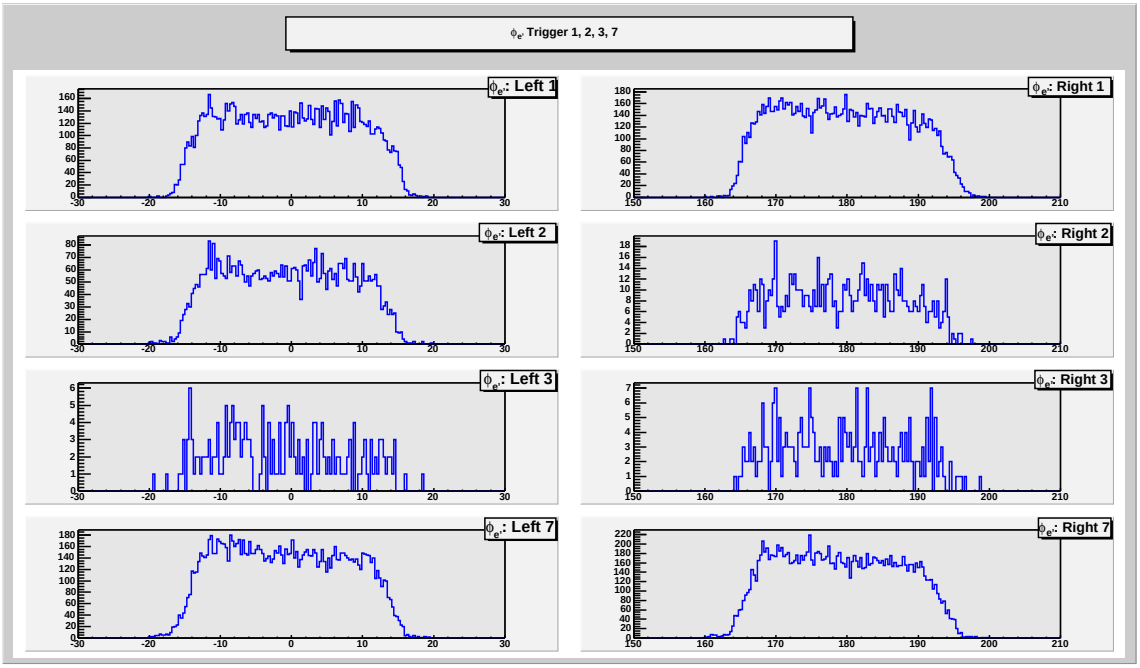

Figure 4-27: Distribution of ϕ_e [°] for each trigger type (1, 2, 3, 7) for empty target data. Left sector is on the left, right sector on the right.

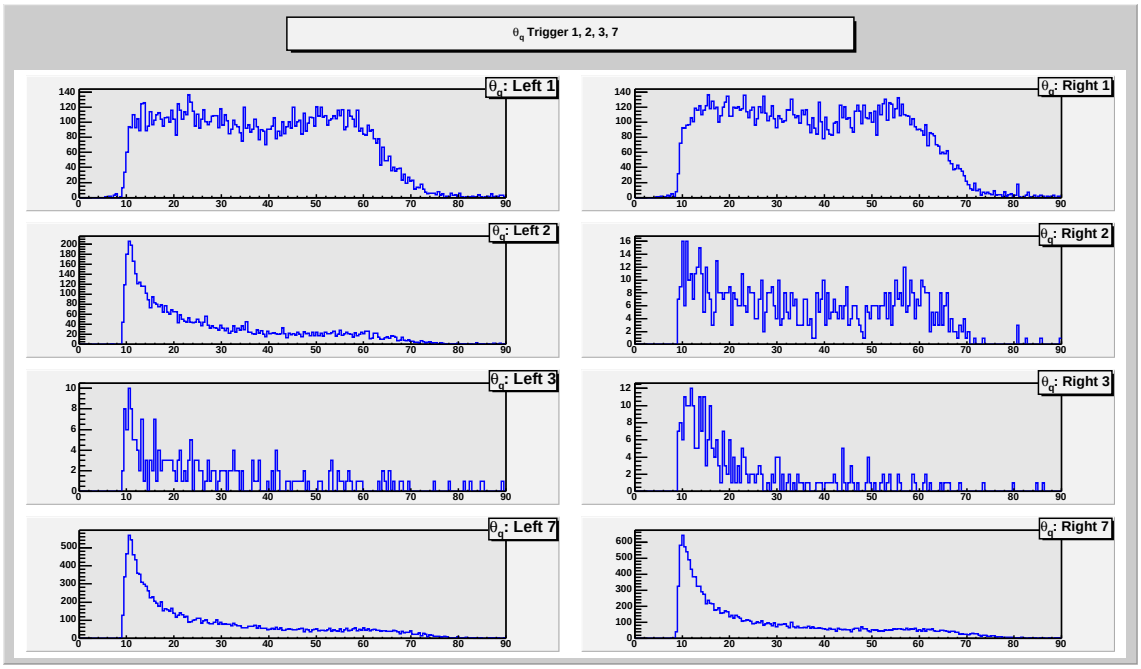

Figure 4-28: Distribution of θ_q [°] for each trigger type (1, 2, 3, 7) for empty target data. Left sector is on the left, right sector on the right.

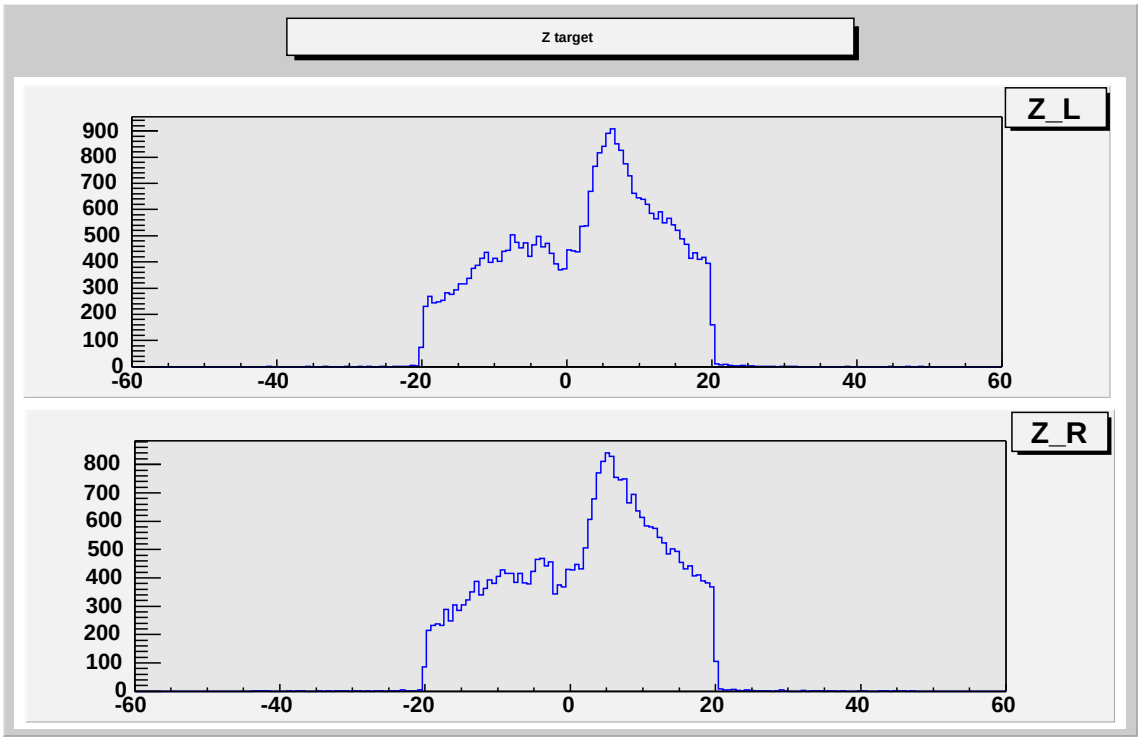

Figure 4-29: Distribution of Z_{target} $[cm]$ for empty target data. Left sector is on top, right sector on the bottom.

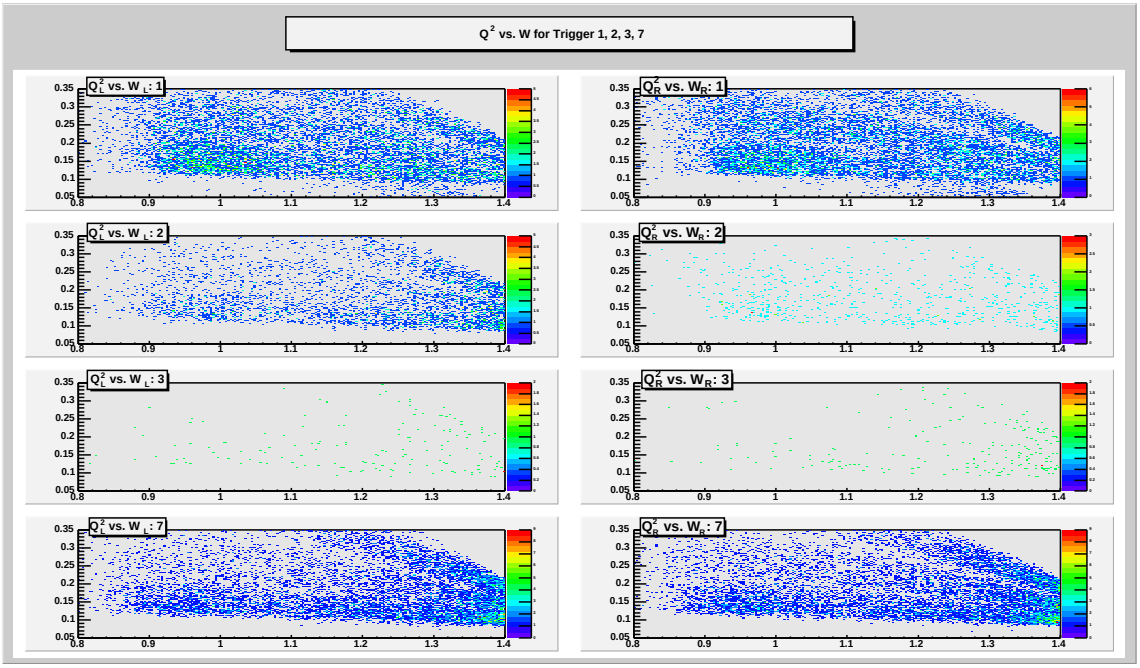

Figure 4-30: Q^2 $[GeV^2]$ vs. W $[GeV]$ for each trigger type (1, 2, 3, 7) for empty target data. Left sector is on the left, right sector on the right.

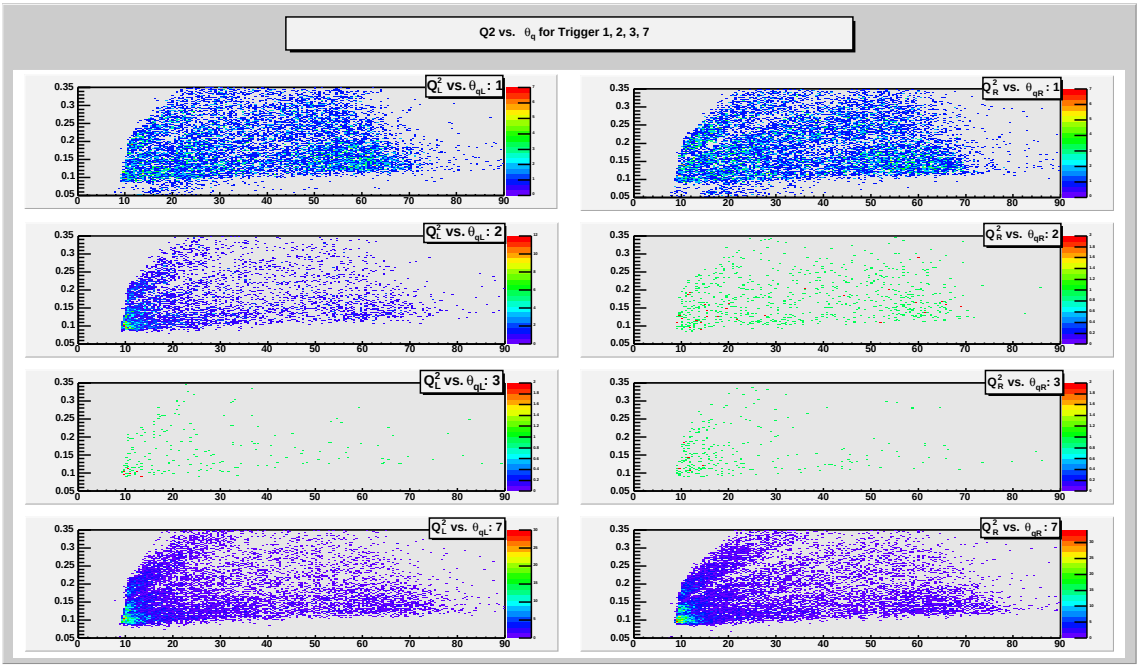

Figure 4-31: $Q^2\,[GeV^2]$ vs. $\theta_q\,[^\circ]$ for each trigger type (1, 2, 3, 7) for empty target data. Left sector is on the left, right sector on the right.

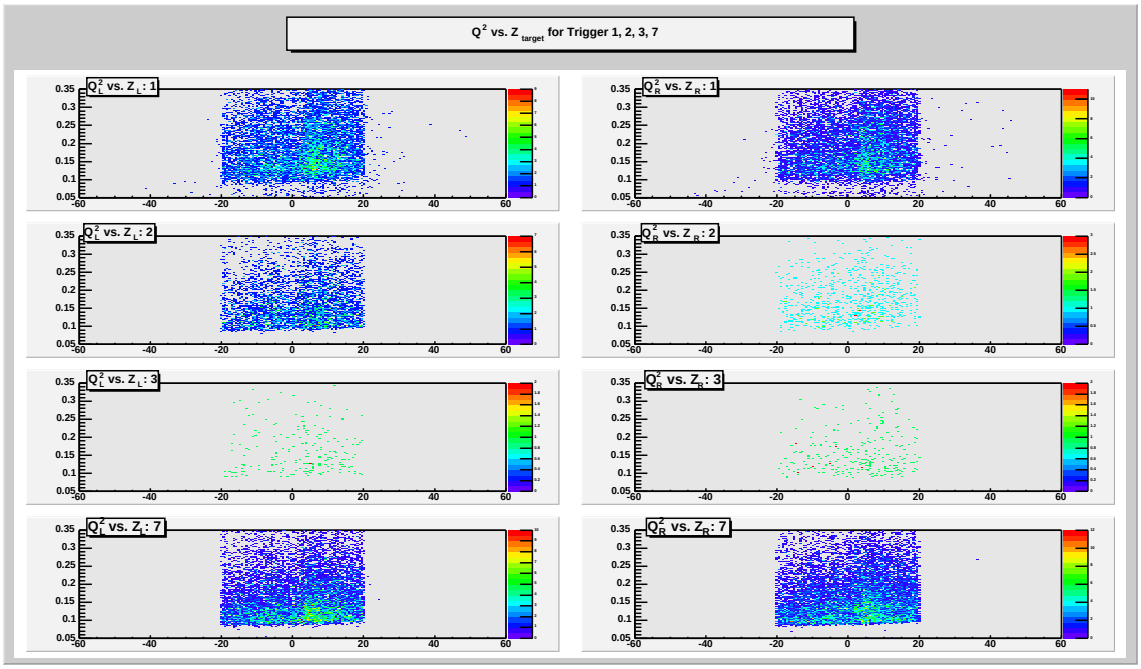

Figure 4-32: $Q^2\,[GeV^2]$ vs. $Z_{target}\,[cm]$ for each trigger type (1, 2, 3, 7) for empty target data. Left sector is on the left, right sector on the right.

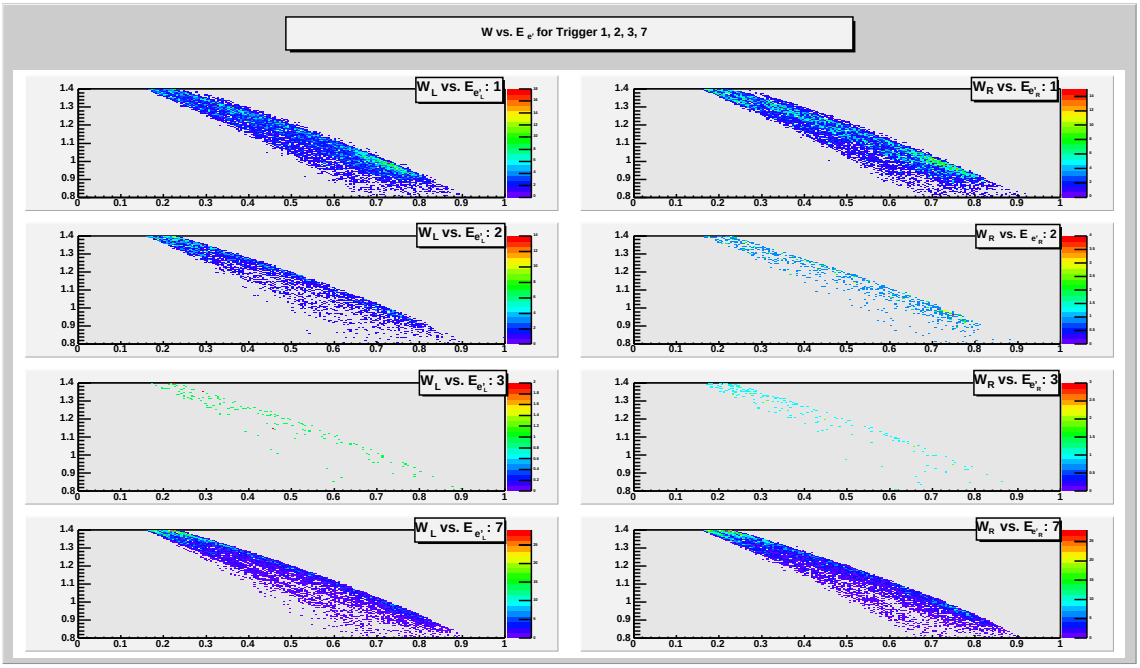

Figure 4-33: $W\,[GeV]$ vs. $E_{e'}\,[GeV]$ for each trigger type (1, 2, 3, 7) for empty target data. Left sector is on the left, right sector on the right.

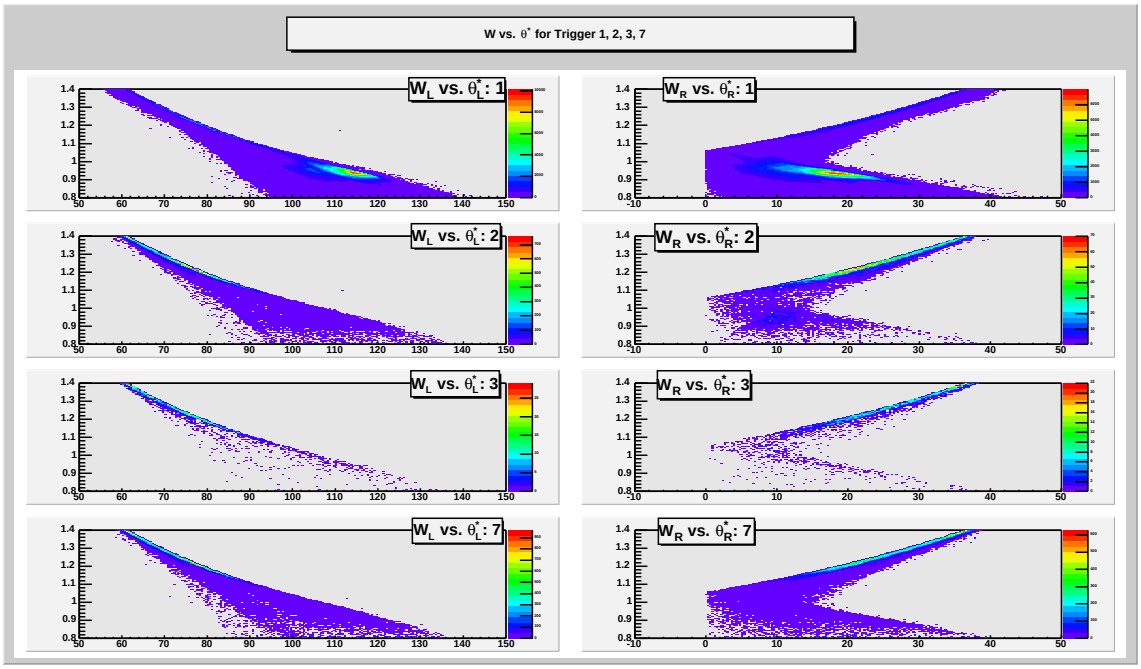

Figure 4-34: $W\,[GeV]$ vs. $\theta^*\,[^\circ]$ for each trigger type (1, 2, 3, 7) for empty target data. Left sector is on the left, right sector on the right.

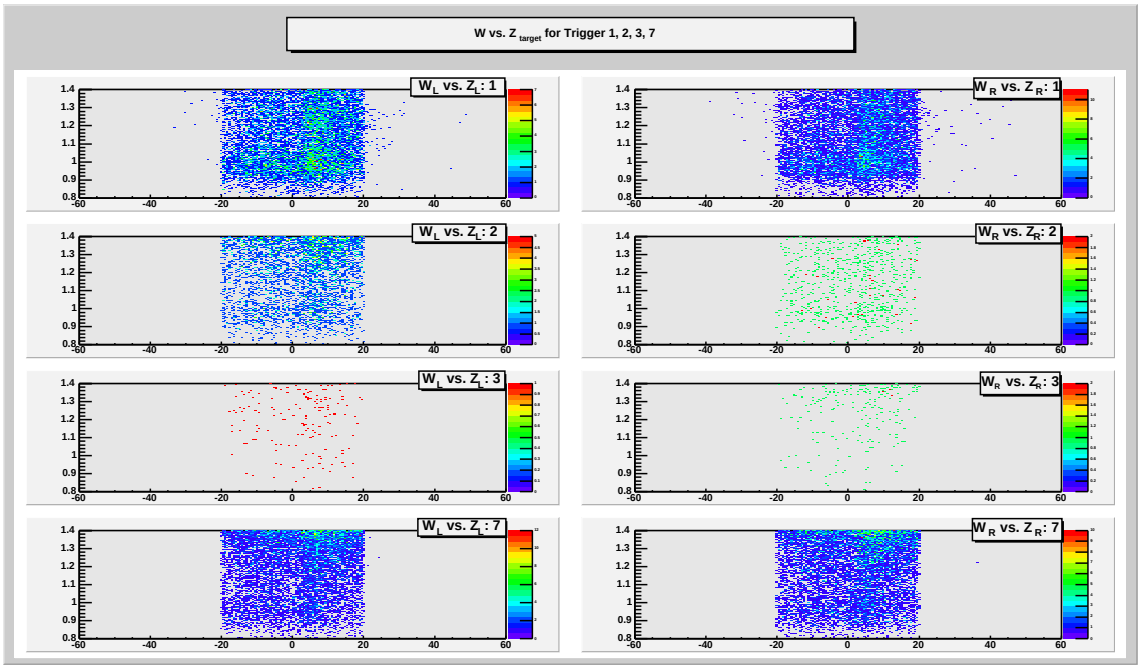

Figure 4-35: $W\,[GeV]$ vs. $Z_{target}\,[cm]$ for each trigger type (1, 2, 3, 7) for empty target data. Left sector is on the left, right sector on the right.

was quantified at BLAST through the $(e, e'n)$ reaction channel [89]. Since there are no neutrons in the hydrogen target, this channel measures strictly the background. The beam blow-up is defined as the ratio of the $(e, e'n)$ for the hydrogen target yields over the empty target yields for the $(e, e'n)$ reaction:

$$f_{blowup} = \frac{Y^n_H}{Y^n_{empty}} \tag{4.18}$$

with Y^n_H being the yields for $(e, e'n)$ reaction with the ABS hydrogen target, and Y^n_{empty} the yields $(e, e'n)$ reaction with the empty target cell.

This factor has been found to be $f_{blowup} \approx 1.05$ [89, 106, 108]. Since the beam blow-up effect should be the same for both sectors, in the case of the ratio measurements (asymmetry), the beam blow-up is not a significant factor, because it cancels out in the asymmetry, provided backgrounds are subtracted correctly.

4.2.2 False Asymmetries

Additional investigation is obtained from the beam only and target only asymmetries, which in the case of the inclusive electron scattering are expected to be zero, due to the vanishing of the TT'- and TL'-terms in the calculation of the cross section (Equation 2.33).

These asymmetries are independent measurements of the false asymmetries. They are obtained by replacing the spin-dependent rates, R^+, R^-, in Equation 4.16 with

$$BEAM \quad : \quad R^+ = \frac{N^{++}}{Q^{++}} + \frac{N^{+-}}{Q^{+-}}, \qquad R^- = \frac{N^{--}}{Q^{--}} + \frac{N^{-+}}{Q^{-+}} \tag{4.19}$$

$$TARGET \quad : \quad R^+ = \frac{N^{++}}{Q^{++}} + \frac{N^{-+}}{Q^{-+}}, \qquad R^- = \frac{N^{--}}{Q^{--}} + \frac{N^{+-}}{Q^{+-}} \tag{4.20}$$

The beam and target asymmetries are given in Figures 4-36 and 4-37.

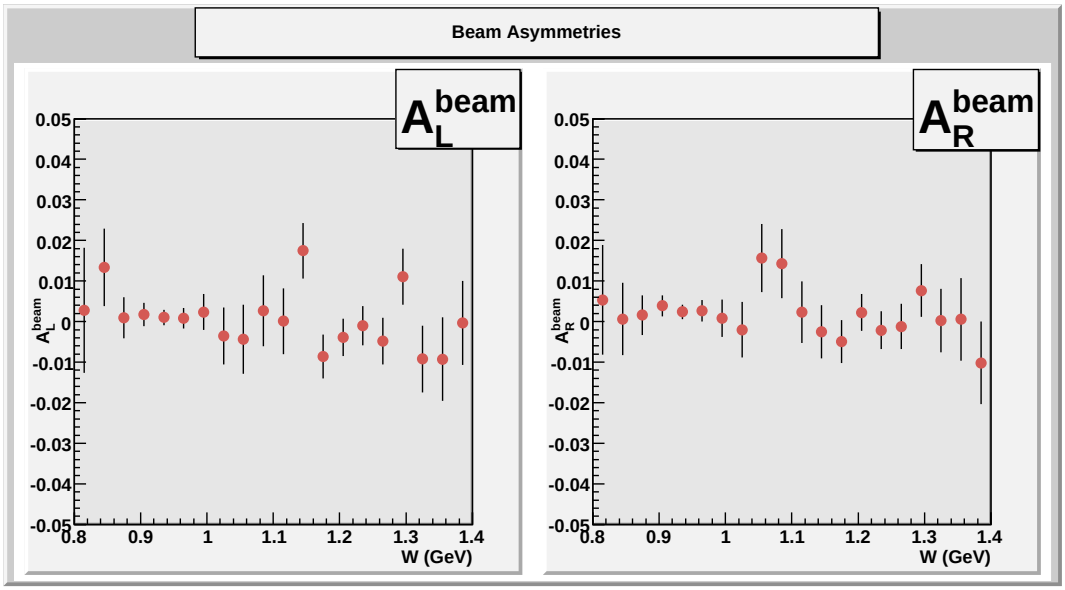

Figure 4-36: Beam asymmetry for left (left) and right (right) sectors.

All false asymmetries are observed to be small and consistent with zero. The contribution to the uncertainty errors in the asymmetry due to the false asymmetries is thus

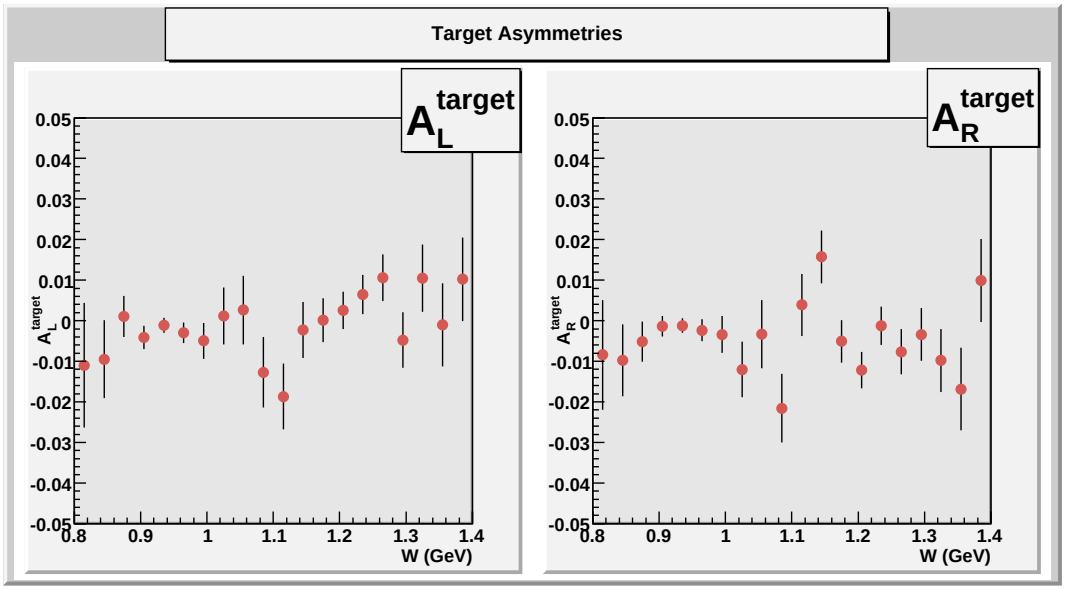

Figure 4-37: Target asymmetry for left (left) and right (right) sectors.

small, but they still enter in the systematic errors for this analysis.

4.3 Radiative Corrections

4.3.1 Introduction

When electrons are scattered from protons, or in the field of the nucleus, they can accelerate or decelerate. This causes the electrons to emit real photons, and the process is called *bremsstrahlung* [115]. These radiative events accompany all processes with charged particle scattering, but are more prevalent for relativistic energies. Besides contributions from the usual Born process, experimental data on lepton-nucleon scattering contain contributions from QED radiative effects [116, 117]. These effects have to be taken into account in the BLAST Monte Carlo simulator, by generating the radiated photons.

In the case of inclusive scattering of electrons from protons, depending on the four-

momentum transfer, Q^2, and the energy transfer, ω [6], there are two basic channels: elastic and inelastic. In the case of the elastic scattering, $\omega = Q^2/2M_p$, the electron is scattered off the proton, leaving the proton in its ground state, while inelastic scattering occurs when the pion production threshold is reached, $\omega \geq Q^2/2M_p + m_\pi$, leaving the proton in an excited state. Due to limitation of energy at BLAST, the proton is in its first excited state, namely $\Delta^+(1232MeV)$. In Table 4.4 the basic properties of the Δ^+ are listed.

Particle	Symbol	Makeup	Rest Mass MeV/c^2	Spin	Lifetime (seconds)	Decay Modes %
Delta	Δ^+	uud	1232	$\frac{3}{2}$	0.6×10^{-23}	$p + \pi^0(66.6)$ $n + \pi^+(33.3)$

Table 4.4: Basic properties of Δ^+

At the Born level both Q^2 and ω are fixed by measuring the scattered elecron momentum and in-plane angle, while at the level of radiative corrections, in case of the presence of the radiated photon, this constraint is removed, hence the four-momentum of the radiated photon has to be included into the kinematics calculations. The unpolarized and polarized observed cross section can be written as [118]

$$\sigma_{obs}^{u,p} = (1 + \delta)\, \sigma_0^{u,p} + \sigma_{RC}^{u,p} \tag{4.21}$$

where both the factorized correction, δ, and the unfactorized cross section, $\sigma_{RC}^{u,p}$, come from the bremsstrahlung process contribute to the cross section. In the case of BLAST, where the polarization asymmetries are measured, the factorized part of the cross section has tendency to cancel out, but the unfactorized part could give important contributions. These contributions come from:

[6] In some papers this is denoted by $\nu = E_e - E_{e'} \equiv \omega$

- hard radiation.
- higher order corrections.
- box-type diagrams.

The first two are called *model independent* corrections, since they do not depend on nuclear interactions. The third is called *model dependent* because it takes into account the two-photon exchange graphs that require additional assumptions. The calculation of radiative effects for the model dependent correction necessitates additional information about the hadron interaction. Hence it has extra theoretical uncertainities, which cannot be controlled. In this work we consider only the model independent correction.

There are two methods to calculate model independent corrections. Mo and Tsai [119] introduced an artificial parameter which separates the momentum phase space into soft and hard parts. The soft part is performed in the soft photon approximation, when the photon energy is considered small compared to the all momenta and masses in the system, but it cannot be chosen too small, because of the numerical instabilities that occur in the hard part. This artificial parameter is a disadvantage for correct radiative effects calculations. Bardin and Shumeiko [120] developed an approach of extraction and cancellation of the infrared divergence without introducing this artificial parameter. Almost all of the recent work in calculating the radiative effects has used this approach.

4.3.2 Radiative Effects in Elastic Electron-Proton Scattering

In order to describe the phase space of the radiative process

$$e(K) + p(P) \rightarrow e'(K') + p'(P') + \gamma(K_\gamma) \tag{4.22}$$

besides the squared momentum transfer, Q^2, and azimuthal angle, ϕ_e, three new kinematic variables have to be considered, namely, the proton transfer momentum squared, $t =$

$-(K - K' - K_\gamma)^2$, the inelasticity, $v = (P' + K_\gamma)^2 - M_p^2$, and the azimuthal angle, ϕ_K, between the planes $(\mathbf{q}, \mathbf{k})$ and $(\mathbf{k}, \mathbf{k}')$. This set of variables defines the four-vectors of all final particles in any frame.

The separation of the scattering process into the radiative and non-radiative parts requires an additional parameter to be introduced, which is normally associated with the photon resolution in the detector, denoted by v_{min}, and is called minimal inelasticity. The contributions to the observed cross section are shown in Figure 4-38. The observed cross section can be written as [121]

$$\sigma_{obs} = \sigma^{non-rad}(v_{min}) + \sigma^{rad}(v_{min}) \tag{4.23}$$

where the non-radiative part of the cross section, $\sigma^{non-rad}$, includes the Born cross

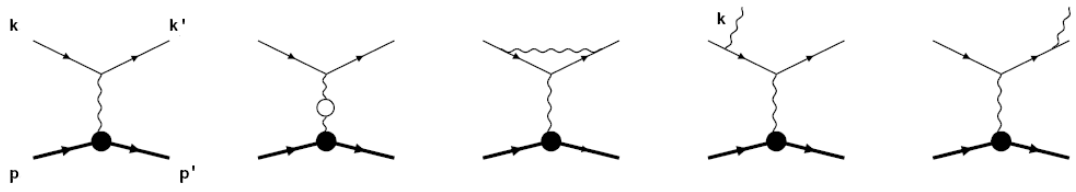

Figure 4-38: Feynman diagrams contributing to the observed cross section in elastic electron-proton scattering.

section, σ_0 (Figure 4-38(a)), as well as loop effects (Figure 4-38(b, c)), plus the soft photon radiation ($v < v_{min}$), and the radiative part contains the radiated photon contributions from Figure 4-38(d, e). These cross sections can be written as [118, 121]

$$\sigma^{non-rad}(v_{min}) = \sigma_0 e^{\delta_{inf}}(1 + \delta_{VR} + \delta vac + \delta^{add}(v_{min})) + \sigma_R^{add}(v_{min}) \tag{4.24}$$

$$\sigma^{rad}(v_{min}) = -\frac{\alpha^3}{2S^2}\int_{t_1}^{t_2} dt \sum_i \frac{\mathcal{F}_i(t)}{t^2}\Theta_i(t) \tag{4.25}$$

where

$$\begin{aligned}
\sigma_0 &= \frac{2\pi\alpha^2}{S^2Q^4}\sum_i \theta_i^B \mathcal{F}_i(Q^2) && (4.26)\\
\delta_{VR} &= \frac{\alpha}{\pi}\Big(\frac{3}{2}\log\frac{Q^2}{m_e} - 2 - \frac{1}{2}\log^2\frac{S}{S-Q^2} \\
&+ Li_2\left(1 - \frac{M_p^2Q^2}{S(S-Q^2)}\right) - \frac{\pi^2}{6}\Big) && (4.27)\\
\delta_{vac} &= \delta_{vac}^{lepton} + \delta_{vac}^{hadron} && (4.28)\\
\delta_{inf} &= \frac{\alpha}{\pi}(l_m - 1)\log\frac{v_{max}}{S(S-Q^2)} && (4.29)\\
\delta^{add}(v_{min}) &= \frac{2\alpha}{\pi}\log\left(\frac{v_{max}}{v_{min}}\right)\left[1 - \log\left(\frac{Q^2}{m_e^2}\right)\right] && (4.30)\\
\sigma_R^{add}(v_{min}) &= -\frac{\alpha^3}{2S^2}\int_{t_1'}^{t_2'} dt \sum_i \left(\theta_i\frac{\mathcal{F}_i(t)}{t^2} - 4\theta_i^B\mathcal{F}_{IR}\frac{\mathcal{F}_i(Q^2)}{Q^4}\right) && (4.31)\\
\mathcal{F}_{IR} &= \left(\frac{K}{2KK_\gamma} - \frac{K'}{2K'K_\gamma}\right)^2 && (4.32)\\
\Theta_i(t) &= \int_{v_1}^{v_{max}} dv\theta_i(t,v) = \int_{v_1}^{v_{max}} dv\int_0^{2\pi} d\phi_K\theta_i(t,v,\phi_K) && (4.33)\\
v_1 &= max\left(v_{min}, \frac{(t-Q^2)(\sqrt{t} \mp \sqrt{4M_P^2 + t})}{s\sqrt{t}}\right) && (4.34)\\
v_2 &= v_{max} = S - Q^2 - \frac{M_p^2Q^2}{S} && (4.35)\\
t_{1,2} &= \frac{2M_p^2Q^2 + v_{max}\left(Q^2 + v_{max} \mp \sqrt{\lambda}\right)}{2(M_p^2 + v_{max})} && (4.36)\\
\lambda &= (Q^2 + v_{max})^2 + 4M_p^2Q^2 && (4.37)\\
t_{1,2}' &= t_{1,2}(v_{max} \to v_{min}) && (4.38)
\end{aligned}$$

and $S = 2KP$, $v = (P + K - K')^2 - M_p^2$, $l_m = \log(Q^2/m_e^2)$, $Li_2 = \int_0^x dy \ln(1-y)/y$ is the dilogarithm or Spence function, $\mathcal{F}_i(t)$ are the squared combinations of the electric and magnetic elastic form factors, and θ_i and θ_i^B are analytical functions [118, 116] of

kinematic invariants for the radiative and Born subprocesses, respectively. The index i takes into account both the unpolarized part, $i = 1, 2$, and the polarized part, $i = 3, 4$.

For the radiative effects calculations in the elastic electron-proton scattering, the code MASCARAD [122] is used, based on the calculations mentioned above.

4.3.3 Radiative Effects in Inelastic Electron-Proton Scattering

For the case of electron-proton inelastic scattering

$$e(K) + p(P) \rightarrow e'(K') + X \tag{4.39}$$

the radiative contributions to the observed cross section are shown in Figure 4-39. The

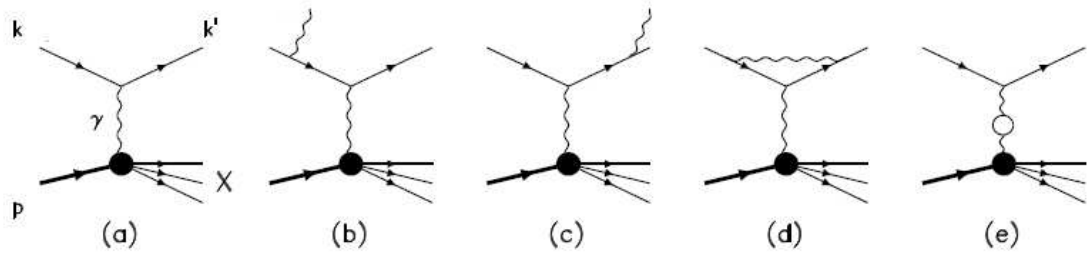

Figure 4-39: Feynman diagrams contributing to the observed cross section in inelastic electron-proton scattering.

observed cross section can be written as [123, 117, 116]

$$\sigma_{obs} = \sigma_{non-rad}(E^{\gamma}_{min}) + \sigma_{in}(E^{\gamma}_{min}) + \sigma_{el} \tag{4.40}$$

where E^{γ}_{min} is the minimal detectable photon energy. Here, σ_{in} and σ_{el} are contributions of the radiative tails from continuous spectrum and elastic scattering, and $\sigma_{non-rad}$ contains the Born process (Figure 4-39(a)), loop corrections (Figure 4-39(d, e)), and soft-photon

production (Figure 4-39(b, c)) with $E_\gamma < E^\gamma_{min}$. This can be written more explicitely as

$$\sigma = \delta_R(E^\gamma_{min})(1 + \delta_{vert} + \delta_{vac} + \delta_{sm})\sigma_0 + \sigma^{add}(E^\gamma_{min}) + \sigma_{el} + \sigma_{in}(E^\gamma_{min}) \tag{4.41}$$

where

$$\begin{aligned}
\delta_R(E^\gamma_{min}) &= exp\left[-\frac{\alpha}{\pi}\left(\ln\frac{E}{E^\gamma_{min}} + \ln\frac{E'}{E^\gamma_{min}}\right)\left(\ln\frac{Q^2}{m_e^2} - 1\right)\right] && (4.42)\\
\delta_{vert} &= \frac{\alpha}{\pi}\left(-2 + \frac{3}{2}\ln\frac{Q^2}{m_e^2}\right) && (4.43)\\
\delta_{vac} &= \frac{\alpha}{\pi}\left(-\frac{20}{9} + \frac{2}{3}\ln\frac{Q^2}{m_e^2} + \frac{3}{2}\ln\frac{Q^2}{m_\mu^2}\right) && (4.44)\\
\delta_{sm} &= \frac{\alpha}{\pi}\left(-\frac{\pi^2}{6} + Li_2\left(\cos^2\frac{\theta}{2}\right) - \frac{1}{2}\ln^2(1-y)\right) && (4.45)
\end{aligned}$$

δ_{vert} is the vertex correction, δ_{vac} is the correction due to vacuum polarization by electron and muon, and δ_{sm} is a residuum correction of the cancellation of the infrared divergent terms independent of E^γ_{min}; θ is the angle between the real and virtual photon, and $y = \omega/E$ is the Bjorken scaling variable.

For calculations of these radiative effects a modified version of the POLRAD code [122, 124] has been used [6, 125, 126, 127], based on the above relations. In the POLRAD code σ_{in} corresponds to the deep inelastic scattering (DIS) cross section, while in the modified version, it corresponds to one of the two MAID channels $e\,p \to e'\,p\,\pi^0$ or $e\,p \to e'\,n\,\pi^+$. A large (x, y) grid that covers the BLAST acceptance over the inelastic (Δ) region is used as input, i.e. $Q^2 \in [0.0, 0.5]$ $(GeV/c)^2$ and $W \in [1.08, 1.4]$ GeV. These calculations show that the main contribution arises from elastically scattered electrons, due to the relatively high elastic electron scattering cross section.

4.3.4 Generation of Radiative Events

Unpolarized Electron-Proton Scattering

The generation of the radiative events is completely different than calculating them [128]. If one takes into account the radiative effects, then the strategy for generating one event is as follows [127, 128, 121]:

- For the fixed initial energy, E_e, and momentum transfer squared, Q^2, both the non-radiative and radiative parts of the observed cross section are calculated.
- The scattering channel is simulated in accordance with the partial contributions of these two parts into the total cross section.
- The azimuthal angle, ϕ_e, is simulated uniformly over the detector acceptance.
- For the radiative event, the kinematic variables t, v, and ϕ_K are simulated in accordance with their analytically calculated distributions; first t, then v by taking into account t, and finally ϕ_K according to t and v.
- The four-momenta of all final particles are calculated.
- If Q^2 is simulated in accordance with some distribution, i.e. the Born cross section, then the Born cross section has to be reweighted.

In order to generate unpolarized radiative events the ELRADGEN code [122, 121] is used, which is incorporated into the BLAST Monte Carlo event generator. The code needs as input, the observed momentum transfer, $Q \equiv Q_{obs}$, which is simulated inside the BLAST Monte Carlo generator, the parameter v_{min}, and the beam energy, E_e. If a radiative event is generated, it returns the true momentum transfer, Q_{true}, the radiated photon four-momentum, K_γ, and a weight, $\sigma_{obs}/\sigma_{Born}$, which is used to multiply the Born

cross section in order to get the observed cross section. The electron, virtual photon and proton final momenta are then calculated from E_e, Q_{true} and K_γ.

In Figure 4-40 the simulation results using ELRADGEN (green line) are presented for the invariant mass, W, averaged over the entire range of transfer momentum squared, $Q^2 \in [0.08, 0.38] GeV^2$.

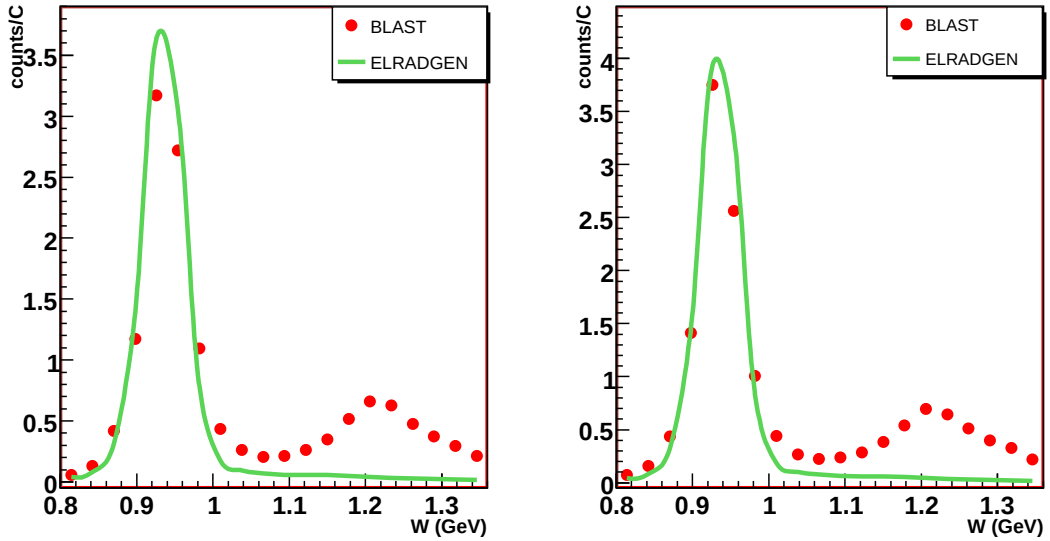

Figure 4-40: BLAST invariant mass (red dots), $W\,(GeV)$, for left (left) and right (right) sectors and Monte Carlo simulations of radiative effects (green line) using unpolarized ELRADGEN and Hoehler form factors model, $Q^2 \in [0.08, 0.38] GeV^2$.

Polarized Electron-Proton Scattering

If we take into account the polarization vectors (see Figure 4-41) of the initial electron and proton, denoted by ξ and η, respectively, than we have

$$e(K, \xi) + p(P, \eta) \rightarrow e'(K') + p'(P') + \gamma(K_\gamma) \tag{4.46}$$

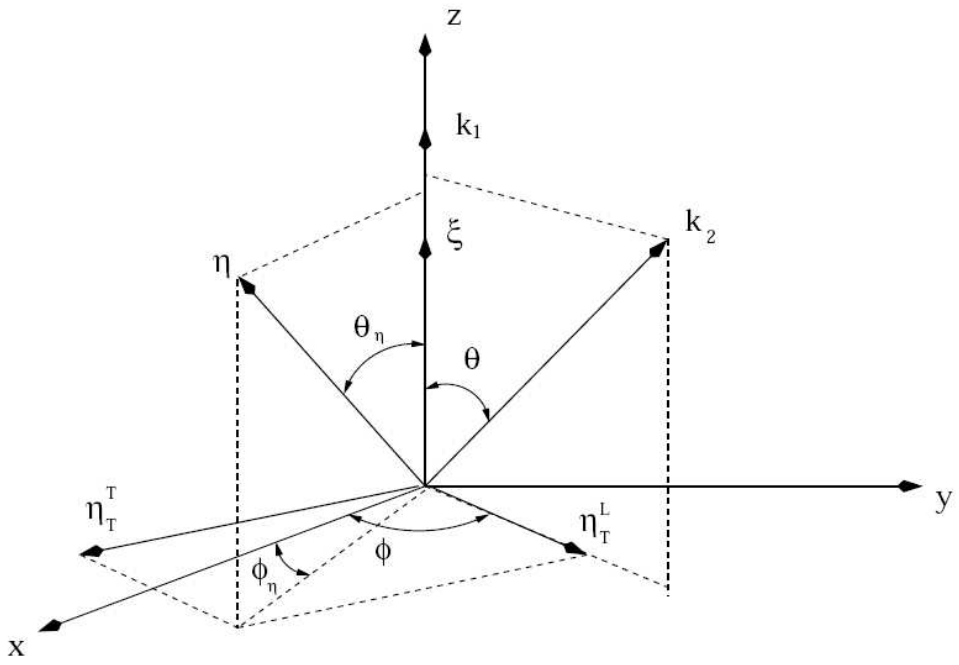

Figure 4-41: The polarization vectors for initial electron (ξ) and proton (η) in the laboratory frame.

At BLAST, the electrons are longitudinally polarized, $\xi||\mathbf{z}$. Therefore the polarized vector has the form (using the notation from Figure 4-4)

$$\xi = \frac{P_b}{\sqrt{\lambda_s}}\left(\frac{S}{m_e}K - 2m_e P\right) \tag{4.47}$$

where $S = 2KP$, $\lambda_s = S^2 - 4m_e^2 M_p^2$, $K^2 = K'^2 = m_e^2$, $P^2 = P'^2 = M_p^2$, P_b is the degree of the beam polarization (%). In the BLAST laboratory frame, the target polarization vector can be decomposed into longitudinal

$$\eta_L = \frac{1}{\sqrt{\lambda_s}}\left(2M_p K - \frac{S}{M_p}P\right) \tag{4.48}$$

and transverse components

$$\eta_T = \cos(\phi - \phi_\eta)\eta_T^L + \sin(\phi - \phi_\eta)\eta_T^T \tag{4.49}$$

where

$$\eta_T^L = \frac{1}{\sqrt{\lambda\lambda_s}}\left[(4m_e^2M_p^2 + 2Q^2M_p^2 - 2SX)K + \lambda_s K' - (SQ^2 + 2m_e^2S_x)P\right] \tag{4.50}$$

$$\eta_T^T = \left(0,\ \frac{\mathbf{k}' \times \mathbf{k}}{|\mathbf{k}||\mathbf{k}'|\sin\theta}\right) \tag{4.51}$$

and $\theta = \theta_e$, is the electron in-plane scattering angle, $\phi = \phi_e$ is the electron azimuthal angle; $X = 2PK'$, $S_x = S - X$, $\lambda = SXQ^2 - M_p^2Q^4 - m_e^2(S_x + 4Q^2M_p^2)$. The target polarization vector can be written now as

$$\eta = P_t(\eta_L \cos\theta_\eta + \eta_T \sin\theta_\eta) \tag{4.52}$$

where P_t is the degree of target polarization (%).

At BLAST:

$$P_b \approx 65\%,\ P_t \approx 80\%,\ \phi_\eta \approx 0^\circ,\ \theta_\eta \approx 48.84^\circ \tag{4.53}$$

The code ELRADGEN has been generalized to include these polarization contributions from the initial electron and proton, by A. Ilyichev [127].

4.4 Monte Carlo Simulations

The BLAST Monte Carlo event generator is divided into two parts: event generation and particle propagation. The event generation component is a C++ object oriented library, developed specifically for the BLAST experiment. It allows for different theo-

retical models to be implemented (added) separately, and it handles both hydrogen and deuterium targets. For a given reaction channel and target, it generates initial event kinematics for all the particles in the reaction either according to the cross section or to a flat, "white" distribution. The elastic channel uses Hőhler form factors [103, 106], which are computed on a two-dimensional grid, (ϕ_e, θ_e). In the case of radiative effects simulations, the ELRADGEN code is added to the elastic model at the event kinematics reconstruction level, that is, for each ϕ_e, θ_e generated event, the observed momentum transfer is reconstructed as follows

$$\begin{aligned}
q^2_{obs} &= -Q^2_{obs} = -4E_eE_{e'}\sin^2\frac{\theta_e}{2} \\
S &= 2E_eM_p \\
v_{max} &= S - Q^2_{obs} - \frac{M_p^2Q^2_{obs}}{S} \\
Q^{(1)}_{obs} &= -\sqrt{\frac{Q^2_{obs}v_{max}}{S}}\cos\phi_e \\
Q^{(2)}_{obs} &= -\sqrt{\frac{Q^2_{obs}v_{max}}{S}}\sin\phi_e \\
Q^{(3)}_{obs} &= Q^2_{obs}\frac{2M_p^2+S}{2M_pS} \\
Q^{(4)}_{obs} &= \frac{Q^2_{obs}}{2M_p}
\end{aligned} \tag{4.54}$$

The values of Q_{obs}, E_e, v_{min} are then fed to ELRADGEN, which returns Q_{true}, K_γ and a weight with which the Born cross section is multiplied in order to get the observed cross section. ELRADGEN is initialized at the initialization stage, that is, at the begining of event generation. Note that

$$\begin{aligned}
Q^2_{obs} &= Q^{(1)^2}_{obs} + Q^{(2)^2}_{obs} + Q^{(3)^2}_{obs} - Q^{(4)^2}_{obs} \\
&= \left(Q^{(1)}_{true} + K^{(1)}_\gamma\right)^2 + \left(Q^{(2)}_{true} + K^{(2)}_\gamma\right)^2 + \left(Q^{(3)}_{true} + K^{(3)}_\gamma\right)^2 - \left(Q^{(4)}_{true} + K^{(4)}_\gamma\right)^2
\end{aligned} \tag{4.55}$$

but, for radiative events

$$Q_{obs}^{(i)} \neq Q_{true}^{(i)} + K_{\gamma}^{(i)}, \qquad i = \overline{1,4} \tag{4.56}$$

The MAID 2003 and SL models use a five-dimensional grid $(\theta_e, \phi_e, \theta_\pi^{cm}, \phi_\pi^{cm}, W)$ to calculate the differential cross section for each individual Δ^+, Δ^0 channel.

Because of its object oriented design, individual channels can be added together in the BLAST Monte Carlo generator. In the case of the inclusive scattering of polarized electrons from polarized protons, the elastic channel, $\vec{p}(\vec{e}, e'p)$, and both MAID pion production channels from the proton, $\vec{p}(\vec{e}, e')p\pi^0$, $\vec{p}(\vec{e}, e')n\pi^+$, are added together, and each channel is generated according to its cross section. Note that for the two MAID channels mention above, some of the generated events do make it into the detector acceptance, i.e. $\vec{p}(\vec{e}, e'p)\pi^0$, $\vec{p}(\vec{e}, e'n)\pi^+$, etc..

The second component of the BLAST Monte Carlo generator, the particle propagation, is handled by a GEANT Monte Carlo code which simulates the beam, target, and detector hardware, as well as physics processes occuring during propagation (i.e. energy loss, hadronic interactions, multiple scattering, etc.). The detectors are positioned within a master coordinate system, namely, the BLAST laboratory system, which is described in **Appendix B**. The output of the reconstruction allows direct comparison of the kinematics of the generated events to the data.

CHAPTER 5

Results and Discussion

5.1 Asymmetry Extraction

The measured spin-dependent rates are corrected for background and radiative contributions and are given by

$$\begin{aligned} R^{+} &= \frac{N^{++}}{Q^{++}} + \frac{N^{--}}{Q^{--}} - \frac{N^{++}_{empty}}{Q^{++}_{empty}} - \frac{N^{--}_{empty}}{Q^{--}_{empty}} - \frac{N^{++}_{rad}}{Q^{++}_{rad}} - \frac{N^{--}_{rad}}{Q^{--}_{rad}} \\ R^{-} &= \frac{N^{+-}}{Q^{+-}} + \frac{N^{-+}}{Q^{-+}} - \frac{N^{+-}_{empty}}{Q^{+-}_{empty}} - \frac{N^{-+}_{empty}}{Q^{-+}_{empty}} - \frac{N^{+-}_{rad}}{Q^{+-}_{rad}} - \frac{N^{-+}_{rad}}{Q^{-+}_{rad}} \end{aligned} \tag{5.1}$$

where the radiative yields, $N^{++}_{rad}/Q^{++}_{rad}$, $N^{--}_{rad}/Q^{--}_{rad}$, $N^{+-}_{rad}/Q^{+-}_{rad}$, and $N^{-+}_{rad}/Q^{-+}_{rad}$ are determined by normalizing the Monte Carlo simulations with radiative effects using polarized ELRADGEN [127] (see also subsection 4.3.4) to the data elastic peak (see Figure 5-1). The spin-dependent radiative corrections demonstrate a helicity behavior, the $+-$ and $-+$ spin states have more radiative contributions than the $++$ and $--$ states (see Figure 5-2).

For the corresponding Q^2 values (see Table 5.1) these radiative contributions are shown in Figures 5-3, 5-4, 5-5, 5-6. $N^{\pm\pm}$ represents the number of events, and $Q^{\pm\pm}$ is the charge for each spin-state combination for the ABS hydrogen data, the first $\pm$ sign represents the orientation of the electron helicity (spin projection parallel $(+)$ or anti-parallel $(-)$ to its momentum), and the second $\pm$ sign represents the spin orientation of the target nucleon, i.e. proton (parallel $(+)$ or anti-parallel $(-)$ to the magnetic holding field); $N^{\pm\pm}_{empty}$ and $Q^{\pm\pm}_{empty}$ denote the same quantities, but for the empty target data (section 4.2).

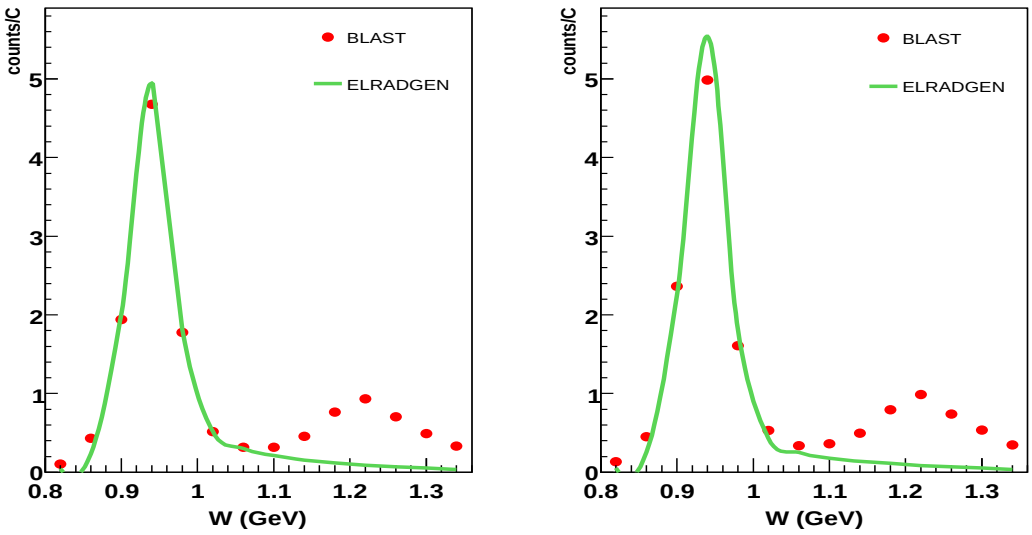

Figure 5-1: Normalized yields as a function of the invariant mass, $W(GeV)$ over $0.08 < Q^2 < 0.38\,GeV^2$. The dots show the BLAST ABS hydrogen data corrected for the background contributions, and the solid line represents the Monte Carlo simulations with radiative effects (polarized ELRADGEN). Left sector is on the left, right sector on the right.

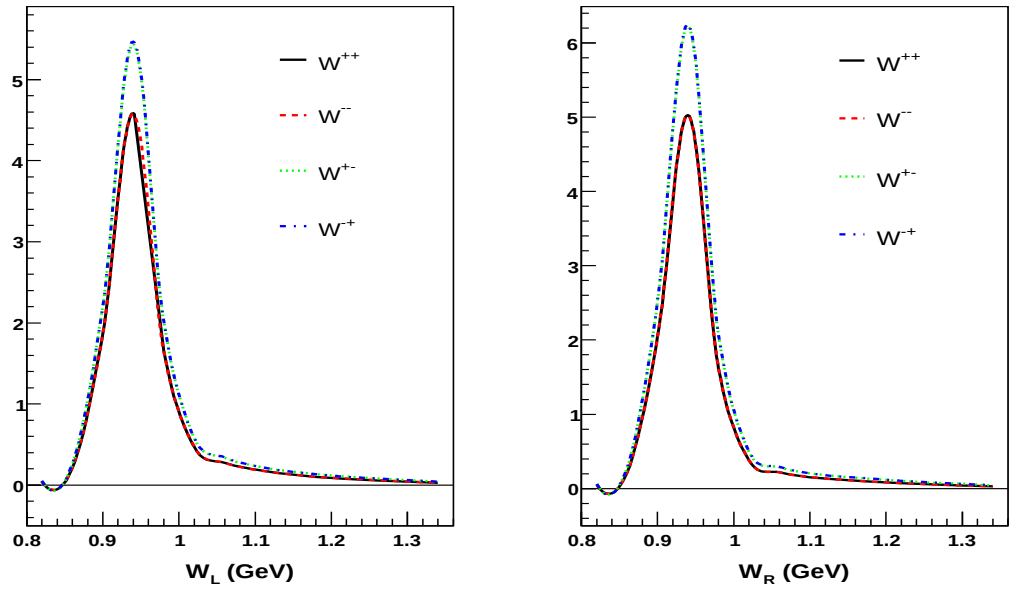

Figure 5-2: Normalized yields as a function of the invariant mass, $W(GeV)$ over $0.08 < Q^2 < 0.38\,GeV^2$, for the radiative simulations obtained with the polarized ELRADGEN code, for all the electron-target spin states. Left sector is on the left, right sector on the right.

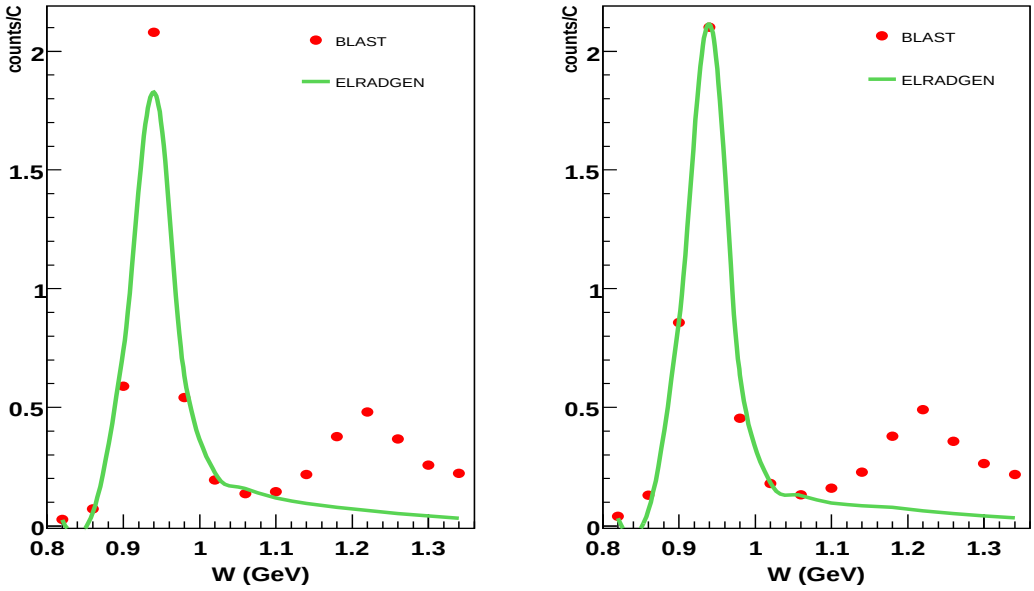

Figure 5-3: Normalized yields as a function of the invariant mass, W, for $Q^2 = 0.123\,GeV^2$. The dots show the BLAST ABS hydrogen data corrected for the background contributions, and the solid line represents the Monte Carlo simulations with radiative effects (polarized ELRADGEN). Left sector is on the left, right sector on the right.

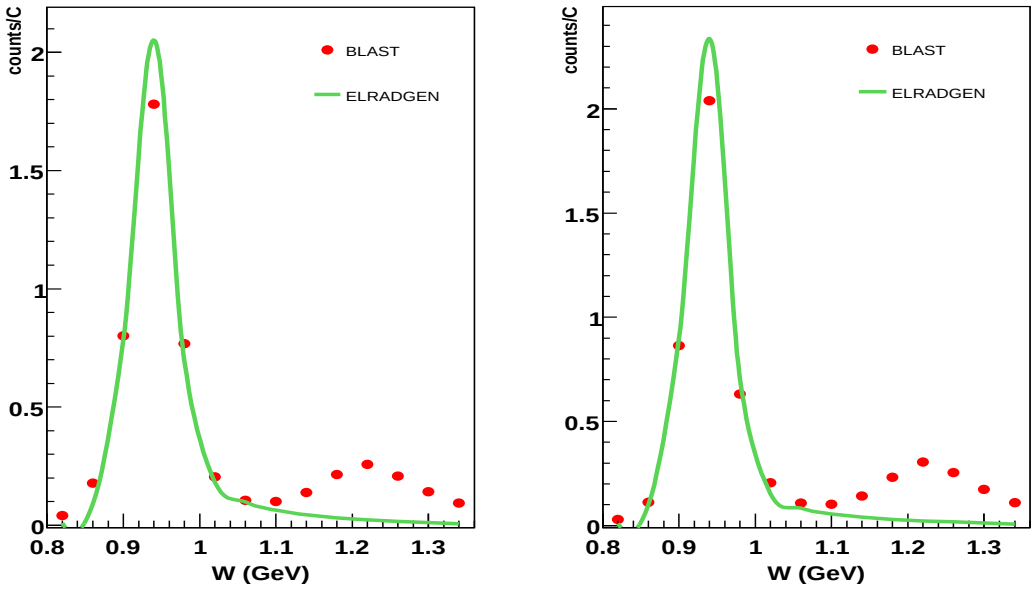

Figure 5-4: Normalized yields as a function of the invariant mass, W, for $Q^2 = 0.175\,GeV^2$. The dots show the BLAST ABS hydrogen data corrected for the background contributions, and the solid line represents the Monte Carlo simulations with radiative effects (polarized ELRADGEN). Left sector is on the left, right sector on the right.

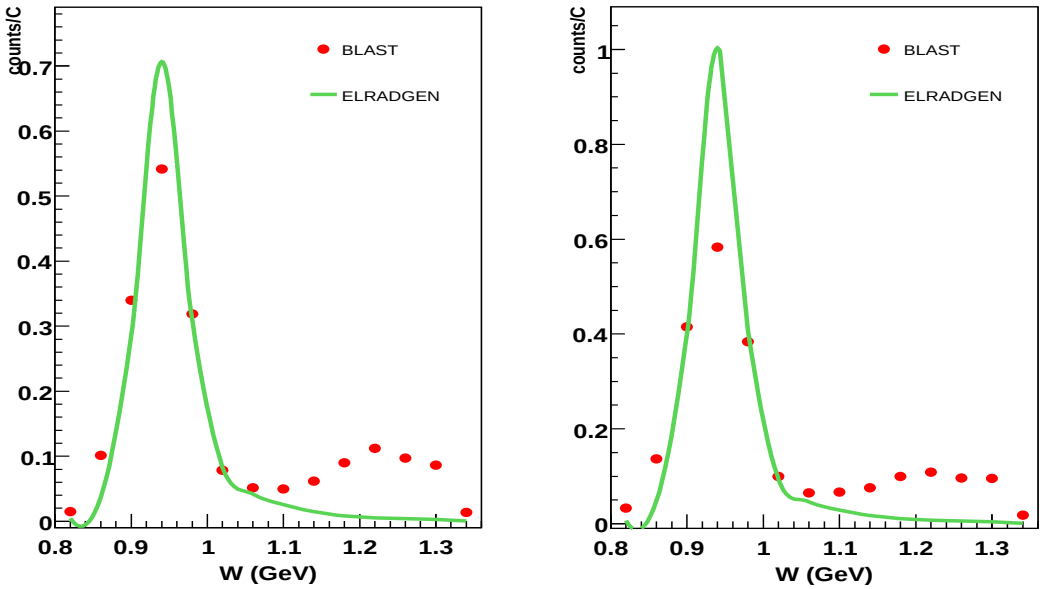

Figure 5-5: Normalized yields as a function of the invariant mass, W, for $Q^2 = 0.24\,GeV^2$. The dots show the BLAST ABS hydrogen data corrected for the background contributions, and the solid line represents the Monte Carlo simulations with radiative effects (polarized ELRADGEN). Left sector is on the left, right sector on the right.

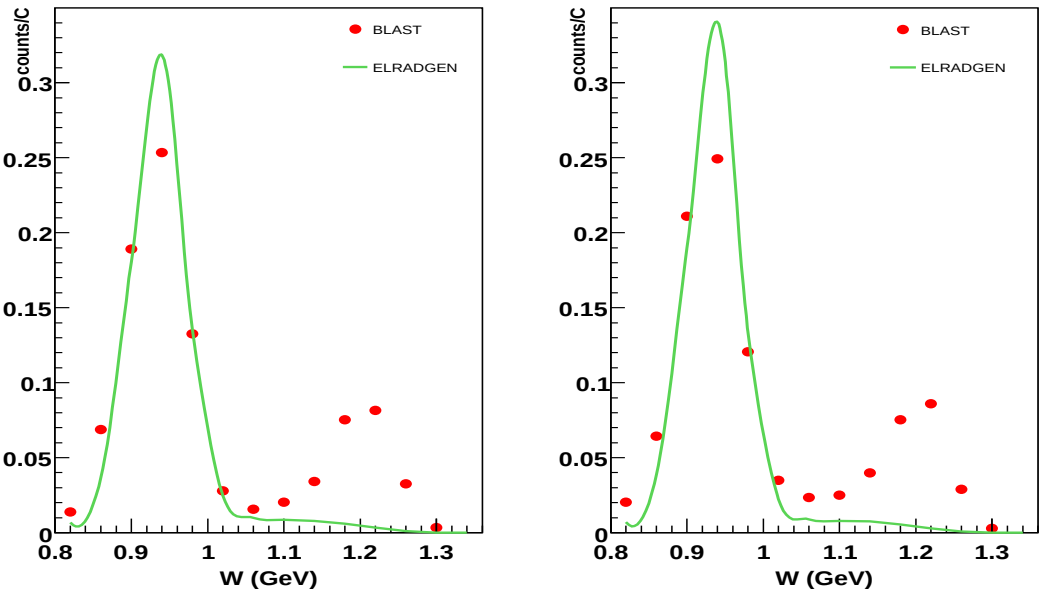

Figure 5-6: Normalized yields as a function of the invariant mass, W for $Q^2 = 0.312\,GeV^2$. The dots show the BLAST ABS hydrogen data corrected for the background contributions, and the solid line represents the Monte Carlo simulations with radiative effects (polarized ELRADGEN). Left sector is on the left, right sector on the right.

Using these measured rates (5.1), the measured asymmetry is given by:

$$A_{meas} = \frac{R^+ - R^-}{R^+ + R^-} \tag{5.2}$$

The extracted asymmetry, A, is related to the measured asymmetry by

$$A = \frac{A_{meas}}{P_b P_t} \tag{5.3}$$

where $P_b P_t$ is the beam-target polarization product, and for BLAST polarized hydrogen is $P_b P_t = 0.537$ [106, 103, 129]. The radiative effects to the extracted asymmetry are presented in Figure 5-7, where the asymmetries for both left and right sectors are shown with and without radiative corrections (for $0.08 < Q^2 < 0.38\,GeV^2$). The extracted asymmetry, A, for both left and right sectors is shown in Figures 5-8, 5-9, 5-10, 5-11, for different Q^2 values, using the standard cuts discussed in subsection 4.1.2.

We divided the momentum transfer squared interval in 4 bins, for the asymmetries and spin-correlation parameters as a function of the invariant mass, W. These bins are given in Table 5.1.

Q^2 bin	Q^2 range $[(GeV/c)^2]$	$< Q^2 >$ $[(GeV/c)^2]$
1	0.08 - 0.15	0.123
2	0.15 - 0.22	0.175
3	0.22 - 0.29	0.240
4	0.29 - 0.38	0.312

Table 5.1: The four Q^2 bins used in this analysis as a function of W.

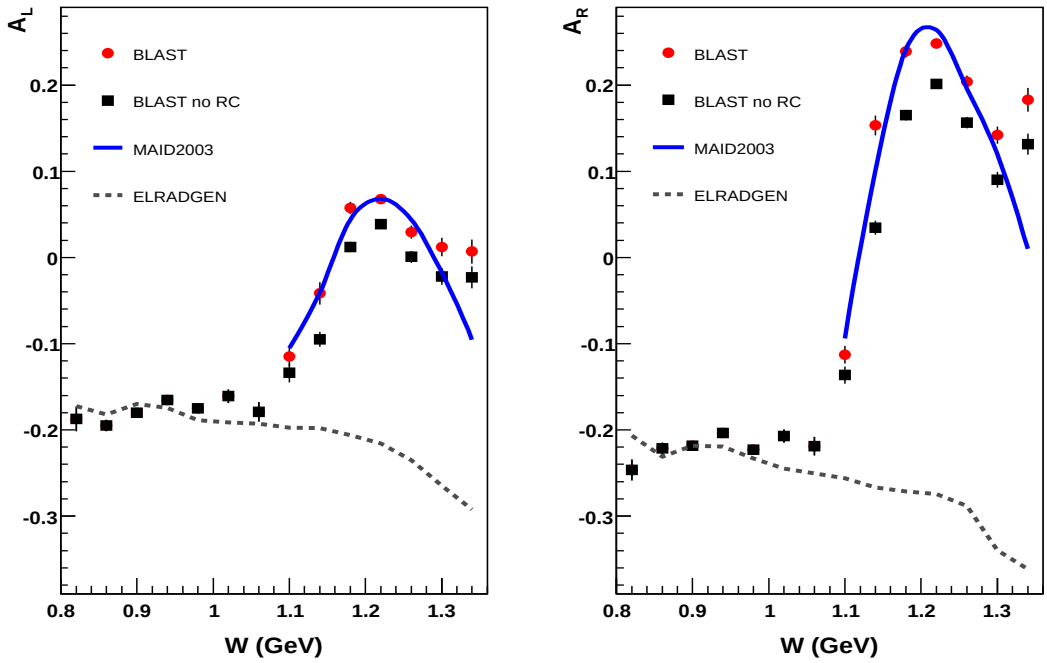

Figure 5-7: The effect of the radiative contributions to the asymmetry. The left (left) and right (right) asymmetries are shown with (red dots) and without (black squares) radiative corrections (RC), $0.08 < Q^2 < 0.38\,GeV^2$.

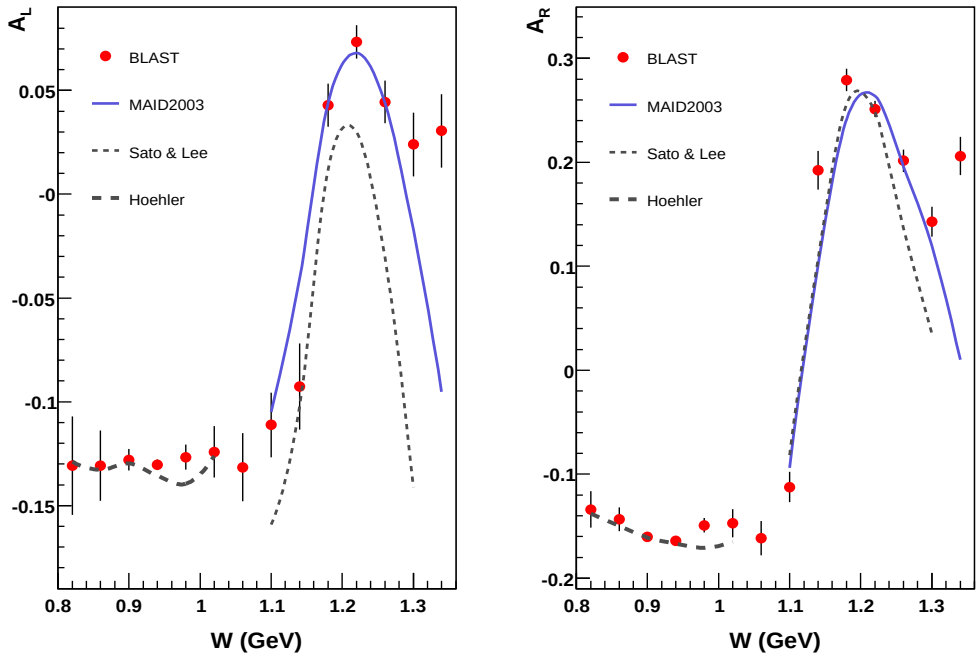

Figure 5-8: Extracted asymmetry, A, for left (left) and right (right) sectors as a function of invariant mass, W, and for $Q^2 = 0.123\,GeV^2$.

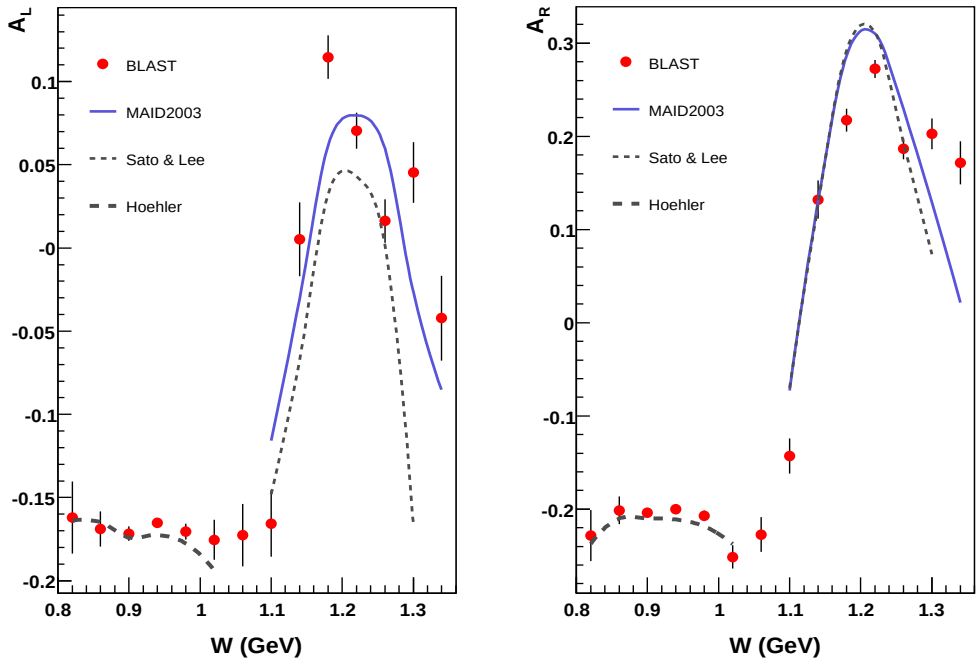

Figure 5-9: Extracted asymmetry, A, for left (left) and right (right) sectors as a function of invariant mass, W, and for $Q^2 = 0.175\,GeV^2$.

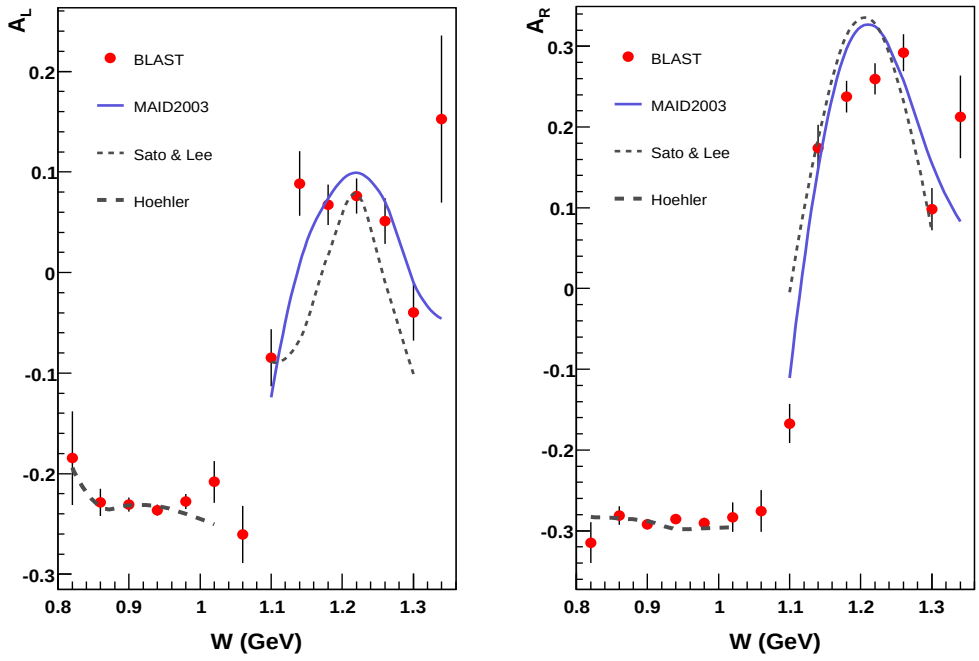

Figure 5-10: Extracted asymmetry, A, for left (left) and right (right) sectors as a function of invariant mass, W, and for $Q^2 = 0.24\,GeV^2$.

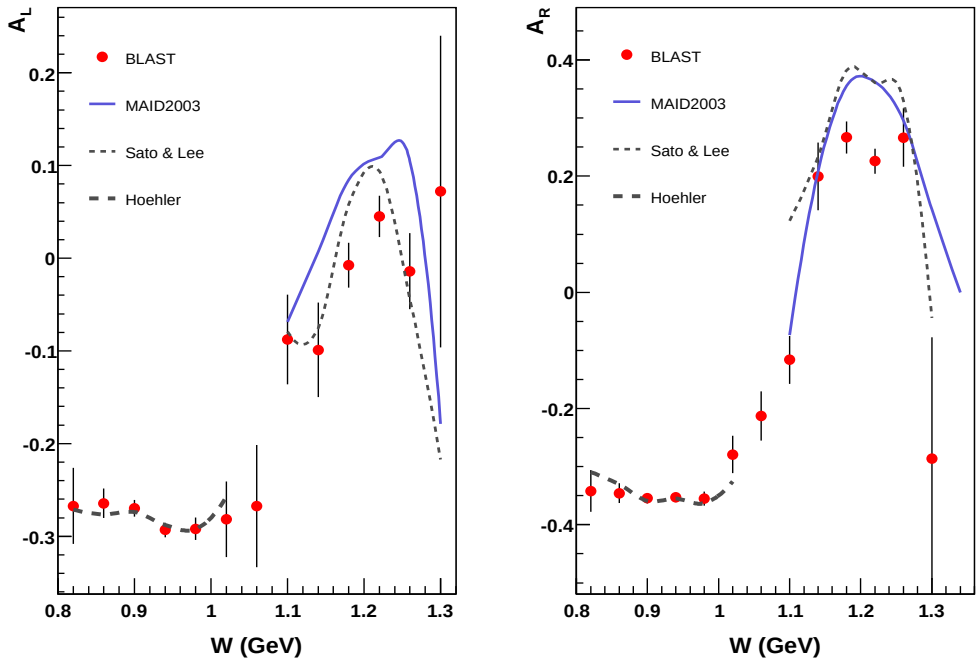

Figure 5-11: Extracted asymmetry, A, for left (left) and right (right) sectors as a function of invariant mass, W, and for $Q^2 = 0.312\,GeV^2$.

5.2 Spin Correlation Parameters

The spin-correlation parameters, $A_{TT'}$, $A_{TL'}$, are related to the extracted asymmetry, A by:

$$\begin{aligned} A &= \frac{\sigma_{P=+1} - \sigma_{P=-1}}{\sigma_{P=+1} + \sigma_{P=-1}} = \\ &= A_{TT'} \cos\theta^* + A_{TL'} \sin\theta^* \cos\phi^* \end{aligned} \tag{5.4}$$

where $\sigma_{P=\pm 1}$ is given in (2.35), and θ^*, ϕ^* are the target spin angle relative to $\mathbf{q}$ (see **Appendix B**).

For each left and right sector we get:

$$\begin{cases} A_L = A_{TT'} \cos\theta^*_L + A_{TL'} \sin\theta^*_L \cos\phi^*_L = A_{TT'}\, z^*_L + A_{TL'}\, x^*_L \\ A_R = A_{TT'} \cos\theta^*_R + A_{TL'} \sin\theta^*_R \cos\phi^*_R = A_{TT'}\, z^*_R + A_{TL'}\, x^*_R \end{cases} \tag{5.5}$$

where $z^*_{L,R} = \cos\theta^*_{L,R}$ and $x^*_{L,R} = \sin\theta^*_{L,R}\cos\phi^*_{L,R}$ are the target spin angle projections in the $q-$ system (axes u_x and u_z in Figure 2-2). From the left and right asymmetries we extract the spin-correlation parameters:

$$A_{TT'} = \frac{A_L x^*_R - A_R x^*_L}{x^*_R z^*_L - x^*_L z^*_R} \tag{5.6}$$

$$A_{TL'} = \frac{A_R z^*_L - A_L z^*_R}{x^*_R z^*_L - x^*_L z^*_R} \tag{5.7}$$

The spin correlation parameters, $A_{TT'}$, $A_{TL'}$ are shown in Figures 5-12, 5-13, 5-14, 5-15, using the standard cuts (subsection 4.1.2). For each bin in $A_{L,R}$, using the standard cuts (Table 4.2), we histogram each of $x^*_{L,R}$, $z^*_{L,R}$, and $\epsilon_{L,R}$ and then get their mean values (given in **Appendices D, E**). These values are used in the extraction of the spin-correlation parameters ($x^*_{L,R}$, $z^*_{L,R}$) and the partial cross-sections ($\epsilon_{L,R}$), together with the left and right asymmetries (A_L, A_R). Using the relation between the correlation parameters, $A_{TT'}$, $A_{TL'}$, and the partial cross sections, $\sigma_{TT'}$, $\sigma_{TL'}$ given in (2.36) we get the ratios $\sigma_{TT'}/\sigma_0$, $\sigma_{TL'}/\sigma_0$, where $\sigma_0 = \sigma_T + \epsilon\sigma_L$, is the total unpolarized cross-section (spin-independent). These ratios are given in Figures 5-16, 5-17, 5-18, 5-19.

5.3 Electric and Coulomb Quadrupole Strength Extraction

The spin-correlation parameters, $A_{TT'}$ and $A_{TL'}$ are used to extract the electric and coulomb quadrupole strengths, $E2$ and $C2$ respectively, in the $\gamma N\Delta$ transition, by optimizing the agreement between the data and the model predictions for different quadrupole strengths using the least square method [95, 130]. We used the MAID model [1, 21] for this extraction. In this model the standard values are given by $E2/M1_{std.} = -2.2\,\%$ and $C2/M1_{std.} = -6.5\,\%$. In the first step we vary $E2$ from $E2 = 1\,\%$ to $E2 = 6\,\%$, and we keep $M1$ and $C2$ to their standard values. The second step, we vary $C2$ from $C2 = 1\,\%$ to $C2 = 6\,\%$, and we keep $M1$ and $E2$ fixed to their standard values.

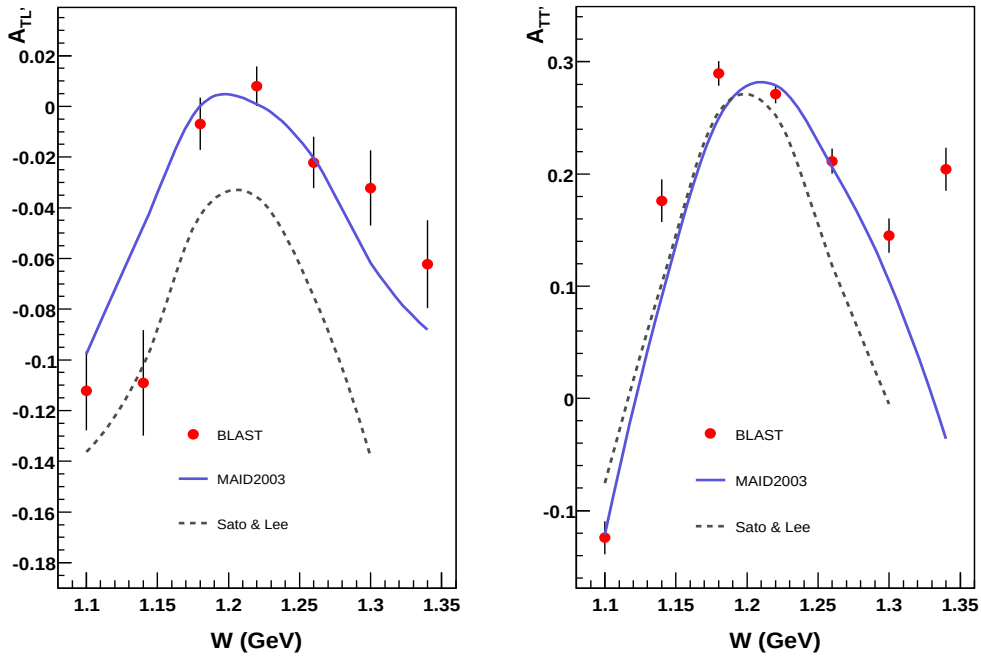

Figure 5-12: Spin correlation parameters, $A_{TT'}$, $A_{TL'}$, as a function of invariant mass, W, and for $Q^2 = 0.123\,GeV^2$.

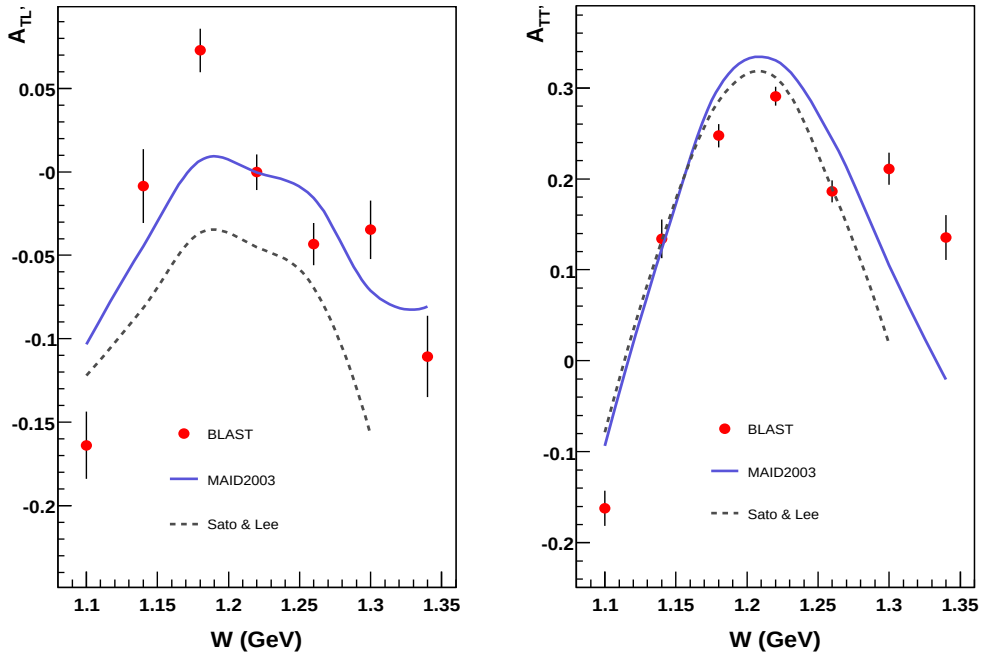

Figure 5-13: Spin correlation parameters, $A_{TT'}$, $A_{TL'}$, as a function of invariant mass, W, and for $Q^2 = 0.175\,GeV^2$.

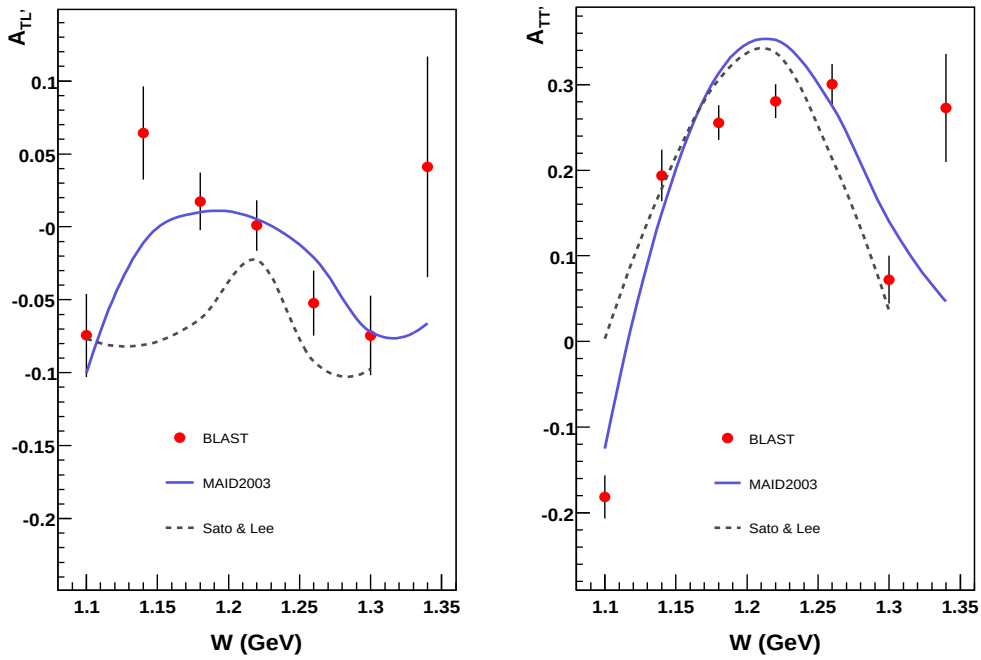

Figure 5-14: Spin correlation parameters, $A_{TT'}$, $A_{TL'}$, as a function of invariant mass, W, and for $Q^2 = 0.24\,GeV^2$.

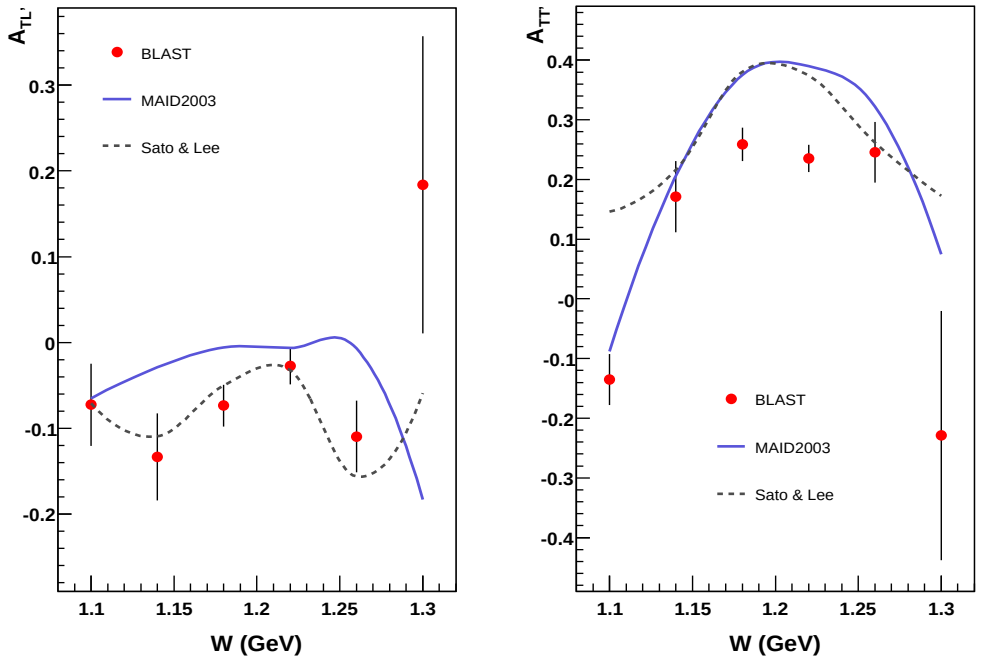

Figure 5-15: Spin correlation parameters, $A_{TT'}$, $A_{TL'}$, as a function of invariant mass, W, and for $Q^2 = 0.312\,GeV^2$.

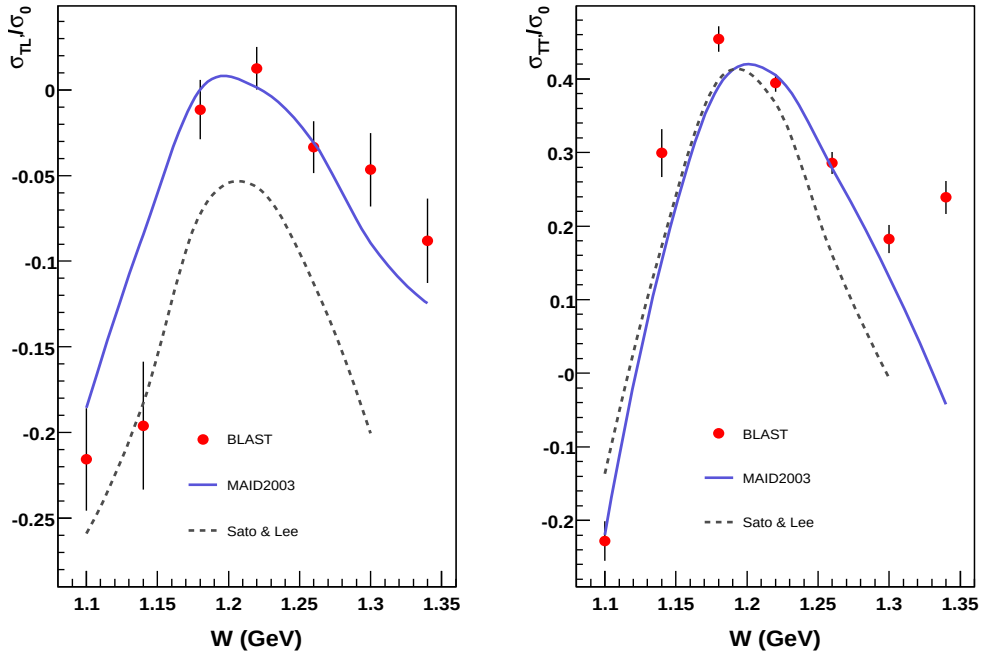

Figure 5-16: The ratios $\sigma_{TT'}/\sigma_0$, $\sigma_{TL'}/\sigma_0$, as a function of invariant mass, W, and for $Q^2 = 0.123\,GeV^2$.

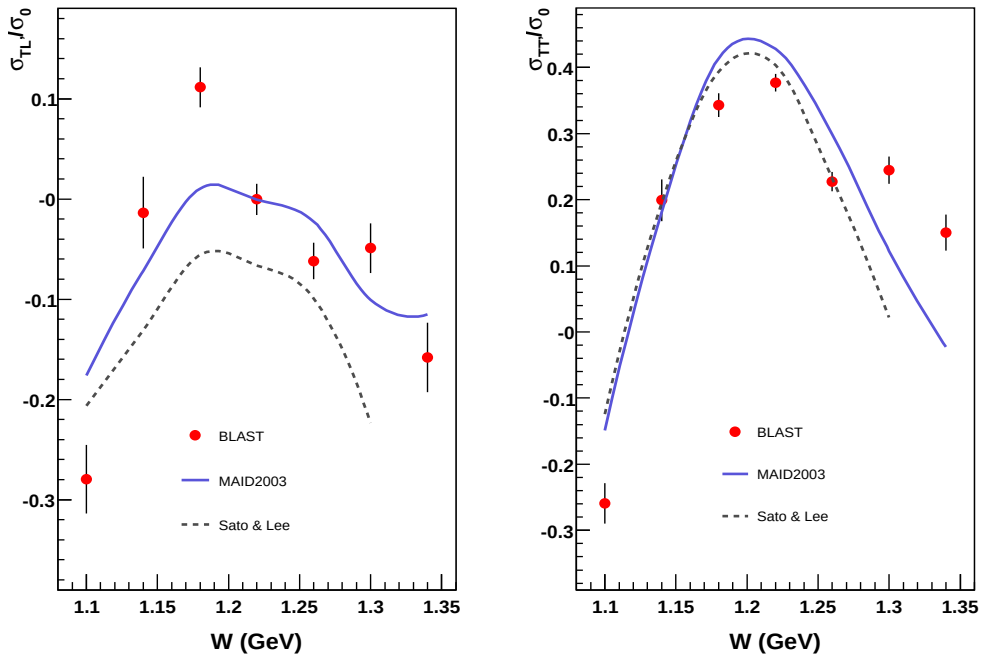

Figure 5-17: The ratios $\sigma_{TT'}/\sigma_0$, $\sigma_{TL'}/\sigma_0$, as a function of invariant mass, W, and for $Q^2 = 0.175\,GeV^2$.

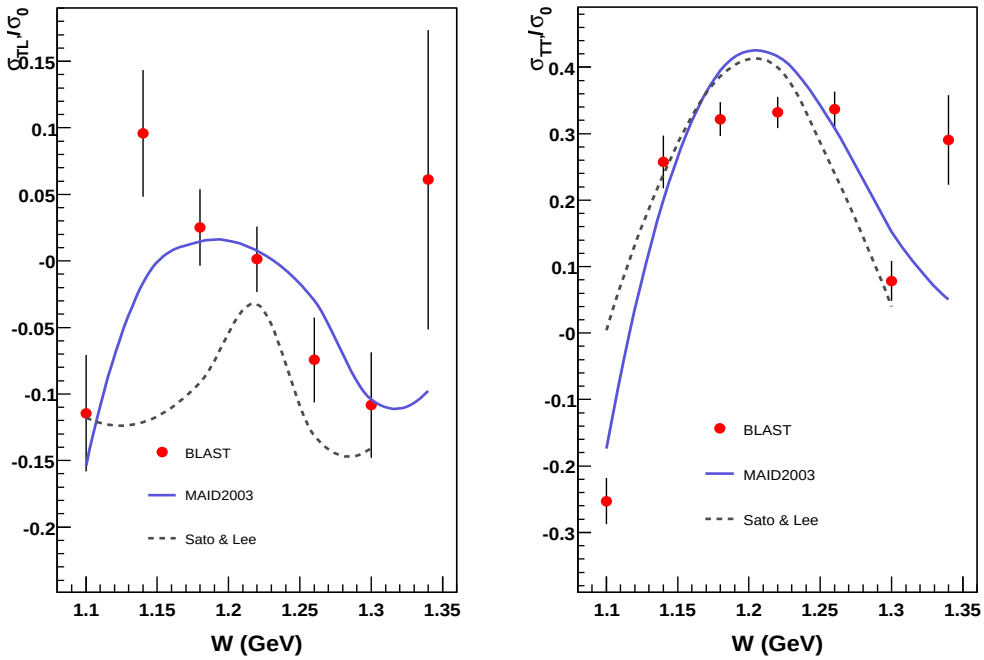

Figure 5-18: The ratios $\sigma_{TT'}/\sigma_0$, $\sigma_{TL'}/\sigma_0$, as a function of invariant mass, W, and for $Q^2 = 0.24\,GeV^2$.

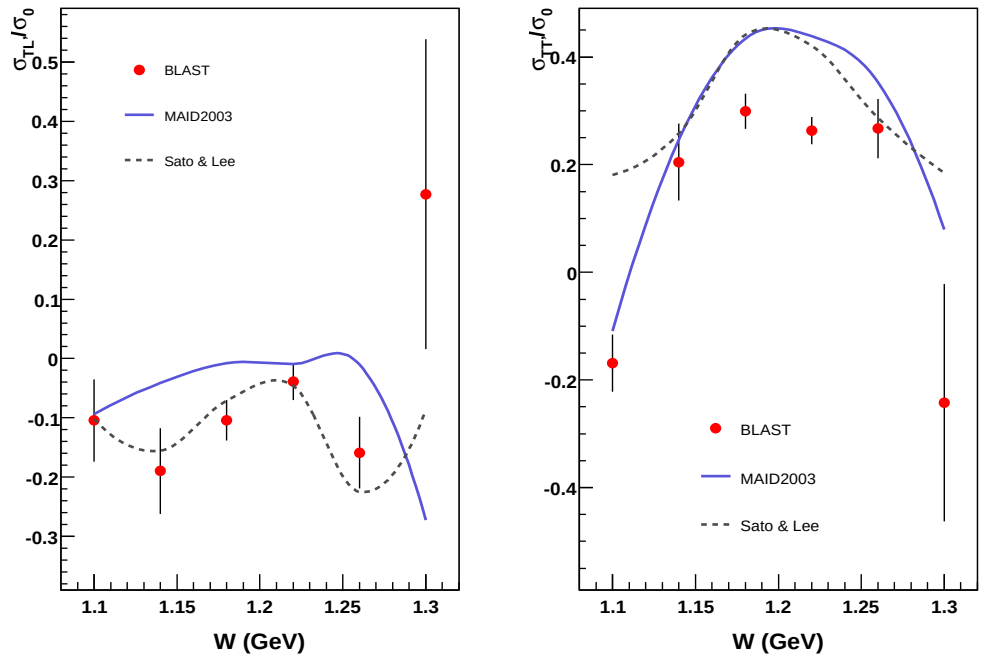

Figure 5-19: The ratios $\sigma_{TT'}/\sigma_0$, $\sigma_{TL'}/\sigma_0$, as a function of invariant mass, W, and for $Q^2 = 0.312\,GeV^2$.

For this extraction, we used the three bins around the delta peak, W = 1.184, 1.22, 1.258 GeV, where the maximum predicted values have been obtained for $A_{TL'}$ and $A_{TT'}$. A χ^2 is calculated as follows:

$$\chi^2 = \frac{1}{3}\sum_{k=1}^{3}\frac{(f_k^{DATA} - f_k^{MAID})^2}{\sigma_k^2} \tag{5.8}$$

where the summation over k runs over the three points mentioned above, $f_k^{DATA} = A_{TT'}, A_{TL'}$ are the BLAST results, σ_k represents the statistical and systematic errors of the data points. The spin-correlation parameters results, using the MAID model, are given in Figures 5-20, 5-21, 5-22, 5-23, 5-24, 5-25, 5-26, 5-27, for the four Q^2 bins (Table 5.1).

The results for the minimization procedure are given in Table 5.2 and shown in Figures 5-28 and 5-29, as a function of Q^2 $[(GeV/c)^2]$, relative to their standard values in the MAID model.

Q^2 $[GeV^2]$	$E2/M1$ [%]	$C2/M1$ [%]
0.123	-2.10 ± 0.018 (*stat.*) ± 0.246 (*syst.*)	-5.89 ± 0.015 (*stat.*) ± 0.994 (*syst.*)
0.175	-2.09 ± 0.017 (*stat.*) ± 0.291 (*syst.*)	-6.45 ± 0.017 (*stat.*) ± 0.761 (*syst.*)
0.240	-2.05 ± 0.034 (*stat.*) ± 0.253 (*syst.*)	-6.49 ± 0.031 (*stat.*) ± 0.838 (*syst.*)
0.312	-2.03 ± 0.057 (*stat.*) ± 0.178 (*syst.*)	-5.83 ± 0.048 (*stat.*) ± 0.747 (*syst.*)

Table 5.2: Extracted $E2/M1$, $C2/M1$ [%] using the MAID model, for each Q^2 bin (Table 5.1).

This analysis shows that the electric, $E2$, and coulomb, $C2$, quadrupole strengths of the $\gamma N\Delta$ transition can be extracted in an elegant way in the case of inclusive scattering of polarized electrons from polarized protons. In the exclusive scattering, besides E_{1+} and S_{1+}, other multipoles interfere with M_{1+}, whereas, in the inclusive scattering, only the E_{1+} and S_{1+} multipoles interfere with the dominating M_{1+} multipole.

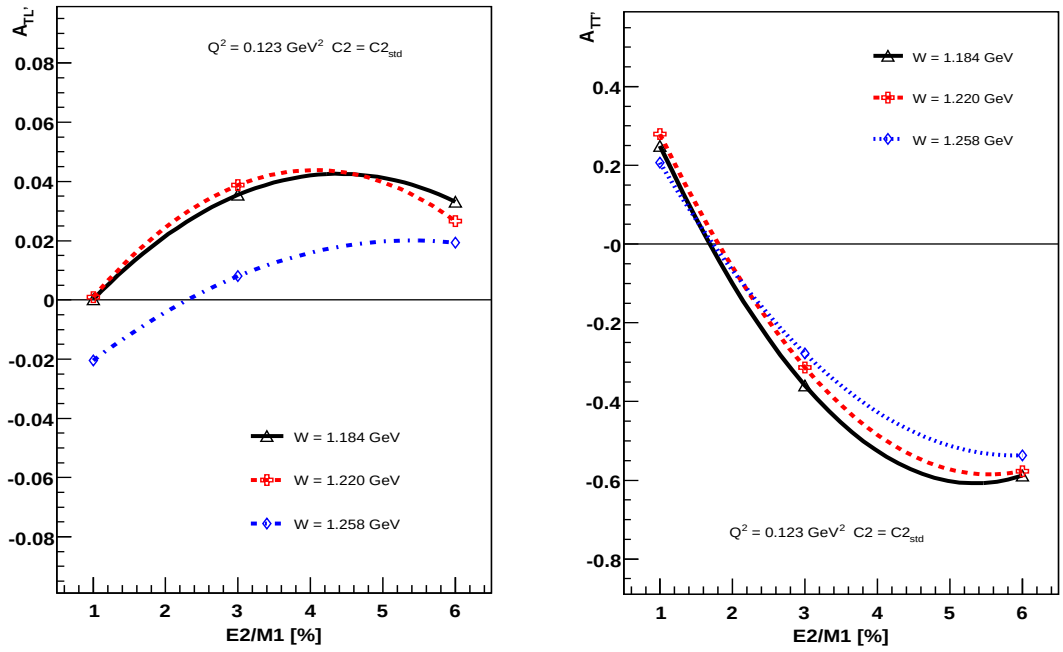

Figure 5-20: Dependence of the spin-correlation parameters, $A_{TL'}$ and $A_{TT'}$, on the $E2$ quadrupole strength for $Q^2 = 0.123\,GeV^2$, in the MAID model.

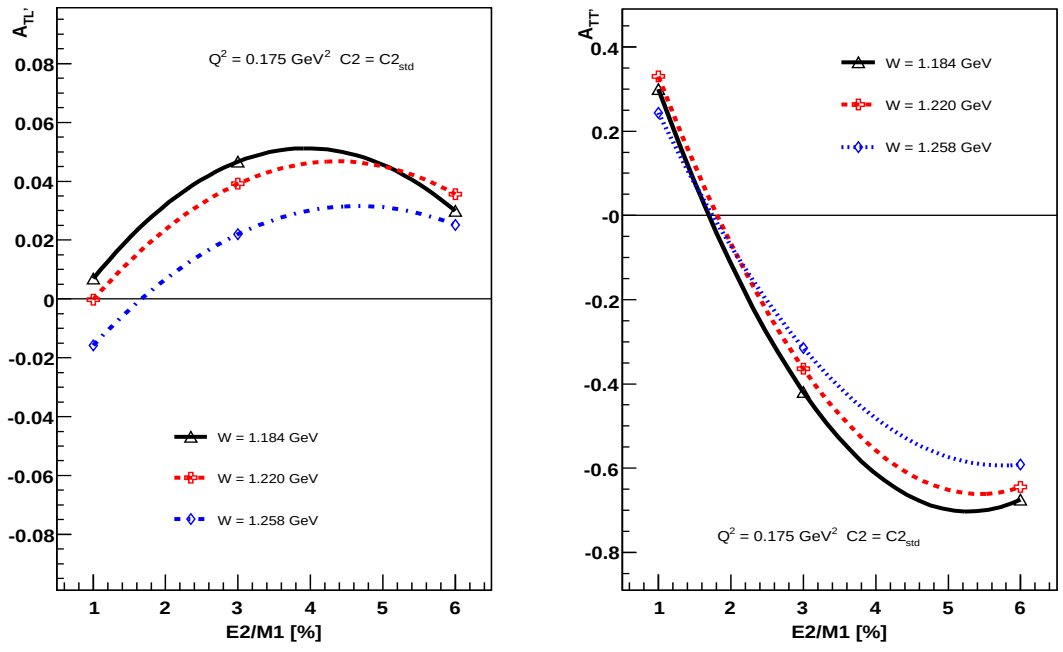

Figure 5-21: Dependence of the spin-correlation parameters, $A_{TL'}$ and $A_{TT'}$, on the $E2$ quadrupole strength for $Q^2 = 0.175\,GeV^2$, in the MAID model.

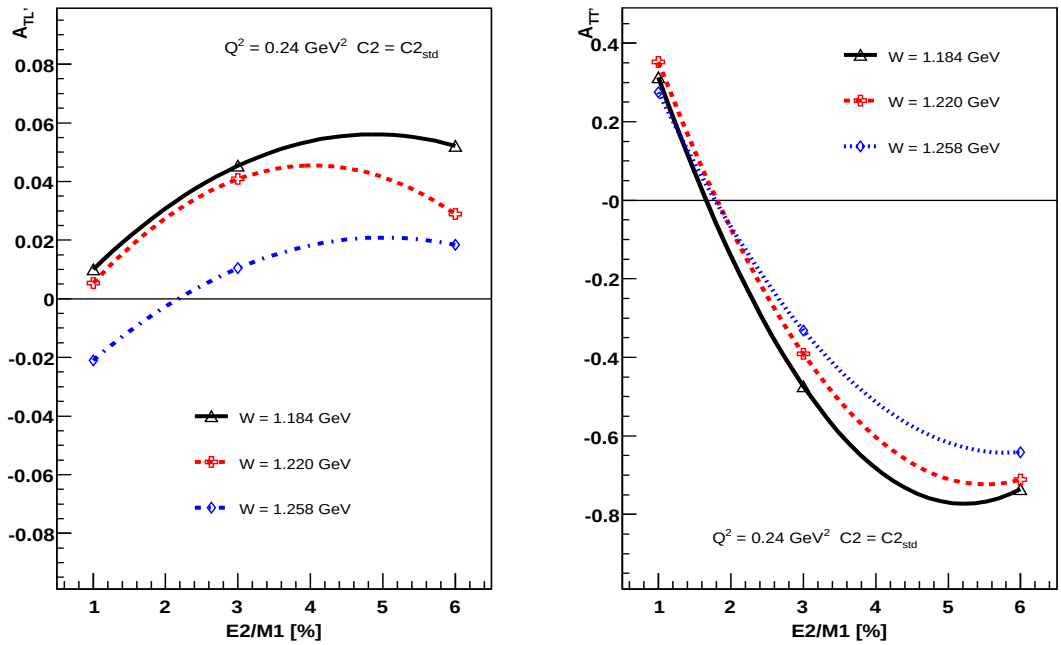

Figure 5-22: Dependence of the spin-correlation parameters, $A_{TL'}$ and $A_{TT'}$, on the $E2$ quadrupole strength for $Q^2 = 0.24\,GeV^2$, in the MAID model.

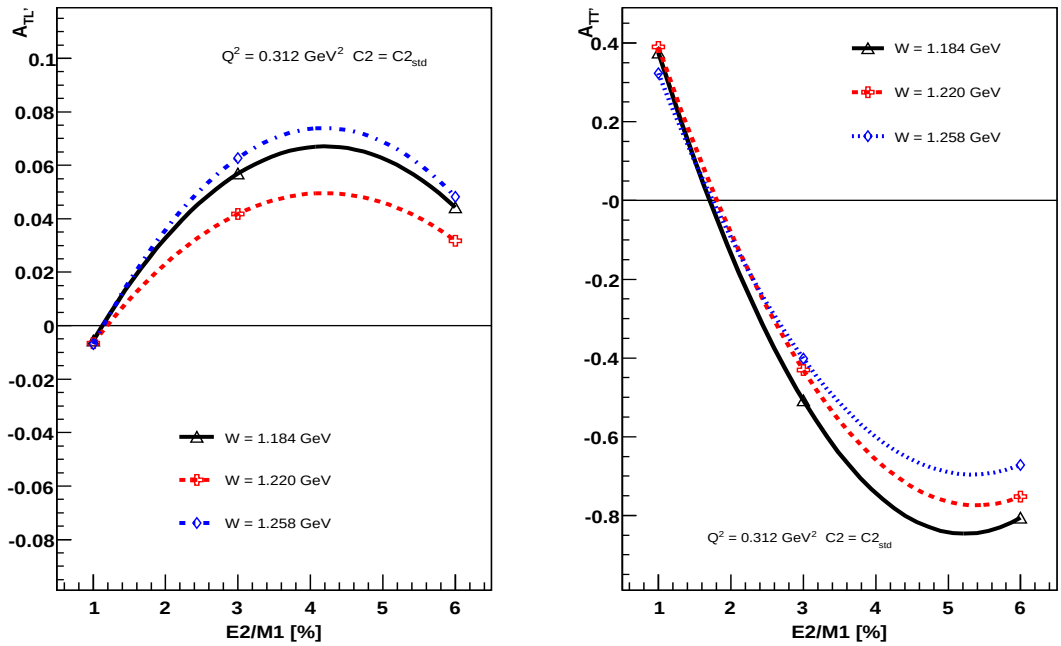

Figure 5-23: Dependence of the spin-correlation parameters, $A_{TL'}$ and $A_{TT'}$, on the $E2$ quadrupole strength for $Q^2 = 0.312\,GeV^2$, in the MAID model.

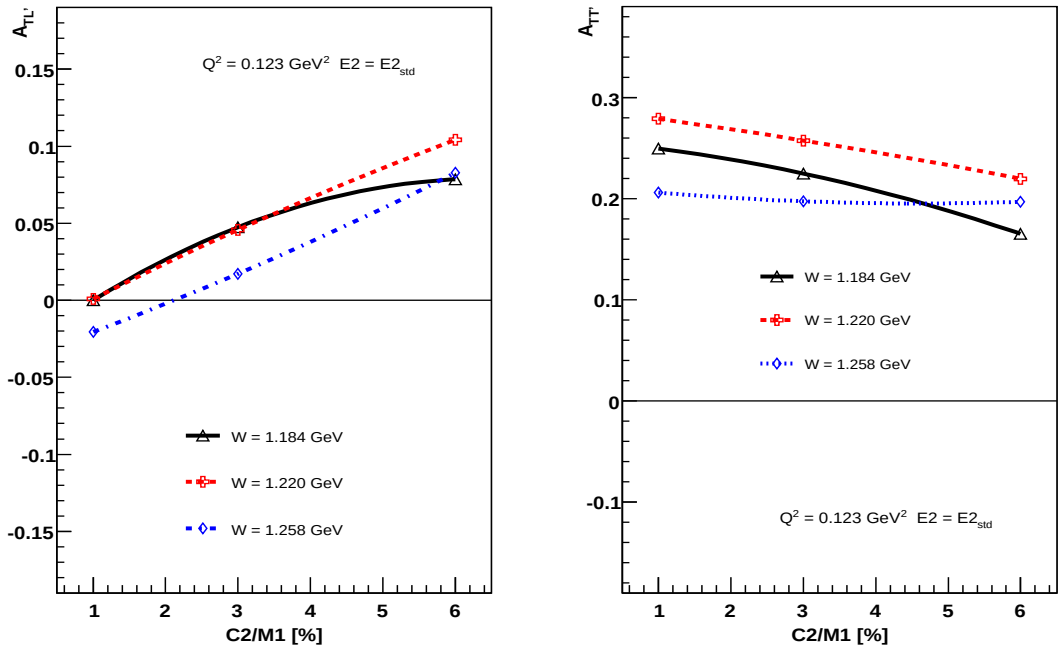

Figure 5-24: Dependence of the spin-correlation parameters, $A_{TL'}$ and $A_{TT'}$, on the $C2$ quadrupole strength for $Q^2 = 0.123\,GeV^2$, in the MAID model.

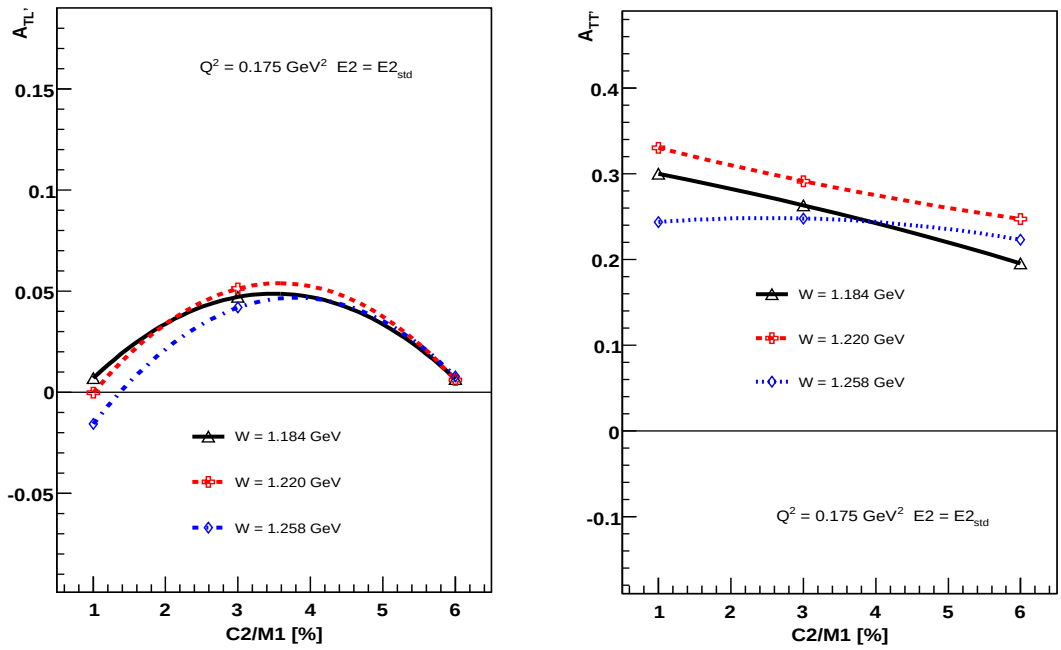

Figure 5-25: Dependence of the spin-correlation parameters, $A_{TL'}$ and $A_{TT'}$, on the $C2$ quadrupole strength for $Q^2 = 0.175\,GeV^2$, in the MAID model.

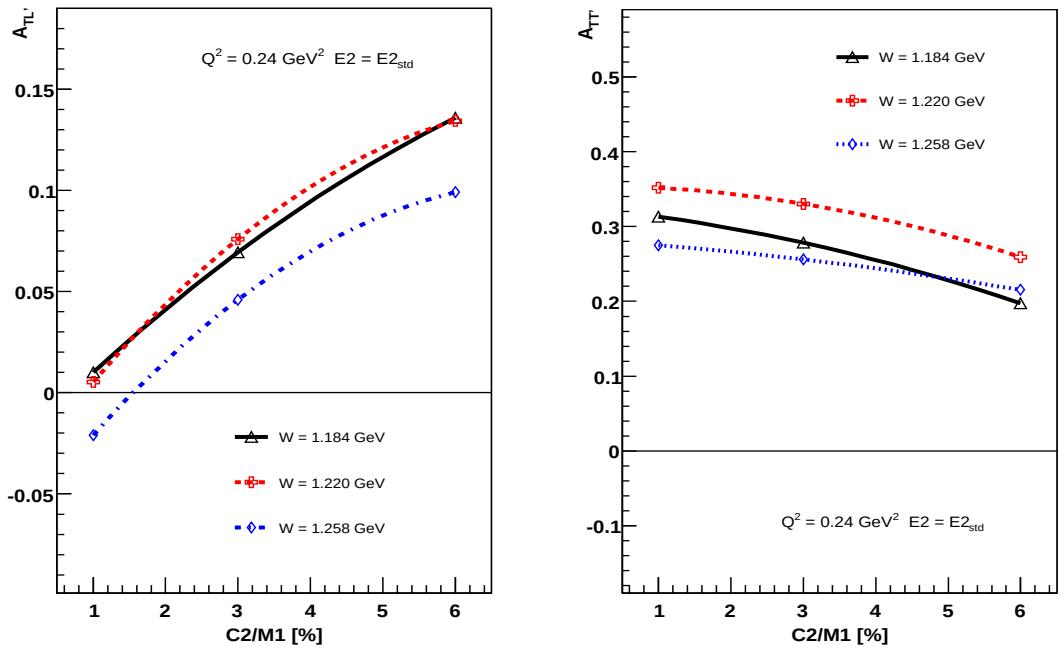

Figure 5-26: Dependence of the spin-correlation parameters, $A_{TL'}$ and $A_{TT'}$, on the $C2$ quadrupole strength for $Q^2 = 0.24\,GeV^2$, in the MAID model.

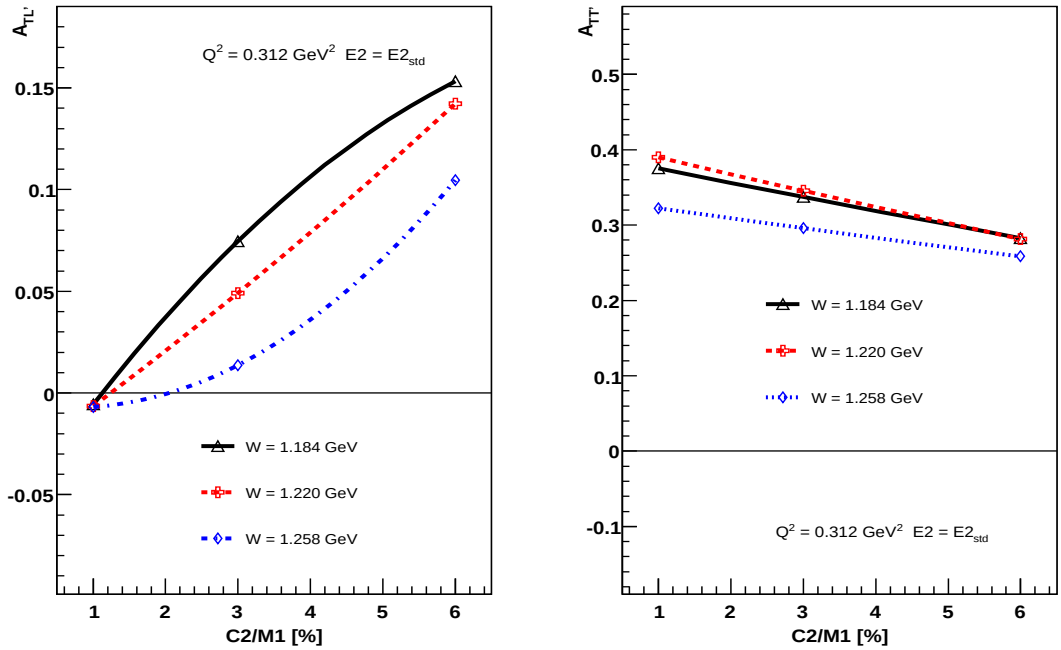

Figure 5-27: Dependence of the spin-correlation parameters, $A_{TL'}$ and $A_{TT'}$, on the $C2$ quadrupole strength for $Q^2 = 0.312\,GeV^2$, in the MAID model.

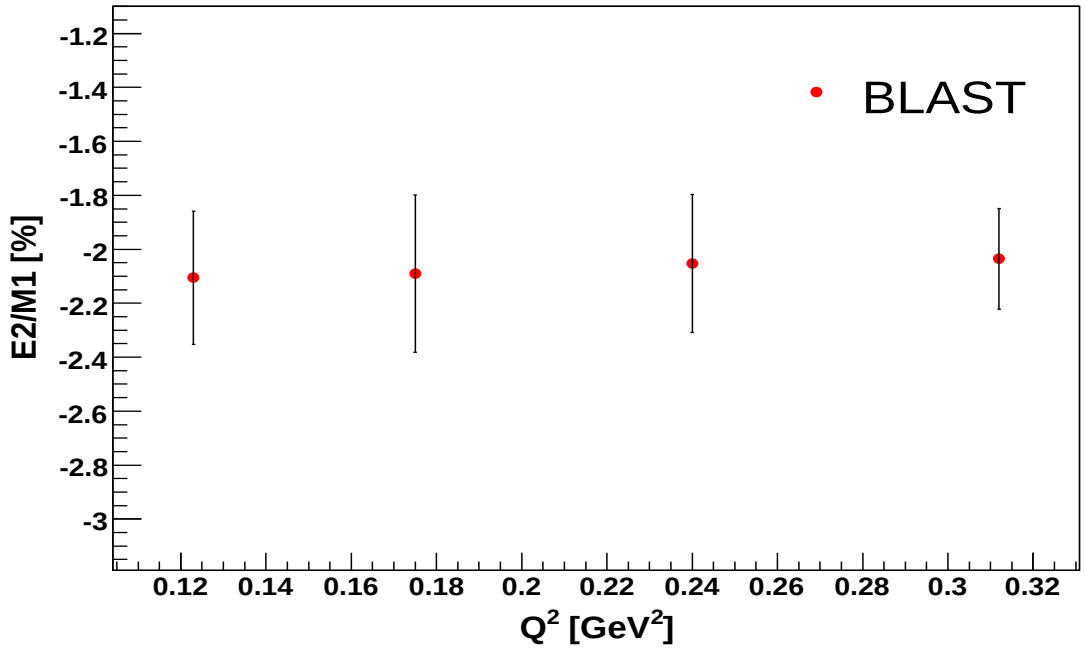

Figure 5-28: Extracted $E2$ quadrupole strength as a function of Q^2 $[(GeV/c)^2]$, using the MAID model.

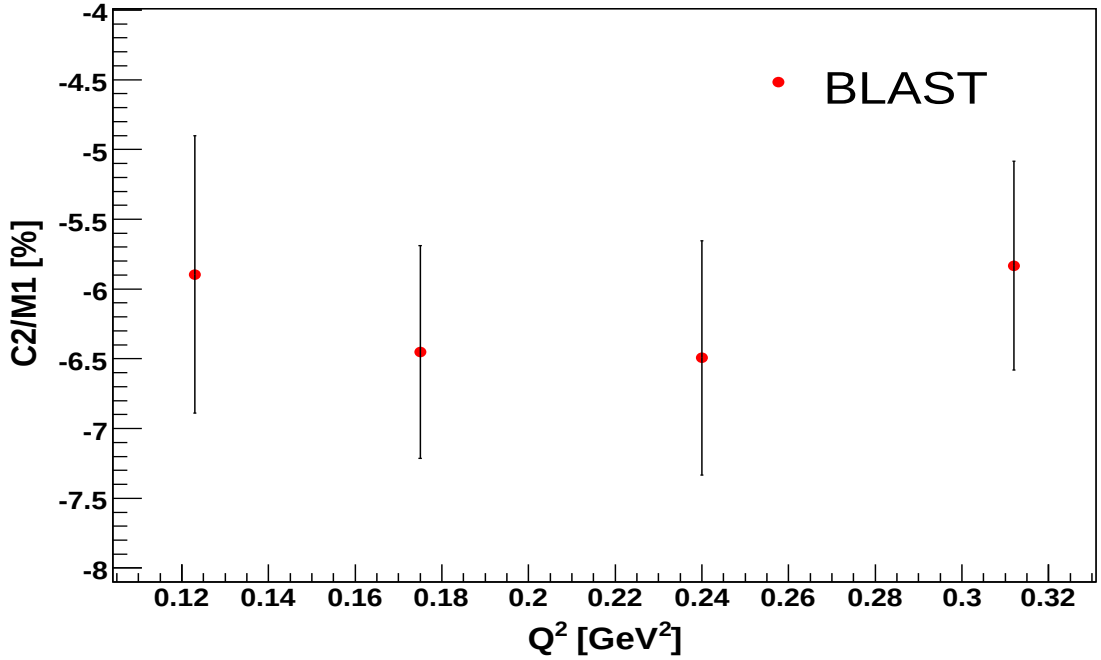

Figure 5-29: Extracted $C2$ quadrupole strength as a function of Q^2 $[(GeV/c)^2]$, using the MAID model.

5.4 Spin Structure Functions

The partial cross sections, $\sigma_{TT'}$ and $\sigma_{TL'}$ are related to the spin structure functions, g_1 and g_2, depending on $x = Q^2/2M_p\omega$ and Q^2, and these relations are given by [21]

$$\sigma_{TL'} = -\frac{4\pi^2\alpha}{M_pK}\gamma(g_1 + g_2) \tag{5.9}$$

$$\sigma_{TL'} = -\frac{4\pi^2\alpha}{M_pK}(g_1 - \gamma^2 g_2) \tag{5.10}$$

where $\gamma = Q/\omega$, $\omega = E_e - E_{e'}$, and K is the "equivalent photon energy", i.e. the laboratory energy required by a real photon to excite the $\pi - p$ system to an invariant mass. The conventional choice for K is known as Hand's convention [26] and is given by

$$K = K_H = \frac{W^2 - M^2}{2M} = \omega(1 - x) \tag{5.11}$$

where M is the nucleon mass, in this case proton, M_p. Solving (5.9) for $g_{1,2}$ we get the spin structure functions

$$g_1(Q^2, x) = -\frac{MK}{4\pi^2\alpha}\frac{\gamma\sigma_{TL'} + \sigma_{TT'}}{1 + \gamma^2} \tag{5.12}$$

$$g_2(Q^2, x) = -\frac{MK}{4\pi^2\alpha}\frac{\frac{1}{\gamma}\sigma_{TL'} - \sigma_{TT'}}{1 + \gamma^2} \tag{5.13}$$

The spin-structure functions, g_1 and g_2, depend on both x and Q^2. Hence the asymmetries are extracted as a function of these quantities, then the spin-correlation parameters, the partial cross sections and finally the spin-structure functions, by using the mean value of the histograms for K and γ for each (Q^2, W) bin. The radiative contributions are shown in Figures 5-30, 5-31, 5-32, 5-33, and 5-34. The extracted asymmetries are given in Figures 5-35, 5-36, 5-37, 5-38, and 5-39. The extracted spin structure functions are presented in Figures 5-40, 5-41, 5-42, 5-43, and 5-44, as a function of Q^2 and x.

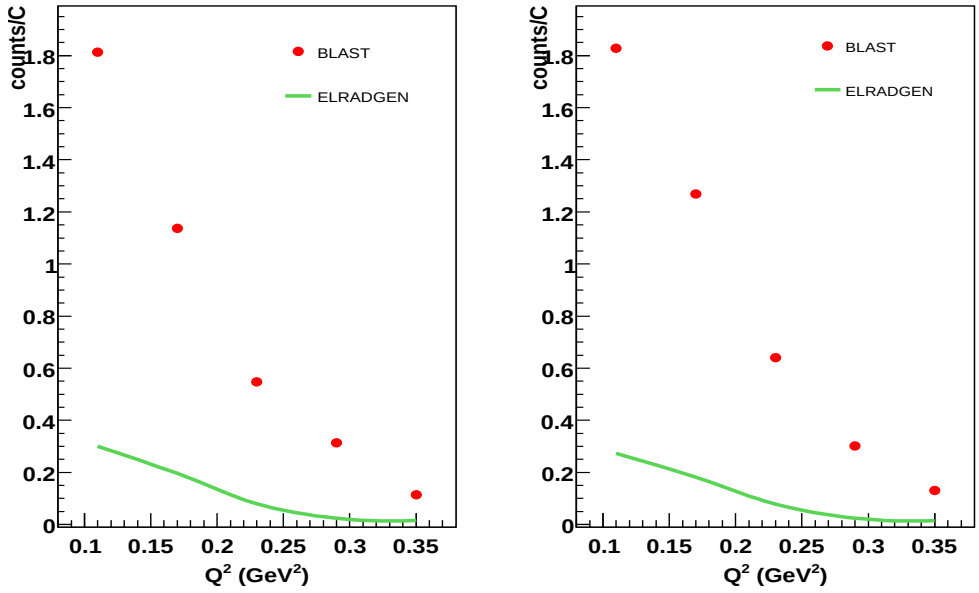

Figure 5-30: Normalized yields as a function of the momentum transfer squared Q^2 in the Δ region ($1.1 < W < 1.36\,GeV$), and for $x \in [0.08, 0.48]$. The dots show the BLAST ABS hydrogen data corrected for the background contributions, and the line shows the Monte Carlo radiative effects. Left sector is on the left, right sector on the right.

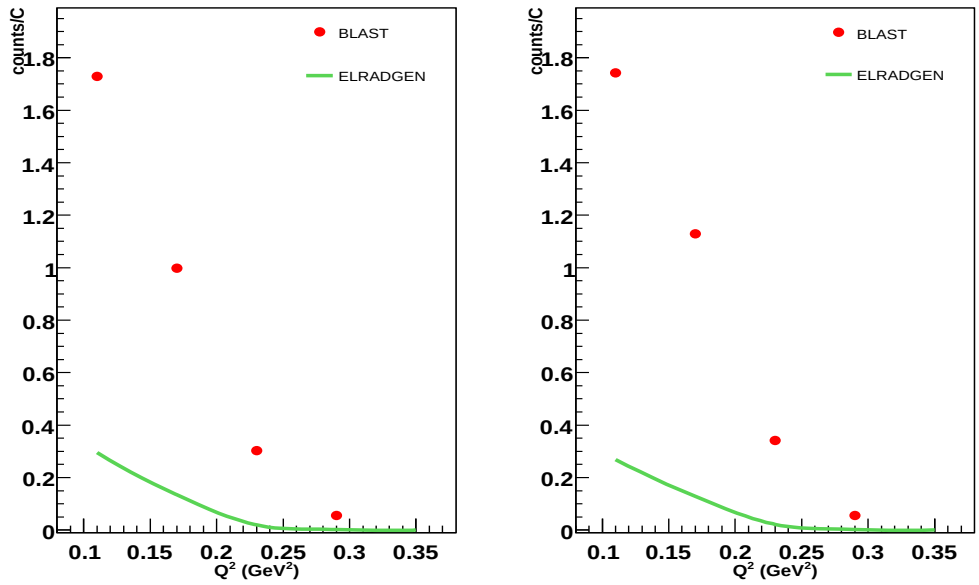

Figure 5-31: Normalized yields as a function of the momentum transfer squared Q^2 in the Δ region ($1.1 < W < 1.36\,GeV$), and for $x \in [0.08, 0.28]$. The dots show the BLAST ABS hydrogen data corrected for the background contributions, and the line shows the Monte Carlo radiative effects. Left sector is on the left, right sector on the right.

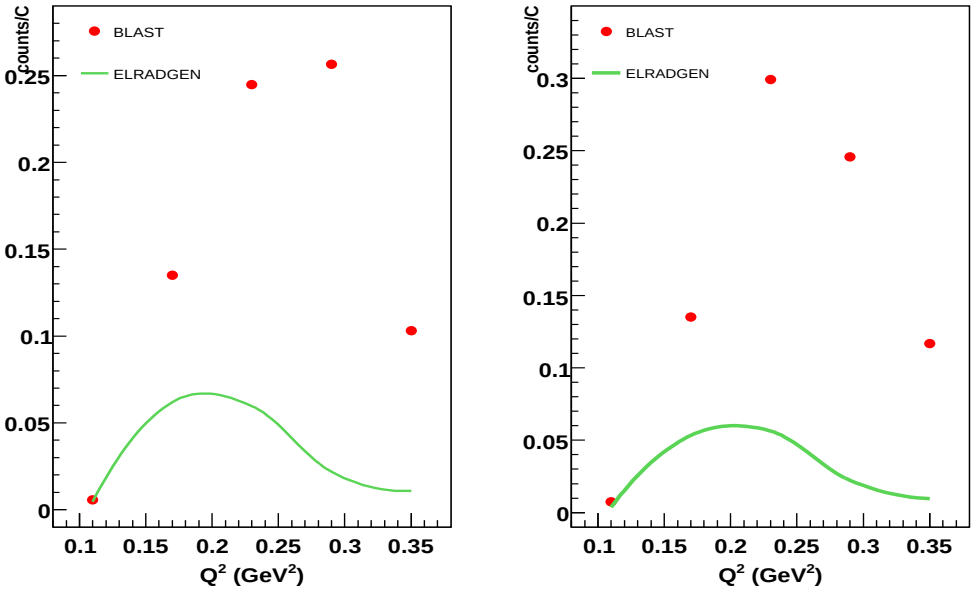

Figure 5-32: Normalized yields as a function of the momentum transfer squared Q^2 in the Δ region ($1.1 < W < 1.36\,GeV$), and for $x \in [0.28, 0.48]$. The dots show the BLAST ABS hydrogen data corrected for the background contributions, and the line shows the Monte Carlo radiative effects. Left sector is on the left, right sector on the right.

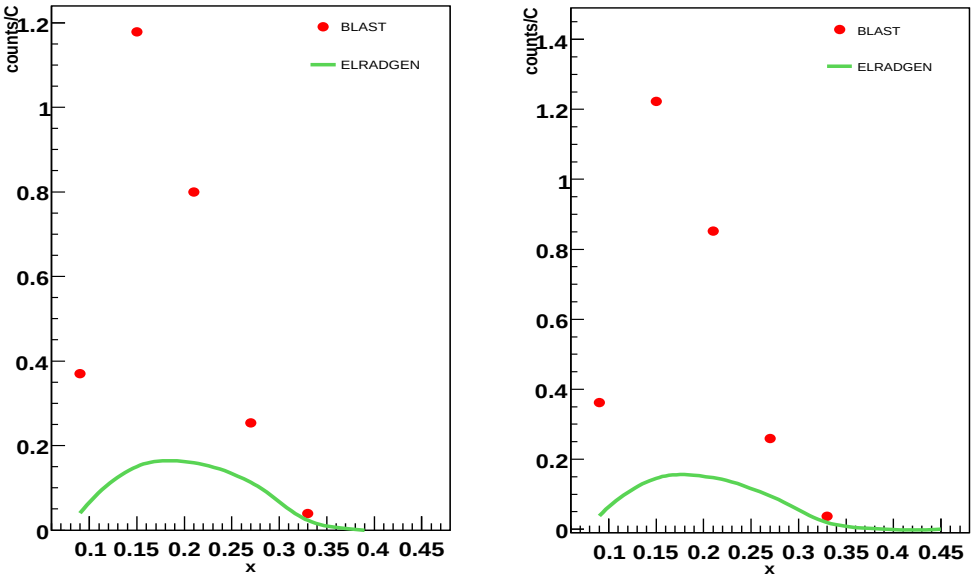

Figure 5-33: Normalized yields as a function of the Bjorken scaling variable x in the Δ region ($1.1 < W < 1.36\,GeV$), and for $Q^2 \in [0.08, 0.18]\,GeV^2$. The dots show the BLAST ABS hydrogen data corrected for the background contributions, and the line shows the Monte Carlo radiative effects. Left sector is on the left, right sector on the right.

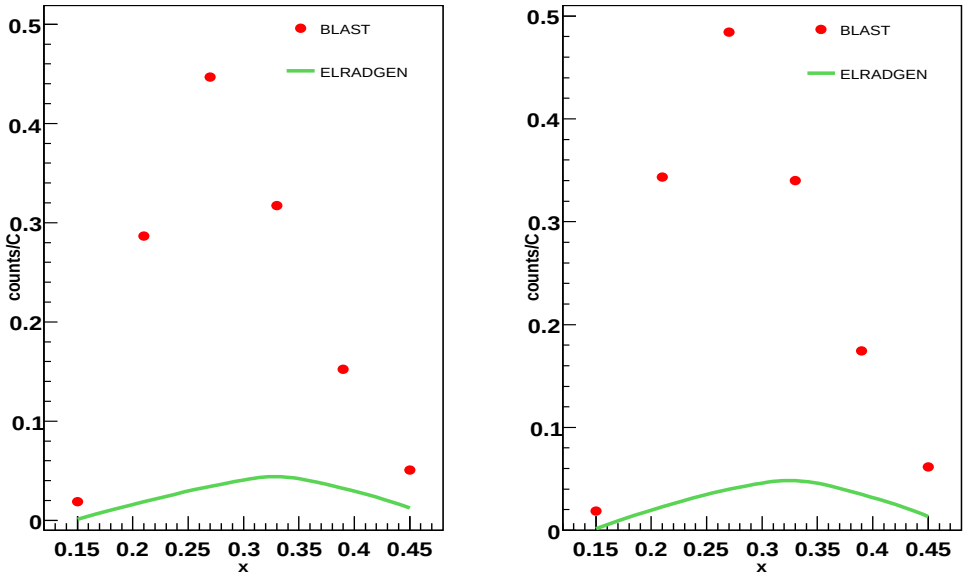

Figure 5-34: Normalized yields as a function of the Bjorken scaling variable x in the Δ region ($1.1 < W < 1.36\,GeV$), and for $Q^2 \in [0.18, 0.38]\,GeV^2$. The dots show the BLAST ABS hydrogen data corrected for the background contributions, and the line shows the Monte Carlo radiative effects. Left sector is on the left, right sector on the right.

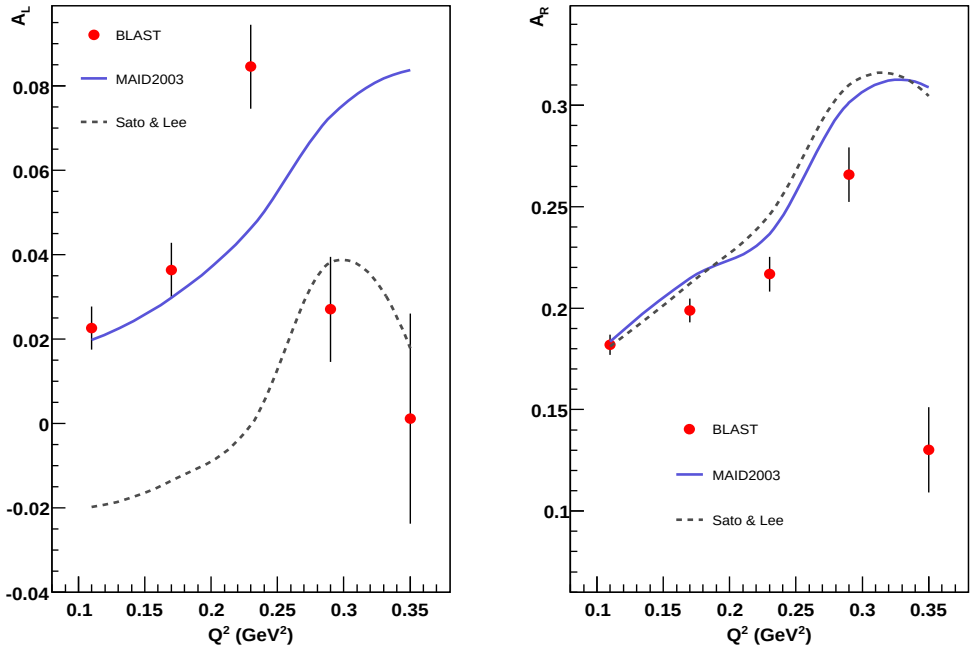

Figure 5-35: Extracted asymmetry, A, for left (left) and right (right) sectors as a function of $Q^2\,[GeV^2]$ in the Δ region ($1.1 < W < 1.36\,GeV$) and for $x \in [0.08, 0.48]$.

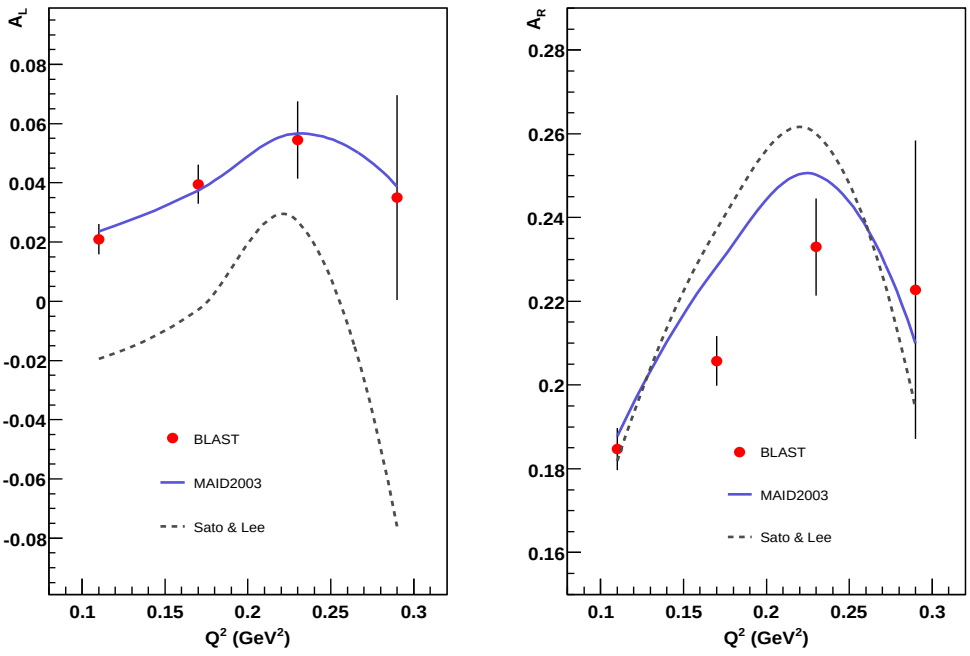

Figure 5-36: Extracted asymmetry, A, for left (left) and right (right) sectors as a function of $Q^2\,[GeV^2]$ in the Δ region $(1.1 < W < 1.36\,GeV)$ and for $x \in [0.08, 0.28]$.

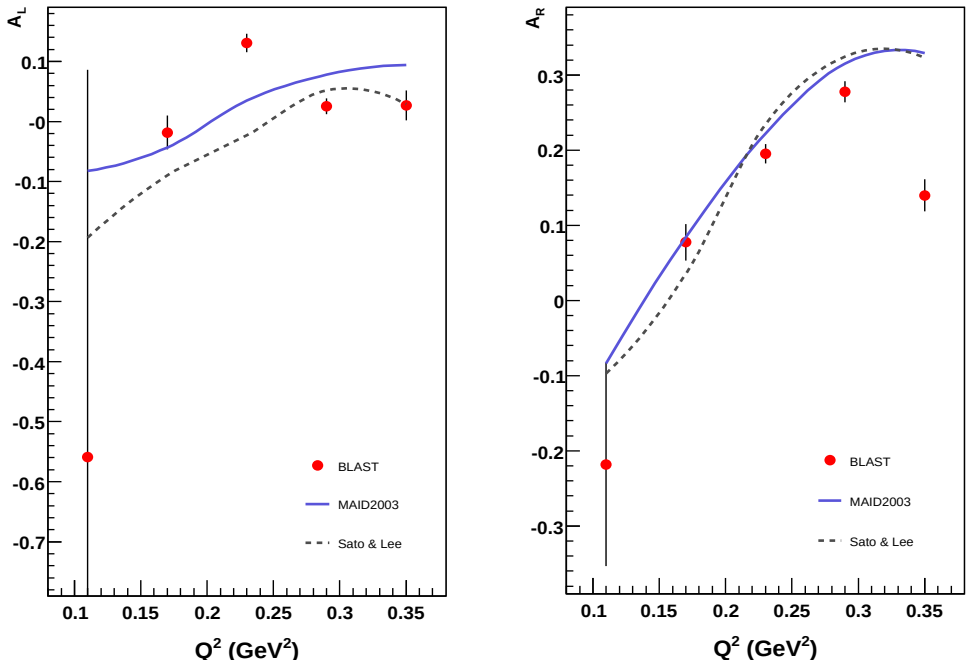

Figure 5-37: Extracted asymmetry, A, for left (left) and right (right) sectors as a function of $Q^2\,[GeV^2]$ in the Δ region $(1.1 < W < 1.36\,GeV)$ and for $x \in [0.28, 0.48]$.

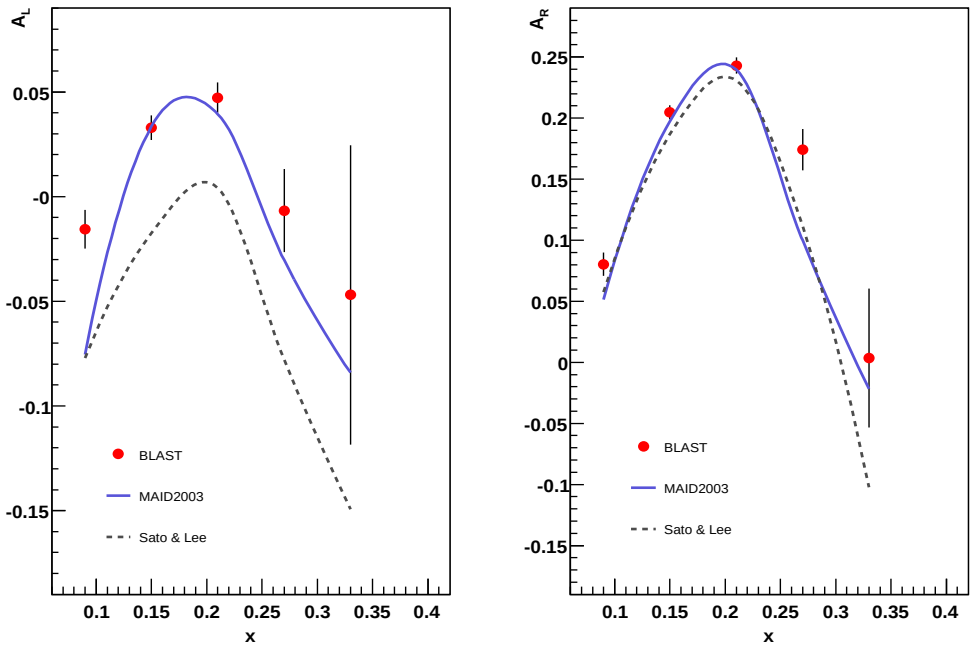

Figure 5-38: Extracted asymmetry, A, for left (left) and right (right) sectors as a function of x, in the Δ region ($1.1 < W < 1.36\,GeV$), and for $Q^2 \in [0.08, 0.18]\,GeV^2$.

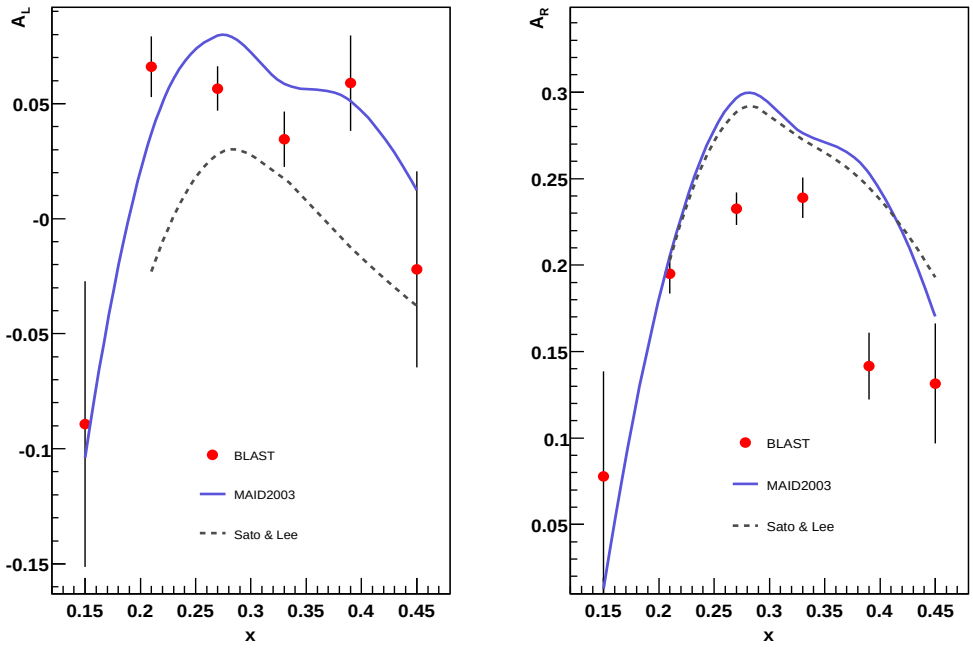

Figure 5-39: Extracted asymmetry, A, for left (left) and right (right) sectors as a function of x, in the Δ region ($1.1 < W < 1.36\,GeV$), and for $Q^2 \in [0.18, 0.38]\,GeV^2$.

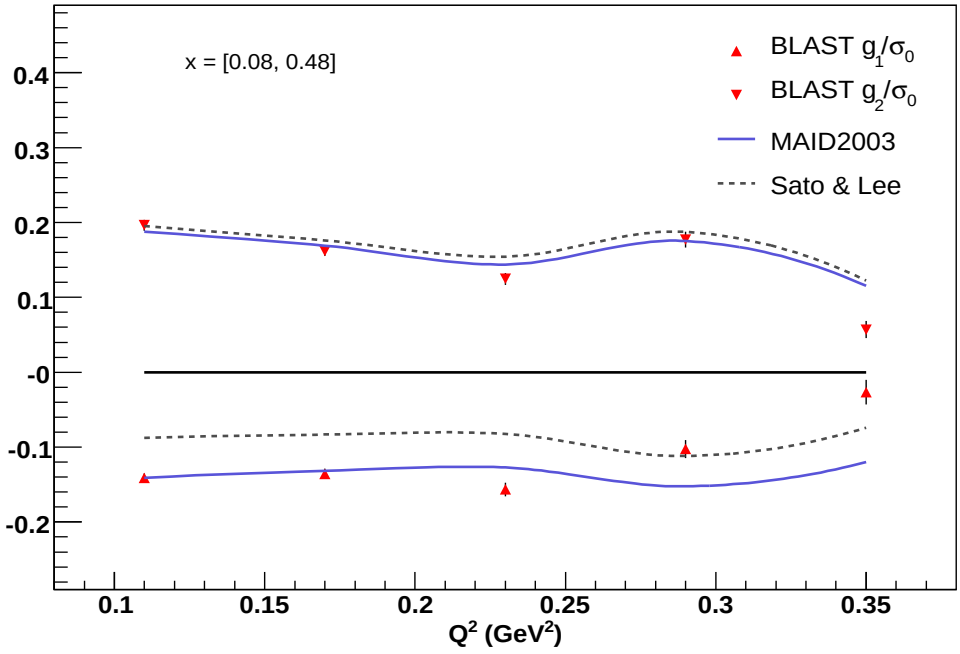

Figure 5-40: The spin-structure functions, g_1/σ_0 and g_2/σ_0 as a function of $Q^2[GeV^2]$ in the Δ region ($1.1 < W < 1.36\,GeV$), and for $x \in [0.08, 0.48]$, $\langle x \rangle = 0.21$, using Hand's convention.

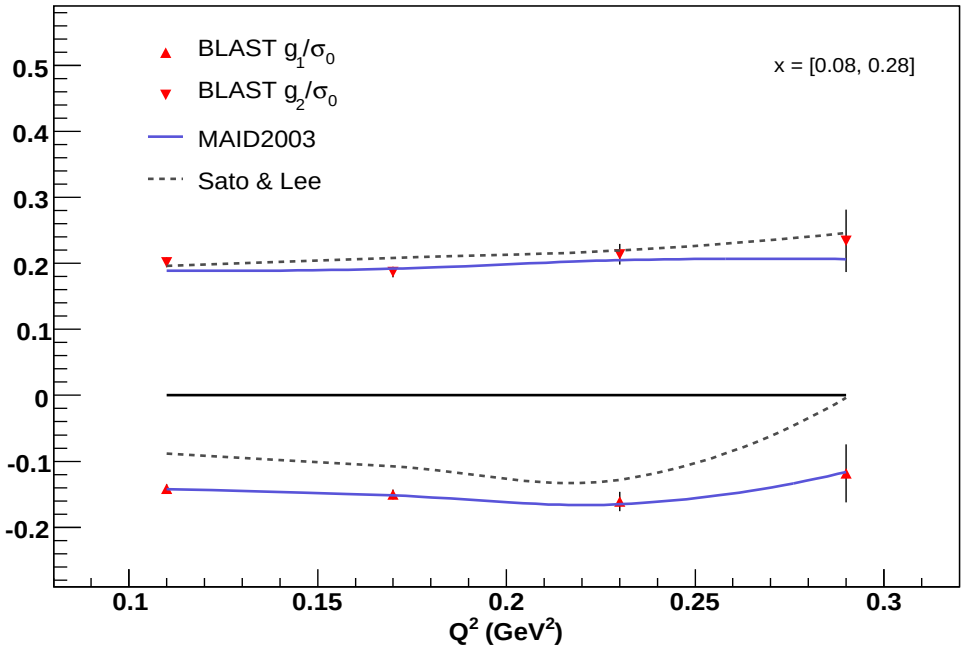

Figure 5-41: The spin-structure functions, g_1/σ_0 and g_2/σ_0 as a function of $Q^2[GeV^2]$ in the Δ region ($1.1 < W < 1.36\,GeV$), and for $x \in [0.08, 0.28]$, $\langle x \rangle = 0.185$, using Hand's convention.

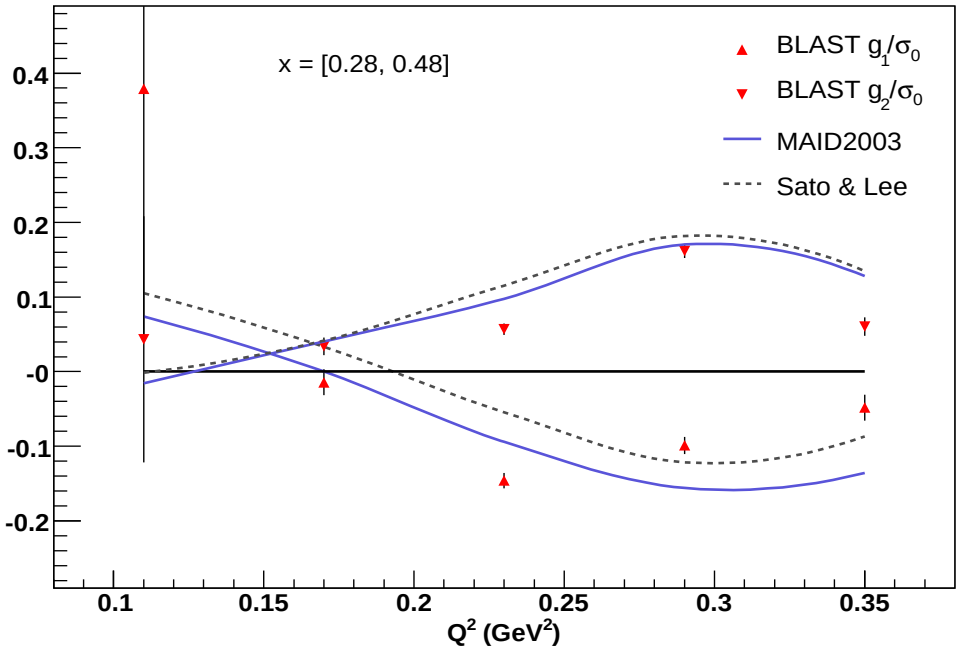

Figure 5-42: The spin-structure functions, g_1/σ_0 and g_2/σ_0 as a function of $Q^2[GeV^2]$ in the Δ region ($1.1 < W < 1.36\,GeV$), and for $x \in [0.28, 0.48]$, $\langle x \rangle = 0.32$, using Hand's convention.

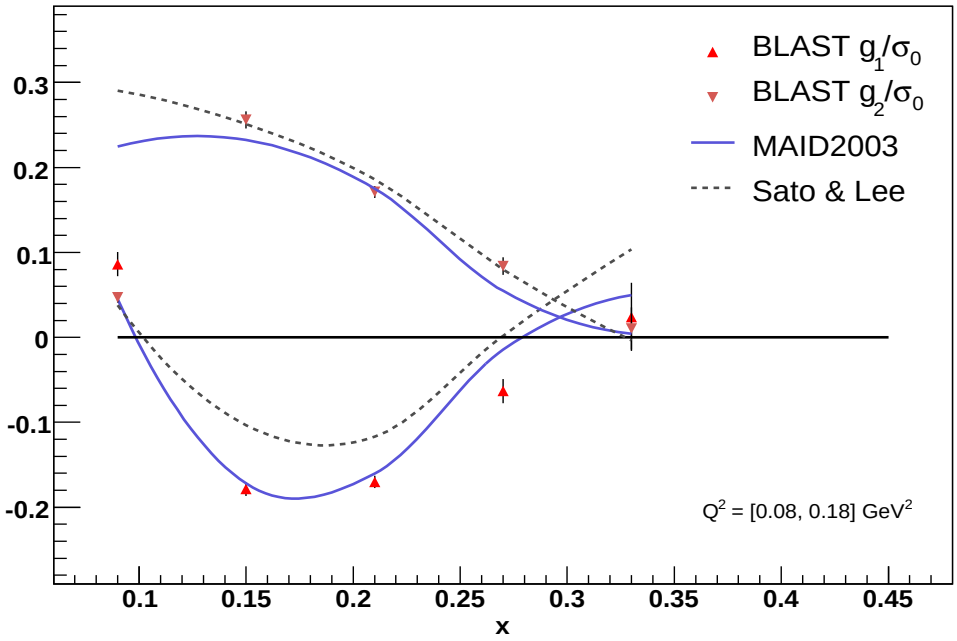

Figure 5-43: The spin-structure functions, g_1/σ_0 and g_2/σ_0 as a function of x in the Δ region ($1.1 < W < 1.36\,GeV$), and for $0.08 < Q^2 < 0.18\,GeV^2$, $\langle Q^2 \rangle = 0.129\,[GeV^2]$, using Hand's convention.

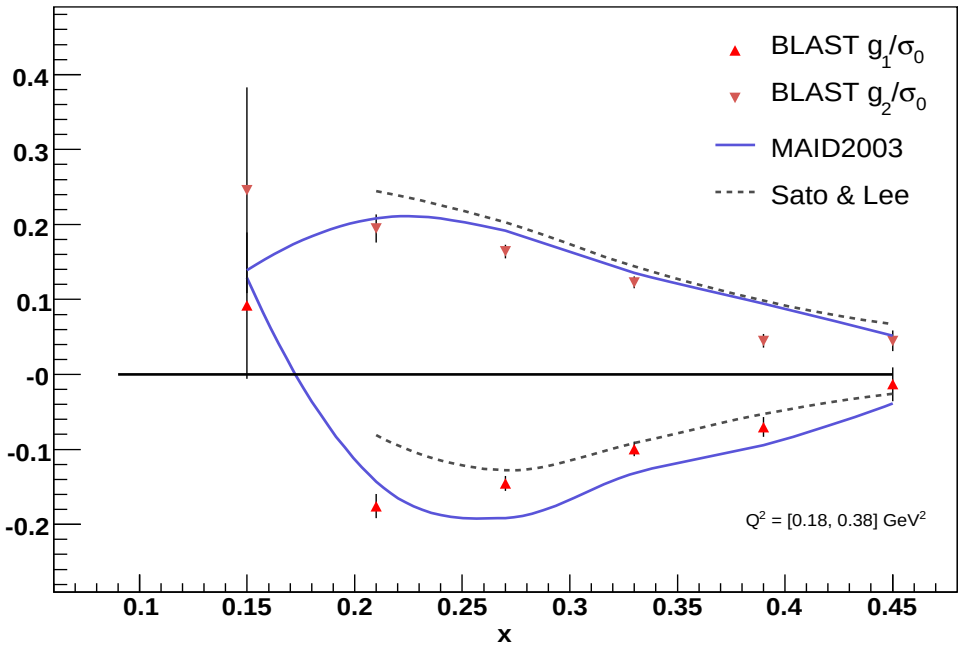

Figure 5-44: The spin-structure functions, g_1/σ_0 and g_2/σ_0 as a function of x in the Δ region ($1.1 < W < 1.4\,GeV$), and for $0.18 < Q^2 < 0.38\,GeV^2$, $\langle Q^2 \rangle = 0.225\,[GeV^2]$, using Hand's convention.

5.5 Systematic Uncertainties

5.5.1 Reconstruction Uncertainty

The internal geometry of the wire chambers was corrected but there are still discrepancies between the measured angles and momenta of scattered electrons and recoil protons from the well known benchmark in elastic kinematics [113]. The first order contributions to the kinematic constraints are the momentum (after accounting for proton's energy loss) and polar angle defined within the BLAST frame. The azimuthal angle shows a systematic deviation of 0.3° from the constraint of coplanarity and can thus be neglected since this deviation is less than the resolution in ϕ_e for BLAST, and is only a second order contribution to the elastic constraints on Q^2. A χ^2 minimization over Q^2 was attempted over all four first order variables, $E_{e'}$, P_p, θ_e, and θ_p. The resolution of the wire chambers

proves much better in θ, e.g. $\theta_e - \theta_e(\theta_p)$ gives a $\sigma < 0.5°$, whereas $E_{e'} - E_{e'}(P_p)$ gives a σ of roughly 14% of the value of $E_{e'}$ and a systematic deviation from zero that is greater than 14% of $E_{e'}$. The χ^2 minimization effectively determines the systematic deviations in θ_e and θ_p with very little influence from the values of $E_{e'}$ and P_p. Hence, the first step was to use the measured values of θ_e and θ_p event by event, along with the well known beam energy, and determine the first corrections to $E_{e'}$ and P_p via the relations $E_{e'} = E_{e'} - E_{e'}(\theta_e)$ and $P_p = P_p - P_p(\theta_p)$.

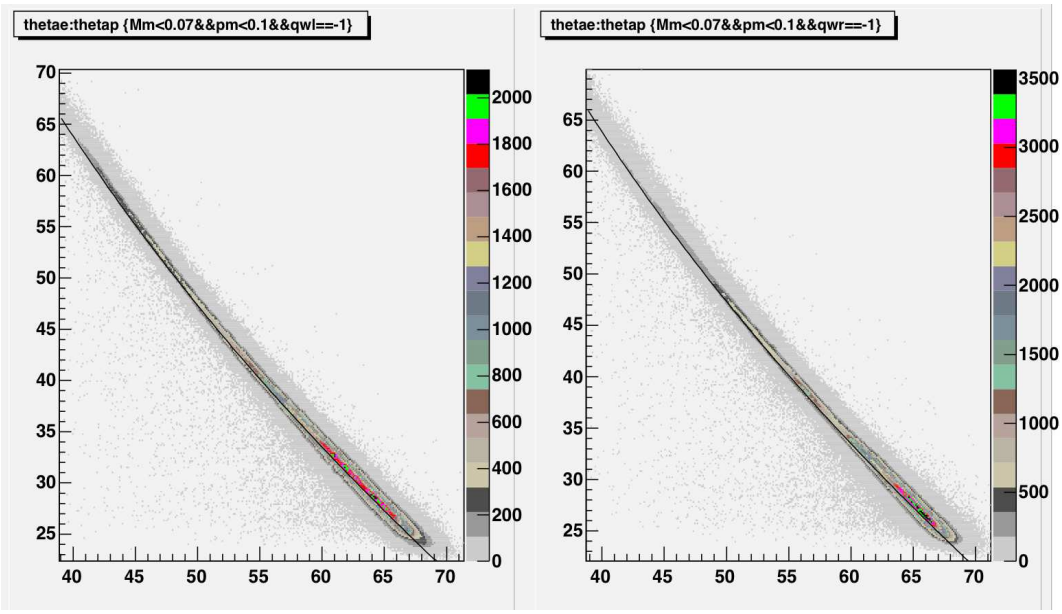

Figure 5-45: Best θ_e ° versus θ_p ° for the left (left) and right (right) sectors for the elastic electron-proton scattering.

These corrections were input and then the χ^2 minimization in Q^2 was taken over the new values of $E_{e'}$, P_p, and the old values of θ_e and θ_p in order to determine the best values of θ_e and θ_p (Figure 5-45) from the best value of Q^2 as determined from the measured values of θ_e and θ_p and the corrected values of $E_{e'}$ and P_p

$$\chi^2(E_{e'}, P_p, \theta_e, \theta_p) = \frac{(Q^2 - Q^2(E_{e'}))^2}{\delta E_{e'}^2} + \frac{(Q^2 - Q^2(P_p))^2}{\delta P_p^2} + \frac{(Q^2 - Q^2(\theta_e))^2}{\delta \theta_e^2} + \frac{(Q^2 - Q^2(\theta_p))^2}{\delta \theta_p^2}$$

The values of $E_{e'}$ and P_p were corrected to prevent the large systematic discrepancies from influencing the χ^2 minimization. After the best Q^2 was found, we convert backwards and bin the data to find the sector dependent corrections to θ_e and θ_p, i.e. correction to $\theta_e = \theta_e - \theta_e(Q^2_{best})$, etc.

These corrections were found to be less than 0.3° nearly everywhere, and when plotting the corrected distribution of $\theta_e - \theta_e(\theta_p)$ and $\theta_p - \theta_p(\theta_e)$ the mean was found to be centered on zero where it was originally off by 0.3°. The corrections to the momentum were then determined by using the functional dependence of $E_{e'}(\theta_e)$ and $P_p(\theta_p)$ since the corrected values of θ_e and θ_p were found to be well within the resolution and the constraints from elastic kinematics.

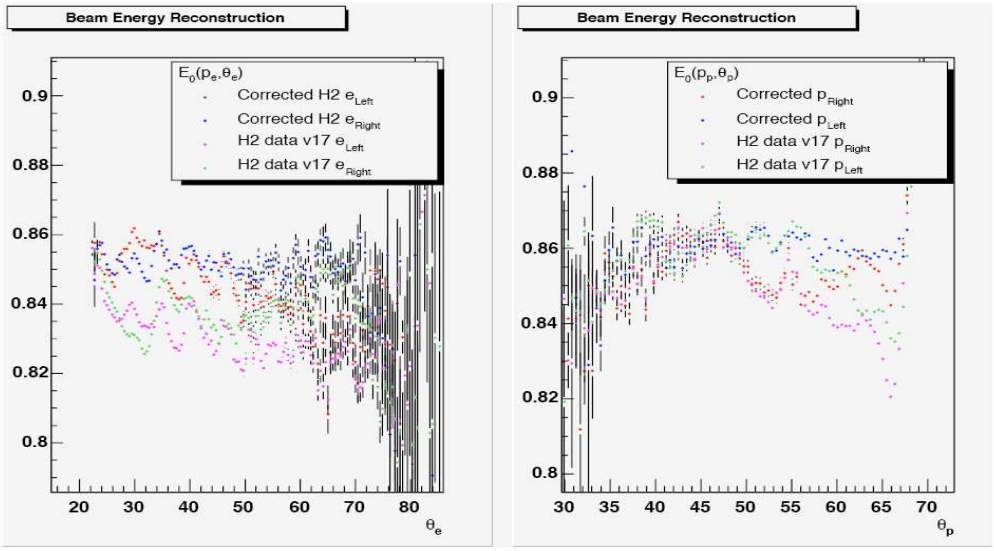

Figure 5-46: Beam Energy corrections using $E_{e'}$ and θ_e (left), and P_p and θ_p (right) as a function of the polar angle(°).

When convoluting these first order contributions and reconstructing the beam energy from final corrected values, we see a correlation with the expected beam energy and deviations that are at least a factor of 2 less than the resolution of the momentum of both

the proton and electron. The reconstructed beam energy is shown in Figure 5-46.

Since these corrections have been done over the elastic region and the momentum of the electron was corrected, it is reasonable to consider half of this deviation over the inelastic region. The systematic errors due to electron momentum and polar angle are presented in **Appendices D, C** together with the measured values of the physical quantities discussed in section 5.2.

5.5.2 Target Spin Angle Uncertainty

In this analysis the target spin angle is used in the extraction of the spin correlation parameters, $A_{TL'}$, $A_{TT'}$, and enters in the determination of the target spin projections onto the $\mathbf{u}_x$ and $\mathbf{u}_z$ axes, namely x^* and z^*. Although the asymmetries measurements depend on the orientation of the target spin, we extract them without any knowledge of it.

A new method used at Jefferson Laboratory was implemented in order to redo the target holding field mapping. This method is based on a compass principle, where the field angle is measured directly. The compass device is a magnetic probe which sits on an air pillow and can be sled along the BLAST z axis. A mirror is attached to the probe and the angle of the probe orientation is measured by the direction of the reflected light from a laser placed on the axis. With this method, the uncertainty of the target spin angle was found to be 0.45°.

Throughout this analysis, the spin angle map from [131] was used. Figure 5-47 shows the target spin angle profile as a function of the target cell length, z_{target}.

5.5.3 False Asymmetries

The beam only and target only asymmetries discussed in (4.2.2) are independent measurements of the false asymmetries.

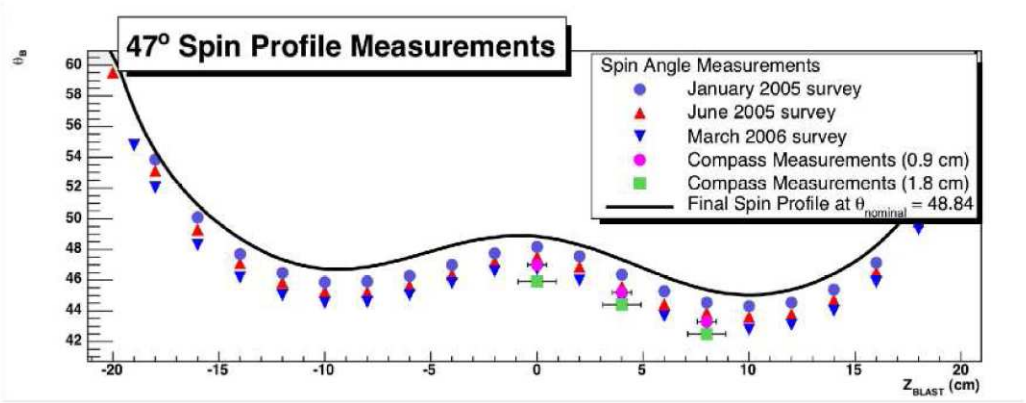

Figure 5-47: Target spin angle map as a function of the target cell length.

The beam and target asymmetries are shown in Figures 5-48, 5-49, 5-50, 5-51, 5-52, 5-53, 5-54, 5-55, 5-56, 5-57, 5-58, 5-59, 5-60, 5-61, for all the cases discussed in section 5.1.

5.5.4 Beam and Target Polarization Uncertainty

The beam-target polarization product is used in the extraction of the correlation parameter, A, from the measured asymmetries for both left and right sectors. The average beam and target polarizations for the hydrogen production run period from October to December of 2004 were $P_b = 0.6558 \pm 0.0007_{stat} \pm 0.04_{sys}$, and $P_t = 0.80 \pm 0.0007_{stat} \pm 0.04_{sys}$.

The raw experimental asymmetries for the elastic electron-proton scattering are fit to a parametrization using the Hőhler form factors [106] in order to extract the product of beam and target polarization, $P = P_b \cdot P_t$. The result is shown in Figure 5-62.

The systematic error contributions due to the polarization product, P, are given in **Appendix C** together with the measured values for the correlation parameter, A, for both left and right sectors.

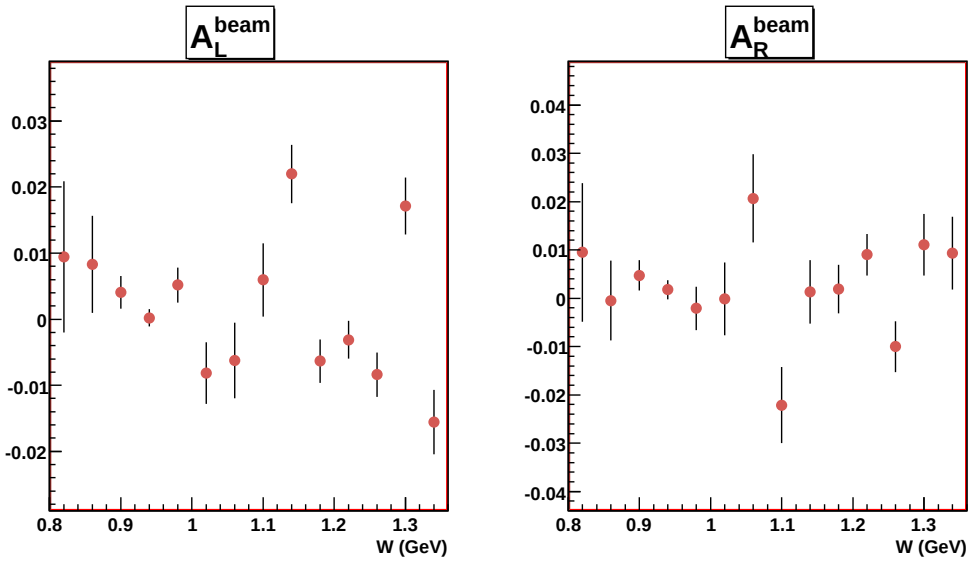

Figure 5-48: Beam only asymmetry for left (left) and right (right) sectors as a function of invariant mass, W, at $Q^2 = 0.123\,GeV^2$.

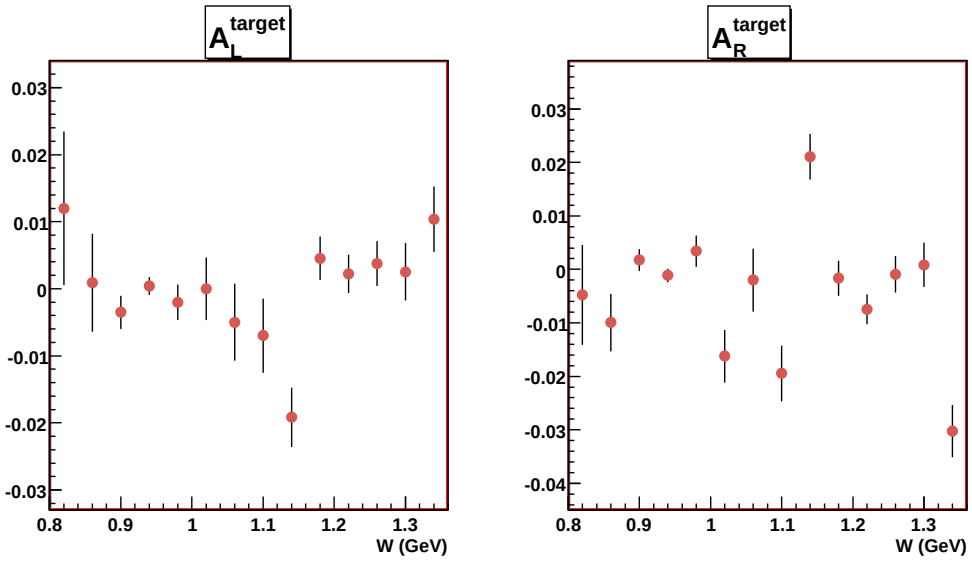

Figure 5-49: Target only asymmetry for left (left) and right (right) sectors as a function of invariant mass, W, at $Q^2 = 0.123\,GeV^2$.

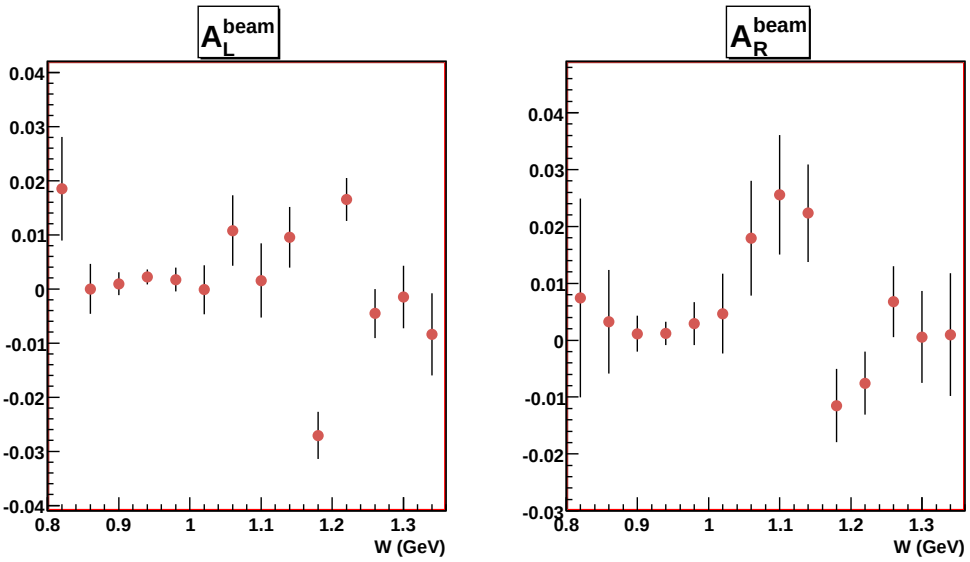

Figure 5-50: Beam only asymmetry for left (left) and right (right) sectors as a function of invariant mass, W, at $Q^2 = 0.175\,GeV^2$.

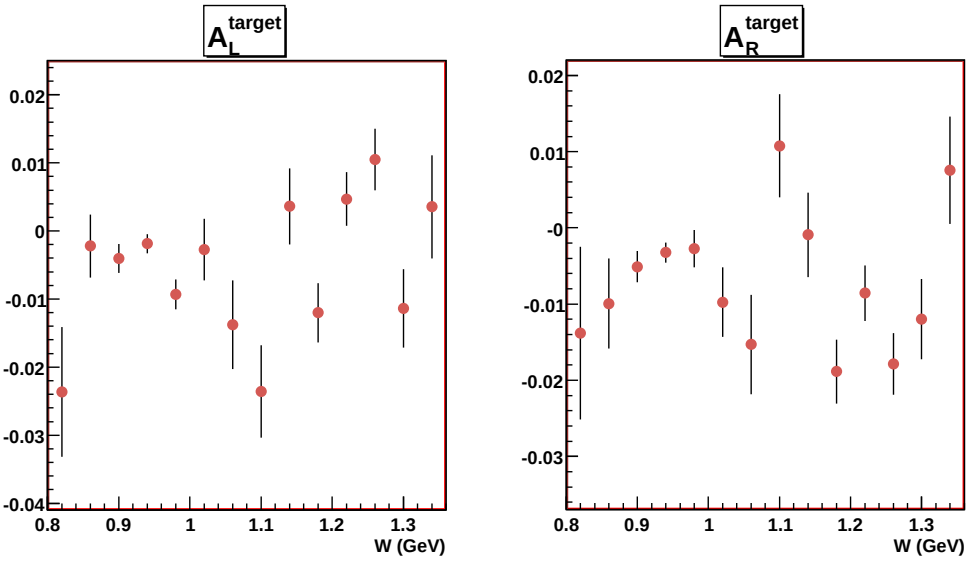

Figure 5-51: Target only asymmetry for left (left) and right (right) sectors as a function of invariant mass, W, at $Q^2 = 0.175\,GeV^2$.

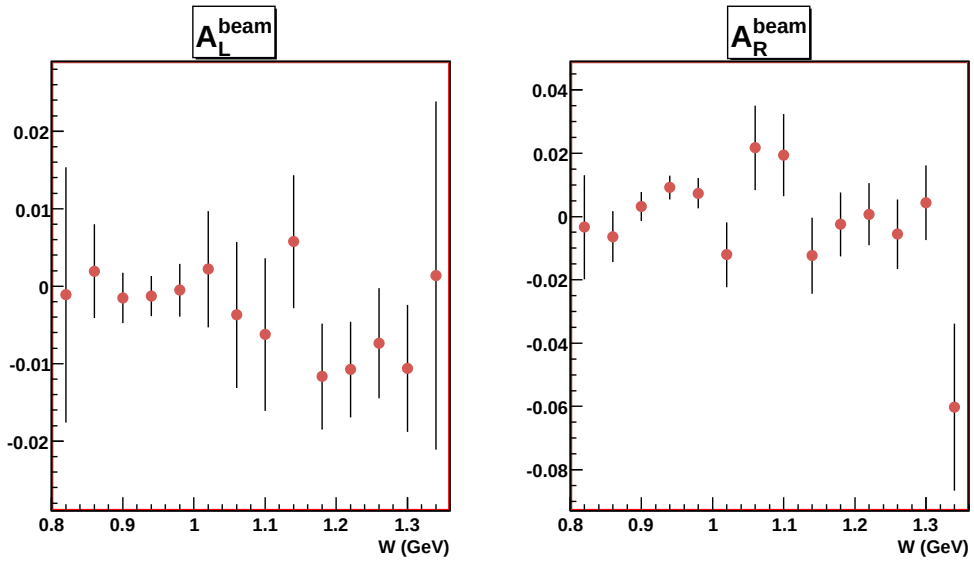

Figure 5-52: Beam only asymmetry for left (left) and right (right) sectors as a function of invariant mass, W, at $Q^2 = 0.24\,GeV^2$.

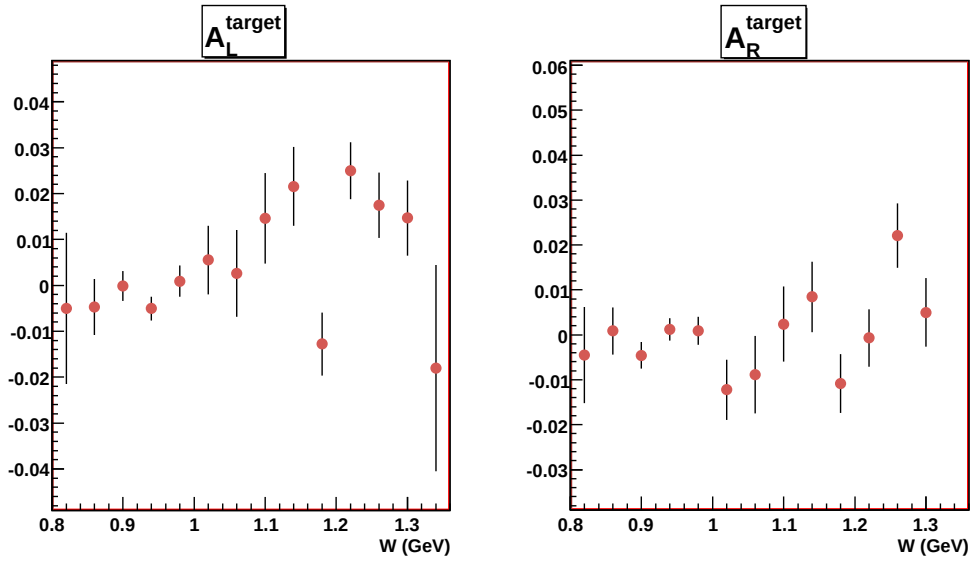

Figure 5-53: Target only asymmetry for left (left) and right (right) sectors as a function of invariant mass, W, at $Q^2 = 0.24\,GeV^2$.

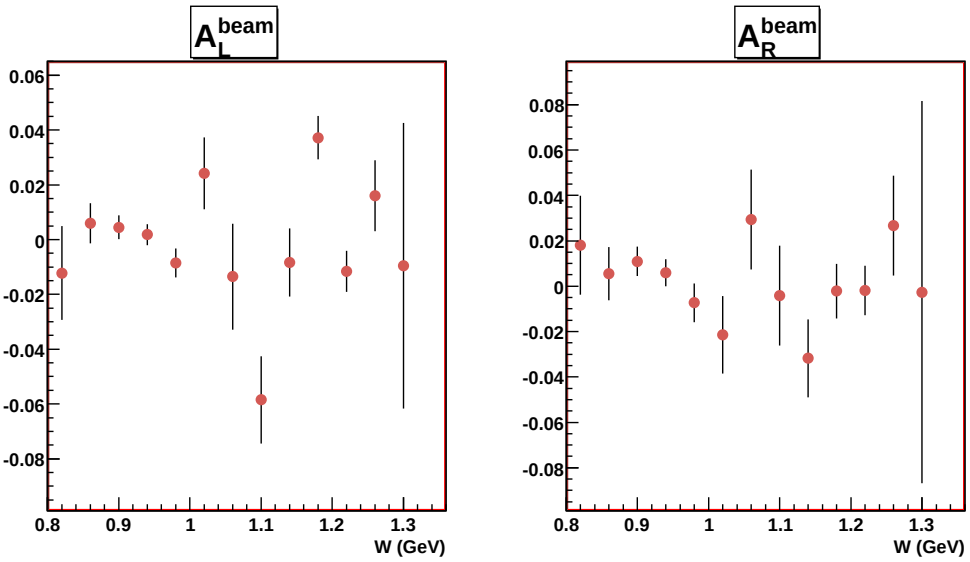

Figure 5-54: Beam only asymmetry for left (left) and right (right) sectors as a function of invariant mass, W, at $Q^2 = 0.312\,GeV^2$.

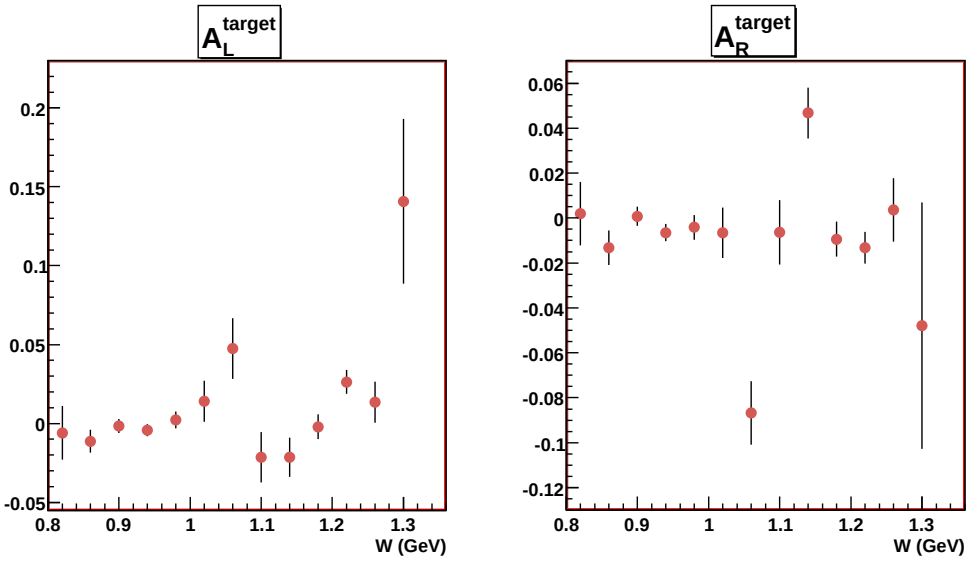

Figure 5-55: Target only asymmetry for left (left) and right (right) sectors as a function of invariant mass, W, at $Q^2 = 0.312\,GeV^2$.

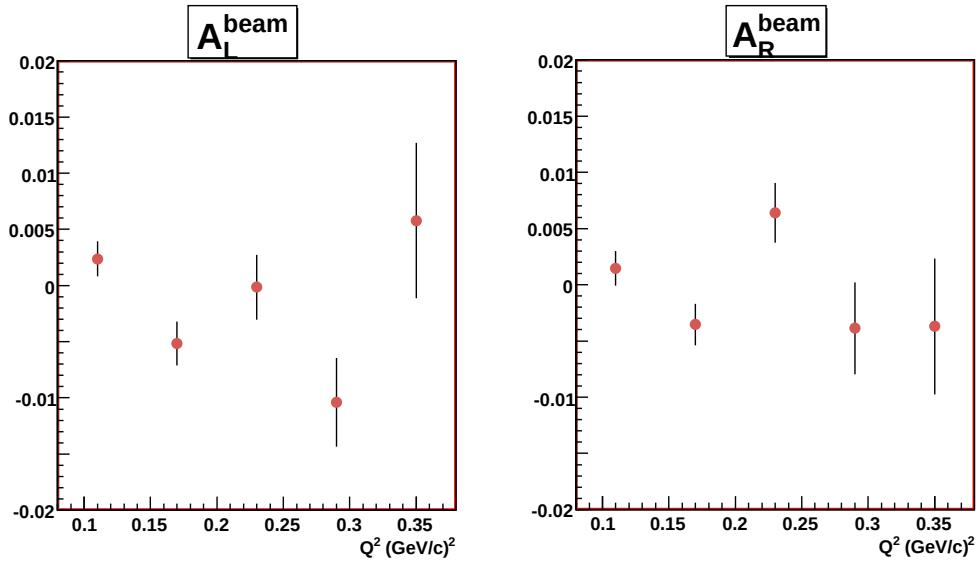

Figure 5-56: Beam only asymmetry for left (left) and right (right) sectors as a function of Q^2, over the Δ region ($1.1 < W < 1.4\,GeV$).

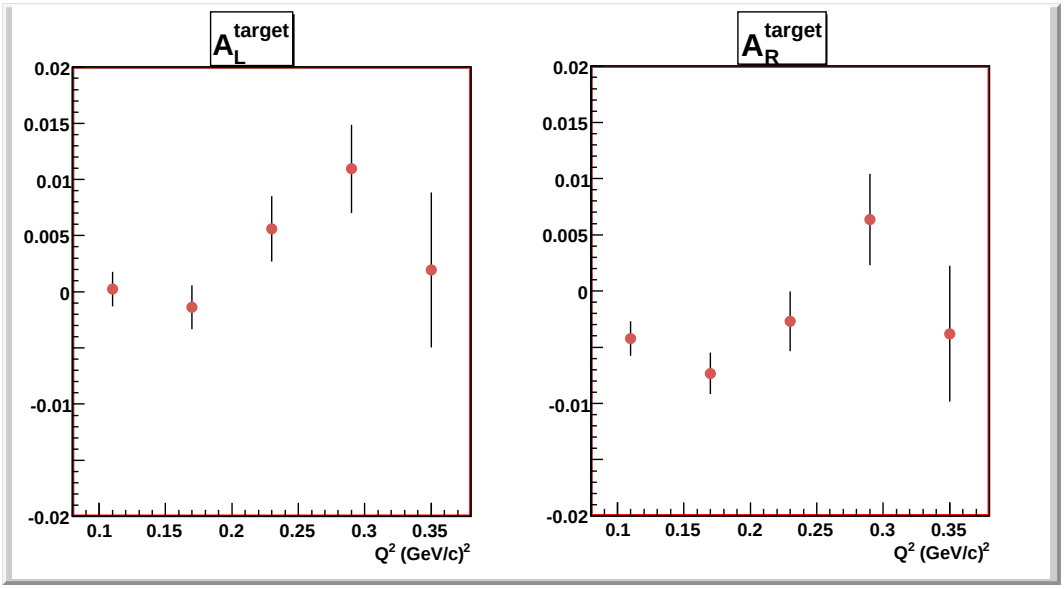

Figure 5-57: Target only asymmetry for left (left) and right (right) sectors as a function of Q^2, over the Δ region ($1.1 < W < 1.4\,GeV$).

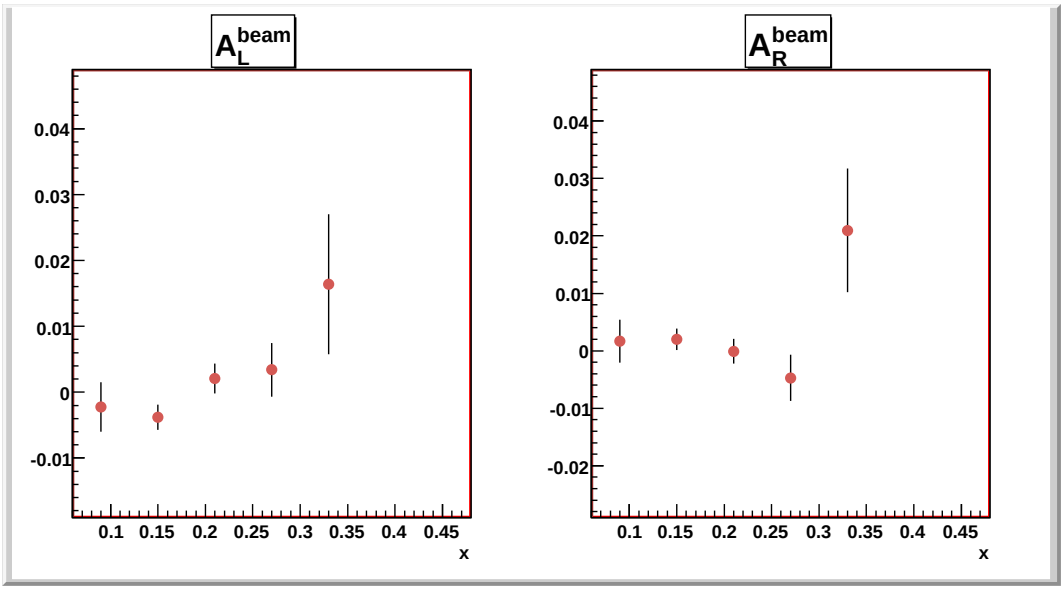

Figure 5-58: Beam only asymmetry for left (left) and right (right) sectors as a function of x, over the Δ region ($1.1 < W < 1.4\,GeV$), and for $0.08 < Q^2 < 0.18\,GeV^2$.

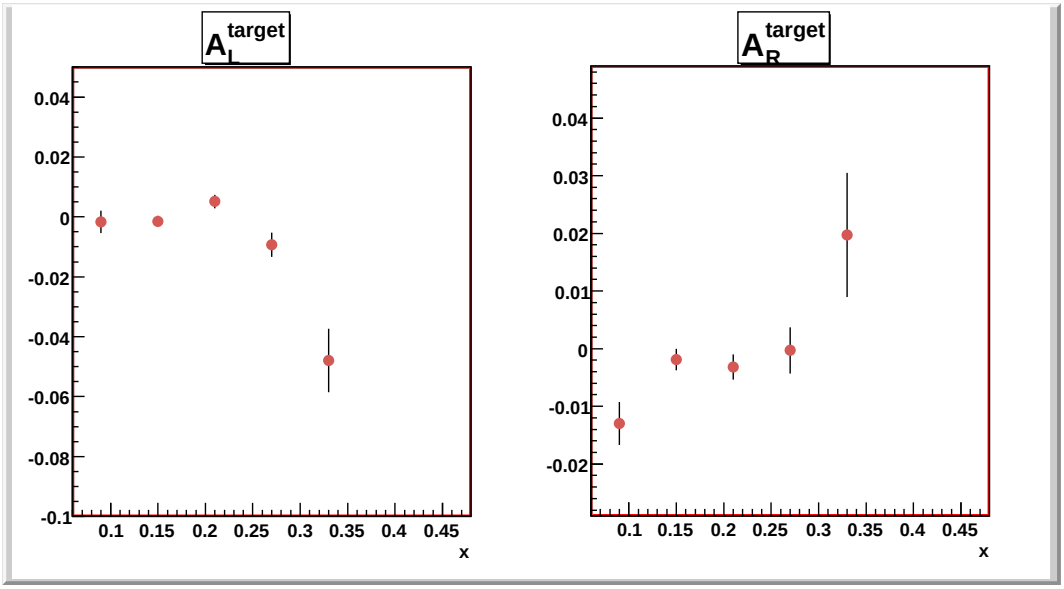

Figure 5-59: Target only asymmetry for left (left) and right (right) sectors as a function of x, over the Δ region ($1.1 < W < 1.4\,GeV$), and for $0.08 < Q^2 < 0.18\,GeV^2$.

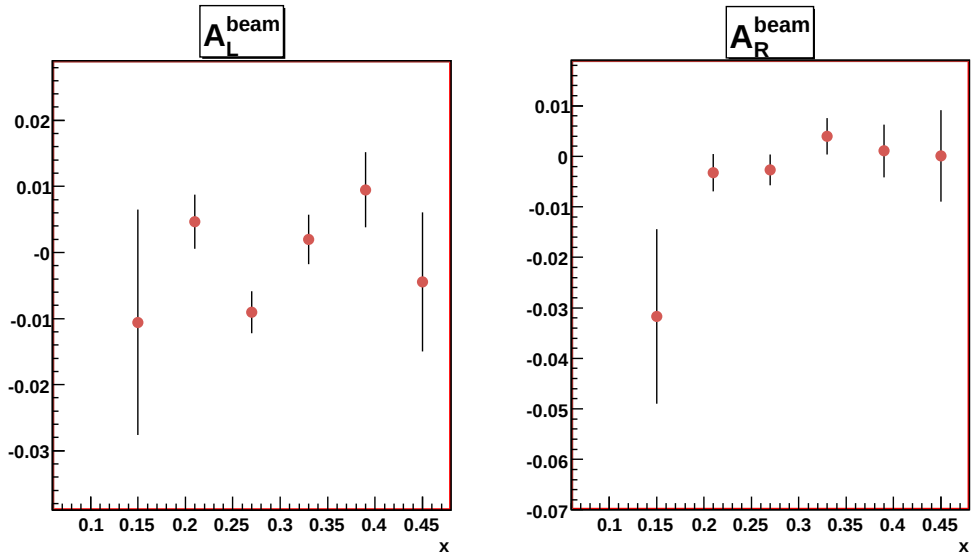

Figure 5-60: Beam only asymmetry for left (left) and right (right) sectors as a function of x, over the Δ region ($1.1 < W < 1.4\,GeV$), and for $0.18 < Q^2 < 0.38\,GeV^2$.

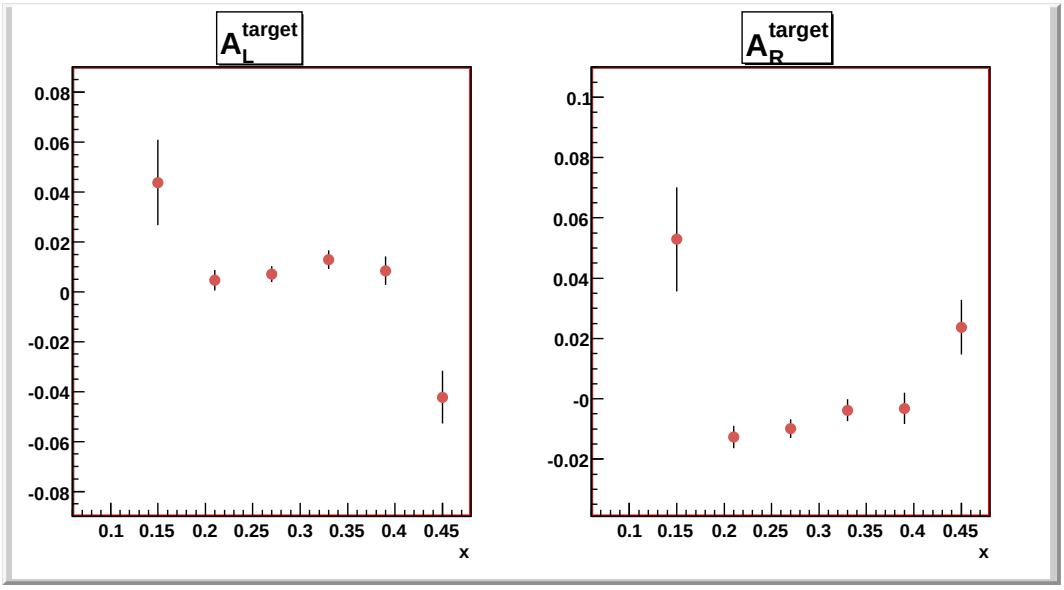

Figure 5-61: Target only asymmetry for left (left) and right (right) sectors as a function of x, over the Δ region ($1.1 < W < 1.4\,GeV$), and for $0.18 < Q^2 < 0.38\,GeV^2$.

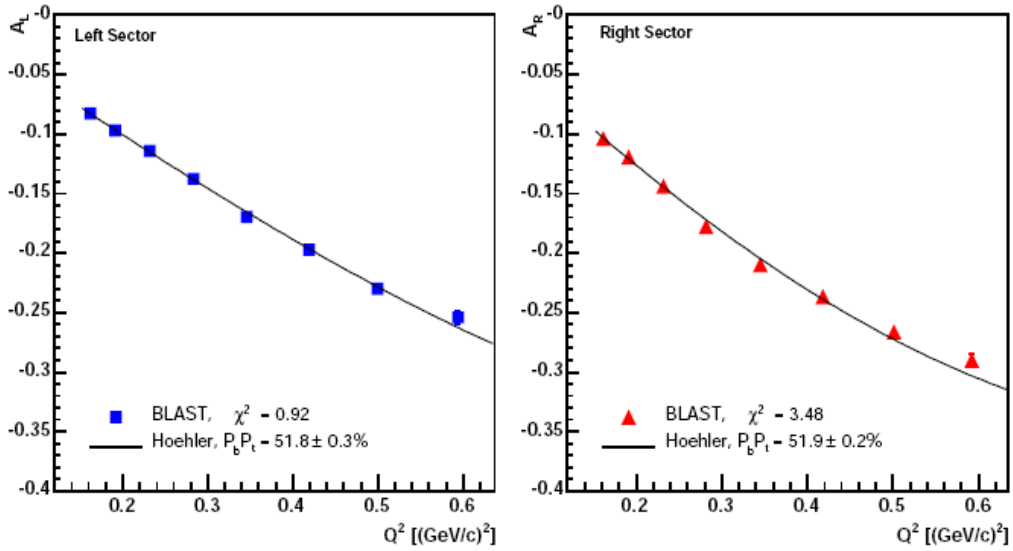

Figure 5-62: The raw experimental asymmetries for the elastic electron-proton scattering for both left (left) and right (right) sectors. They are fit to the Hőhler form factor parametrization to extract the beam-target polarization product, $P = P_b \cdot P_t$.

5.5.5 Background Uncertainty

Background contributions are discussed in section 4.2. The kinematics corrections (subsection 5.5.1) are applied to the empty target data also. Hence the systematic error contributions from the background reconstruction uncertainty are added to the total reconstruction uncertainty and given as a whole in **Appendix C**.

5.5.6 Normalization and Radiative Corrections Uncertainty

The radiative effects were generated using the ELRADGEN code [122, 121]. This code only takes into account the radiative contributions coming from the elastic scattering. In the Δ region, contributions coming from the inelastic scattering are present as well. In order to estimate them, calculations using the MASCARAD and POLRAD codes were performed (see section 4.3). This analysis showed that these effects are small compared with the radiative tail coming from the elastic electron-proton scattering and they are

less than the statistical error bars of the asymmetry measurements. Hence they are not included into the systematic errors.

The Monte Carlo simulations with radiative effects are normalized to the experimental elastic peak, in order to get the elastic radiative tail over the Δ excitation region. This is done using all the data in the elastic scattering region. However, a tighter region was chosen around the elastic peak, in order to calculate the uncertainties of this normalization technique. The differences were found to be less than 5 %, with the exception when it was normalized to the maximum peak only, where the difference was less than 20 %. When normalized to the whole experimental elastic peak, the difference in the radiative and the experimental yields in the vicinity of the pion-production threshold ($W = 1.07$ GeV), was also fount to be less than 10 %. Hence this percentage was added to the amount of radiative yields, and then the asymmetries were taken and compared with the extracted ones, in order to estimate the uncertainties caused by the normalization and radiative effects to the asymmetry, and they were added to the total systematic errors in **Appendix C**.

5.6 Results Discussion

In this section we discuss the results presented in sections 5.1 and 5.2.

The extracted asymmetry is affected by the background and radiative contributions. A large amount of data have been collected with BLAST, which makes the statistical error bars relatively small, for both the data taken and empty target runs. The asymmetry systematic errors are caused by the statistical and systematic uncertainties of the beam-target polarization product, $P = P_b \cdot P_t$; the false asymmetries; statistical uncertainties of the empty-target runs; the radiative corrections and normalization uncertainties.

The overall structure predicted by the theoretical models is observed in the extracted spin correlation parameters almost over the entire Δ region. At lower Q^2 ranges, the extracted asymmetry seems to be in much better agreement with the predicted values,

while at higher Q^2 values, it seems that it "shifts" away, although the overall structure is preserved.

The background and radiative contributions over the Δ excitation region are summarized in Tables 5.3, 5.5, 5.4, 5.6, for each bin in the invariant mass, W, and for each Q^2 average value used. The overall contributions to the data over the Δ excitation region are given in Tables 5.7, 5.8.

Q^2	$W = 1.09$	1.13	1.18	1.22	1.25	1.30	1.33
0.123	21.57 %	18.40 %	13.02 %	11.44 %	16.03 %	26.15 %	34.45 %
0.175	25.12 %	19.68 %	14.08 %	13.33 %	18.02 %	26.62 %	35.82 %
0.240	27.77 %	24.18 %	17.77 %	18.87 %	29.12 %	39.50 %	49.69 %
0.312	32.91 %	35.01 %	26.22 %	24.78 %	36.67 %	61.04 %	-

Table 5.3: Empty target background as a percentage of the data used in the extraction of the left asymmetry, A_L, as a function of $W = [1.1, 1.36]\, GeV$, for each $Q^2\, [GeV^2]$ bin (Table 5.1).

Q^2	$W = 1.09$	1.13	1.18	1.22	1.25	1.30	1.33
0.123	82.03 %	44.25 %	21.11 %	13.81 %	14.57 %	16.45 %	14.77 %
0.175	63.73 %	32.24 %	14.62 %	9.07 %	8.30 %	8.40 %	7.32 %
0.240	51.39 %	23.58 %	9.17 %	4.66 %	3.91 %	3.40 %	4.35%
0.312	41.54 %	22.57 %	7.75 %	4.13 %	2.87 %	1.25 %	-

Table 5.4: Radiative contributions as a percentage of the data used in the extraction of the left asymmetry, A_L, as a function of $W = [1.1, 1.36]\, GeV$, for each $Q^2\, [GeV^2]$ bin (Table 5.1).

The background contributions increase at higher W and Q^2, while the radiative contributions decrease. The radiative effects from pion-production processes, although, cause the radiative tail to decrease very slow at higher W values. These effects were not included in this analysis. Hence, this might explain the difference between the data and theoretical

Q^2	$W = 1.09$	1.13	1.18	1.22	1.25	1.30	1.33
0.123	18.74 %	16.48 %	13.44 %	9.99 %	16.21 %	22.51 %	32.96 %
0.175	25.12 %	19.68 %	14.08 %	13.33 %	18.02 %	26.62 %	35.82 %
0.240	26.04 %	26.01 %	19.38 %	20.58 %	29.74 %	37.58 %	39.34 %
0.312	32.36 %	31.84 %	24.15 %	19.79 %	40.06 %	60.43 %	-

Table 5.5: Empty target background as a percentage of the data used in the extraction of the right asymmetry, A_R, as a function of $W = [1.1, 1.36]\, GeV$, for each $Q^2\, [GeV^2]$ bin (Table 5.1).

Q^2	$W = 1.09$	1.13	1.18	1.22	1.25	1.30	1.33
0.123	60.62 %	37.90 %	20.98 %	13.09 %	14.87 %	15.93 %	15.49 %
0.175	54.29 %	28.02 %	12.94 %	7.52 %	6.96 %	7.37 %	6.93 %
0.240	42.53 %	22.58 %	10.68 %	6.94 %	5.72 %	4.66 %	4.23 %
0.312	67.24 %	39.56 %	15.31 %	7.31 %	5.75 %	4.50 %	-

Table 5.6: Radiative contributions as a percentage of the data used in the extraction of the right asymmetry, A_R, as a function of $W = [1.1, 1.36]\, GeV$, for each $Q^2\, [GeV^2]$ bin (Table 5.1).

Q^2	Background	Radiative Tail
0.123	19.02 %	23.70 %
0.175	20.20 %	17.24 %
0.240	27.53 %	11.91 %
0.312	30.01 %	10.65 %

Table 5.7: Empty target data and radiative contributions as a percentage of the data used in the extraction of the left asymmetry, A_L, as a function of $W = [1.1, 1.36]\, GeV$, for each $Q^2\, [GeV^2]$ bin (Table 5.1).

Q^2	Background	Radiative Tail
0.123	17.61 %	21.76 %
0.175	20.44 %	14.15 %
0.240	27.47 %	13.28 %
0.312	27.85 %	20.24 %

Table 5.8: Empty target data and radiative contributions as a percentage of the data used in the extraction of the right asymmetry, A_R, as a function of $W = [1.1, 1.36]\, GeV$, for each $Q^2\, [GeV^2]$ bin (Table 5.1).

models in the last bin of the analysis as a function of the invariant mass, W, and the first bin of the analysis as a function of the transfer momentum squared, Q^2 and the Bjorken scaling variable, x.

The overall background and radiative tail contributions to the data over the Δ excitation region for the Q^2 and x analysis are summarized in Tables 5.9, 5.10.

Q^2 range	Background	Radiative Tail
0.08 - 0.38	22.09 %	15.66 %
0.08 - 0.18	20.43 %	18.41 %
0.18 - 0.38	25.13 %	11.21 %

Table 5.9: Empty target data and radiative contributions as a percentage of the data used in the extraction of the left asymmetry, A_L as a function of $Q^2\,[GeV^2]$, over the Δ region.

Q^2 range	Background	Radiative Tail
0.08 - 0.38	21.09 %	13.70 %
0.08 - 0.18	19.12 %	16.28 %
0.18 - 0.38	24.45 %	11.29 %

Table 5.10: Empty target data and radiative contributions as a percentage of the data used in the extraction of the right asymmetry, A_R as a function of $Q^2\,[GeV^2]$, over the Δ region.

5.6.1 Discussion of the Correlation Parameters Results

The correlation parameters, $A_{TT'}$ and $A_{TL'}$, are extracted using the left and right asymmetries, $A_{L,R}$, and the target spin angle $x-$ and $z-$components onto the u_x and u_z axes in the $q-$frame. These components are obtained by histograming them for each corresponding data bin, in both the data analysis as well as the Monte Carlo simulations. For the data analysis, the main errors in the extraction of the spin correlation parameters

come from the systematic uncertainties in the target spin angle θ_T and the scattered electron polar angle, θ_e, as well as the extracted asymmetries for both left (perpendicular kinematics, $\theta^* \approx 90^\circ$) and right (parallel kinematics, $\theta^* \approx 0^\circ$) sectors.

The overall structure predicted by the theoretical models is observed in the extracted spin correlation parameters almost over the entire Δ region. At lower Q^2 ranges, this difference is quite small, while, with the increase in the transfer momentum squared Q^2, this difference increases also, but, as in the asymmetry case, the overall structure is preserved.

A reduced χ^2 is constructed for each theoretical model as follows [95, 99, 109]:

$$\chi^2 = \frac{1}{n} \sum_{k=1}^{n} \frac{(f_k^{DATA} - f_k^{MODEL})^2}{\sigma_k^2} \tag{5.14}$$

where n represents the number of bins (degree of freedom), σ_k are the quadratic sum of all the uncertainties, statistical and systematic, of the data. The functions $f_k^{DATA,\,MODEL}$ represent the data and the theoretical quantities, respectively, namely $A_{TT'}, A_{TL'}, g_1, g_2$, for the k^{th} bin. For the spin-correlation parameters, the χ^2 tests are given in Tables 5.11 for each Q^2 average value used in this analysis (Figures 5-12, 5-13, 5-14, 5-15).

$Q^2\,[GeV^2]$	$\chi^2(A_{TT'}^{MAID})$	$\chi^2(A_{TT'}^{SL})$	$\chi^2(A_{TL'}^{MAID})$	$\chi^2(A_{TL'}^{SL})$
0.123	0.61	3.73	0.13	1.11
0.175	1.02	2.54	0.43	1.66
0.240	1.25	1.75	0.44	1.17
0.312	3.01	3.79	0.92	0.12

Table 5.11: Reduced χ^2 values for the correlation parameters $A_{TT'}$ and $A_{TL'}$ as a function of W for each Q^2 average value used in this analysis by comparing BLAST data with MAID and SL models.

From these tests we see that the MAID model follows closely the BLAST data, than the Sato & Lee (SL) model, with the exception of the highest momentum transfered squared value, i.e. for $Q^2 = 0.312\,GeV^2$.

5.6.2 Discussion of the Spin-Structure Function Results

The proton spin-structure functions, g_1 and g_2, are extracted in four steps: first, the left (perpendicular kinematics, $\theta^* \approx 90°$) and right (parallel kinematics, $\theta^* \approx 0°$) sectors asymmetries are extracted as a function of Q^2 and x; second, using the target spin angle $x-$ and $z-$components onto the u_x and u_z axes in the $q-$frame (i.e. mean value of their histogram for each bin), we extract the spin correlation parameters; third, we extract the partial cross sections, $\sigma_{TT'}/\sigma_0$ and $\sigma_{TL'}/\sigma_0$, using the virtual photon transverse polarization, ϵ (mean value of its histogram for each bin); and finally, we extract g_1 and g_2, using the mean values for ω, x, γ, as discussed in section 5.2.

The overall structure of the data follows the theoretical predictions, with exception at low x, which means a high W. Note that the high W bins are dominated by high background contributions. The χ^2 tests are given in Tables 5.12 and 5.13 for the results shown in Figures 5-40, 5-41, 5-42, 5-43 and 5-44. This χ^2 tests have been done by neglecting this first bin for g_1, g_2 as a function of x (middle raw).

Q^2 range $[GeV^2]$	$\chi^2(g_1^{MAID})$	$\chi^2(g_1^{SL})$	$\chi^2(g_2^{MAID})$	$\chi^2(g_2^{SL})$
0.08 - 0.18	0.10	1.10	0.08	0.12
0.18 - 0.38	0.81	1.94	0.71	0.98

Table 5.12: Reduced χ^2 values for the spin-structure functions g_1 and g_2 as a function of x for the two Q^2 intervals used in this analysis, by comparing BLAST data with MAID and SL models.

5.7 Conclusion

It has been shown that unique studies of the $\gamma^* p \to \Delta$ transition has been made possible with BLAST, utilizing the polarized beam and target, along with the BLAST detector. For the first time, extraction of the spin correlation parameters, $A_{TT'}$, $A_{TL'}$, and the proton

x range	$\chi^2(g_1^{MAID})$	$\chi^2(g_1^{SL})$	$\chi^2(g_2^{MAID})$	$\chi^2(g_2^{SL})$
0.08 - 0.48	1.77	1.27	0.55	0.70
0.08 - 0.28	0.01	1.44	0.03	0.02
0.28 - 0.48	1.92	1.25	0.79	1.03

Table 5.13: Reduced χ^2 values for the spin-structure functions g_1 and g_2 as a function of Q^2 for the three x intervals used in this analysis, by comparing BLAST data with MAID and SL models.

spin-structure functions, g_1, g_2 have been accomplished (to the extent of knowing the total unpolarized cross section, $\sigma_0 = \sigma_T + \epsilon\sigma_L$), over a small transfer momentum squared region, $0.08 < Q^2 < 0.38 GeV^2$, all in one experiment. These measurements provide a sensitive test to the pion-production models, and they show the important role of the pion in the Δ excitation region.

There is no world data available to compare the spin correlation parameters, $A_{TT'}$ and $A_{TL'}$ extracted with BLAST and given in Figures 5-12, 5-13, 5-14, 5-15. These spin correlation parameters are sensitive to the electric and coulomb quadrupole strengths, $E2$ and $C2$ respectively, and they provide a stringent test to measure these strengths. Note that we used the standard values for $E2$ and $C2$ provided by the two theoretical models used for comparison in this analysis, namely MAID and SL.

There is one measurement of the transverse spin structure function, g_2, performed at NIKHEF [9, 6], but since we did not measure the total unpolarized cross section, $\sigma_0 = \sigma_T + \epsilon\sigma_L$, we cannot fully compare these results. However, we can compare the overall structure and, of big importance, its zero crossing. For the longitudinal spin structure function, g_1, the data are available. The world data results taken from [9, 7, 8] are shown in Figures 5-65, 5-66, 5-63, and 5-64. Compare to the BLAST data (Figures 5-40, 5-41, 5-42, 5-43 and 5-44), we see a good agreement for g_1 and g_2 as a function of x between BLAST results (Figure 5-43) and NIKHEF data (Figures 5-65, 5-66), and a good agreement for the zero crossing of g_1 as a function of Q^2 between BLAST points (Figure

5-40) and the global results from [8] (Figure 5-64).

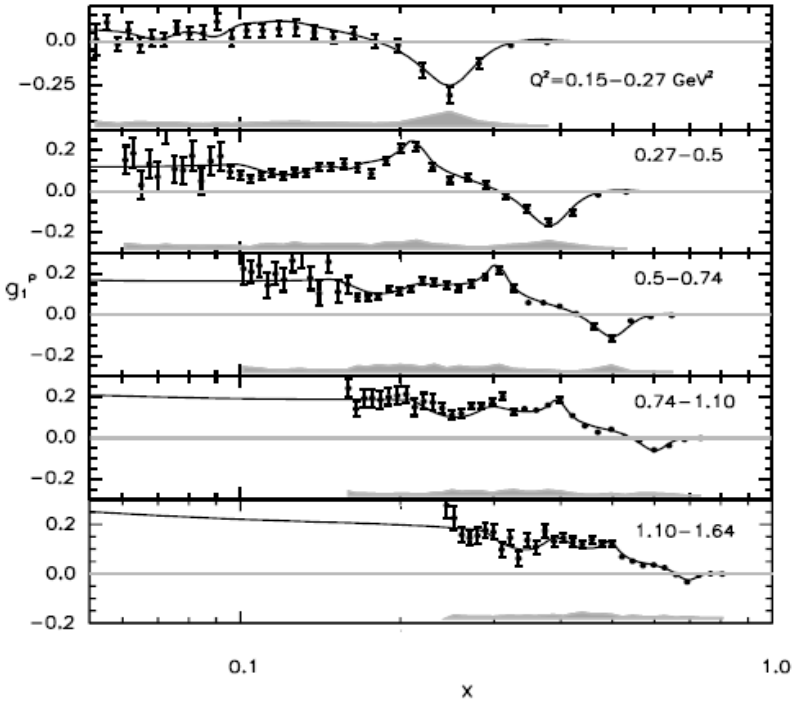

Figure 5-63: The spin structure function, g_1, obtained from JLab [7] as a function of x, for different Q^2 bins.

The extracted electric and coulomb quadrupole strengths, $E2/M1$ and $C2/M1$, together with the world data at low momentum transfer squared, $Q^2\,[GeV^2]$, are given in Figure 5-67. The total errors are given in Table 5.2 and Figures 5-28 and 5-29. From this figure, we see how BLAST fills in the missing gaps at this Q^2 range. The results stand between the chiral EFT calculations and the phenomenological models (see Figure 5-68 and [10]).

This analysis offers new unique data for the pion-production models.

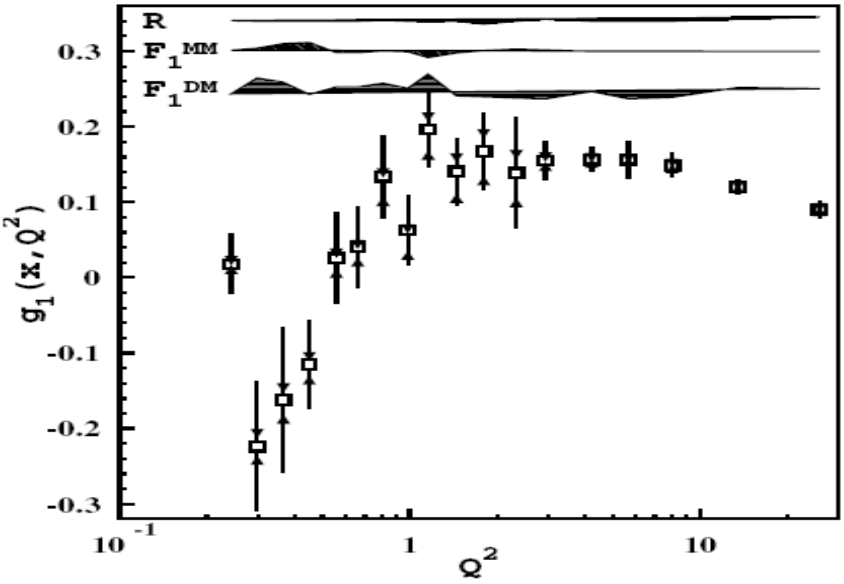

Figure 5-64: World data results for the spin structure function, g_1, from [8] as a function of Q^2.

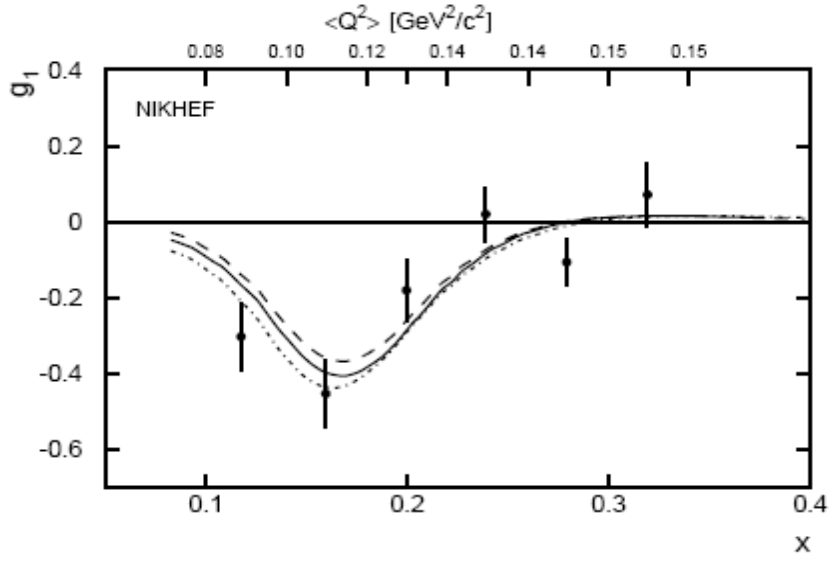

Figure 5-65: The spin structure function, g_1, obtained from NIKHEF [9] as a function of x, and for $Q^2 = [0.09, 0.15] GeV^2$.

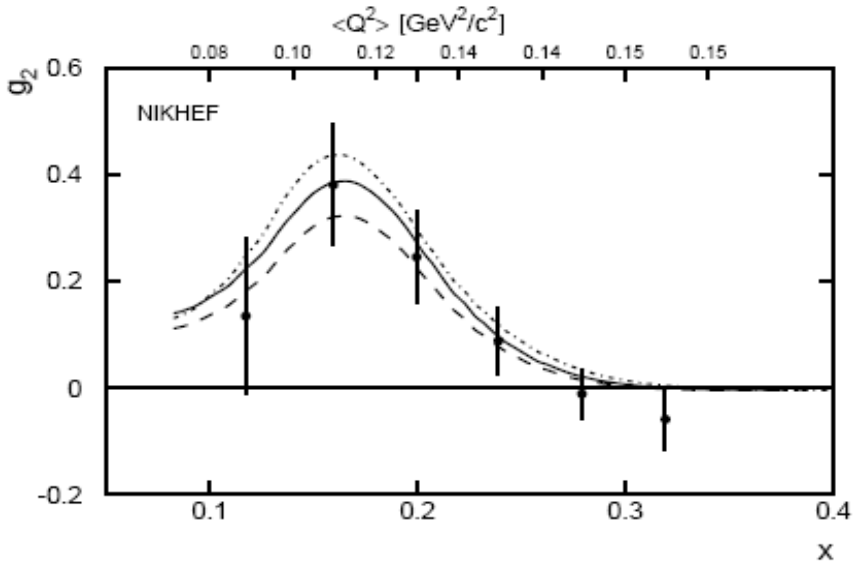

Figure 5-66: The spin structure function, g_2, obtained from NIKHEF [9] as a function of x, and for $Q^2 = [0.09, 0.15] GeV^2$.

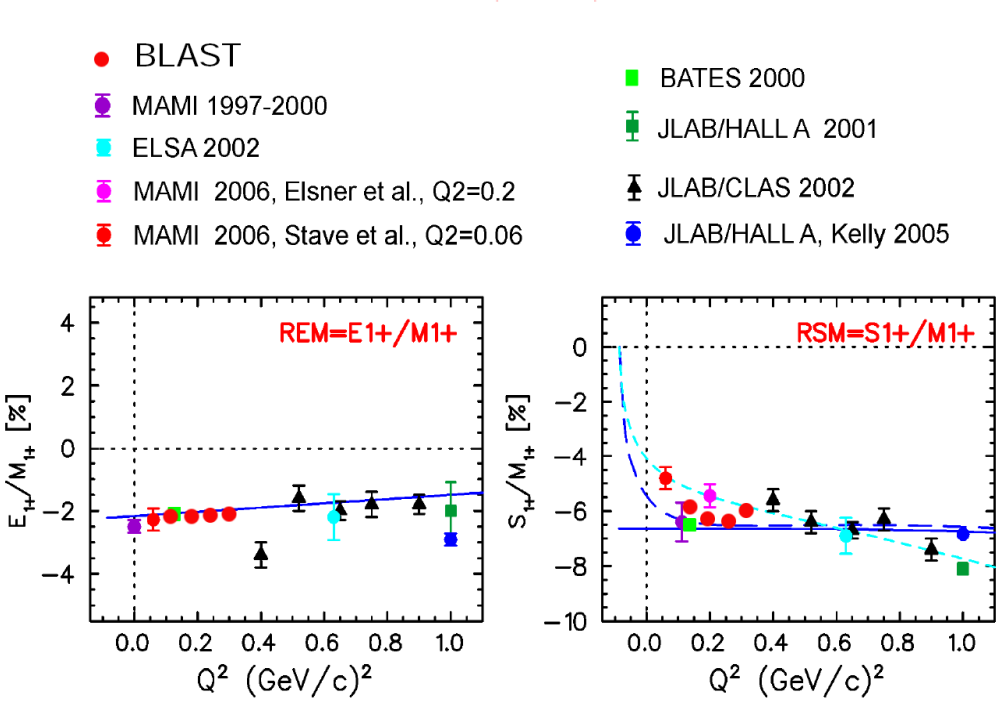

Figure 5-67: Extracted $E2/M1$ and $C2/M1$ together with the world data as a function of Q^2 $[GeV^2]$. The blue-dashed curve represents the DMT model [20], and the light-blue small-dashed curve, the SAID model [10].

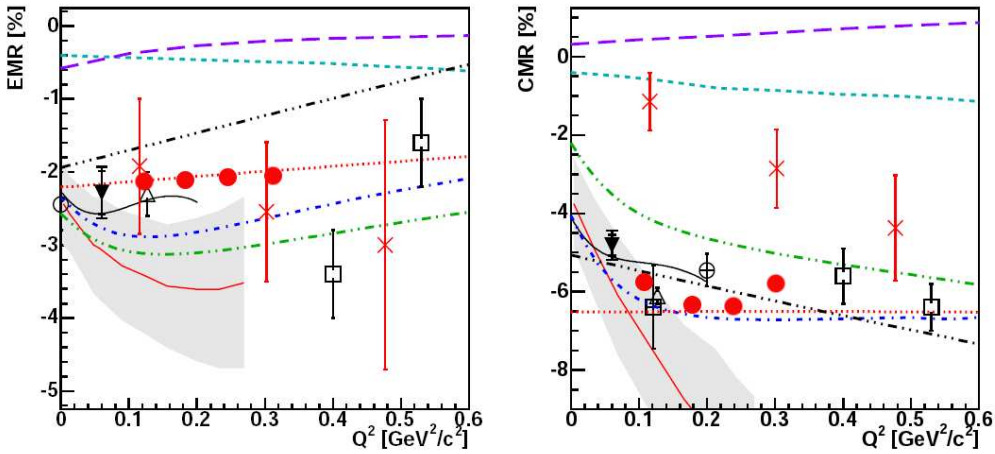

Figure 5-68: Extracted $E2/M1$ (left) and $C2/M1$ (right) - red dots, together with the world data as a function of $Q^2\,[GeV^2]$. The data are from MAMI: ◯ [11] ⊕ [12] ⊞ [13] ▼ [14]; Bates: △ [15], red dots (BLAST); CLAS: □ [16]. The lattice QCD calculations with linear pion mass extrapolations are shown as × [17]. Two chiral EFT calculations are shown: the δ-expansion result from [10] (red solid curves), and the ϵ-expansion result [18] (black solid curves). The dynamical model predictions from [19] (green dashed-double-dotted curves) and DMT [20] (blue dashed-dotted curves) are shown alongside the phenomenological MAID2003 [21] (red dotted curves) and SAID [22] (black dashed-triple-dotted curves) models. The hypercentral (long dashed curves) [23] and relativistic (short dashed curves) [3] constituent quark models have been included. Figure from [10].

List of References

[1] D. Drechsel and L. Tiator. *J. Phys. G: Nucl. Part. Phys.*, 18:449–497, 1992.

[2] N. Isgur et al. *Phys. Rev.*, D25:2394, 1982.

[3] S. Capstick and G. Karl. *Phys. Rev.*, D41:2767, 1990.

[4] A.J. Buchmann et al. *Phys. Rev.*, C55:448, 1997.

[5] H. Walker and G. Holzwarth. *Z. Phys.*, A357:317, 1997.

[6] L.D. van Buuren. PhD thesis, Vrije Universiteit Amsterdam, 2003.

[7] R. Fatemi et al. *Phys. Rev. Let.*, 91(22), 2003.

[8] M. Osipenko et al. *Phys. Rev. D*, 71:054007, 2005.

[9] L.D. van Buuren et al. *Phys. Rev. Let.*, 89:012001–1, 2002.

[10] V. Pascaluta et al. *Phys. Rept.*, 437:125, 2007.

[11] R.Beck et al. *Phys. Rev. C*, 61:035204, 2000.

[12] D. Elsner et al. *Eur. Phys. J*, A 27:91, 2006.

[13] Th. Pospischil et al. *Phys. Rev. Let.*, 86:2959, 2001.

[14] S. Stave et al. *Eur. Phys. J.*, A30:471, 2006.

[15] N.F. Sparveris et al. *Phys. Rev. Lett.*, 94:022003, 2005.

[16] K. Joo et al. *Phys. Rev. Let.*, 88:122001, 2002.

[17] C. Alexandrou. *Phys. Rev. Lett.*, page 94, 2005.

[18] T.A. Gail and T.R. Hemmert. *arXiv:nucl-th/0512082*, 2006.

[19] T. Sato and T. S. H. Lee. *Phys. Rev.*, C63:055201, 2001.

[20] S.S. Kamalov et al. *Phys. Rev. C*, 64:032201, 2001.

[21] D. Drechsel et al. *Phys. Rev. D*, 63:114010, 2001.

[22] R.A. Arndt et al. *Phys. Rev. C*, 66:055213, 2002.

[23] m. De Sanctis et al. *Nucl. Phys. A*, A755:294, 2005.

[24] B. Povh et al. *Particles and Nuclei.* Springer-Verlag Berlin Heidelberg NewYork, 1999.

[25] R. H. Landau. *Quantum Mechanics 2: A Second Course in Quantum Theory.* John Wiley and Sons, Inc., 1996.

[26] A. D. Martin F. Halzen. *Quarks and Leptons: An Introductory Course in Modern Particle Physics.* John Wiley and Sons, Inc., 1984.

[27] S. Weinberg. *Phys. Rev. Lett.*, 19:1264, 1967.

[28] A. Salam. *Elementary Particle Theory.* Stockholm: Almquist and Wiksell, 1968.

[29] K. G. Wilson. *Phys. Rev.*, 10:2445, 1974.

[30] S. Capstick and W. Roberts. *Phys. Rev.*, 58:074011, 1998.

[31] D. O. Riska and G. E. Brown. *Nucl. Phys.*, A679:577, 2001.

[32] N. M. Kroll and M.A. Ruderman. *Phys. Rev.*, 93:233, 1954.

[33] G. F. Chew et al. *Phys. Rev.*, 106:1345, 1957.

[34] S. Fubini et al. *Nuovo Cim.*, 40:1171, 1965.

[35] F. A. Berends et al. *Nucl. Phys.*, B4:1, 1967.

[36] R. D. Peccei. *Phys. Rev.*, 181:1902, 1969.

[37] I. Blomqvist and J. M. Laget. *Nucl. Phys.*, A280:405, 1977.

[38] L. Tiator et al. *Nucl. Phys.*, A333:343, 1980.

[39] L. Tiator and L.E. Wright. *Phys. Rev.*, C30:989, 1984.

[40] T. Sato and T. S. H. Lee. *Phys. Rev.*, C54:055201, 1996.

[41] D. Drechsel et al. *Nucl. Phys.*, A645:145, 1999.

[42] R. L. Walker. *Phys. Rev.*, 182:1729, 1969.

[43] R.D. Morehouse et al. *Electromagnetic Interactions of Hadrons.* Plenum-Press, New York and London, 1978.

[44] G.L. Caia et al. *Phys. Rev.*, C72:035203, 2005.

[45] G. Blanpied et al. *Phys. Rev. Let.*, 79:4337, 1997.

[46] R.Beck et al. *Phys. Rev. Let.*, 78:606, 1997.

[47] G. Galler et al. *Phys. Let.*, B 503:245, 2001.

[48] F. Kalleicher et al. *Z. Phys.*, A359:201, 1997.

[49] C. Mertz et al. *Phys. Rev. Let.*, 86:2963, 2001.

[50] J.J. Kelly et al. *Phys. Rev. Lett.*, 95:102001, 2005.

[51] L.D. van Buuren et al. *Nucl. Phys.*, A684:324–326, 2001.

[52] S.D. Drell J.D. Bjorken. *Relativistic Quantum Mechanics*. McGraw-Hill, 1965.

[53] T.W. Donnelly and A.S. Raskin. *Ann. Phys.*, 169:247–351, 1986.

[54] T.W. Donnelly. Polarization degrees of freedom in electron scattering from nuclei, 1985.

[55] T.W. Donnelly. Spin observables in electron scattering from nuclei. In *Spin Observables of Nuclear Probes*, 1988.

[56] M. Jacob and G.C. Wick. *Ann. Phys.*, 7:404, 1959.

[57] J.J. Kubis. *Phys. Rev.*, D6:547, 1972.

[58] G. Penner. PhD thesis, Giessen University, 2002.

[59] G.V. Gehlen. *Nucl. Phys.*, B9:17, 1969.

[60] G.L. Caia. PhD thesis, Ohio University, 2004.

[61] J. R. Lopez. PhD thesis, Mainz University, 2003.

[62] A. Chodos et al. *Phys. Rev.*, D9:3471, 1974.

[63] A. Chodos and C.B. Thorn. *Phys. Rev.*, D12:2733, 1975.

[64] R.D. Viollier et al. *Nucl. Phys.*, A406:269, 1983.

[65] V. Vento et al. *Phys. Lett.*, B102:97, 1981.

[66] G. Kälbermann and J.M. Eisenberg. *Phys. Rev.*, D28:71, 1983.

[67] V. Vento. *Phys. Lett.*, B121:370, 1983.

[68] A.W. Thomas. *Advances in Nuclear Physics vol. 13*. New York: Plenum, 1984.

[69] T.H.R. Skyrme. *Proc. R. Soc.*, A260:127, 1961.

[70] G. Eckart and B. Schwesinger. *Nucl. Phys.*, A458:620, 1986.

[71] H.J. Schnitzer. *Nucl. Phys.*, B261:546, 1985.

[72] G. 't Hooft. *Nucl. Phys.*, B72:461, 1973.

[73] E. Witten. *Nucl. Phys.*, B160:57, 1979.

[74] http://mitbates.lns.mit.edu/bates/control/main MIT-Bates Website, 2004.

[75] M. Farkhondeh et al. Operation of the MIT-Bates polarized source for a high average current storage ring. In *Proceedings of the SPIN-2004 Symposium*, 2004. PESP-2004 Workshop.

[76] G.T. Zwart. *Polarized electrons at the Bates Accelerator Center South Hall Ring: Extracted beams and internal targets.* PhD thesis, Boston University, 1986.

[77] The BLAST Collaboration. *MIT-Bates South Hall Ring Technical Design Report*, 1994. Internal report.

[78] K. Dow. (private communication), 2005.

[79] K. A. Dow, M. Farkhondeh, and J. D. Zumbro. South hall ring: Magnetic measurements of the lattice dipoles. Technical report, Bates Linear Accelerator Center, 1993.

[80] Townsend Zwart. (private communication), 2005.

[81] K. B. Unser. The parametric current transformer: A beam current monitor developed for LEP. *AIP Conf. Proc.*, 252:266–275, 1991.

[82] Martina H. Hurwitz. The Compton polarimeter at bates. Technical report, Bates Linear Accelerator Center, 2003.

[83] W. Franklin. The bates south hall ring: a unique instrument for studying polarization. In *Proceedings of the SPIN-2004 Symposium*, 2004.

[84] W.E. Adams. *Pockels cells: Theory, test procedures, characteristics*, 1968. UCRL-50463.

[85] V.S. Morozov et al. Spin-flipping polarized electrons. *Phys. Rev. ST Accel. Beams*, 4:104002, 2001.

[86] Taylan Akdogan. (private communication), 2005.

[87] M. Ferro-Luzzi. *Phys. Rev. Lett.*, 77:2630, 1996.

[88] E. Ihloff et al. Hydrogen/deuterium polarized target at MIT-Bates. In *Proceedings for the SPIN 2004 Conference, Trieste, Italy*, 2005.

[89] V. Ziskin. PhD thesis, Massachusetts Institute of Technology, 2005.

[90] A. Beiser. *Concepts of Modern Physic.* McGraw-Hill, 1995.

[91] A. Roth. *Vacuum Technology.* North-Holland, Amsterdam, 1982.

[92] R. Alarcon (BLAST Collaboration). *Electronuclear Physics with Internal Targets and the BLAST Detector*, page 1, 1999.

[93] The BLAST Collaboration. The BLAST technical design report, 1997.

[94] K. Dow et al.. *Magnetic Measurements of the BLAST Spectrometer*, 2005.

[95] W.R. Leo. *Techniques for Nuclear and Particle Physics Experiments*. Springer-Verlag, 1994.

[96] W. Blum and L. Rolandi. *Particle Detection with Drift Chambers*. Springer-Verlag, 1993.

[97] F. Sauli. *Principles of Operation of Multiwire Proportional and Drift Chambers*. Lectures given in the Academic Programme of CERN 1975-1976, 1977.

[98] D. Hasell. (private communication), 2005.

[99] A.J. Maschinot. PhD thesis, Massachusetts Institute of Technology, 2005.

[100] Frederick Tong uk Lee. (private communication), 2005.

[101] B. Tonguc et al. *Nucl. Instrum. Meth.*, A553:364–369, 2005.

[102] D. Green. *The Physics of Particle Detectors*. Cambridge University Press, 2000.

[103] A.T. Sindile. PhD thesis, University of New Hampshire, 2006.

[104] Bicron Saint-Gobain Detectors. Bc-408: Premium plastic scintillator, 2003.

[105] http://coda.jlab.org CODA Website.

[106] C.B. Crawford. PhD thesis, Massachusetts Institute of Technology, 2005.

[107] P.J. Karpius. PhD thesis, University of New Hampshire, 2005.

[108] N. Meitanis. PhD thesis, Massachusetts Institute of Technology, 2006.

[109] C. Zhang. PhD thesis, Massachusetts Institute of Technology, 2006.

[110] W.H. Press et al. *Numerical Recipes in C*. Cambridge University Press, 1988.

[111] M. Kohl. (private communication), 2006.

[112] A.J. Maschinot. (private communication), 2005.

[113] E.J. Geis. (private communication), 2006.

[114] I. Passchier. PhD thesis, Vrije Universiteit Amsterdam, 2000.

[115] W. Greiner and J. Reinhardt. *Quantum Electrodynamics*. Springer-Verlag Berlin Heidelberg New York, 1992.

[116] I. Akushevich N. Shumeiko, A. Ilyichev. *arXiv:hep-ph/0106180*, 2001.

[117] I. Akushevich et al. *arXiv:hep-ph/9906408*, 1999.

[118] A. Afanasev et al. *Phys. Rev.*, D64:113009, 2001.

[119] L.W. Mo and Y. Tsai. *Rev. Mod. Phys.*, 41:205, 1969.

[120] D.Y. Bardin and N.M. Shumeiko. *Nucl. Phys.*, B127:242, 1977.

[121] A. Afanasev et al. *arXiv:hep-ph/0308106*, 2003.

[122] Radiative Corrections Website: http://www.jlab.org/RC/.

[123] I. Akushevich and N. Shumeiko. *J. Phys.*, G20:513, 1994.

[124] I. Akushevich et al. *arXiv:hep-ph/9706516*, 1997.

[125] L.D. van Buuren. (private communication), 2004.

[126] I. Akushevich. (private communication), 2004.

[127] A. Ilyichev. (private communication), 2006.

[128] A. Ilyichev. Blast collaboration meeting, July 14 2006.

[129] C.B. Crawford et al. *Phys. Rev. Lett.*, 98:052301, 2007.

[130] L. Lyons. *Statistics for Nuclear and Particle Physicists*. Cambridge University Press, 1986.

[131] E.J. Geis. PhD thesis, Arizona State University, 2007.

APPENDIX A

Differential Cross Section for Electron Scattering

Recall that

$$\mathcal{R}_{fi} = \chi_e(K';K,S)_{\mu\nu} W^{\mu\nu}(q)_{fi}$$

By contracting the nuclear tensor $W^{\mu\nu}$ with the electron tensor χ_e we get using current conservation and denoting $P = K + K'$ [53]

$$\mathcal{R}_{fi} = |P_\mu J^\mu(\mathbf{q})_{fi}| + q^2 J^*_\mu(\mathbf{q})_{fi} J^\mu(\mathbf{q})_{fi} - 2hi\epsilon_{\mu\nu\alpha\beta} K^\alpha K'^\beta J^{\mu *}(\mathbf{q})_{fi} J^\nu(\mathbf{q})_{fi}$$

where

$$J^0(\mathbf{q})_{fi} = \rho(\mathbf{q})_{fi}$$

is the Fourier transform of the transition charge density, while

$$\mathbf{J}(\mathbf{q})_{fi} = \sum_{m=0,\pm 1} J(\mathbf{q};m)_{fi} \mathbf{e}^*(\mathbf{q};1,m)$$

is the expansion of the Fourier transform of the transition three-curent distribution (convection and magnetization) in terms of the standard unit spherical vectors (see Figure 2-2 for the definition of the $\mathbf{u}$ vectors)

$$\begin{aligned} \mathbf{e}(\mathbf{q};1,0) &= \mathbf{u}_z \\ \mathbf{e}(\mathbf{q};1,\pm 1) &= \mp(1/\sqrt{2})\,(\mathbf{u}_x \pm i\mathbf{u}_y) \end{aligned}$$

From current conservation

$$Q^0 J^0(\mathbf{q})_{fi} - \mathbf{q}\cdot\mathbf{J}(\mathbf{q})_{fi} = \omega\rho(\mathbf{q})_{fi} - qJ(\mathbf{q};0)_{fi} = 0$$

so that $J(\mathbf{q};0)_{fi} = (\omega/q)\rho(\mathbf{q})_{fi}$, then eliminating $J(\mathbf{q};0)_{fi}$ from $\mathcal{R}_{fi}$ we get

$$\begin{aligned} (\mathcal{R}_{fi})^{unpol} &= |P^0 J^0(\mathbf{q})_{fi} - \mathbf{P}\cdot\mathbf{J}(\mathbf{q})_{fi}|^2 + (q^2)^2(|J^0(\mathbf{q})_{fi}|^2 - \mathbf{J}^*(\mathbf{q})_{fi}\cdot\mathbf{J}(\mathbf{q})_{fi}) \\ (\mathcal{R}_{fi})^{unpol} &\equiv v_0(v_L\mathcal{R}^L_{fi} + v_T\mathcal{R}^T_{fi} + v_{TT}\mathcal{R}^{TT}_{fi} + v_{TL}\mathcal{R}^{TL}_{fi}) \end{aligned}$$

and for the polarized part

$$\begin{aligned} (\mathcal{R}_{fi})^{pol} &= -2hi\epsilon_{\mu\nu\alpha\beta} K^\alpha K'^\beta J^{\mu *}(\mathbf{q})_{fi} J^\nu(\mathbf{q})_{fi} \\ (\mathcal{R}_{fi})^{pol} &\equiv hv_0(v_{T'}\mathcal{R}^{T'}_{fi} + v_{TL'}\mathcal{R}^{TL'}_{fi}) \end{aligned}$$

We can identify now the nuclear response functions, $\mathcal{R}^K_{fi}$ as

$$\begin{aligned}
\mathcal{R}^L_{fi} &= |\rho(\mathbf{q})_{fi}|^2 \\
\mathcal{R}^T_{fi} &= |J(\mathbf{q};+1)_{fi}|^2 + |J(\mathbf{q};-1)_{fi}|^2 \\
\mathcal{R}^{TT}_{fi} &= 2\Re\{J^*(\mathbf{q};+1)_{fi} J(\mathbf{q};-1)_{fi}\} \\
\mathcal{R}^{TL}_{fi} &= -2\Re\{\rho^*(\mathbf{q})_{fi}(J(\mathbf{q};+1)_{fi} - J(\mathbf{q};-1)_{fi})\} \\
\mathcal{R}^{T'}_{fi} &= |J(\mathbf{q};+1)_{fi}|^2 - |J(\mathbf{q};-1)_{fi}|^2 \\
\mathcal{R}^{TL'}_{fi} &= -2\Re\{\rho^*(\mathbf{q})_{fi}(J(\mathbf{q};+1)_{fi} + J(\mathbf{q};-1)_{fi})\}
\end{aligned}$$

Thus the differential cross section becomes

$$\begin{aligned}
\left(\frac{d\sigma}{d\Omega_e}\right)^h_{fi} &= \sigma_{Mott} f^{-1}_{rec}\Big[\left(v_L\mathcal{R}^L_{fi} + v_T\mathcal{R}^T_{fi} + v_{TT}\mathcal{R}^{TT}_{fi} + v_{TL}\mathcal{R}^{TL}_{fi}\right) \\
&\qquad + h\left(v_{T'}\mathcal{R}^{T'}_{fi} + v_{TL'}\mathcal{R}^{TL'}_{fi}\right)\Big] \\
&\equiv \Sigma_{fi} + h\Delta_{fi}
\end{aligned}$$

Partial cross sections in terms of multipoles

The four partial cross sections, that appear in the inclusive cross section, can be expressed in terms of the CGLN amplitudes [33] as follows

$$\sigma_T = 4\pi\frac{|\vec{k}_\pi|}{k^{cm}_\gamma}\sum_l \frac{1}{2}(l+1)^2\left[(l+2)\left(|E_{l+}|^2 + |M_{l+1,-}|^2\right) + l\left(|M_{l+}|^2 + |E_{l+1,-}|^2\right)\right]$$

$$\sigma_L = 4\pi\frac{|\vec{k}_\pi|}{k^{cm}_\gamma}\sum_l (l+1)^3\left[|L_{l+}|^2 + |L_{l+1,-}|^2\right]$$

$$\sigma_{TL'} = 4\pi\frac{|\vec{k}_\pi|}{k^{cm}_\gamma}\sum_l \frac{1}{2}(l+1)^2\left[-L^*_{l+}\left((l+2)E_{l+} + lM_{l+}\right) + L^*_{l+1,-}\left(lE_{l+1,-} + (l+2)M_{l+1,-}\right)\right]$$

$$\begin{aligned}
\sigma_{TT'} = 4\pi\frac{|\vec{k}_\pi|}{k^{cm}_\gamma}\sum_l \frac{1}{2}(l+1)\Big[&-(l+2)\left(|E_{l+}|^2 + |M_{l+1,-}|^2\right) + l\left(|M_{l+}|^2 + |E_{l+1,-}|^2\right) \\
&- 2l(l+2)\left(E^*_{l+}M_{l+} - E^*_{l+1,-}M_{l+1,-}\right)\Big]
\end{aligned}$$

where

$$\mathbf{k}_\gamma = \frac{M}{W}\mathbf{q}, \qquad W = \sqrt{2M\nu + M^2 - Q^2}, \qquad \nu = E_e - E'_e$$

and k_γ and k_π are the center of mass momenta of the photon and pion, respectively.

APPENDIX B

BLAST Laboratory Frame

The center of the BLAST system is the center of the target cell (the target cell is a cylinder whose inside gas cavity is $60cm$ in length). The BLAST $+z$-axis is defined to point in the direction of the electron beam; this direction is also the direction along which the target cell runs. The BLAST $+y$-axis points vertically upward (i.e. perpendicular to and away from the floor of the BLAST setup). The BLAST $+x$-axis points in the remaining direction so as to form a right-handed coordinate system with the $+y_B$ and the $+z_B$ axes; the $+x_B$ axis points to the left sector of the BLAST detector. This is shown schematically in Figures 5-69 and 3-12.

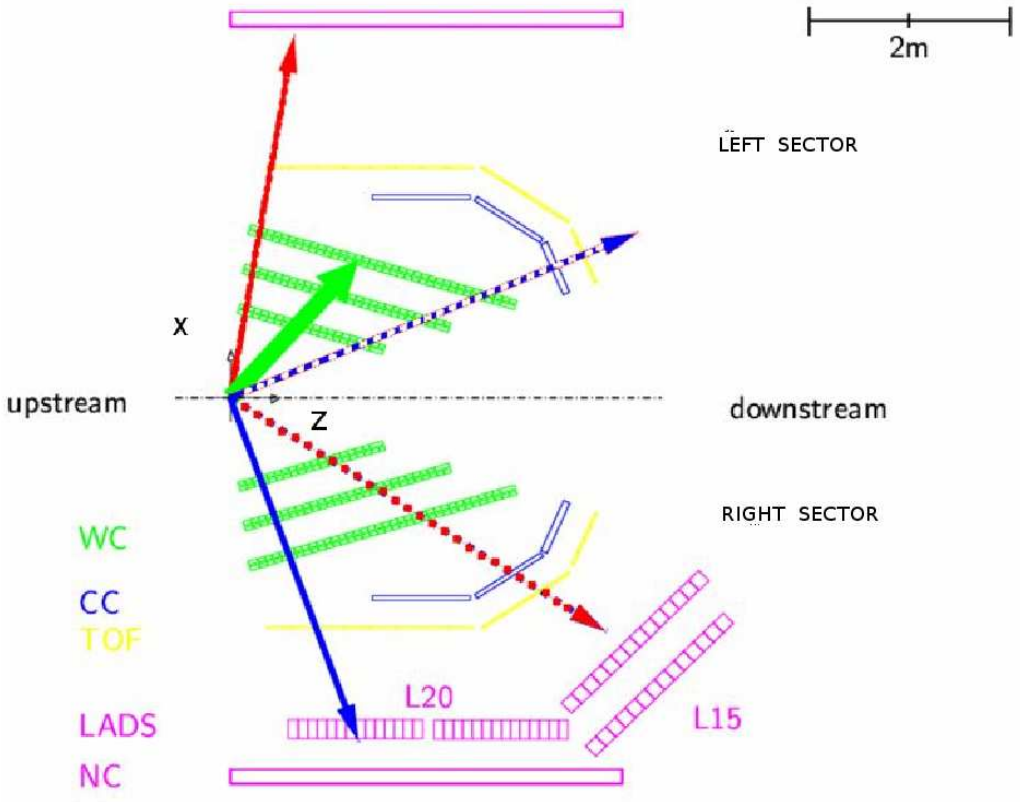

Figure 5-69: Top view of the BLAST detector (schematic).

BLAST Target Spin Angle

In order to get the target spin angles in the q-system (defined by $\mathbf{u}_x$, $\mathbf{u}_y$, and $\mathbf{u}_z$ as given in Figure 2-2), we need to perform two rotations as shown in Figure 5-70: one of angle ϕ_e from BLAST laboratory frame to the scattering plane around the z_B-axis, and the other one of angle θ_q around y_{SC}-axis.

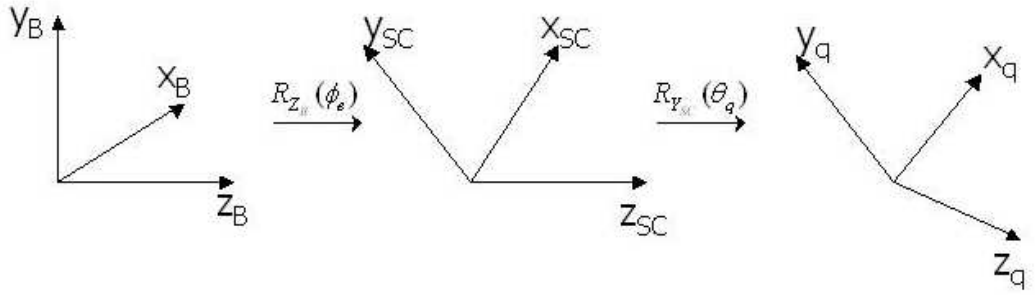

Figure 5-70: The two rotations from BLAST laboratory frame to q-system.

We denote the axes in the BLAST laboratory frame by x_B, y_B, z_B,in the scattering frame by x_{SC}, y_{SC}, z_{SC}, and in the q-frame by $x_q \equiv \mathbf{u}_x$, $y_q \equiv \mathbf{u}_y$, $z_q \equiv \mathbf{u}_z$.

The 3×3 rotation matrix can be written in the following form:

$$\hat{R} = \begin{pmatrix} R_{11}\, R_{12}\, R_{13} \\ R_{21}\, R_{22}\, R_{23} \\ R_{31}\, R_{32}\, R_{33} \end{pmatrix}$$

In the case of the first rotation from the BLAST frame to the scattering frame by the angle ϕ_e around z_B, the matrix elements are:

$$\begin{aligned}
R_{11} &= \mathbf{x}_{SC} \cdot \mathbf{x}_B = \cos\phi_e \\
R_{12} &= \mathbf{x}_{SC} \cdot \mathbf{y}_B = \cos\left(\frac{\pi}{2} - \phi_e\right) = \sin\phi_e \\
R_{13} &= \mathbf{x}_{SC} \cdot \mathbf{z}_B = 0 \\
R_{21} &= \mathbf{y}_{SC} \cdot \mathbf{x}_B = \cos\left(\frac{\pi}{2} + \phi_e\right) = -\sin\phi_e \\
R_{22} &= \mathbf{y}_{SC} \cdot \mathbf{y}_B = \cos\phi_e \\
R_{23} &= \mathbf{y}_{SC} \cdot \mathbf{z}_B = 0 \\
R_{31} &= \mathbf{z}_{SC} \cdot \mathbf{x}_B = 0 \\
R_{32} &= \mathbf{z}_{SC} \cdot \mathbf{y}_B = 0 \\
R_{33} &= \mathbf{z}_{SC} \cdot \mathbf{z}_B = 1
\end{aligned}$$

Thus the first rotation matrix is:

$$\hat{R}_{Z_B}(\phi_e) = \begin{pmatrix} \cos\phi_e & \sin\phi_e & 0 \\ -\sin\phi_e & \cos\phi_e & 0 \\ 0 & 0 & 1 \end{pmatrix}$$

In the case of the second rotation from the scattering frame to the q-frame by the angle θ_q around y_{SC}, the matrix elements are:

$$\begin{aligned} R_{11} &= \mathbf{x}_q \cdot \mathbf{x}_{SC} = \cos\theta_q \\ R_{12} &= \mathbf{x}_q \cdot \mathbf{y}_{SC} = 0 \\ R_{13} &= \mathbf{x}_q \cdot \mathbf{z}_{SC} = \cos\left(\frac{\pi}{2} - \theta_q\right) = \sin\theta_q \\ R_{21} &= \mathbf{y}_q \cdot \mathbf{x}_{SC} = 0 \\ R_{22} &= \mathbf{y}_q \cdot \mathbf{y}_{SC} = 1 \\ R_{23} &= \mathbf{y}_q \cdot \mathbf{z}_{SC} = 0 \\ R_{31} &= \mathbf{z}_q \cdot \mathbf{x}_{SC} = \cos\left(\frac{\pi}{2} + \theta_q\right) = -\sin\theta_q \\ R_{32} &= \mathbf{z}_q \cdot \mathbf{y}_{SC} = 0 \\ R_{33} &= \mathbf{z}_q \cdot \mathbf{z}_{SC} = \cos\theta_q \end{aligned}$$

So the second rotation matrix is:

$$\hat{R}_{Z_B}(\theta_q) = \begin{pmatrix} \cos\theta_q & 0 & \sin\theta_q \\ 0 & 1 & 0 \\ -\sin\theta_q & 0 & \cos\theta_q \end{pmatrix}$$

Now, the rotation matrix from the BLAST frame to the q-frame can be written

$$\hat{R} = \hat{R}_{Z_B}(\theta_q) \cdot \hat{R}_{Z_B}(\phi_e) = \begin{pmatrix} \cos\theta_q & 0 & \sin\theta_q \\ 0 & 1 & 0 \\ -\sin\theta_q & 0 & \cos\theta_q \end{pmatrix} \begin{pmatrix} \cos\phi_e & \sin\phi_e & 0 \\ -\sin\phi_e & \cos\phi_e & 0 \\ 0 & 0 & 1 \end{pmatrix}$$

$$\hat{R} = \begin{pmatrix} \cos\phi_e\cos\theta_q & \sin\phi_e\cos\theta_q & \sin\theta_q \\ -\sin\phi_e & \cos\phi_e & 0 \\ -\cos\phi_e\sin\theta_q & -\sin\phi_e\sin\theta_q & cos\theta_q \end{pmatrix}$$

If we denote the target spin in the BLAST frame by $\mathbf{s}_B$ and in the q-frame by $\mathbf{s}_q$, which, in matrix form are defined by

$$\mathbf{s}_B = \begin{pmatrix} \sin\theta_T \\ 0 \\ \cos\theta_T \end{pmatrix}, \qquad \mathbf{s}_q = \begin{pmatrix} x^* \\ y^* \\ z^* \end{pmatrix} = \begin{pmatrix} \sin\theta^*\cos\phi^* \\ \sin\theta^*\sin\phi^* \\ \cos\theta^* \end{pmatrix}$$

where θ_T is the target spin angle and lies in the $x_B - z_B$ plane (the thick green arrow in

Figure 5-69), and makes an angle of 48° relative to the beam line (z_B-axis). Then

$$\mathbf{s}_q = \hat{R} \cdot \mathbf{s}_B$$

From Figure 2-2 we see that

$$\cos\theta^* = \frac{\mathbf{s}_q \cdot \mathbf{q}}{|\mathbf{q}|} = s_{qz}$$

Hence

$$\cos\theta^* = -\sin\theta_T \cos\phi_e \sin\theta_q + \cos\theta_T \cos\theta_q$$

and

$$\cos\phi^* = \frac{\sin\theta_T \cos\phi_e \cos\theta_q + \cos\theta_T \sin\theta_q}{\sin\theta^*}$$

At BLAST:

$$\phi_q = \phi_e + \pi$$

$$\phi_e^{RIGHT} = 180^\circ - \phi_e^{LEFT}$$

Summarizing, the BLAST laboratory frame is shown in Figures 5-69 and 3-12, and has the center in the middle of the target cell; its axes are defined as follows:

$$\mathbf{z} = \mathbf{z}_B = \mathbf{k}, \qquad \mathbf{y} = \mathbf{y}_B = \textit{upward to the sky}, \qquad \mathbf{x} = \mathbf{x}_B = \mathbf{y}_B \times \mathbf{z}_B$$

The scattering frame is defined by

$$\mathbf{z}_{SC} = \mathbf{z}_B = \mathbf{k}, \qquad \mathbf{y}_{SC} = \mathbf{k} \times \mathbf{k}', \qquad \mathbf{x}_{SC} = \mathbf{y}_{SC} \times \mathbf{z}_{SC}$$

The q-frame is given by

$$\mathbf{z}_q = \frac{\mathbf{q}}{|\mathbf{q}|}, \qquad \mathbf{y}_q = \mathbf{y}_{SC} = \mathbf{z}_q \times \mathbf{z}_B, \qquad \mathbf{x}_q = \mathbf{y}_q \times \mathbf{z}_q$$

See Figures 2-2, 2-1 and 4-4 for notation.

APPENDIX C

Asymmetries Values and Errors

In this appendix we present the values and errors for the results given in section 5.1.

Runs type	$Q^{++}(C)$	$Q^{--}(C)$	$Q^{+-}(C)$	$Q^{-+}(C)$	$Q_{TOTAL}(C)$
Empty runs	8212.0566	7947.0034	8113.4727	7805.4653	32077.998
Data runs	72184.3359	71615.7344	72057.2578	71922.2578	287779.5859

Table 5.14: Charge information for $\vec{p}(\vec{e},e')p$ runs.

The following notation is used:

W	: average W value
Q^2	: average Q^2 value
x	: average x value
$Y^{\pm\pm} = \frac{N^{\pm\pm}}{Q^{\pm\pm}}$	: total yields for the data runs
$Y^{\pm\pm}_{rad} = \frac{N^{\pm\pm}_{rad}}{Q^{\pm\pm}_{rad}}$	: normalized radiative tail yields
$Y^{\pm\pm}_{empty} = \frac{N^{\pm\pm}_{empty}}{Q^{\pm\pm}_{empty}}$	: total yields for the empty target data
$A_{L,R}$	: left and right sectors asymmetries
$\delta A^{stat}_{L,R}$	: $A_{L,R}$ statistical errors
$A^{beam}_{L,R}$	: left and right sectors beam asymmetries
$\delta A^{beam}_{L,R}$	: $A^{beam}_{L,R}$ statistical errors
$A^{target}_{L,R}$	: left and right sectors target asymmetries
$\delta A^{target}_{L,R}$	: $A^{target}_{L,R}$ statistical errors
δP	: $P = P_b \cdot P_t$ systematic errors
$\delta A^{syst}_{L,R}$	: $A_{L,R}$ systematical errors

$W\,[GeV]$	1.096	1.138	1.184	1.22	1.258	1.303	1.33
Y^{++}	0.17685	0.25376	0.42690	0.54883	0.43564	0.34852	0.32872
Y^{--}	0.17715	0.25254	0.42827	0.54969	0.43905	0.33843	0.33103
Y^{+-}	0.19105	0.26998	0.44336	0.53798	0.44117	0.34827	0.35421
Y^{-+}	0.19480	0.28785	0.43515	0.53285	0.43225	0.35578	0.34268
Y^{++}_{empty}	0.04042	0.03860	0.03811	0.04286	0.05467	0.07915	0.08268
Y^{--}_{empty}	0.02491	0.04114	0.04441	0.04542	0.05473	0.07122	0.08795
Y^{+-}_{empty}	0.02428	0.03340	0.04375	0.05657	0.05990	0.08356	0.09367
Y^{-+}_{empty}	0.03625	0.04048	0.05611	0.04291	0.05303	0.06815	0.10800
Y^{++}_{rad}	0.11089	0.08924	0.07095	0.05990	0.04599	0.03514	0.02844
Y^{--}_{rad}	0.10859	0.08959	0.07280	0.05992	0.04876	0.03620	0.02772
Y^{+-}_{rad}	0.13236	0.10685	0.08796	0.07470	0.06028	0.04971	0.03779
Y^{-+}_{rad}	0.12988	0.10344	0.09008	0.07374	0.06088	0.04919	0.03843
A_L	-0.11117	-0.09264	0.04282	0.07337	0.04437	0.02391	0.03048
δA_L^{stat}	0.01605	0.01769	0.01040	0.00810	0.01051	0.01578	0.01840
A_L^{beam}	0.01147	0.04244	-0.01226	-0.00602	-0.01620	0.03307	-0.03002
δA_L^{beam}	0.00552	0.00442	0.00325	0.00285	0.00335	0.00428	0.00488
A_L^{target}	-0.01347	-0.03700	0.00876	0.00428	0.00725	0.00485	0.02003
δA_L^{target}	0.00552	0.00442	0.00325	0.00285	0.00335	0.00428	0.00488
δP_L	0.00129	0.00117	0.00045	0.00080	0.00045	0.00022	0.00044
δA_L^{syst}	0.00924	0.02919	0.00782	0.00390	0.00920	0.01732	0.01870

Table 5.15: BLAST left sector yields and asymmetries for $Q^2 = 0.123\,GeV^2$, and for each $W\,[GeV]$ bin over the Δ region.

$W\,[GeV]$	1.096	1.138	1.184	1.22	1.258	1.303	1.33
Y^{++}	0.18021	0.27940	0.47576	0.59221	0.44857	0.35586	0.33091
Y^{--}	0.19382	0.26941	0.47560	0.59087	0.45646	0.34962	0.34049
Y^{+-}	0.20791	0.27453	0.39624	0.48966	0.40229	0.32604	0.30489
Y^{-+}	0.20702	0.26574	0.39891	0.50581	0.39574	0.33138	0.32249
Y^{++}_{empty}	0.02922	0.02666	0.04030	0.03921	0.06149	0.06222	0.07196
Y^{--}_{empty}	0.03233	0.03674	0.05612	0.03926	0.05209	0.06505	0.08732
Y^{+-}_{empty}	0.03007	0.03845	0.04375	0.05484	0.05657	0.07025	0.09330
Y^{-+}_{empty}	0.03228	0.03984	0.04407	0.04035	0.05547	0.04765	0.08750
Y^{++}_{rad}	0.09101	0.08058	0.07163	0.05863	0.04674	0.03562	0.02758
Y^{--}_{rad}	0.09936	0.08305	0.07759	0.06196	0.04978	0.03559	0.03064
Y^{+-}_{rad}	0.11075	0.10054	0.09201	0.07505	0.06252	0.05236	0.04038
Y^{-+}_{rad}	0.11061	0.09990	0.09361	0.07511	0.06421	0.05234	0.04272
A_R	-0.11230	0.19230	0.27915	0.25117	0.20143	0.14274	0.20598
δA_R^{stat}	0.01496	0.01695	0.01076	0.00812	0.01101	0.01488	0.01929
A_R^{beam}	-0.04268	0.00258	0.00362	0.01738	-0.01934	0.02139	0.01793
δA_R^{beam}	0.00788	0.00658	0.00501	0.00432	0.00522	0.00636	0.00753
A_R^{target}	-0.03755	0.04070	-0.00320	-0.01446	-0.00180	0.00163	-0.05842
δA_R^{target}	0.00516	0.00427	0.00325	0.00280	0.00340	0.00412	0.00487
δP_R	0.00086	0.00124	0.00214	0.00199	0.00164	0.00112	0.00178
δA_R^{syst}	0.02947	0.02120	0.00383	0.01202	0.01031	0.01122	0.03175

Table 5.16: BLAST right sector yields and asymmetries for $Q^2 = 0.123\,GeV^2$, and for each $W\,[GeV]$ bin over the Δ region.

$W\,[GeV]$	1.096	1.138	1.184	1.22	1.258	1.303	1.33
Y^{++}	0.12193	0.17003	0.24314	0.30696	0.25401	0.19181	0.14149
Y^{--}	0.12634	0.16640	0.25985	0.29603	0.25155	0.19550	0.14241
Y^{+-}	0.14037	0.17530	0.24975	0.29073	0.25744	0.19420	0.15312
Y^{-+}	0.14539	0.17692	0.24330	0.29683	0.25120	0.19703	0.15086
Y^{++}_{empty}	0.02666	0.03409	0.02703	0.03239	0.03640	0.04310	0.04249
Y^{--}_{empty}	0.02755	0.02365	0.02189	0.02617	0.03737	0.03510	0.03888
Y^{+-}_{empty}	0.03167	0.02797	0.03315	0.03142	0.03537	0.04042	0.04498
Y^{-+}_{empty}	0.02216	0.02152	0.03113	0.03241	0.03382	0.04304	0.04022
Y^{++}_{rad}	0.05754	0.03807	0.02607	0.01872	0.01391	0.00908	0.00539
Y^{--}_{rad}	0.05580	0.03930	0.02621	0.02025	0.01337	0.00861	0.00474
Y^{+-}_{rad}	0.07163	0.05145	0.03654	0.02804	0.02093	0.01454	0.00868
Y^{-+}_{rad}	0.07248	0.05105	0.03705	0.02712	0.02100	0.01570	0.00878
A_L	-0.16558	0.00507	0.11466	0.07053	0.01622	0.04542	-0.04219
δA_L^{stat}	0.02074	0.02094	0.01341	0.01117	0.01368	0.01919	0.02698
A_L^{beam}	0.00299	0.01836	-0.05226	0.03185	-0.00876	-0.00290	-0.01622
δA_L^{beam}	0.00681	0.00559	0.00434	0.00394	0.00451	0.00575	0.00757
A_L^{target}	-0.04551	0.00700	-0.02316	0.00902	0.02021	-0.02201	0.00687
δA_L^{target}	0.00681	0.00559	0.00434	0.00394	0.00451	0.00575	0.00757
δP_L	0.00192	0.00017	0.00122	0.00089	0.00022	0.00049	0.00036
δA_L^{syst}	0.02371	0.01019	0.02964	0.01718	0.01142	0.01151	0.00914

Table 5.17: BLAST left sector yields and asymmetries for $Q^2 = 0.175\,GeV^2$, and for each $W\,[GeV]$ bin over the Δ region.

$W\,[GeV]$	1.096	1.138	1.184	1.22	1.258	1.303	1.33
Y^{++}	0.13347	0.18118	0.28470	0.37999	0.32299	0.25012	0.17836
Y^{--}	0.12617	0.17522	0.29897	0.38990	0.32881	0.25413	0.17649
Y^{+-}	0.14546	0.17445	0.24913	0.31606	0.28037	0.22681	0.16788
Y^{-+}	0.14839	0.18093	0.25263	0.31669	0.29305	0.23121	0.16645
Y^{++}_{empty}	0.02886	0.02873	0.02910	0.03689	0.03726	0.05224	0.04578
Y^{--}_{empty}	0.02491	0.02629	0.03800	0.03133	0.04114	0.05071	0.04441
Y^{+-}_{empty}	0.02686	0.02970	0.03056	0.04560	0.04202	0.05262	0.05410
Y^{-+}_{empty}	0.02690	0.02741	0.02856	0.03420	0.04112	0.06367	0.05009
Y^{++}_{rad}	0.05050	0.03402	0.02500	0.01893	0.01382	0.00889	0.00568
Y^{--}_{rad}	0.04930	0.03388	0.02426	0.01712	0.01411	0.00914	0.00569
Y^{+-}_{rad}	0.06444	0.04689	0.03507	0.02807	0.02078	0.01683	0.00962
Y^{-+}_{rad}	0.06486	0.04884	0.03792	0.02909	0.02343	0.01682	0.00998
A_R	-0.14284	0.13216	0.21731	0.27230	0.18667	0.20253	0.17162
δA_R^{stat}	0.01958	0.01988	0.01272	0.01018	0.01170	0.01730	0.02411
A_R^{beam}	0.04940	0.04309	-0.02222	-0.01459	0.01311	0.00109	0.00187
δA_R^{beam}	0.01049	0.00855	0.00643	0.00556	0.00625	0.00810	0.01080
A_R^{target}	0.02079	-0.00177	-0.03641	-0.01655	-0.03446	-0.02312	0.01458
δA_R^{target}	0.00676	0.00551	0.00420	0.00362	0.00405	0.00526	0.00702
δP_R	0.00110	0.00077	0.00164	0.00210	0.00149	0.00162	0.00145
δA_R^{syst}	0.02779	0.02235	0.02216	0.01162	0.01916	0.01210	0.00775

Table 5.18: BLAST right sector yields and asymmetries for $Q^2 = 0.175\,GeV^2$, and for each $W\,[GeV]$ bin over the Δ region.

$W\,[GeV]$	1.096	1.138	1.184	1.22	1.258	1.303	1.33
Y^{++}	0.06624	0.08202	0.10728	0.14341	0.14205	0.13876	0.02567
Y^{--}	0.06541	0.07864	0.11167	0.14020	0.14008	0.13807	0.02612
Y^{+-}	0.07213	0.08410	0.10938	0.13915	0.13604	0.14852	0.02816
Y^{-+}	0.07006	0.08214	0.10957	0.13111	0.13121	0.14416	0.02869
Y^{++}_{empty}	0.01546	0.01327	0.01436	0.02338	0.03543	0.05004	0.00645
Y^{--}_{empty}	0.01270	0.01560	0.01283	0.01749	0.03548	0.04152	0.01145
Y^{+-}_{empty}	0.01552	0.01479	0.02009	0.01959	0.02958	0.04276	0.01663
Y^{-+}_{empty}	0.01332	0.01908	0.01306	0.02165	0.03254	0.05355	0.01063
Y^{++}_{rad}	0.02094	0.01224	0.00680	0.00411	0.00256	0.00220	0.00048
Y^{--}_{rad}	0.02234	0.01209	0.00657	0.00405	0.00250	0.00203	0.00034
Y^{+-}_{rad}	0.02912	0.01693	0.01027	0.00623	0.00523	0.00367	0.00085
Y^{-+}_{rad}	0.03042	0.01773	0.00961	0.00661	0.00481	0.00378	0.00068
A_L	-0.08465	0.08849	0.06741	0.07608	0.05128	-0.03970	0.15263
δA_L^{stat}	0.02940	0.03236	0.02093	0.01838	0.02420	0.02999	0.08682
A_L^{beam}	-0.01205	0.01107	-0.02252	-0.02074	-0.01419	-0.02049	0.00264
δA_L^{beam}	0.00986	0.00860	0.00685	0.00617	0.00709	0.00816	0.02247
A_L^{target}	0.02823	0.04163	-0.02463	0.04826	0.03374	0.02833	-0.03479
δA_L^{target}	0.00986	0.00859	0.00685	0.00617	0.00709	0.00816	0.02247
δP_L	0.00098	0.00090	0.00098	0.00105	0.00074	0.00028	0.00177
δA_L^{syst}	0.01593	0.02234	0.01732	0.02723	0.01898	0.01812	0.01816

Table 5.19: BLAST left sector yields and asymmetries for $Q^2 = 0.24\,GeV^2$, and for each $W\,[GeV]$ bin over the Δ region.

$W\,[GeV]$	1.096	1.138	1.184	1.22	1.258	1.303	1.33
Y^{++}	0.08467	0.10337	0.13164	0.14856	0.15136	0.15755	0.03268
Y^{--}	0.08179	0.10399	0.13432	0.14855	0.14827	0.15578	0.03140
Y^{+-}	0.09664	0.10357	0.11330	0.12428	0.12741	0.14882	0.03165
Y^{-+}	0.09887	0.10039	0.11499	0.12459	0.12216	0.14870	0.02566
Y^{++}_{empty}	0.01972	0.02228	0.01741	0.02325	0.03105	0.04566	0.00706
Y^{--}_{empty}	0.01761	0.01711	0.02277	0.02051	0.02881	0.04605	0.00767
Y^{+-}_{empty}	0.02144	0.02489	0.01750	0.02403	0.03352	0.04930	0.00591
Y^{-+}_{empty}	0.01947	0.02049	0.02229	0.02318	0.03215	0.04214	0.01101
Y^{++}_{rad}	0.02266	0.01450	0.00815	0.00626	0.00365	0.00314	0.00050
Y^{--}_{rad}	0.02306	0.01341	0.00849	0.00532	0.00390	0.00274	0.00059
Y^{+-}_{rad}	0.03419	0.02160	0.01282	0.00953	0.00761	0.00606	0.00116
Y^{-+}_{rad}	0.03646	0.02082	0.01388	0.00951	0.00701	0.00585	0.00087
A_R	-0.16723	0.17382	0.23771	0.25961	0.29194	0.09803	0.21278
δA_R^{stat}	0.02523	0.02877	0.02032	0.01981	0.02373	0.02729	0.05321
A_R^{beam}	0.03754	-0.02382	-0.00478	0.00140	-0.01076	0.00833	-0.11633
δA_R^{beam}	0.01297	0.01203	0.01011	0.00977	0.01099	0.01177	0.02641
A_R^{target}	0.00463	0.01632	-0.02093	-0.00133	0.04261	0.00962	0.21162
δA_R^{target}	0.00837	0.00785	0.00657	0.00635	0.00716	0.00764	0.01762
δP_R	0.00128	0.00120	0.00185	0.00200	0.00231	0.00083	0.00171
δA_R^{syst}	0.01964	0.01501	0.01127	0.00224	0.02288	0.00665	0.12511

Table 5.20: BLAST right sector yields and asymmetries for $Q^2 = 0.24\,GeV^2$, and for each $W\,[GeV]$ bin over the Δ region.

$W\,[GeV]$	1.096	1.138	1.184	1.22	1.258	1.303	1.33
Y^{++}	0.02598	0.04931	0.10313	0.11122	0.05334	0.00942	-
Y^{--}	0.02923	0.05135	0.09785	0.10884	0.05142	0.00855	-
Y^{+-}	0.03375	0.05447	0.10077	0.10996	0.05038	0.00835	-
Y^{-+}	0.03225	0.05537	0.10669	0.10379	0.05055	0.00736	-
Y^{++}_{empty}	0.00730	0.01595	0.01960	0.02070	0.02045	0.00572	-
Y^{--}_{empty}	0.00490	0.01635	0.02176	0.02189	0.01157	0.00314	-
Y^{+-}_{empty}	0.01195	0.01133	0.01528	0.01898	0.01220	0.00357	-
Y^{-+}_{empty}	0.00679	0.01691	0.02434	0.02113	0.01370	0.00371	-
Y^{++}_{rad}	0.00657	0.00562	0.00402	0.00235	0.00068	0.00004	-
Y^{--}_{rad}	0.00657	0.00642	0.00408	0.00216	0.00056	0.00004	-
Y^{+-}_{rad}	0.01008	0.00914	0.00753	0.00470	0.00111	0.00001	-
Y^{-+}_{rad}	0.01068	0.00981	0.00755	0.00413	0.00133	0.00006	-
A_L	-0.08767	-0.09892	-0.00757	0.04498	-0.01402	0.07188	-
δA_L^{stat}	0.04994	0.05234	0.02550	0.02326	0.04304	0.17625	-
A_L^{beam}	-0.11290	-0.01611	0.07175	-0.02241	0.03099	-0.01857	-
δA_L^{beam}	0.01594	0.01250	0.00790	0.00752	0.01297	0.05212	-
A_L^{target}	-0.04138	-0.04142	-0.00406	0.05062	0.02597	0.27168	-
δA_L^{target}	0.01595	0.01250	0.00790	0.00752	0.01297	0.05225	-
δP_L	0.00102	0.00088	0.00010	0.00052	0.00009	0.00120	-
δA_L^{syst}	0.06230	0.02304	0.03723	0.02868	0.02095	0.14106	-

Table 5.21: BLAST left sector yields and asymmetries for $Q^2 = 0.312\,GeV^2$, and for each $W\,[GeV]$ bin over the Δ region.

$W\,[GeV]$	1.096	1.138	1.184	1.22	1.258	1.303	1.33
Y^{++}	0.03378	0.05873	0.10431	0.11544	0.05301	0.00725	-
Y^{--}	0.03432	0.05779	0.10608	0.11808	0.05130	0.00756	-
Y^{+-}	0.03987	0.06213	0.09251	0.09681	0.04385	0.00720	-
Y^{-+}	0.03998	0.05594	0.09361	0.09879	0.04514	0.00748	-
Y^{++}_{empty}	0.00888	0.01169	0.01656	0.01656	0.01899	0.00280	-
Y^{--}_{empty}	0.00729	0.01749	0.01988	0.01761	0.01296	0.00604	-
Y^{+-}_{empty}	0.00936	0.01984	0.01861	0.01750	0.01774	0.00172	-
Y^{-+}_{empty}	0.01165	0.00973	0.02216	0.01447	0.01473	0.00461	-
Y^{++}_{rad}	0.01290	0.01181	0.00969	0.00559	0.00122	0.00013	-
Y^{--}_{rad}	0.01660	0.01490	0.00915	0.00503	0.00141	0.00000	-
Y^{+-}_{rad}	0.02062	0.01965	0.01441	0.00772	0.00200	0.00022	-
Y^{-+}_{rad}	0.02091	0.01994	0.01469	0.00798	0.00224	0.00014	-
A_R	-0.11618	0.19951	0.26662	0.22567	0.26644	-0.28586	-
δA_R^{stat}	0.04264	0.04443	0.02617	0.02176	0.05103	0.2129	-
A_R^{beam}	-0.00821	-0.06137	-0.00422	-0.00371	0.05143	-0.00511	-
δA_R^{beam}	0.02200	0.01714	0.01199	0.01090	0.02198	0.08426	-
A_R^{target}	-0.01225	0.09020	-0.01822	-0.02563	0.00708	-0.09237	-
δA_R^{target}	0.01432	0.01128	0.00780	0.00709	0.01414	0.05485	-
δP_R	0.00089	0.00061	0.00186	0.00162	0.00199	0.00226	-
δA_R^{syst}	0.00769	0.05652	0.00987	0.01351	0.02697	0.04798	-

Table 5.22: BLAST right sector yields and asymmetries for $Q^2 = 0.312\,GeV^2$, and for each $W\,[GeV]$ bin over the Δ region.

$Q^2\,[GeV^2]$	0.115	0.153	0.213	0.276	0.325
Y^{++}	2.25931	1.39387	0.72828	0.43890	0.17549
Y^{--}	2.24986	1.40882	0.72231	0.43856	0.17373
Y^{+-}	2.29763	1.43833	0.73033	0.44317	0.18305
Y^{-+}	2.30537	1.42972	0.72402	0.42979	0.18393
Y^{++}_{empty}	0.34157	0.23441	0.14576	0.10557	0.04870
Y^{--}_{empty}	0.36013	0.19453	0.13074	0.09387	0.05561
Y^{+-}_{empty}	0.37998	0.23417	0.15418	0.09391	0.04917
Y^{-+}_{empty}	0.38703	0.22561	0.15463	0.09147	0.05265
Y^{++}_{rad}	0.27497	0.16940	0.06507	0.01679	0.01033
Y^{--}_{rad}	0.27965	0.16997	0.06320	0.01670	0.01110
Y^{+-}_{rad}	0.33115	0.22535	0.09449	0.03108	0.02080
Y^{-+}_{rad}	0.32992	0.22652	0.09610	0.03042	0.02115
A_L	0.02257	0.03639	0.08460	0.02704	0.00109
δA_L^{stat}	0.00509	0.00650	0.01037	0.01310	0.02572
A_L^{beam}	0.00457	-0.00999	-0.00029	-0.02007	0.01116
δA_L^{beam}	0.00155	0.00195	0.00290	0.00393	0.00690
A_L^{target}	0.00045	-0.00269	0.01083	0.02112	0.00373
δA_L^{target}	0.00155	0.00195	0.00290	0.00393	0.00690
δP_L	0.00019	0.00036	0.00108	0.00047	0.00005
δA_L^{syst}	0.00239	0.00537	0.00572	0.01511	0.00610

Table 5.23: BLAST left sector yields and asymmetries for each $Q^2\,[GeV^2]$ bin over the Δ region, and for $x = [0.08, 0.48]$.

$Q^2\,[GeV^2]$	0.115	0.153	0.213	0.276	0.325
Y^{++}	2.37094	1.64190	0.88535	0.46715	0.18231
Y^{--}	2.38106	1.66964	0.88067	0.46567	0.18428
Y^{+-}	2.12929	1.48592	0.78355	0.41048	0.17862
Y^{-+}	2.15012	1.49565	0.79518	0.40431	0.17864
Y^{++}_{empty}	0.32878	0.22771	0.15087	0.10922	0.03470
Y^{--}_{empty}	0.33861	0.23379	0.14684	0.09802	0.04391
Y^{+-}_{empty}	0.37061	0.25648	0.16984	0.11031	0.04535
Y^{-+}_{empty}	0.33566	0.24239	0.14425	0.12132	0.03548
Y^{++}_{rad}	0.24375	0.15204	0.05940	0.01630	0.00789
Y^{--}_{rad}	0.24566	0.15311	0.05797	0.01638	0.00865
Y^{+-}_{rad}	0.31106	0.21142	0.09604	0.03127	0.01997
Y^{-+}_{rad}	0.30712	0.21730	0.09932	0.03211	0.02047
A_R	0.18201	0.19878	0.21672	0.26582	0.13007
δA_R^{stat}	0.00513	0.00600	0.00894	0.01409	0.02185
A_R^{beam}	0.00282	-0.00682	0.01236	-0.00747	-0.00715
δA_R^{beam}	0.00153	0.00184	0.00265	0.00408	0.00604
A_R^{target}	-0.00813	-0.01415	-0.00521	0.01228	-0.00734
δA_R^{target}	0.00153	0.00184	0.00265	0.00408	0.00604
δP_R	0.00139	0.00156	0.00169	0.00214	0.00102
δA_R^{syst}	0.00467	0.00829	0.00715	0.00775	0.00541

Table 5.24: BLAST right sector yields and asymmetries for each $Q^2\,[GeV^2]$ bin over the Δ region, and for $x = [0.08, 0.48]$.

x	0.103	0.146	0.2	0.258	0.317	0.385	0.438
Y^{++}	0.68076	1.44269	0.94318	0.30365	0.04427	-	-
Y^{--}	0.68522	1.45509	0.93173	0.30666	0.04674	-	-
Y^{+-}	0.71320	1.47487	0.95255	0.31618	0.05131	-	-
Y^{-+}	0.71616	1.46945	0.94764	0.32264	0.05635	-	-
Y^{++}_{empty}	0.13821	0.21858	0.10935	0.04712	0.00840	-	-
Y^{--}_{empty}	0.13980	0.20812	0.10431	0.04970	0.00767	-	-
Y^{+-}_{empty}	0.15098	0.24046	0.11499	0.04128	0.01318	-	-
Y^{-+}_{empty}	0.15437	0.22266	0.12235	0.05175	0.00602	-	-
Y^{++}_{rad}	0.03589	0.12809	0.14193	0.06662	0.02147	-	-
Y^{--}_{rad}	0.03537	0.13164	0.14512	0.06771	0.01959	-	-
Y^{+-}_{rad}	0.04519	0.17227	0.17752	0.08164	0.02573	-	-
Y^{-+}_{rad}	0.04488	0.17427	0.17910	0.08235	0.02711	-	-
A_L	-0.01563	0.03286	0.04721	-0.00669	-0.04697	-	-
δA_L^{stat}	0.00968	0.00610	0.00721	0.01625	0.04996	-	-
A_L^{beam}	-0.00430	-0.00729	0.00394	0.00654	0.03160	-	-
δA_L^{beam}	0.00374	0.00191	0.00226	0.00410	0.01060	-	-
A_L^{target}	-0.00318	-0.00286	0.00987	-0.01798	-0.09256	-	-
δA_L^{target}	0.00374	0.00191	0.00226	0.00410	0.01059	-	-
δP_L	0.00010	0.00029	0.00054	0.00007	0.00163	-	-
δA_L^{syst}	0.00277	0.00407	0.00553	0.00992	0.05069	-	-

Table 5.25: BLAST left sector yields and asymmetries for $0.08 < Q^2 < 0.18\,GeV^2$, and for each x bin over the Δ region.

x	0.103	0.146	0.2	0.258	0.317	0.385	0.438
Y^{++}	0.65667	1.60814	1.05428	0.31185	0.04638	-	-
Y^{--}	0.65942	1.60794	1.05986	0.31445	0.04339	-	-
Y^{+-}	0.64743	1.41149	0.91052	0.30966	0.04866	-	-
Y^{-+}	0.64075	1.42102	0.91579	0.30736	0.04875	-	-
Y^{++}_{empty}	0.12298	0.22040	0.09559	0.03957	0.00608	-	-
Y^{--}_{empty}	0.11740	0.23379	0.11211	0.04290	0.00767	-	-
Y^{+-}_{empty}	0.14309	0.24514	0.11339	0.03808	0.00912	-	-
Y^{-+}_{empty}	0.12568	0.22266	0.10338	0.04868	0.00474	-	-
Y^{++}_{rad}	0.03103	0.11956	0.12833	0.08271	0.01697	-	-
Y^{--}_{rad}	0.03150	0.12181	0.12668	0.08425	0.01802	-	-
Y^{+-}_{rad}	0.04500	0.17148	0.16912	0.10967	0.02162	-	-
Y^{-+}_{rad}	0.04494	0.17204	0.17027	0.10818	0.02107	-	-
A_R	0.08023	0.20473	0.24303	0.17412	0.00357	-	-
δA_R^{stat}	0.01004	0.00606	0.00689	0.01569	0.04958	-	-
A_R^{beam}	0.00322	0.00384	-0.00017	-0.00910	0.04042	-	-
δA_R^{beam}	0.00372	0.00187	0.00217	0.00401	0.01076	-	-
A_R^{target}	-0.02510	-0.00367	-0.00612	-0.00056	0.03802	-	-
δA_R^{target}	0.00372	0.00187	0.00217	0.00401	0.01076	-	-
δP_R	0.00075	0.00162	0.00185	0.00090	0.00024	-	-
δA_R^{syst}	0.01313	0.00320	0.00367	0.00481	0.02875	-	-

Table 5.26: BLAST right sector yields and asymmetries for $0.08 < Q^2 < 0.18\,GeV^2$, and for each x bin over the Δ region.

x	0.103	0.146	0.2	0.258	0.317	0.385	0.438
Y^{++}	-	0.02838	0.39870	0.57691	0.40939	0.21409	0.07678
Y^{--}	-	0.02714	0.39340	0.57862	0.39992	0.20862	0.08151
Y^{+-}	-	0.03172	0.39688	0.57239	0.40826	0.22048	0.08290
Y^{-+}	-	0.02969	0.39694	0.55794	0.40133	0.22081	0.08673
Y^{++}_{empty}	-	0.00803	0.08840	0.10411	0.07537	0.04420	0.02788
Y^{--}_{empty}	-	0.01019	0.07600	0.09487	0.06656	0.04668	0.02353
Y^{+-}_{empty}	-	0.00751	0.09354	0.09662	0.07419	0.04363	0.02699
Y^{-+}_{empty}	-	0.01140	0.09775	0.10287	0.05906	0.05854	0.02037
Y^{++}_{rad}	-	0.00089	0.01505	0.02760	0.03636	0.02690	0.00893
Y^{--}_{rad}	-	0.00069	0.01443	0.02755	0.03710	0.02614	0.00928
Y^{+-}_{rad}	-	0.00164	0.02250	0.04221	0.05278	0.03821	0.01542
Y^{-+}_{rad}	-	0.00154	0.02282	0.04034	0.05124	0.03922	0.01606
A_L	-	-0.08925	0.06608	0.05653	0.03449	0.05891	-0.02195
δA_L^{stat}	-	0.06502	0.01387	0.01006	0.01235	0.02085	0.04346
A_L^{beam}	-	-0.02040	0.00901	-0.01745	0.00386	0.01832	-0.00859
δA_L^{beam}	-	0.01707	0.00409	0.00315	0.00373	0.00568	0.01054
A_L^{target}	-	0.08454	0.00881	0.01374	0.02493	0.01627	-0.08161
δA_L^{target}	-	0.01706	0.00409	0.00315	0.00373	0.00568	0.01054
δP_L	-	0.00108	0.00085	0.00073	0.00046	0.00063	0.00018
δA_L^{syst}	-	0.04507	0.00659	0.01153	0.01308	0.01271	0.04251

Table 5.27: BLAST left sector yields and asymmetries for $0.18 < Q^2 < 0.38\,GeV^2$, and for each x bin over the Δ region.

x	0.103	0.146	0.2	0.258	0.317	0.385	0.438
Y^{++}	-	0.03162	0.47936	0.67306	0.46015	0.23984	0.08875
Y^{--}	-	0.03097	0.49042	0.68536	0.46006	0.24057	0.08588
Y^{+-}	-	0.03061	0.43966	0.57224	0.40443	0.23644	0.09357
Y^{-+}	-	0.02750	0.44618	0.57933	0.40971	0.23793	0.09071
Y^{++}_{empty}	-	0.01181	0.08865	0.11069	0.07622	0.05224	0.02118
Y^{--}_{empty}	-	0.00755	0.08267	0.11853	0.06581	0.04655	0.01937
Y^{+-}_{empty}	-	0.00801	0.10624	0.11634	0.08418	0.05336	0.02760
Y^{-+}_{empty}	-	0.00896	0.10326	0.10697	0.07187	0.05444	0.02152
Y^{++}_{rad}	-	0.00124	0.01774	0.03153	0.04013	0.02826	0.00871
Y^{--}_{rad}	-	0.00127	0.01720	0.03192	0.03915	0.02738	0.01023
Y^{+-}_{rad}	-	0.00185	0.02845	0.04837	0.05902	0.04269	0.01728
Y^{-+}_{rad}	-	0.00183	0.02910	0.05080	0.05917	0.04398	0.01793
A_R	-	0.07771	0.19496	0.23260	0.23900	0.14162	0.13146
δA_R^{stat}	-	0.06358	0.01197	0.00966	0.01175	0.01925	0.03457
A_R^{beam}	-	-0.06119	-0.00634	-0.00517	0.00765	0.00208	0.00012
δA_R^{beam}	-	0.01727	0.00369	0.00304	0.00361	0.00521	0.00904
A_R^{target}	-	0.10215	-0.02436	-0.01911	-0.00734	-0.00611	0.04582
δA_R^{target}	-	0.01727	0.00369	0.00304	0.00361	0.00521	0.00904
δP_R	-	0.00065	0.00153	0.00179	0.00177	0.00099	0.00083
δA_R^{syst}	-	0.06169	0.01313	0.01041	0.00577	0.00349	0.02375

Table 5.28: BLAST right sector yields and asymmetries for $0.18 < Q^2 < 0.38\,GeV^2$, and for each x bin over the Δ region.

APPENDIX D

Spin Correlation Parameters Values and Total Errors

In this appendix we present the values and errors for the results given in section 5.2. The following notation is used:

W	: average W value
Q^2	: average Q^2 value
x	: average x value
$x^*_{L,R}$	: average target spin angle $x-$component in the $q-$system for left and right sectors
$z^*_{L,R}$	: average target spin angle $z-$component in the $q-$system for left and right sectors
ϵ	: average virtual photon transverse polarization
ω	: average virtual photon energy
γ	: average γ value
$A_{TT'}$	: extracted $A_{TT'}$ value
$\delta A^{stat}_{TT'}$	: $A_{TT'}$ statistical errors
$\delta A^{syst}_{TT'}$	: $A_{TT'}$ systematical errors
$A_{TL'}$	: extracted $A_{TL'}$ value
$\delta A^{stat}_{TL'}$	: $A_{TL'}$ statistical errors
$\delta A^{syst}_{TL'}$	: $A_{TL'}$ systematical errors
$g_{1,2}/\sigma_0$	: extracted proton spin-structure functions over the unpolarized cross section
$\delta g^{stat}_{1,2}$	: $g_{1,2}/\sigma_0$ statistical errors
$\delta g^{syst}_{1,2}$	: $g_{1,2}/\sigma_0$ systematical errors

$W\,[GeV]$	1.096	1.138	1.184	1.22	1.258	1.303	1.33
x_L^*	0.99362	0.98992	0.97894	0.96385	0.94444	0.92226	0.89883
x_R^*	-0.09414	-0.18610	-0.26624	-0.33445	-0.39591	-0.45600	-0.50717
z_L^*	-0.00300	0.08731	0.17109	0.24215	0.30876	0.36967	0.42344
z_R^*	0.98923	0.97634	0.95751	0.93582	0.91143	0.88289	0.85478
ϵ	0.83852	0.80842	0.77071	0.72617	0.67210	0.60434	0.52011
$A_{TT'}$	-0.12421	0.17616	0.28963	0.27125	0.21139	0.14504	0.20406
$\delta A_{TT'}^{stat}$	0.01526	0.01749	0.01117	0.00850	0.01152	0.01597	0.02030
$\delta A_{TT'}^{syst}$	0.08353	0.01872	0.07068	0.07151	0.05124	0.03362	0.05916
$A_{TL'}$	-0.11226	-0.10912	-0.00687	0.00797	-0.02212	-0.03220	-0.06221
$\delta A_{TL'}^{stat}$	0.01617	0.01761	0.01027	0.00792	0.01025	0.01511	0.01782
$\delta A_{TL'}^{syst}$	0.02165	0.03897	0.05464	0.04910	0.04819	0.02219	0.04004

Table 5.29: Extracted spin-correlation parameters for $Q^2 = 0.123\,GeV^2$, and for each $W\,[GeV]$ bin over the Δ region.

$W\,[GeV]$	1.096	1.138	1.184	1.22	1.258	1.303	1.33
x_L^*	0.99226	0.98733	0.97700	0.96228	0.94401	0.92191	0.89819
x_R^*	-0.10526	-0.18932	-0.26651	-0.33094	-0.39209	-0.44811	-0.49838
z_L^*	0.01838	0.10025	0.17589	0.24316	0.30673	0.36663	0.42159
z_R^*	0.98693	0.97453	0.95635	0.93622	0.91204	0.88604	0.85878
ϵ	0.77936	0.73938	0.69102	0.63540	0.57295	0.50476	0.42919
$A_{TT'}$	-0.16221	0.13397	0.24751	0.29079	0.18607	0.21105	0.13563
$\delta A_{TT'}^{stat}$	0.02004	0.02057	0.01329	0.01080	0.01269	0.01875	0.02642
$\delta A_{TT'}^{syst}$	0.08604	0.01311	0.07072	0.06996	0.03960	0.05323	0.02842
$A_{TL'}$	-0.16387	-0.00846	0.07280	-0.00017	-0.04326	-0.03466	-0.11063
$\delta A_{TL'}^{stat}$	0.02088	0.02085	0.01321	0.01089	0.01313	0.01832	0.02547
$\delta A_{TL'}^{syst}$	0.02362	0.01488	0.03595	0.04146	0.02593	0.02532	0.03212

Table 5.30: Extracted spin-correlation parameters for $Q^2 = 0.175\,GeV^2$, and for each $W\,[GeV]$ bin over the Δ region.

$W\,[GeV]$	1.096	1.138	1.184	1.22	1.258	1.303	1.33
x_L^*	0.98955	0.98295	0.97207	0.95527	0.93393	0.91157	0.89622
x_R^*	-0.14602	-0.21400	-0.28423	-0.35220	-0.41775	-0.46705	-0.50073
z_L^*	0.06072	0.13105	0.19768	0.26820	0.33382	0.39032	0.42476
z_R^*	0.98127	0.96869	0.95023	0.92721	0.89963	0.87512	0.85646
ϵ	0.69572	0.65802	0.60862	0.53765	0.45368	0.38360	0.35453
$A_{TT'}$	-0.18149	0.19363	0.25536	0.28034	0.30019	0.07226	0.27250
$\delta A_{TT'}^{stat}$	0.02604	0.02998	0.02125	0.02062	0.02518	0.02962	0.06710
$\delta A_{TT'}^{syst}$	0.05014	0.04752	0.06334	0.07152	0.07395	0.01332	0.09306
$A_{TL'}$	-0.07441	0.06421	0.01741	0.00093	-0.05238	-0.07449	0.04115
$\delta A_{TL'}^{stat}$	0.02946	0.03212	0.02060	0.01808	0.02344	0.02857	0.07859
$\delta A_{TL'}^{syst}$	0.02474	0.02858	0.03110	0.03180	0.03915	0.01091	0.02303

Table 5.31: Extracted spin-correlation parameters for $Q^2 = 0.24\,GeV^2$, and for each $W\,[GeV]$ bin over the Δ region.

$W\,[GeV]$	1.096	1.138	1.184	1.22	1.258	1.303	1.33
x_L^*	0.98434	0.97487	0.96120	0.94463	0.92471	0.90263	0.87807
x_R^*	-0.20889	-0.26948	-0.32681	-0.380361	-0.42498	-0.47240	-0.51960
z_L^*	0.12078	0.18232	0.24364	0.30032	0.35563	0.41095	0.45865
z_R^*	0.96986	0.95510	0.93665	0.91559	0.89510	0.86911	0.84557
ϵ	0.59804	0.54943	0.50155	0.44933	0.39198	0.33217	-
$A_{TT'}$	-0.13539	0.17123	0.25900	0.23520	0.24562	-0.22896	-
$\delta A_{TT'}^{stat}$	0.04447	0.04697	0.02735	0.02318	0.05252	0.21805	-
$\delta A_{TT'}^{syst}$	0.04264	0.01443	0.03403	0.04996	0.04442	0.02447	-
$A_{TL'}$	-0.07245	-0.13350	-0.07353	-0.02715	-0.10963	0.18388	-
$\delta A_{TL'}^{stat}$	0.04964	0.05147	0.02505	0.02257	0.04286	0.17711	-
$\delta A_{TL'}^{syst}$	0.01641	0.01541	0.03095	0.02721	0.03114	0.04690	-

Table 5.32: Extracted spin-correlation parameters for $Q^2 = 0.312\,GeV^2$, and for each $W\,[GeV]$ bin over the Δ region.

$Q^2\,[GeV^2]$	0.115	0.153	0.213	0.276	0.325
x_L^*	0.95113	0.95414	0.95192	0.94343	0.95664
x_R^*	-0.34964	-0.34178	-0.33282	-0.37343	-0.32166
z_L^*	0.26355	0.24833	0.25834	0.29453	0.25143
z_R^*	0.92330	0.92529	0.92860	0.91549	0.93608
ϵ	0.68176	0.62743	0.56441	0.47396	0.48192
$\omega\,[GeV]$	0.42055	0.43107	0.44496	0.48280	0.44813
γ	0.85348	0.98915	1.09949	1.13248	1.32120
x	0.15540	0.21529	0.27247	0.32382	0.41244
g_1/σ_0	-0.14127	-0.13558	-0.15645	-0.10252	-0.02688
δg_1^{stat}	0.00659	0.00688	0.01003	0.01240	0.01686
δg_1^{syst}	0.04396	0.04760	0.05670	0.04667	0.03178
g_2/σ_0	0.19640	0.16184	0.12472	0.17701	0.05697
δg_2^{stat}	0.00775	0.00697	0.01003	0.01083	0.01183
δg_2^{syst}	0.13841	0.09227	0.05860	0.06710	0.03668

Table 5.33: Extracted spin-structure functions over σ_0 for each $Q^2\,[GeV^2]$ bin over the Δ region.

x	0.103	0.146	0.2	0.258	0.317	0.385	0.438
x_L^*	0.28194	0.94192	0.97293	0.98846	0.99185	-	-
x_R^*	-0.48953	-0.39684	-0.28112	-0.17274	-0.11874	-	-
z_L^*	0.78852	0.30734	0.18796	0.08381	0.03819	-	-
z_R^*	0.86489	0.90836	0.95044	0.97682	0.98547	-	-
ϵ	0.52647	0.64368	0.72682	0.78128	0.78646	-	-
$\omega\,[GeV]$	0.54450	0.44958	0.36606	0.30011	0.27757	-	-
γ	0.41433	0.80188	1.03719	1.28982	1.46232	-	-
g_1/σ_0	0.08622	-0.17855	-0.17008	-0.06312	0.02413	-	-
δg_1^{stat}	0.02338	0.00833	0.00723	0.01204	0.02970	-	-
δg_1^{syst}	0.03116	0.05183	0.06915	0.04166	0.08419	-	-
g_2/σ_0	0.04711	0.25617	0.17128	0.08386	0.01031	-	-
δg_2^{stat}	0.06457	0.01048	0.00696	0.00918	0.01993	-	-
δg_2^{syst}	0.17439	0.15628	0.12734	0.06207	0.08308	-	-

Table 5.34: Extracted spin-structure functions over σ_0 for each x bin over the Δ region, and for $0.08 < Q^2 < 0.18\,[GeV^2]$; $\langle Q^2 \rangle = 0.129\,[GeV^2]$.

x	0.103	0.146	0.2	0.258	0.317	0.385	0.438
x_L^*	-	0.90050	0.92736	0.94955	0.96264	0.96992	0.974322
x_R^*	-	-0.48687	-0.42420	-0.35336	-0.29879	-0.26007	-0.25276
z_L^*	-	0.41500	0.3483459	0.27660	0.22242	0.18934	0.17614
z_R^*	-	0.86411	0.89558	0.92436	0.94240	0.95395	0.95774
ϵ	-	0.42513	0.49321	0.54729	0.57158	0.57786	0.56037
$\omega\,[GeV]$	-	0.57193	0.51448	0.45932	0.42134	0.39774	0.39134
γ	-	0.75391	0.89000	1.05626	1.22177	1.36288	1.46585
g_1/σ_0	-	0.09192	-0.17566	-0.14537	-0.09949	-0.07021	-0.01305
δg_1^{stat}	-	0.10230	0.01679	0.01005	0.00979	0.01317	0.02272
δg_1^{syst}	-	0.07838	0.04793	0.04997	0.04453	0.04001	0.06586
g_2/σ_0	-	0.24592	0.19477	0.16393	0.12283	0.04485	0.04474
δg_2^{stat}	-	0.14230	0.01936	0.00944	0.00779	0.00916	0.01383
δg_2^{syst}	-	0.12534	0.07004	0.06820	0.05740	0.03778	0.06741

Table 5.35: Extracted spin-structure functions over σ_0 for each x bin over the Δ region, and for $0.18 < Q^2 < 0.38\,[GeV^2]$; $\langle Q^2 \rangle = 0.225\,[GeV^2]$.

APPENDIX E

Asymmetries Values and Errors (Extra Cases)

Note that the notation in this appendix is the same as **Appendices C,D**.

$Q^2\,[GeV^2]$	0.115	0.153	0.213	0.276	0.325
Y^{++}	2.11020	1.23046	0.41986	0.09438	-
Y^{--}	2.09916	1.24172	0.41867	0.09535	-
Y^{+-}	2.14945	1.25796	0.42148	0.09875	-
Y^{-+}	2.15006	1.24373	0.40995	0.09016	-
Y^{++}_{empty}	0.29639	0.20372	0.09802	0.03080	-
Y^{--}_{empty}	0.30703	0.17138	0.08946	0.03133	-
Y^{+-}_{empty}	0.32686	0.20139	0.09428	0.03229	-
Y^{-+}_{empty}	0.33002	0.19921	0.10236	0.03074	-
Y^{++}_{rad}	0.27023	0.11407	0.01532	0.00115	-
Y^{--}_{rad}	0.27577	0.11543	0.01434	0.00109	-
Y^{+-}_{rad}	0.32637	0.15421	0.02428	0.00279	-
Y^{-+}_{rad}	0.32453	0.15694	0.02442	0.00236	-
A_L	0.02098	0.03952	0.05445	0.03497	-
δA_L^{stat}	0.00511	0.00656	0.01302	0.03459	-
A_L^{beam}	0.00168	-0.00638	-0.00855	-0.04249	-
δA_L^{beam}	0.00157	0.00208	0.00398	0.01018	-
A_L^{target}	0.00150	0.00074	0.01052	0.03385	-
δA_L^{target}	0.00157	0.00208	0.00398	0.01018	-
δP_L	0.00024	0.00046	0.00063	0.00041	-
δA_L^{syst}	0.00239	0.00538	0.00565	0.01510	-

Table 5.36: BLAST left sector yields and asymmetries for each $Q^2\,[GeV^2]$ bin over the Δ region, and for $x = [0.08, 0.28]$.

$Q^2\,[GeV^2]$	0.115	0.153	0.213	0.276	0.325
Y^{++}	2.22461	1.46770	0.49300	0.10485	-
Y^{--}	2.23066	1.49453	0.49176	0.10222	-
Y^{+-}	1.98650	1.30835	0.42324	0.08949	-
Y^{-+}	2.01035	1.31234	0.43135	0.08927	-
Y^{++}_{empty}	0.28092	0.19678	0.08901	0.03494	-
Y^{--}_{empty}	0.30237	0.21051	0.08695	0.03309	-
Y^{+-}_{empty}	0.31909	0.22419	0.09841	0.03192	-
Y^{-+}_{empty}	0.28890	0.21292	0.09467	0.03420	-
Y^{++}_{rad}	0.23975	0.10606	0.01577	0.00086	-
Y^{--}_{rad}	0.24183	0.10529	0.01463	0.00126	-
Y^{+-}_{rad}	0.30690	0.15012	0.02794	0.00258	-
Y^{-+}_{rad}	0.30348	0.15621	0.02822	0.00240	-
A_R	0.18471	0.20574	0.23297	0.22276	-
δA_R^{stat}	0.00269	0.00319	0.00622	0.01913	-
A_R^{beam}	0.00256	-0.00503	0.00688	0.01090	-
δA_R^{beam}	0.00155	0.00195	0.00369	0.01037	-
A_L^{target}	-0.00427	-0.00677	-0.00499	0.01295	-
δA_R^{target}	0.00155	0.00195	0.00369	0.01037	-
δP_R	0.00142	0.00158	0.00179	0.00171	-
δA_R^{syst}	0.00468	0.00829	0.00718	0.00764	-

Table 5.37: BLAST right sector yields and asymmetries for each $Q^2\,[GeV^2]$ bin over the Δ region, and for $x = [0.08, 0.28]$.

$Q^2\,[GeV^2]$	0.115	0.153	0.213	0.276	0.325
Y^{++}	0.00831	0.15762	0.30841	0.34427	0.16050
Y^{--}	0.00776	0.16070	0.30363	0.34260	0.15595
Y^{+-}	0.00767	0.17346	0.30884	0.34391	0.16085
Y^{-+}	0.00868	0.17987	0.31406	0.33892	0.16316
Y^{++}_{empty}	0.00012	0.03032	0.04773	0.07476	0.04237
Y^{--}_{empty}	0.00591	0.02227	0.04127	0.06253	0.04819
Y^{+-}_{empty}	0.00061	0.02982	0.05990	0.06162	0.04116
Y^{-+}_{empty}	0.00294	0.02382	0.05227	0.06072	0.04842
Y^{++}_{rad}	0.00473	0.05532	0.04974	0.01553	0.00684
Y^{--}_{rad}	0.00387	0.05454	0.04885	0.01550	0.00743
Y^{+-}_{rad}	0.00478	0.07114	0.07021	0.02810	0.01427
Y^{-+}_{rad}	0.00536	0.06957	0.07168	0.02786	0.01449
A_L	-0.55903	-0.01828	0.13049	0.02550	0.02659
δA_L^{stat}	0.64499	0.02808	0.01537	0.01304	0.02501
A_L^{beam}	0.06835	0.00615	0.01021	-0.00323	0.01661
δA_L^{beam}	0.02937	0.00565	0.00422	0.00425	0.00723
A_L^{target}	-0.02032	-0.01756	-0.00044	0.00648	0.00542
δA_L^{target}	0.02939	0.00565	0.00422	0.00425	0.00723
δP_L	0.00648	0.00021	0.00151	0.00030	0.00031
δA_L^{syst}	0.00690	0.00537	0.00582	0.01510	0.00610

Table 5.38: BLAST left sector yields and asymmetries for each $Q^2\,[GeV^2]$ bin over the Δ region, and for $x = [0.28, 0.48]$.

$Q^2\,[GeV^2]$	0.115	0.153	0.213	0.276	0.325
Y^{++}	0.00863	0.16680	0.39235	0.36182	0.16229
Y^{--}	0.00769	0.16696	0.38890	0.36288	0.16447
Y^{+-}	0.00898	0.17219	0.36030	0.32044	0.15295
Y^{-+}	0.00917	0.17677	0.36383	0.31440	0.15476
Y^{++}_{empty}	0.00024	0.02983	0.06186	0.07415	0.02898
Y^{--}_{empty}	0.00163	0.02189	0.05989	0.06480	0.03724
Y^{+-}_{empty}	0.00135	0.02649	0.07136	0.07838	0.03734
Y^{-+}_{empty}	0.00064	0.02690	0.04958	0.08711	0.02856
Y^{++}_{rad}	0.00400	0.04598	0.04362	0.01531	0.00526
Y^{--}_{rad}	0.00383	0.04782	0.04333	0.01504	0.00555
Y^{+-}_{rad}	0.00415	0.06130	0.06810	0.02862	0.01340
Y^{-+}_{rad}	0.00363	0.06108	0.07110	0.02949	0.01358
A_R	-0.21830	0.07755	0.19503	0.27772	0.13992
δA_R^{stat}	0.13523	0.02431	0.01284	0.01426	0.02139
A_R^{beam}	0.03995	0.00824	0.00586	-0.00716	-0.00079
δA_R^{beam}	0.02356	0.00569	0.00382	0.00442	0.00635
A_L^{target}	0.02604	-0.00866	-0.00006	0.00509	-0.00847
δA_R^{target}	0.02356	0.00569	0.00382	0.00442	0.00635
δP_R	0.00168	0.00060	0.00150	0.00213	0.00107
δA_R^{syst}	0.00414	0.04564	0.04402	0.05724	0.02268

Table 5.39: BLAST right sector yields and asymmetries for each $Q^2\,[GeV^2]$ bin over the Δ region, and for $x = [0.28, 0.48]$.

$Q^2\,[GeV^2]$	0.115	0.153	0.213	0.276	0.325
x_L^*	0.95097	0.94931	0.93345	0.91370	-
x_R^*	-0.35067	-0.36401	-0.40716	-0.45301	-
z_L^*	0.26450	0.27264	0.32940	0.38337	-
z_R^*	0.92303	0.91868	0.90238	0.88157	-
ϵ	0.69527	0.61152	0.49422	0.38370	-
$\omega\,[GeV]$	0.41029	0.44678	0.50361	0.55592	-
γ	0.87086	0.94003	0.95049	0.94110	-
x	0.15879	0.20396	0.23944	0.26195	-
g_1/σ_0	-0.14157	-0.15051	-0.16096	-0.11830	-
δg_1^{stat}	0.00638	0.00730	0.01453	0.04354	-
δg_1^{syst}	0.04156	0.04363	0.05021	0.04544	-
g_2/σ_0	0.20174	0.18686	0.21381	0.23406	-
δg_2^{stat}	0.00737	0.00783	0.01544	0.04678	-
δg_2^{syst}	0.13678	0.09328	0.05271	0.07200	-

Table 5.40: Extracted spin-structure functions over σ_0 for each $Q^2\,[GeV^2]$ bin over the Δ region, and $x = [0.08, 0.28]$.

$Q^2\,[GeV^2]$	0.115	0.153	0.213	0.276	0.325
x_L^*	0.99357	0.98949	0.97777	0.95207	0.95404
x_R^*	-0.09659	-0.16256	-0.23909	-0.34970	-0.33277
z_L^*	0.01065	0.07053	0.15895	0.26879	0.26216
z_R^*	0.98924	0.97857	0.96167	0.92562	0.93246
ϵ	0.82525	0.75949	0.65283	0.49903	0.47279
$\omega\,[GeV]$	0.25352	0.30240	0.37177	0.46253	0.45683
γ	1.45478	1.38473	1.30095	1.18534	1.28923
x	0.28586	0.30671	0.33152	0.34090	0.40131
g_1/σ_0	0.37904	-0.01428	-0.14611	-0.09880	-0.04828
δg_1^{stat}	0.33690	0.01757	0.01033	0.01138	0.01724
δg_1^{syst}	0.09213	0.02831	0.04754	0.03504	0.01247
g_2/σ_0	0.04326	0.03372	0.05687	0.16174	0.06029
δg_2^{stat}	0.16581	0.01198	0.00748	0.00950	0.01248
δg_2^{syst}	0.00414	0.04564	0.04402	0.05724	0.02268

Table 5.41: Extracted spin-structure functions over σ_0 for each $Q^2\,[GeV^2]$ bin over the Δ region, and $x = [0.28, 0.48]$.